PRECISION ENGINEERING CENTER

2005 ANNUAL REPORT
VOLUME XXIII
March 2006

Sponsors:

3M Corporation
Electro-Optics Center at Pennsylvania State University
Los Alamos National Laboratory
Missile Defense Agency
National Aeronautics and Space Administration
National Science Foundation
Optical Research Associates
Precitech Precision, Inc.
Sandia National Laboratory
Vistakon, Johnson & Johnson Vision Care Inc.

Faculty:

Thomas Dow, Editor
Jeffrey Eischen
Ronald Scattergood
Greg Buckner
Paul Ro
David Youden

Graduate Students:

David Brehl
Nathan Buescher
Tim Kennedy
Nadim Wanna
Yanbo Yin
Brett Brocato
Kara Folkert
Lucas Lamonds
Robert Woodside

Undergraduate Students:

Robert Powell

Staff:

Kenneth Garrard
Roxie Gold
Alexander Sohn

TABLE OF CONTENTS

SUMMARY

The goals of the Precision Engineering Center are: 1) to improve the understanding and capability of precision metrology, actuation, manufacturing and assembly processes; and 2) to train a new generation of engineers and scientists with the background and experience to transfer this new knowledge to industry. Because the problems related to precision engineering originate from a variety of sources, significant progress can only be achieved by applying a multidisciplinary approach; one in which the faculty, students, staff and sponsors work together to identify important research issues and find the optimum solutions. Such an environment has been created and nurtured at the PEC for over 22 years; the new technology that has been developed and nearly 100 graduates attest to the quality of the results.

The 2004 Annual Report summarizes the progress over the past year by the faculty, students and staff in the Precision Engineering Center. During the past year, this group included 7 faculty, 13 graduate students, 1 undergraduate student, 2 full-time technical staff members and 1 administrative staff member. Representing two different Departments from the College of Engineering, this diverse group of scientists and engineers provides a wealth of experience to address precision engineering problems. The format of this Annual Report separates the research effort into individual projects; however, this should not obscure the significant interaction that occurs among the faculty, staff and students. Weekly seminars by the students and faculty provide information exchange and feedback as well as practice in technical presentations. Teamwork and group interactions are a hallmark of research at the PEC and this contributes to both the quality of the research as well as the education of the graduates.

The summaries of individual projects that follow are arranged in the same order as the body of the report, that is the five broad categories of 1) design, 2) fabrication, 3) metrology, 4) actuation and 5) control.

1) DESIGN

The emphasis of the metrology projects has been to develop new techniques that can be used to predict surface shape as well as measure important parameters such as tool force.

Design Tools For Freeform Optics

Freeform optical surfaces can be used to control astigmatism at multiple locations in an image. As a result, a freeform surface may replace multiple spherical and aspheric reflective components in a complex optical system. Unfortunately, designers have been reluctant to use freeform or even aspheric surfaces, in most systems, because of the difficulty of obtaining optics that meet form and finish requirements at acceptable cost. A project is in progress with Optical

Research Associates (ORA), the producers of CODE V, to remedy this obstacle by providing feedback to the designer on the manufacturability of an optical surface as part of the design process. Additional parameters such as surface sag, relative cost estimates and allowable form errors can now be included in the system optimization process.

Surface Deconvolution for Diamond Turning

Free-form optical systems can be fabricated using a Diamond Turning Machine (DTM) and a Fast Tool Servo (FTS). The DTM creates the rotationally symmetric component and the FTS simultaneously adds the Non-Rotationally Symmetric (NRS) component to create the desired surface shape. Synchronization between the DTM axes and the FTS is critical if the correct freeform shape is to be produced. The errors caused by the FTS dynamics can be corrected if they are known, repeatable and used to modify the input command to the actuator. The concept for determining the modified input command is known as deconvolution and is a standard element of digital signal processing. It is a form of feed-forward control, but the entire tool path is used to create the modified signal rather than the current value. As a result, the command is not related to the position feedback, so there is no delay in the response. Two demonstrations are presented, an off-center sphere and a cosine wave. For each shape, the surface produced was dramatically improved when compared with the uncompensated shape.

2) FABRICATION

Fabrication of precision components is an emphasis area for the PEC. Current projects include machining of single crystal silicon, MEMS devices and freeform optics.

Analysis Of High Pressure Phase Transformations in Single Crystal Silicon

Diamond cubic silicon (Si-I) is a brittle material under standard temperature and pressure, but when exposed to a high pressure environment, the crystal structure transforms into a ductile ®-tin metallic phase (Si-II). Once the Si-II is unconstrained, it back-transforms into multiple forms of Si, mainly amorphous Si (a-Si) and Si-I. This transformation allows silicon to be machined without brittle fracture occurring, but the back transformation alters the surface (~500 nm in depth). ßIn situ analysis of this transformation during the manufacturing process is impractical. Using transmission electron microscopy (TEM), specifically cross sectional TEM (XTEM) and Raman spectroscopy, a portrait can be formed of how and why the transformations occur.

Micromachining using EVAM

The goal of this research is to demonstrate Elliptical Vibration Assisted Machining (EVAM) as a 3-D micro-structuring tool for MEMS applications. While many MEMS (MicroElectroMechanicalSystems) devices are fabricated using silicon etching techniques developed for the microelectronics industry, micro-machining is an attractive alternative because

of its low start-up cost relative to other capital-intensive MEMS technologies, applicability to a wide range of materials, high flexibility of feature geometry and low cost for prototype manufacturing. The Ultramill Elliptical Vibration Assisted Machining (EVAM) system has unique capabilities among micro-machining techniques. Its features include zero runout and a tunable vibrating tool path. Three-dimensional structures with 15 µm plan-view features, 500 nm elevation features, and 20 nm RMS surface finish have been achieved on a 200 µm part scale.

Live Axis Diamond Turning

The term Live-Axis turning (LAT) has been coined to describe a lightweight, linear-motor driven, air bearing slide that can be used to fabricate non-rotationally symmetric optical components. The system described is the result of a joint effort by the PEC and Precitech to create a long-range fast tool servo to fabricate future NASA optics. The slide uses a triangular cross-section, lightweight (0.6 Kg) honeycomb aluminum piston driven by a linear motor (27 N maximum force) resulting in an acceleration capability of 45 g. The LAT axis has been mounted on a Nanoform 600 diamond turning machine and both flat surfaces and tilted flat surfaces have been machined. The flat surfaces had surface finishes of 75 nm rms and the tilted flat surfaces, using a maximum stroke of ±2 mm at 20 Hz, had a surface finish of 240 nm rms. Current efforts are centered on the control system to improve the surface finish and figure error.

3) METROLOGY

Metrology is at the heart of precision engineering – from measuring fabricated parts to calibration artifacts to dynamic system characterization. Several of these areas have been addressed in research programs.

Metrology Artifact Design

After a part has been manufactured, the part is measured to determine whether it is within its tolerance region. These measurements are often taken on Coordinate Measuring Machines (CMMs). Traditionally, a calibration artifact determines the static influences of the machine such as machine geometry. The goal of this project is to design and fabricate a calibration artifact that will test the CMM dynamically and determine the effects of those influences. The artifact developed is a ring gauge to represent the typical size of parts manufactured by the Y-12 National Security Complex (Y-12). On the ring gauge, small swept sine wave features are placed on the inside and outside diameter. A swept sine wave is a sine wave that continuously varies its frequency. The range of frequencies creates a window for evaluation of the machine capabilities. By knowing the magnitude and phase characteristics of the dynamic system, the operator can make decisions referring to the machine's capabilities based on the measurement speed.

Fast Tool Servo Dynamic Performance Measurement

Getting the most from an actuator is the goal of most servo designs. However as the operating frequency increases, gain and phase issues change the actual motion of the actuator from the desired path. Deconvolution techniques seek to identify the dynamics of the actuator and find a modified signal, that when sent through the actuator, will produce the desired path. The deconvolution algorithm requires accurate knowledge of the system dynamics; that is, the gain and phase of the outlet motion compared to the inlet command for an open-loop or a closed loop system. This section describes a method developed to find the dynamics of a Variform fast tool servo (FTS). A LabView program was developed to generate the appropriate range of input frequencies and amplitudes, send commands to the Variform, collect the resulting motion data and generate the system dynamics.

4) ACTUATION

Implementation of techniques to move or control the position of an object requires a well-characterized actuator that fits the range and resolution of the application. In the past, emphasis has been placed on actuators for real-time control, but other applications such as transporting components for assembly are equally important.

Non-Contact Transportation using Flexural Ultrasonic Wave

A new non-contact transportation system is being designed at the Precision Engineering Center. The system is based on NFAL (Near-Field Acoustic Levitation) and near boundary streaming. In this report, background knowledge is introduced about applications of NFAL and near boundary streaming. Two experiments have been set up at the PEC, one is to check the validity of NFA, and the other is to design a non-contact transportation system. Theoretical approaches are then introduced and finite element analysis is used to conduct modal and transient analysis.

5) CONTROL

Control of a precision fabrication processes involves both the characterization of the electromechanical system and the selection of hardware and software to implement the control algorithm.

Two-Axis Force-Feedback Deflection Compensation Of Miniature Ball End Mills

Correction for bending deflection of small (sub-millimeter diameter) milling tools was the focus of this project. This scheme was implemented on a high-speed, air-bearing spindle capable of speeds up to 60,000 rpm. This spindle was suspended on a pair of load cells and the real-time cutting force in two dimensions was determined based on the readings of each load cell and knowledge of the dynamic response of the spindle. Measurements from the two load cells can be

combined to produce accurate (+/- 0.2 N) cutting force estimates. The load cell supported spindle was mounted on flexure guided piezoelectric actuators that incorporated closed loop capacitance gage feedback for position commands. This system can respond to the real-time cutting forces on the tool and produce the appropriate motion to compensate for tool deflection errors in two orthogonal directions. Through the use of this self-contained spindle actuator and force measurement system, form errors were reduced from 10-15 μm for a fixed spindle to 2-3μm using closed loop force feedback. An overall reduction of 75% in form error was achieved thru the implementation of force feedback machining.

1 DESIGN TOOLS FOR FREEFORM OPTICS

Kenneth P. Garrard
Precision Engineering Center Staff
Thomas Dow
Professor
Department of Mechanical and Aerospace Engineering

Freeform Optical surfaces are defined as any non-rotationally symmetric surface or a symmetric surface that is rotated about any axis that is not its axis of symmetry. These surfaces offer added degrees of freedom that can lead to lower wavefront error and smaller system size as compared to rotationally symmetric surfaces. Unfortunately, freeform optical surfaces are viewed by many designers as more difficult and expensive to manufacture than rotationally symmetric optical surfaces. For most freeform surfaces this is true, but a designer has little or no feedback to quantify the degree of difficulty for manufacturing a surface. This paper describes a joint effort by Optical Research Associates (ORA) and the Precision Engineering Center to integrate metrics related to the cost and difficulty of manufacturing a surface into the merit function that is used during the design of an optical system using CODE V®. By incorporating such information into the merit function, it is possible to balance optical performance and manufacturability early in the design process.

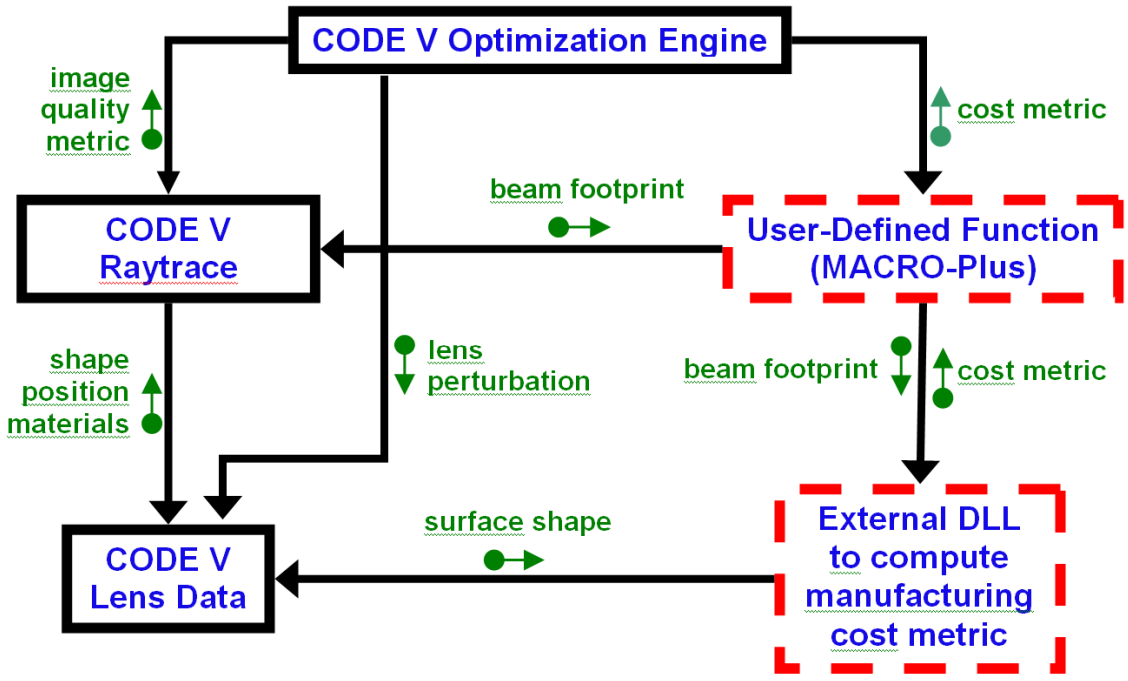

1.1 INTRODUCTION

Advanced optical systems play a pivotal role in military applications, including advanced optical telescopes and imaging LADARs (LAser Detection And Ranging). Optical systems are the eyes for imaging, surveillance, detection, tracking and discrimination. Therefore, improvements in optical design and fabrication are important targets for research and development efforts. One such improvement is the inclusion of freeform elements in optical designs. A recent NASA imaging spectrometer (IRMOS) [1,2] utilized freeform surfaces to help reduce the size of the system by an order of magnitude. Significant reductions in size can dramatically reduce the use of exotic materials (such as beryllium) and the ensuing mass reductions provide enhanced performance for lightweight space systems and missile interceptors that require high accelerations to reach their targets at the correct point in trajectory. Freeform surfaces can also be used to control astigmatism at multiple locations in the field of view and thus reduce wavefront aberration [3-6].

To make these advanced optical systems available for commercial and defense applications, an enhanced software design environment was created, one that gives the designer feedback on the manufacturing feasibility and cost of the design as well as the optical performance. Early feedback enables a designer to explore the possibilities offered by the use of freeform surfaces, while quickly eliminating those design choices that would prove too costly or difficult to fabricate.

1.1.1 ASTIGMATISM FROM OBLIQUE RAYS

An optical wavefront acquires aberration, especially astigmatism, when it reflects obliquely off a curved mirror that is locally rotationally symmetric. This means that the surface is rotationally symmetric about the normal vector at a point intersected by the central ray in the beam. Because of the obliquity, the mirror appears to have more power in the direction of the field angle. A fan of rays in the plane of the field angle will focus closer to the mirror than a fan of rays in the orthogonal direction. The axial separation of the best focus for horizontal and vertical ray fans is a measure of astigmatism. For a locally rotationally symmetric mirror, a field angle whose chief ray is coaxial with the mirror axis (normal incidence) is the only field angle where there is no astigmatism. Otherwise, astigmatism increases as the square of the field angle. Controlling astigmatism in systems with off-axis fields can be accomplished by including one or more non-rotationally symmetric elements in the design. This usually results in a more compact optical layout as well.

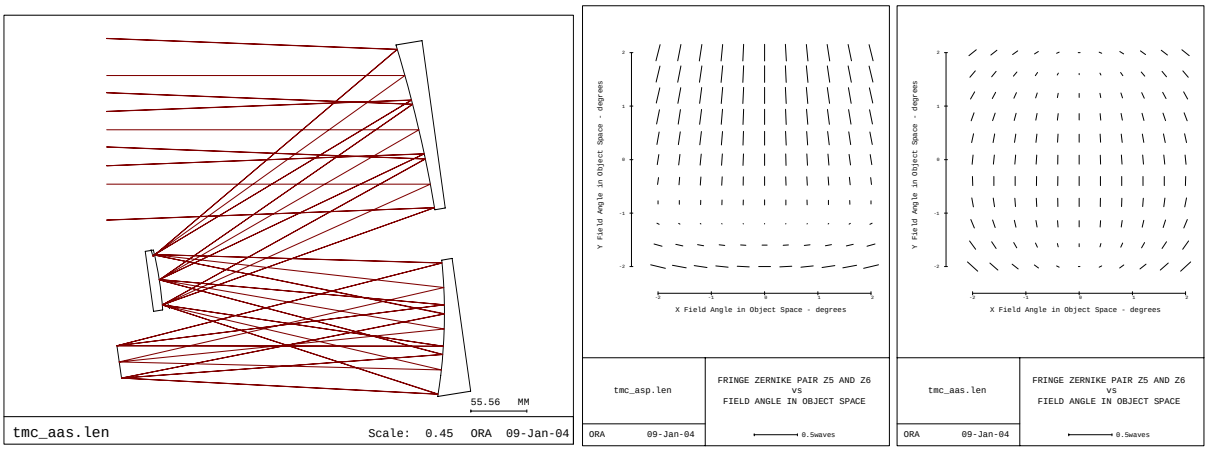

Figure 1. Optimized image quality for a 3-mirror anastigmat imager (left) has more than twice as much astigmatism across the full field using symmetric surfaces (center) as can be achieved with freeform surfaces (right).

1.1.2 BENEFITS OF FREEFORM SURFACES

To avoid astigmatism at a single off-axis field angle, what is needed is a locally anamorphic surface (i.e., not rotationally symmetric about the local surface normal), with a longer radius in the field angle direction than in the orthogonal direction. With an off-axis field, replacing a rotationally symmetric surface with a freeform surface allows the vertical and horizontal fans of rays to focus at the same point. Figure 1 shows a representative unobscured mirror system with associated astigmatism maps across the extended field of view for both the locally rotationally symmetric and freeform versions of the system. The length of the lines in the figure indicates the magnitude of the astigmatism. Note there are two nodes (points where the aberration is zero) in the field of the freeform system. In this illustration, one can zero out the astigmatism for two off axis field angles (mirror images of each other), but for a range of field angles one cannot exactly zero the astigmatism. Distortion and coma also have this nodal behavior. Thus a key benefit of using freeform surfaces is that they offer the designer the ability to control both the number and position of aberration nodes within the field of view. This level of control allows the designer to reduce the worst case wavefront aberration.

1.1.3 MODELING FREEFORM SURFACES

There are at least two ways to model locally anamorphic power. One is to take an axially symmetric surface and add tilt, decenter, and asphericity. In that case the vertex of the surface may be far off of the working aperture and the tilt angle may be large. However, it is simpler and more efficient to model the surface without such an extreme tilt and decenter. This can be accomplished by modeling the surface directly as an anamorphic function such as an aspheric

toroid. This method of modeling can also help the fabrication process. The freeform surface can be thought of as decomposed into an axially symmetric surface plus NRS deformations. If the axis of symmetry of the rotationally symmetric portion is in or near the working aperture, then fabrication is easier using a spindle-based method in which the part rotates about an included axis.

1.2 TECHNICAL OBJECTIVES

There were three technical objectives for this project: first, develop a design environment that could support an optical designer with tools to assess the difficulty to manufacture (i.e. cost to manufacture) a freeform optical surface; second, demonstrate the usefulness of these new design tools by utilizing them during the redesign of an optical system; and finally, demonstrate the ability to evaluate the effect of manufacturing errors inherent in the fabrication of freeform surfaces.

1.3 RESULTS

1.3.1 DEVELOPMENT OF ENHANCED DESIGN ENVIRONMENT

Spherical and aspherical (both on-axis and off-axis) optical surfaces can be machined on a Diamond Turning Machine (DTM) by rotating the part around its axis of symmetry. Off-axis forms are limited to the size of the machine because they must be physically located at their off-axis position from the axis of rotation. Freeform optical surfaces (or off-axis segments machined on axis) have no axis of symmetry and, as a result, this surface shape is a function of both radius (r) and angular position (θ). To produce such a surface, an additional degree of freedom is needed. This has been done by driving the machine tool axis as a function of r and θ (typically a big, heavy axis and thus the spindle speed must be low and production times tend to be long) or adding an auxiliary axis (Fast Tool Servo - FTS) to move the tool. Auxiliary axes can be obtained with strokes from 5 μm to several mm and operating frequencies from 1 KHz to 2 Hz respectively.

A fast tool servo on a DTM is the most efficient way to produce freeform shapes in diamond turnable materials. The FTS can be programmed to create surfaces that are a function of DTM axes positions as well as the spindle angular position as illustrated in Figure 2. The shape of the freeform part can be divided into rotationally symmetric (RS) and non-rotationally symmetric (NRS) components as illustrated in Figure 3 and the magnitude of the NRS component can have a major impact on the fabrication process. The creation of these two components (not necessarily unique) is a technical challenge that has been addressed at the PEC [7,8] and was utilized in this project.

The main axes of the DTM (X and Z) create the symmetric component (function of radius, r) while the FTS adds the non-symmetric component (function of angular location, θ, as well as radius, r). As the tool feeds from the outside of the part to the center, the linear axes of the lathe move the tool along the correct asphere (Figure 3b) and the fast tool servo simultaneously moves the tool in the W direction to add the (r,θ) component (Figure 3c) that will create the desired optical shape (Figure 3a). The range and bandwidth of the FTS will dictate the feed rate and maximum spindle speed, which will have a direct bearing on the time and cost to fabricate the surface.

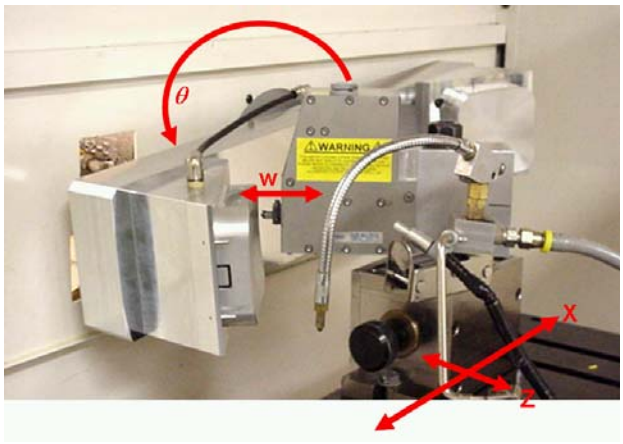

Figure 2. Coordinate system for machining an off-axis freeform surface with a fast tool servo.

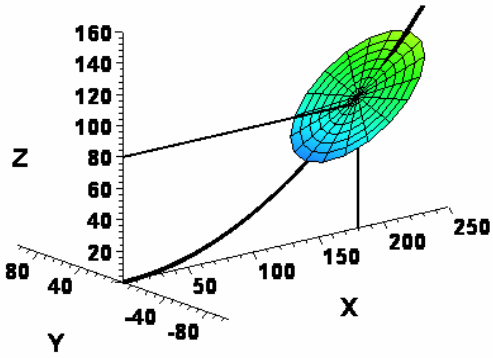

(a) Off-axis conic surface in parent coordinate system.

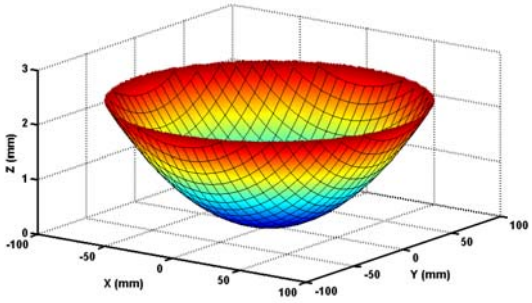

(b) Rotational symmetric component of off-axis conic (best fit radial aspheric surface).

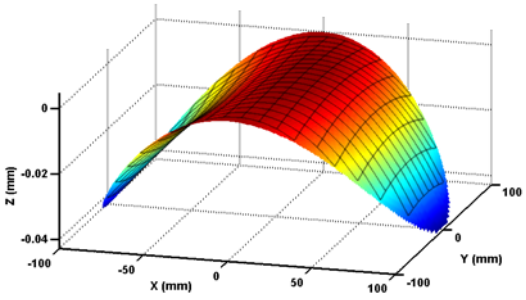

(c) Non-rotationally symmetric component of off axis conic (note the 100x magnification from the surface in (b)).

Figure 3. Off-axis conic segment decomposed into its rotationally and non-rotationally symmetric components.

An integrated design and optimization environment was developed that brought together, for the first time, the existing optical performance predictions with automated feedback of manufacturing costs of FTS machined freeform surfaces. Schematically, the project created the environment shown in Figure 4. The environment is quite powerful, general and extensible; however, the initial scope was limited to consideration of surfaces that were off-axis sections of conic surfaces. These sections are not rotationally symmetric about their center, and therefore have that characteristic of freeform surfaces that is most directly related to their difficulty to manufacture. In addition, the algorithm for decomposing such surfaces into RS and NRS components had been worked out at PEC prior to this program [7]. An implementation of this algorithm in C code was developed at PEC and provided to ORA. A listing of this code was previously reported in the 2004 PEC annual report [9]. The code is based upon an analytic solution first proposed by Thompson for paraboloids [10], generalized to conics by Gerchman [11] and optimized at the PEC under contract to the Oak Ridge Y-12 Optics Modil for use as a real-time trajectory generator in a machine tool controller [7].

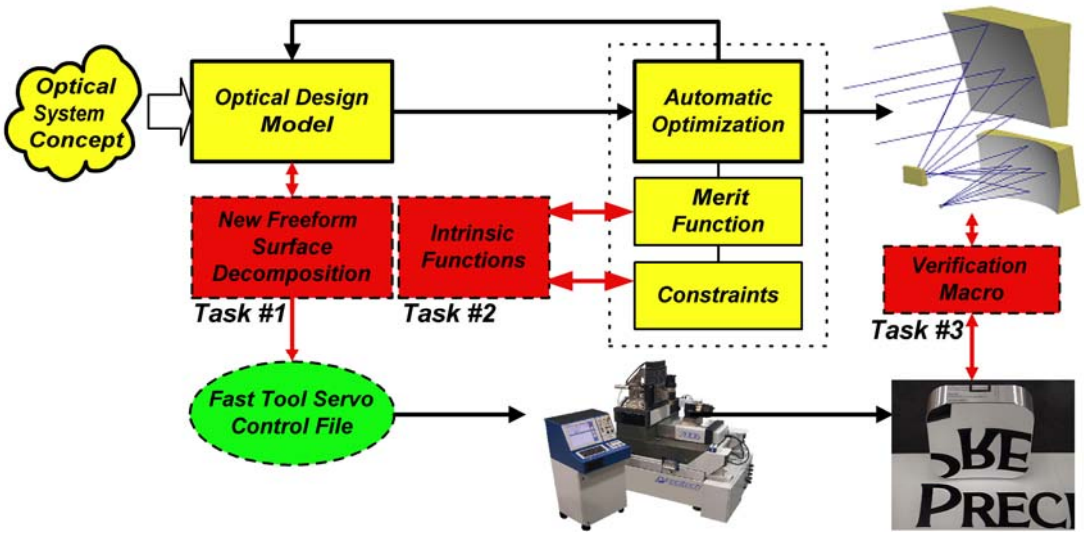

Figure 4. Integration of freeform surface decomposition with automatic optimization.

The decomposition can provide useful information to a designer after surface shapes have been determined. However, maximum benefit is realized by giving the designer feedback during the actual optimization process. This can be done by using the decomposition to generate appropriate metrics, and by incorporating these metrics into the merit function that is used during the optimization process. The proper choice of a metric based on the surface decomposition would require a careful consideration of how a particular manufacturing process is able to generate a surface shape. While this is the ultimate goal of this research, a single metric was chosen that is a reasonable choice for a wide variety of manufacturing technologies.

Specifically, the magnitude of the NRS component of the surface sag as a predictor of manufacturing cost – the larger the NRS sag, the higher the cost.

Determination of the maximum NRS component of the sag is one of the output quantities computed by the decomposition C code [9]. While it was possible to incorporate this code, with slight modifications, directly into CODE V to compute NRS sag during the optimization process, such an approach would lack the flexibility needed to allow generalization of this approach in the future. Specifically, it is anticipated that multiple manufacturing processes will need to be characterized. Each of these processes will have a unique fabrication cost function[1], and the objective was to design the code in such a way that it would anticipate such variations and allow them to be readily incorporated into CODE V in the future.

Another option would be to translate the decomposition algorithm into the CODE V Macro-PLUS™ language, and have this algorithm implemented as a user defined function (UDF). A UDF can be called directly by the CODE V optimization engine and returns a single real value that can be used either as a component of the merit function or as a value that is to be constrained in some manner, such as with an inequality constraint. While this was an option that would allow other manufacturing processes to be modeled in the future, it was not a very desirable one. Lens optimization is a very computationally intensive operation. All components of the merit function and all constrained quantities must be evaluated many times during a single optimization cycle[2]. User defined functions that are written in the Macro-PLUS language are compiled, but the compiler that is used for this process is not an optimizing[3] compiler. For the initial application the decomposition of the surface shape requires a substantial amount of computation. For this reason, it is desirable to perform these computations using code that has been optimized for speed.

---

[1] These cost functions may have an analytic form, but are more likely to be table-driven. That is, they will probably be based on relatively sparse data provided by fabrication houses. The data may be in the form of cost vs. specific surface characteristics. As an example, these data may consist of cost vs. NRS sag, cost vs. NRS slope in the tangential (along track) direction, etc.

[2] Most of these evaluations are needed to compute the derivatives of the merit function components and constraints with respect to each of the lens parameters that is allowed to vary during the optimization. Performance would be dramatically improved by directly evaluating the Jacobian matrix (i.e., partial derivatives with respect to each parameter over the data grid) in the external function.

[3] The word “optimizing” is used in two, completely unrelated contexts in this paragraph. There is the optimization of the lens system, which is performed by CODE V, and the optimization process that that is associated with the translation of source code into efficient(i.e. fast) machine code. This latter optimization is performed by most modern C, C++ and Fortran compilers, as well as those for many other languages.

The interface between the manufacturing cost metric computation and the optimization engine was structured in a way that allowed maximum flexibility in the future, and also was as efficient as possible. To achieve this, the interface implements of the manufacturing cost metric as a dynamically linked library (DLL). This allows the cost metric computation to be written in a standard language, and compiled using an optimizing compiler. This approach required modifications to the CODE V MACRO-Plus language to allow external DLL routines to be accessed via a procedure call mechanism. It was also necessary to create an interface (API) that would allow external DLL's to access information about the lens. This provides a mechanism for the DLL routine to query the lens to determine its surface shape.

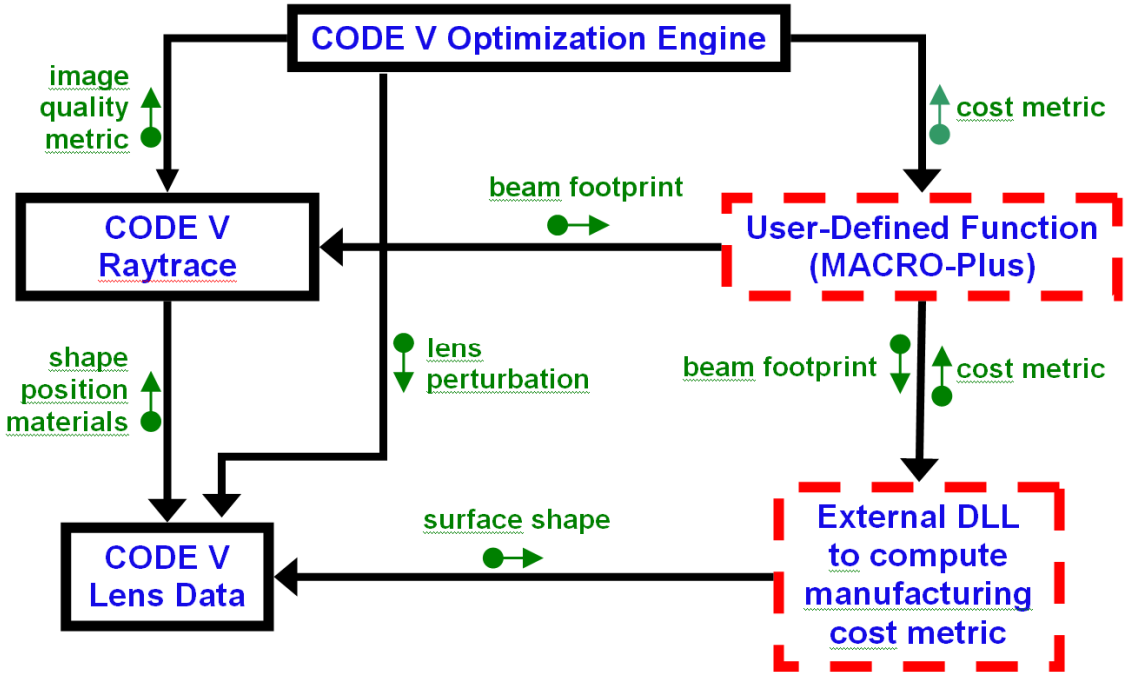

Figure 5. Interaction of components to compute a manufacturing aware merit function.

The basic structure of the computations and interactions between the various computational components is illustrated in Figure 5. A UDF, which will return a manufacturing cost metric, is written in CODE V's MACRO-Plus language (see Appendix A). This UDF will call the DLL that actually performs the computation of the cost metric. The interface specification for this DLL is given in Appendix B. In addition to surface shape information that the DLL is able to obtain directly from the lens database, it is also necessary for the UDF to compute information about the used area of the surface. This information is determined by tracing the bundle of rays from each field point and by determining the footprints of the beams (one beam from each field point) on the surface. The information about the used portion of the surface (the clear aperture) is required by the DLL when it performs its decomposition.

1.3.2 MANUFACTURING AWARE DESIGN ENVIRONMENT DEMONSTRATION

To prove the benefits of this enhanced design environment, a redesign of two different optical systems was performed. In each case, the original system contained aspheric components, and the decomposition algorithm had not yet been extended to handle these surface shapes. A first step was to redesign each of the systems to use conic surfaces. The first system was a three mirror, off-axis, unobscured system with conic surfaces for the first two mirrors and an asphere for the third surface. The asphere was replaced with a conic that did not significantly degrade performance. The second system was a four mirror system for which all four surfaces were aspheres. Three of the four aspheres were replaced with conic surfaces while still maintaining adequate optical performance. The basic layout of each of these systems is shown in Figure 6.

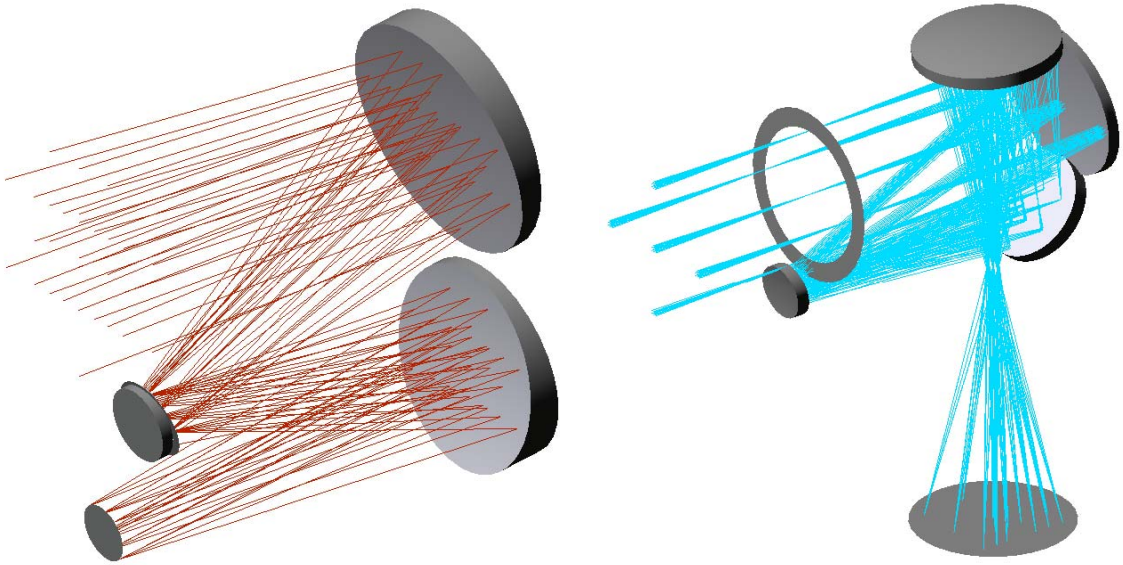

Figure 6. Two demonstration systems are shown. On the left is the three mirror system, which uses only conic surfaces. The four mirror system for which three of the four mirrors were conic surfaces is on the right.

Three Mirror System The three mirror system covered a field of view of ±2 degrees. After the initial redesign to include only conic surfaces, it had an average[4] root-mean-squared wavefront error (RWE) of 0.091 waves (at a wavelength of 1 μm). After this redesign, the maximum NRS sag for each of the three mirrors was examined. The first mirror had peak-to-valley (PV) NRS sag of 0.047 mm, the second mirror had negligible PV NRS sag and the third mirror had PV NRS sag of 0.056 mm. The maximum NRS sag was reduced in successive optimization runs using a UDF and the decomposition DLL function to constrain the maximum

[4] Averaged over the field of view.

NRS sag to be less than or equal to a specified amount. For each optimization run, the RWE was computed.

A plot of the results for the three mirror system is shown in Figure 7. In this case it is possible to reduce the PV NRS sag of mirror three (M3) substantially, without increasing the RWE. However, as the NRS sag of M3 starts to get smaller than that of mirror one (M1), the maximum NRS sag is now determined by the NRS sag of M1. Reducing the NRS sag of this mirror has a much more dramatic impact on the RWE. For this optimized system, Figure 8 shows the distribution of RWE over the ±2 degree field of view. With a maximum NRS sag of 0.046 mm (on mirror one), the RWE can be kept below 0.1 waves. Further reductions in NRS sag lead to sharp increases in RWE.

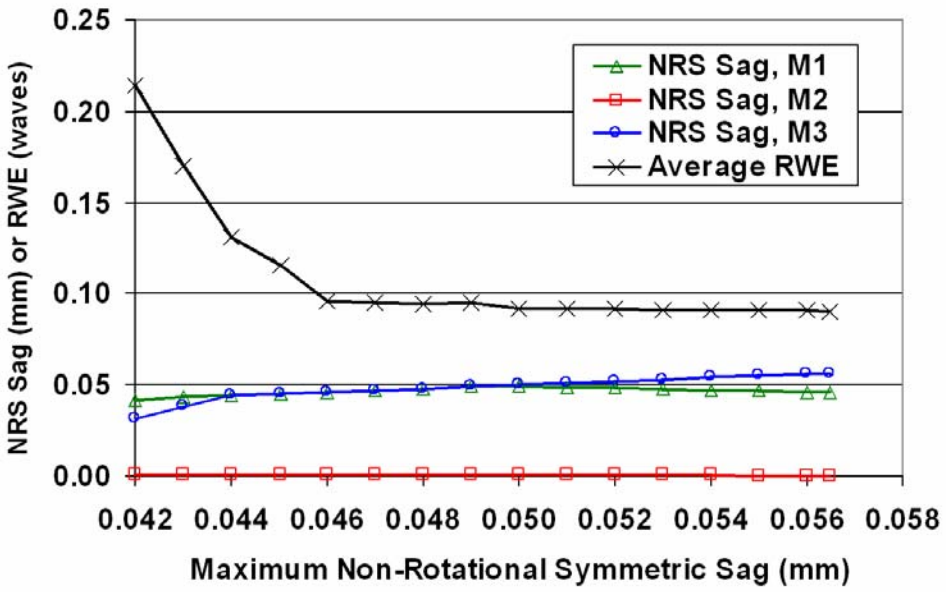

Figure 7. Behavior of RMS wavefront error (RWE) as a function of NRS sag for the three mirror system.

This study of optical performance versus manufacturability was simple to accomplish with the software tools developed. A study such as this would not have been possible without this new design tools. The benefit to a designer is quite clear: at an early stage of a design, it is possible to consider manufacturability aspects of a system. Tradeoffs between performance and cost that allow an appropriate balance between these two conflicting goals can be quickly evaluated. In the absence of this feedback, it is easy for a designer to chase higher performance designs without realizing the cost that will be incurred during the fabrication of the system. It is also easy for a designer to abandon an initial high performance design because of the perceived difficulty of its manufacture.

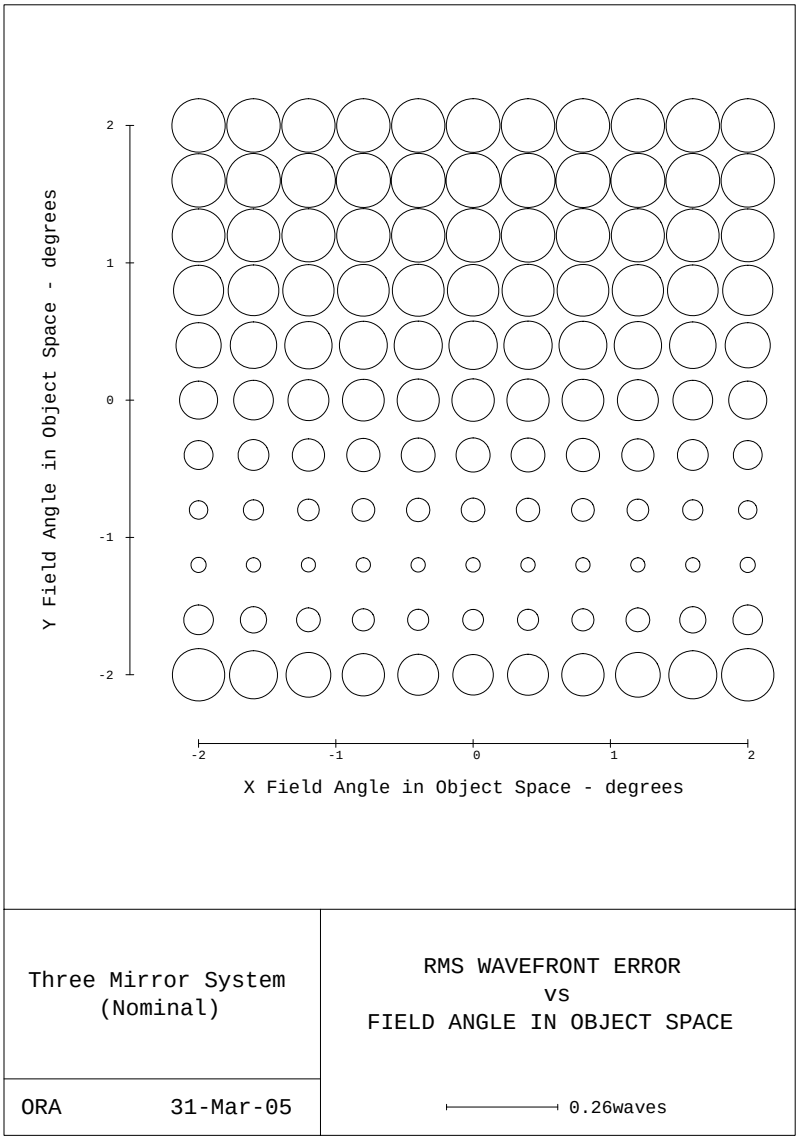

Figure 8. The RMS wavefront error over the field of view for the redesigned three mirror system. For this system, the maximum NRS sag is 0.046 mm and the average RWE is 0.096 waves.

Four Mirror System A similar study was performed with the four mirror system. In this case, the original system that had been redesigned to use only a single asphere had a field of view of ±1 degree and a RWE of 0.028 waves. The maximum NRS sag in this system was on the surface of the first mirror, and its magnitude was 0.1975 mm. This NRS sag was considerably larger than the values for the other two conic mirrors. Again, the maximum NRS sag was constrained to smaller values in multiple optimization runs, and the resulting RWE was computed.

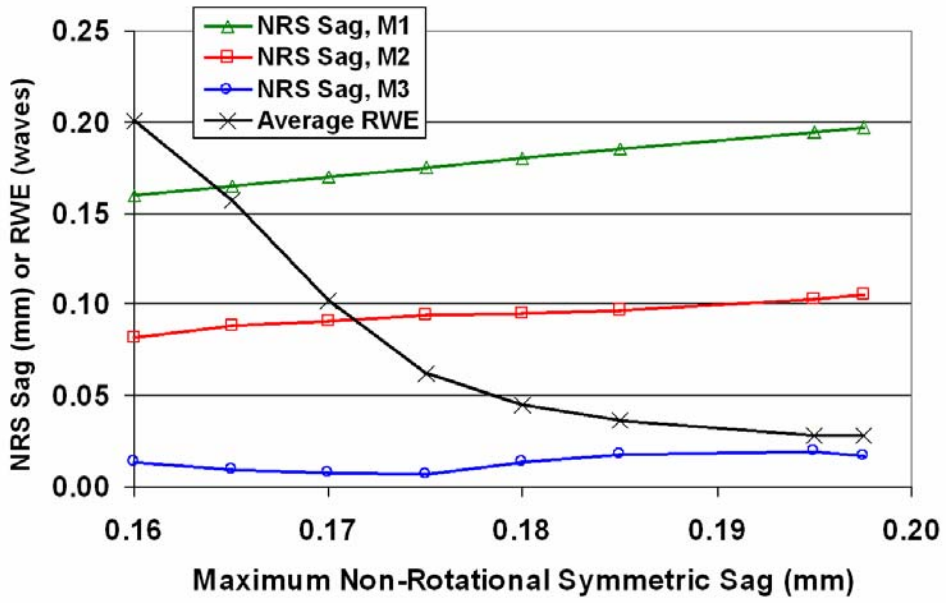

Figure 9. Behavior of RMS wavefront error (RWE) as a function of NRS sag for the four mirror system.

Figure 9 shows the results for this case and they are somewhat different from the three mirror system. Because the NRS sag of the first mirror (M1) was much larger than that of the other two mirrors, the reduction in maximum NRS sag could only be accomplished by reducing the NRS sag of mirror one. However, the wavefront error was a much stronger function of the NRS sag of M1 than what was observed for M3 in the three mirror study. Thus, the best tradeoff appears to occur at around a PV NRS sag value of 0.18, where the RWE has increased to 0.0447, which is a 60% increase in RWE. Forcing the PV NRS sag to be smaller causes a rapid increase in the wavefront error.

1.3.3 Simulation of Dynamic Fabrication Errors

For an optical design environment to be truly manufacturing aware, it must be able to simulate the expected manufacturing errors for manufacturing processes. The approach taken was to gather data about such process errors and to perform a realistic simulation of some of the fabrication errors for one of the demonstration systems (the three mirror system.) In particular, the expected form error of the surface if the mirrors were produced using an FTS system was generated. Once these errors were simulated, their effect on the optical performance was considered. The errors associated with a particular fabrication process can be separated into two distinct categories: roughness and form.

The roughness of a diamond turned surface is typically limited by two factors: material effects and machine vibration. This assumes that other factors that can cause excessive roughness such

as tool condition and theoretical finish are properly addressed in the turning process. Material effects such as grain size, brittle fracture, and inclusions have been thoroughly documented for common materials such as aluminum, copper, electroless nickel, brass, PMMA and germanium. These materials can be placed in a database as part of the manufacturability along with their maximum finish ranges and can be combined with the machine database to provide finish feedback to the designer. This feedback can be supplied simply as an RMS surface roughness value for evaluation in a scattering simulation outside the CODE V environment.

Form errors are estimated so that their effect on the optical performance can be analyzed in CODE V. Estimation of these errors requires a thorough analysis of their origin on one hand and a carefully chosen set of assumptions on the other. Sources of form error seen in diamond turning are: tool centering, tool waviness, radius compensation, axis straightness, axis squareness, axis roll, pitch and yaw, synchronous spindle error motion, scale errors, and servo errors. Many of these form errors are common to all diamond turning systems, and were not considered in this work. Instead, error sources specific to the use of a fast tool servo mechanism are evaluated.

FTS Dynamics The Variform Fast Tool Servo (FTS) employs a lever mechanism with a pair of piezoelectric stacks to produce a 400 µm PV excursion over a frequency range from DC to 300 Hz. The two stacks move 180 degrees out of phase and rock a T-shaped lever that is connected to the tool. The lever amplifies the stack displacement and moves the tool normal to the axis of the stacks. The system includes a closed loop controller using an LVDT as feedback on the tool position. This control system produces unity gain up to about 100 Hz, a bandwidth of 300 Hz, eliminates hysteresis by means of a reference capacitor and provides additional damping.

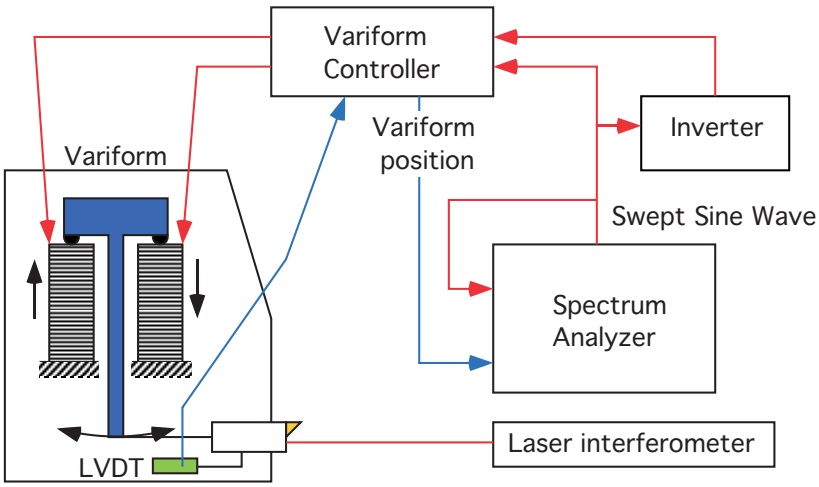

Figure 10. System arrangement to measure the dynamics of the Variform actuator.

The response of the FTS to an input command is influenced by the amplitude and phase of that command. To estimate the errors caused by the dynamics of the FTS, the response of the system to various commands must be measured. The measurement arrangement is illustrated in Figure 10. The Spectrum Analyzer generates a varying frequency sine wave with fixed amplitude that is sent to one of the two actuators and an inverted copy is sent to the other. These out of phase drive signals rock the T-shaped lever and move the tool. Tool position as measured by an internal LVDT is sent back to the analog controller to control the tool motion. An output connection on the Variform Controller shows the tool position as measured by the Variform. This position is compared with the amplitude and phase of the command signal at each input frequency to create the frequency response of the system that is illustrated in Figure 11.

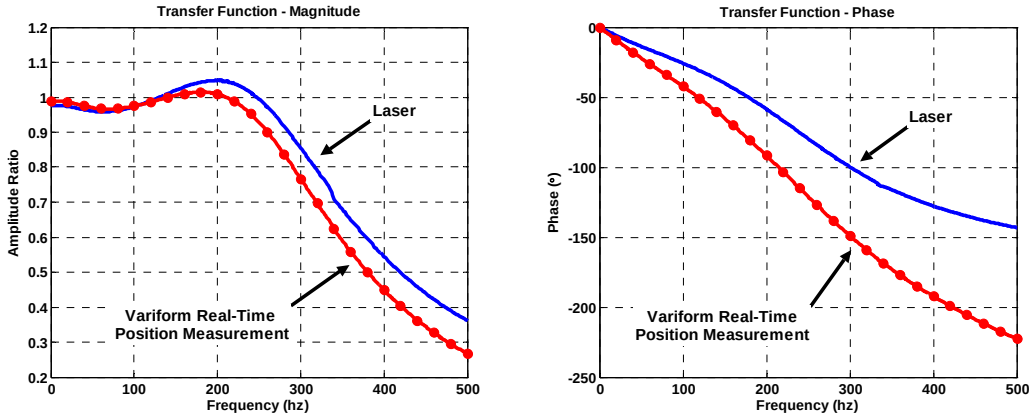

Figure 11. Transfer function (magnitude ratio and phase change vs. frequency) between input command and output motion of the Variform as a function of the input frequency.

Unfortunately, the Variform measurement of the tool motion is not the actual tool motion; it is that motion as modified by the control system. As a result, a second measuring system (a laser interferometer) was used to measure the true position of the tool. Figure 11 shows the transfer function in magnitude and phase between the input command and output motion. The line with dots is the Variform position measurement and the solid line is the measurement of tool position from the external laser interferometer. The Variform position is the result of the analog controller used to modify the magnitude of the tool motion (note it is very flat from 0 to 200 Hz) but it adds phase lag to the position value as shown on the right when compared to the actual motion of the tool.

From the Variform position measurement, the gain is 1 ± 0.02 from DC up to 200 Hz and then drops rapidly as the frequency increases. The output lags the input by about 90° at 200 Hz. The actual tool position is different with the gain changing more from 0 to 200 Hz, 1 ± 0.04, but the phase lag is much less at 200 Hz, 60°. Clearly, the tool position correction must be based on the

actual dynamics of the tool and not that as measured by the Variform position signal. The desired dynamic response can be represented in either the frequency domain (transfer function as shown above) or an equivalent representation in the time domain (impulse response) can be developed.

Error Estimation for the Three Mirror System As a demonstration of the viability of incorporating manufacturing feedback into the optical design process, the NRS form errors for the two systems shown in Figure 6 were modeled. Six of the seven mirror surfaces were off-axis conic segments. Convolution of the FTS dynamic errors were applied to the NRS portion of each of these six mirror surfaces as determined during the decomposition process discussed earlier. Again, each surface point was shifted in amplitude and phase and combined with the previously calculated errors to reveal a simulation of the surface when produced with the method chosen by the designer. This modified surface was saved in the form of an interferometric error map and then inserted into CODE V to determine the impact of the machining process on the optical design.

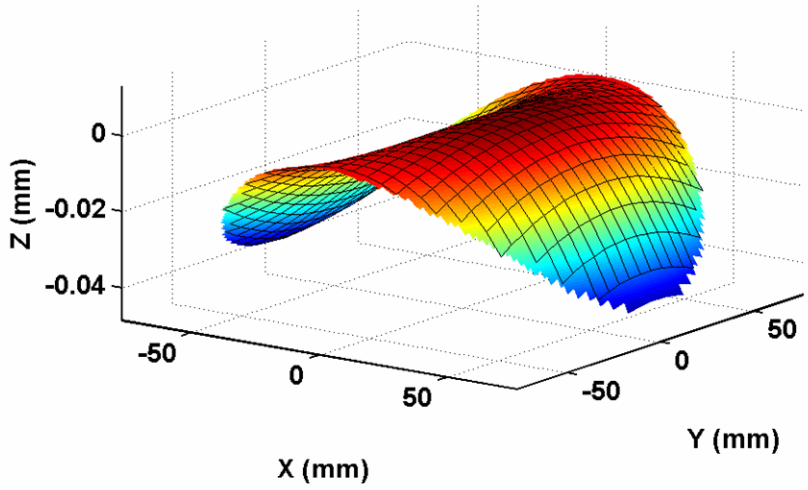

Figure 12. The magnitude of the NRS component of the surface sag for mirror one of the three mirror system.

The NRS shape of mirror one in the three mirror system is shown in Figure 12 and requires a 46 µm excursion of the FTS to machine in an on-axis orientation. To produce a simulated error map the NRS shaped was first transformed into a time based signal for typical machining conditions (e.g., 1200 rpm spindle rotation), convolved with the dynamics of the Variform FTS and interpolated onto a 256 x 256 point Cartesian grid. This error surface is shown in Figure 13. Note that the total range of the error is 5.8 µm over the entire aperture, which has a sag of 2.5 mm. The error is predominately due to phase lag in the actuator response at the 20 Hz rotational velocity of the machining spindle (see Figure 11). The magnitude of this error can be reduced by

either advancing the phase of the actuator command signal or by slowing down the spindle. Errors were simulated with no correction (i.e. no phase advance) applied (Figure 13), and also for the case where a fixed time advance was applied to the drive signal[5] to reduce the effect of actuator dynamics. The result shown in Figure 14 is a plot of the simulated form errors with the fixed time advance correction applied to the drive signal.

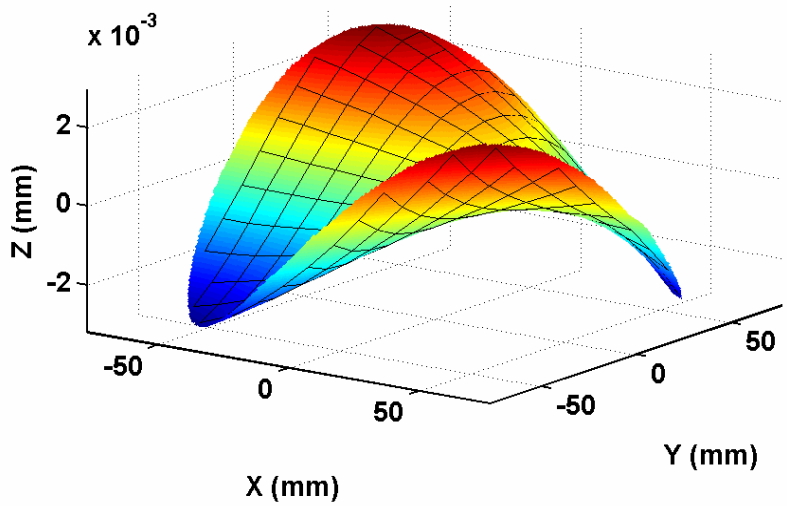

Figure 13. The simulated form errors for mirror one of the three mirror system. This simulation was performed without a correction being applied to counteract the system dynamics of the FTS.

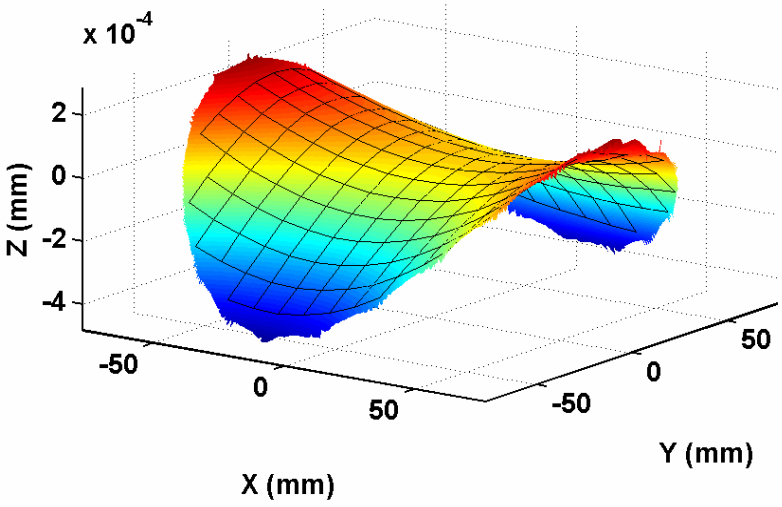

Figure 14. The simulated form errors for mirror one of the three mirror system. This simulation was performed with a correction for the actuator dynamics.

[5] Advancing the drive signal is equivalent to "clocking" the mirror on the tool chuck by a fixed angle.

The important difference to note between the form errors shown in Figures 13 and 14 is the difference in the magnitude of the errors. A simple correction for the system dynamics has reduced the errors from 5.8 µm (Figure 13) to 650 nm (Figure 14). A second subtle difference between Figures 13 and 14 is that the angular orientation about the Z axis of the form error has changed.

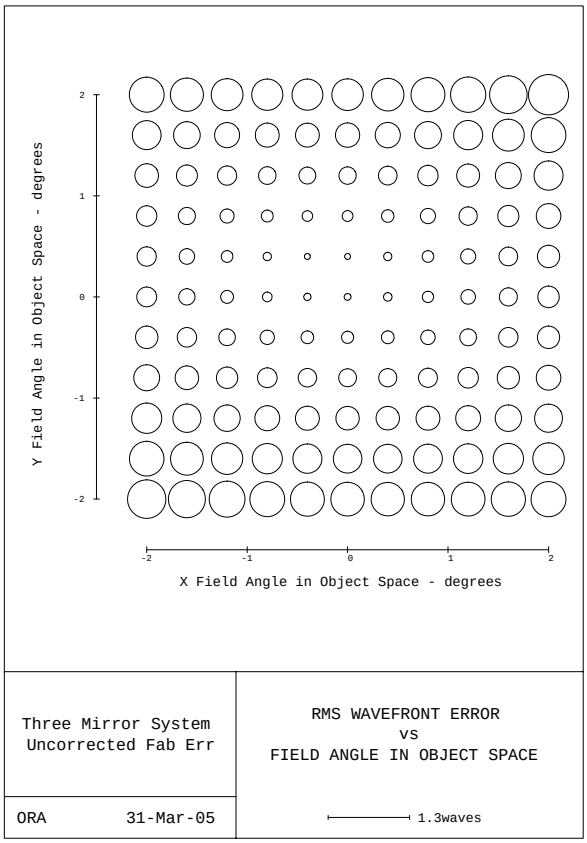

Figure 15. The RMS wavefront error of the simulated, as-built three mirror system without FTS dynamic correction.

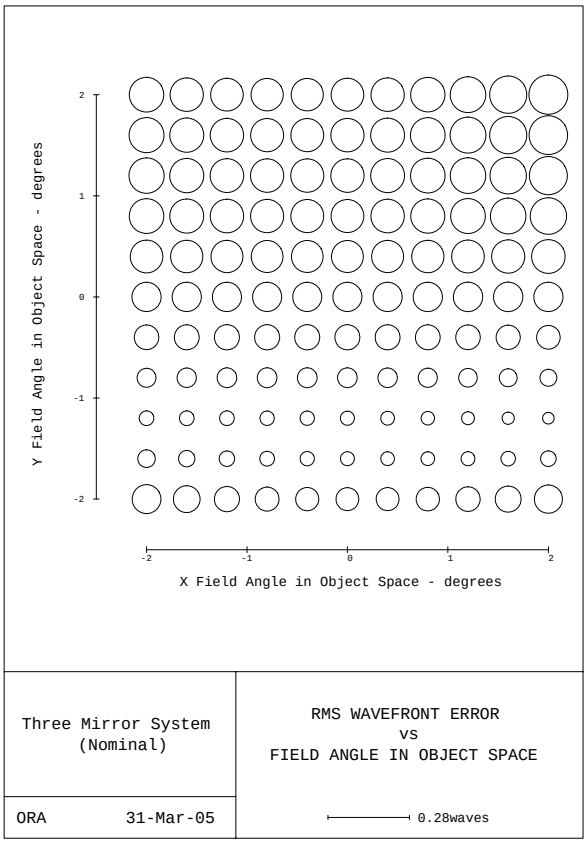

Figure 16. The RMS wavefront error for the simulated as-built three mirror system with FTS with dynamic corrections.

When the as-built system is modeled using the fabrication process with a drive signal without correction for actuator dynamics, the RWE increases to 0.367 waves, nearly a 4x increase in the RWE. The RMS wavefront error over the full field is displayed in Figure 15. When the form errors produced with the fabrication process that accounts for actuator dynamics are added to the system model, the optical performance of the system actually improves as shown in Figure 16.

The average RWE for the system, which was 0.096 waves for the nominal design (see Figure 8), was reduced to 0.093 waves. This effect is apparently due to the fact that the surface errors create a surface form that was not allowed in the original optimization process. That is, the as-

built surfaces are not actually off-axis sections of conic surfaces. The fabrication errors have created different surfaces, which actually produce a slightly better image quality. While such results are unusual, the important fact to note is that the fabrication errors have been modeled and a designer can have confidence in the ability of the as-built system to meet the requirements.

1.4 FUTURE WORK

The initial implementation of the manufacturing aware design environment considered only off-axis conics and their on-axis fabrication using a particular diamond turning process. This limitation is embodied in the external DLL that used preexisting C code as a starting point and is independent of CODE V. The modification to CODE V that allows a UDF to call an external DLL provides a means for including additional fabrication processes and other freeform surface types in merit function optimization. The use of an external C function provides a level of abstraction between the CODE V optimization engine and the details of surface decomposition and fabrication. The example UDF in Appendix A that was used for the two demonstration systems described in this report returns the NRS sag as the cost value for a specific set of input parameters. Additional decomposition results, for example tilt angle, are computed by the DLL but are not considered by the UDF in the merit function calculation. For example, a trivial modification to the UDF could return a weighted sum of tilt and NRS sag as the relative cost. Tangential slopes also have an impact on fabrication complexity and could be computed by the external DLL and considered during calculation of the cost merit function.

1.4.1 EXTENSION TO NON-CONIC SURFACES

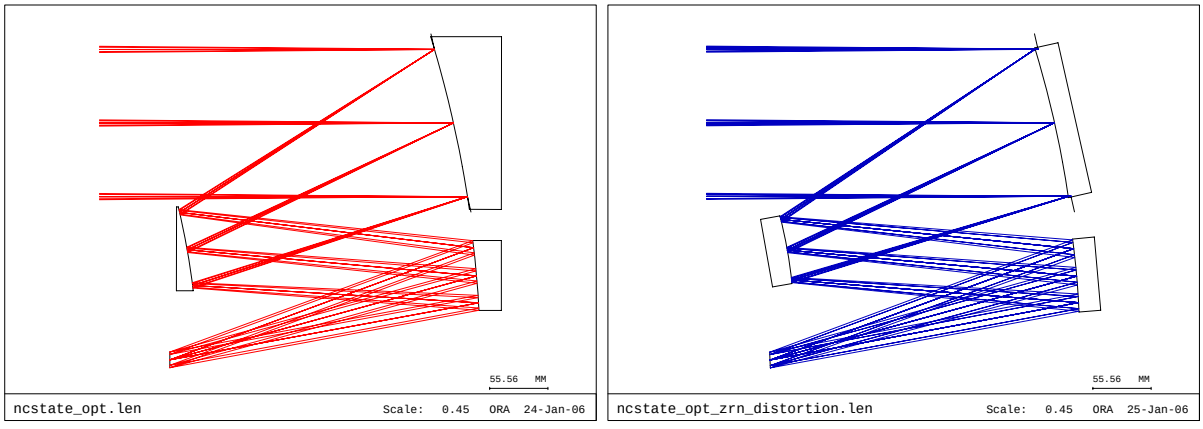

Figure 17. TMA with off-axis conic mirrors (left) and on-axis freeform mirrors (right).

The benefits of extending this software to include additional surface types is clearly demonstrated by considering an alternative design for the three mirror anastigmat described in Section 2 of this report. The all conic TMA is shown on the left in Figure 17. This design has an

average RWE of 0.165 waves and a worst case RWE of 0.246 waves. Overall performance is limited by astigmatism, coma and trefoil which cannot be eliminated with off-axis conics. The decomposed system has a maximum NRS sag of about 200 μm, well within the fabrication capability of the Variform FTS. However a dramatic improvement in both optical performance and NRS sag is obtained if the surfaces are modeled as on-axis tilted freeform Zernike aspheric polynomials. The maximum RWE is reduced by two orders of magnitude to 0.0024 waves and the MTF is diffraction limited. Note that the alternative design retains the mirror spacing, clearances, FOV, EPD and EFL of the all conic TMA. The RWE over the full field of the two systems is compared in Figure 18. The diameters of the circles indicate the magnitude of the RWE at each field location.

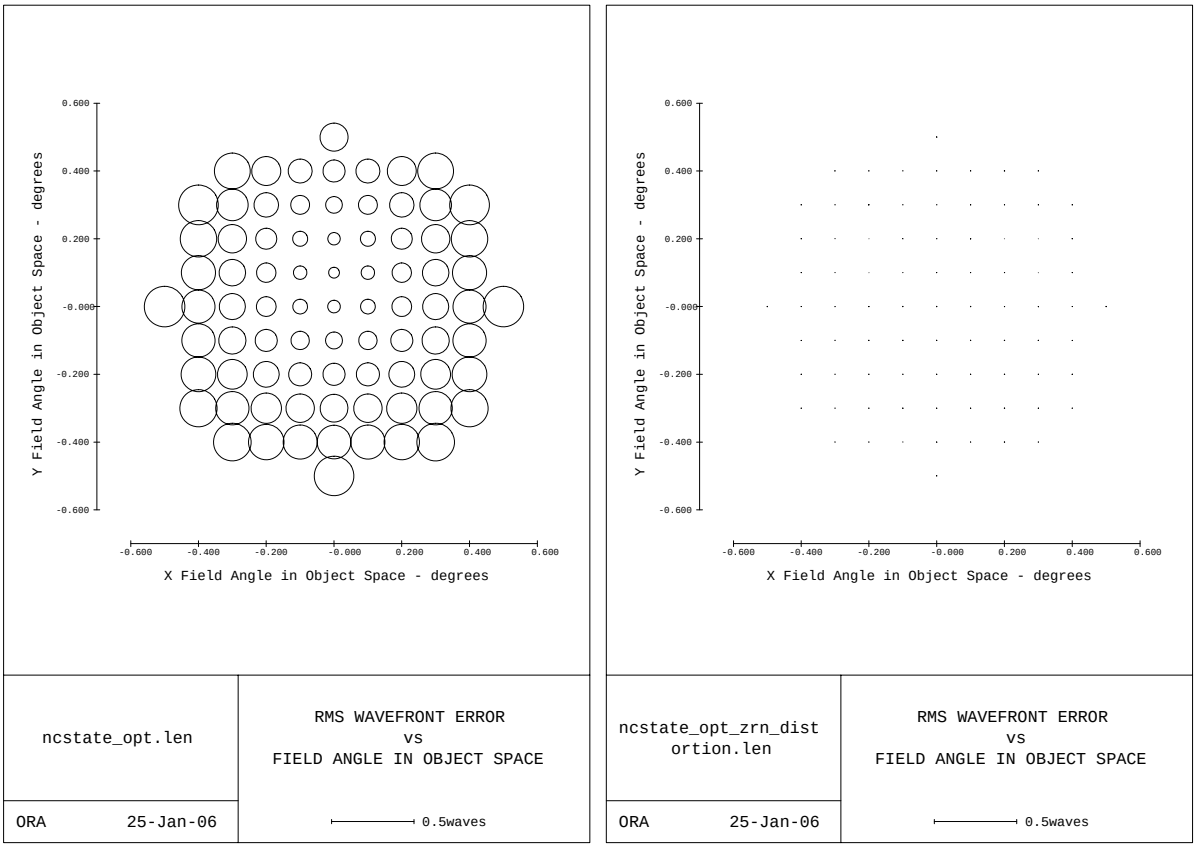

Figure 18. RMS wavefront error for all off-axis conic TMA (left) and on-axis Zernike asphere polynomial TMA (right).

The Zernike decomposition for the worst case field angles is given in Table 1. The dominate astigmatism, coma and trefoil (highlighted rows in the table) have been essentially eliminated in the Zernike asphere design. However the design software does not give immediate feedback on the feasibility of manufacturing or testing these three on-axis non-rotationally symmetric aspheres. Nor can it automatically vary the design to minimize the NRS sag.

Table 1. Zernike polynomial decomposition of wavefront error for two TMA designs.

Fringe Zernike			Off-Axis Conic		Freeform	
			Coefficient	RWE Contribution	Coefficient	RWE Contribution
Primary	4	Focus	-0.0523	0.0302	0.0002	0.0001
	5	Astigmatism (X)	-0.3828	0.1563	0.0023	0.0009
	6	Astigmatism (Y)	0.0000	0.0000	0.0000	0.0000
	7	Coma (X)	0.0000	0.0000	0.0000	0.0000
	8	Coma (Y)	0.4028	0.1424	0.0002	0.0001
	9	Spherical	0.0356	0.0159	-0.0020	0.0009
	10	Trefoil (X)	0.0000	0.0000	0.0000	0.0000
	11	Trefoil (Y)	-0.2849	0.1007	0.0012	0.0004
Secondary	12	Astigmatism (X)	-0.0380	0.0120	-0.0043	0.0013
	13	Astigmatism (Y)	0.0000	0.0000	0.0000	0.0000
	14	Coma (X)	0.0000	0.0000	0.0000	0.0000
	15	Coma (Y)	-0.0007	0.0002	0.0000	0.0000
	16	Spherical	0.0004	0.0001	0.0001	0.0000

It is a relatively straightforward process to determine the NRS sag required for turning Zernike aspheres on-axis with a fast tool servo. A worst case value for each surface can be obtained by examining the fabrication table output produced by CODE V. The output includes a spherical sag difference table over a 51 x 51 XY aperture grid (i.e., deviation from a base sphere aligned with the mirror vertex). By fitting a radial polynomial to the grid data the maximum NRS sag can be found. The NRS sags for the conic and Zernike asphere TMAs are shown in Table 2.

Table 2. NRS sags for two TMA designs.

Mirror	Off-Axis Conic	Freeform
Primary	218 μm	138 μm
Secondary	287 μm	48 μm
Tertiary	24 μm	20 μm

The Zernike asphere decomposed into RS asphere and NRS residual is in principle no more difficult to fabricate by diamond turning with a FTS than if the parent surface were conic. The on-axis Zernike mirrors may in fact be easier to machine and assemble than the conic TMA since there is no tilt introduced by the decomposition. For the off-axis paraboloid shown in Figure 2,

the on-axis DTM-FTS fabrication process would tilt the surface normal at the center of the aperture about 8° with respect to the back surface (or a set of turned coplanar front surface fiducials). Sensitivity of NRS sag to tilt is proportional to the product of aperture radius and the cosine of the tilt angle. The Zernike aspheres (or any other on-axis surface) can be machined with the vertex surface normal coincident to the spindle rotation axis. Figure 19 shows the shape of NRS component of each mirror in the Zernike asphere TMA with a best fit radial polynomial (i.e., rotationally symmetric asphere) removed.

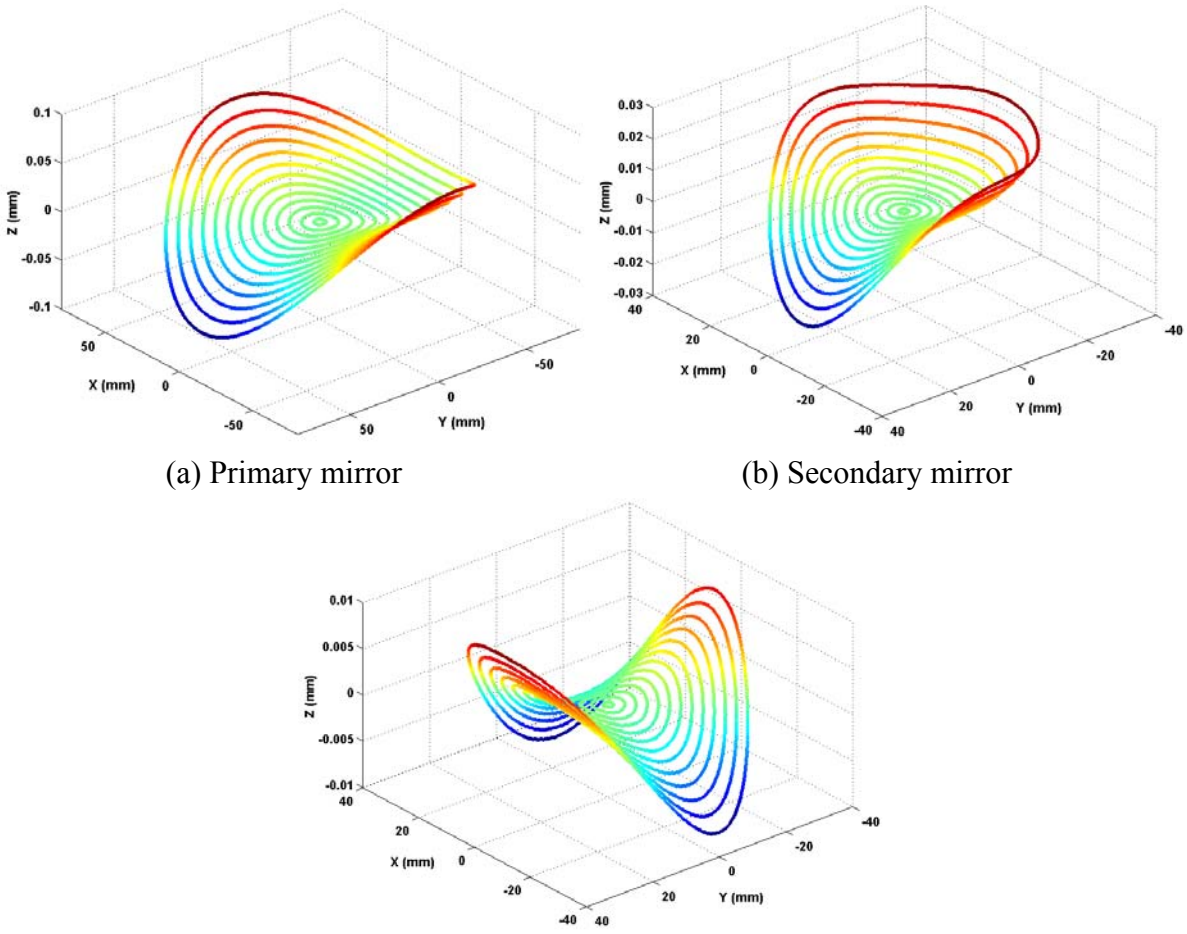

(a) Primary mirror

(b) Secondary mirror

(c) Tertiary mirror

Figure 19. NRS components after removal of best fit rotationally symmetric asphere for the on-axis Zernike asphere polynomial TMA design. Sag values for each surface are given in Table 2.

1.5 CONCLUSIONS

The ability of an optical designer to obtain early feedback about the manufacturability and cost of a freeform surface will ultimately lead designers to employ these surfaces in those designs where the benefits are worth the added cost. In the past, it has been the case that a designer is unsure of what that added cost is, and thus there is no easy way for a compromise between cost and performance to be made for systems utilizing freeform shapes.

This project has taken the following significant steps toward the ultimate goal of a manufacturing aware design process by:

1. Adding functionality to the CODE V optical design program that allows it to compute metrics that are related to cost and difficulty of fabricating NRS surfaces.
2. Incorporating the cost metrics for NRS surfaces to be into the merit function or into constraints that are used during the optimization. This allows the optimization process to automatically trade off performance vs. cost.
3. Demonstrating the benefit of the items (1) and (2) by performing a design using the new capability.
4. Demonstrating the ability to characterize a manufacturing process in a way that allows the prediction of surface form errors for a specific profile.
5. Predicting the as-built performance of a system by incorporating the predicted surface form errors into the model of the nominal design.

1.6 ACKNOWLEDGEMENTS

This work was supported by the United States Army Space and Missile Defense Command under STTR contract W9113M-04-P-0149 and SBIR contract W9113M-05-P-0092.

REFERENCES

1. Garrard, K.P., A. Sohn, R.G. Ohl, R. Mink and V.J. Chambers. Off-axis biconic mirror fabrication. Proceedings of the Third International Meeting of the European Society for Precision Engineering and Nanotechnology (EUSPEN), 277-280, (2002).
2. Ohl, R.G., W. Preuss, A. Sohn, S. Conkey, K. Garrard, J.G. Hagopian, J.M. Howard, J.E. Hylan, S.M. Irish, J.E. Mentzell, M. Schroeder, L.M. Sparr, R.S. Winsor, S.W. Zewari, M.A. Greenhouse and J.W. MacKenty. Design and fabrication of diamond machined, aspheric mirrors for ground-based, near-IR astronomy. Proceedings of the SPIE **4841**, 677-688 (2003).

3. Plummer, W.T. Unusual optics in the Polaroid SX-70 land camera, Applied Optics, **21**, 2, 196-202 (1982).
4. Heinrich, M. and C. Wildsmith. Need for precision engineering in astigmatic contact lenses. Proceedings of the ASPE Topical Meeting on Freeform Optics, **31**, 18-22 (2004).
5. Rodgers, M. and K. Thompson. Benefits of freeform mirror surfaces in optical design. Proceedings of the ASPE 2004 Winter Topical Meeting on Freeform Optics, 31, 73-78 (2004).
6. R.G. Ohl, A. Sohn, T.A. Dow and K.P. Garrard. Highlights of the ASPE 2004 winter topical meeting on freeform optics: design, fabrication, metrology, assembly. Proceedings of the SPIE **5494**, (2004).
7. United States patent 5,467,675. Apparatus and method for forming a workpiece surface into a non-rotationally symmetric shape. Thomas A. Dow, Kenneth P. Garrard, George M. Moorefield, II and Lauren W. Taylor (1995).
8. W.D. Allen, R.J. Fornaro, K.P. Garrard and L.W. Taylor. A high performance embedded machine tool controller. Microprocessors and Microprogramming, **40**, 179-191, (1994).
9. Garrard, K.P. and T.A. Dow. Design tools for freeform optics. Precision Engineering Center Annual Report, 22, 1-23, (2004).
10. Thompson, D.C. Theoretical tool movement required to diamond turn an off-axis paraboloid on axis. Advances in the Precision Machining of Optics, Proceedings of the SPIE **93** (1976).
11. Gerchman, M.C. A description of off-axis conic surfaces for non-axisymmetric surface generation. Proceedings of the SPIE **1266** (1990).

APPENDIX A

A Code V UDF that calls an external DLL to compute a manufacturing cost metric.

```
! ------------------------------------------------------------------------
! myudf: This is a user-defined function that calls a user-defined subroutine.
!        It uses the off-axis conic decomposition DLL, NRS_CONIC2, to
!        estimate a cost metric as the tilt optimized on-axis NRS sag.
! ------------------------------------------------------------------------
FCT @costMetric(NUM ^surfaceNumber)
   NUM ^retVal ^maxRad ^apDecenterY ^sCoefs(6) ^nsCoefs(6) ^angle ^ymax ^ymin
   ^NRSSag
   !-- If the surface is not a conic, then return a zero.
   if ( (typ sur S^surfaceNumber) <> "CON" )
      ^retVal == 0.0
   els
      ^yChief ==(y s^surfaceNumber r1 f2)
      ^ymax == 0
      ^ymin == 1e10
      for ^f 1 (num f)
         if (y s^surfaceNumber r2 f^f) > ^ymax
            ^ymax == (y s^surfaceNumber r2 f^f)
         end if
         if (y s^surfaceNumber r3 f^f) > ^ymax
            ^ymax == (y s^surfaceNumber r3 f^f)
         end if
         if (y s^surfaceNumber r2 f^f) < ^ymin
            ^ymin == (y s^surfaceNumber r2 f^f)
         end if
         if (y s^surfaceNumber r3 f^f) < ^ymin
            ^ymin == (y s^surfaceNumber r3 f^f)
         end if
      end for
      ^maxRad == absf(^ymax-^ymin)/2   !-- Or  ^maxRad     == (cir S^surfaceNumber)
      ^apDecenter == ^yChief           !-- Or  ^apDecenter == (ady s^surfaceNumber)
      !-- Call the external DLL to decompose the off-axis conic
      USR nrs_conic2 ^surfaceNumber  ^maxRad  ^apDecenter  ^sCoefs  ^nsCoefs  ^angle  ^NRSSag
      ^retVal == ^NRSSag
   end if
END FCT ^retVal
```

APPENDIX B

Interface specification for the off-axis conic decomposition external DLL.

```
// ------------------------------------------------------------------------------------------
// nrs_conic2:
//
//  Purpose: This subroutine will perform a decomposition of an off-axis section of a conic
//           surface into a rotationally symmetric component and a non-rotationally symmetric
//           component.
//
// Parameters: surfaceNumber (double*; input)
//                The surface number for which the decomposition is performed.
//
//             apertureRadius (double*; input)
//                The radius of the aperture that is projected onto the off-axis section. The
//                actual part radius will be somewhat larger than this, because it is measured
//                in a plane that is tilted with respect to the parent surface coordinate system.
//
//             apertureDecenterY (double*; input)
//                The distance from the vertex of the parent conic to the aperture center.
//
//             asphereCoefficients[*] (double*; in/out)
//                The polynomial coefficients of an even polynomial that represents the
//                rotationally-symmetric portion of the surface sag.  Currently, the number
//                of coefficients is fixed at nterms=6.  The array must be allocated by the
//                calling routine, but the data is filled in by this subroutine.
//
//             nonSymmetricCoefficients[*] (double*; in/out)
//                The coefficients of a function that describes the non-rotationally symmetric
//                component of the off-axis conic sag. The number of coefficients is fixed at
//                nterms=6.  The array must be allocated by the calling routine, but the data
//                is filled in by this subroutine.
//
//             angleOfTilt (double*; output)
//                The angle at which the base plane is tilted.  The base plane is a plane that
//                contains a point on the parent conic that is at the aperture center.  This
//                plane is tilted so that the sag at each end of the aperture is equal.
//                (In this context, each end of the aperture means those points that are closest
//                and farthest from the vertex of the parent conic.)
//
//             NRSSag (double*; output)
//                A number that is roughly related to the time to fabricate this surface. It is
```

```
//                the magnitude of the non-rotationally symmetric component of the surface sag.
//                (Peak-to-valley of this component of the sag.)
//
// ------------------------------------------------------------------------------------------
void nrs_conic2(double* surfaceNumber,
                double* apertureRadius,
                double* apertureDecenterY,
                double* asphereCoefficients,
                double* nonSymmetricCoefficients,
                double* angleOfTilt,
                double* NRSSag)
```

2 DESIGN OF REFLECTIVE OPTICAL SYSTEMS

Nadim Wanna
Graduate Student

Thomas Dow
Professor, Mechanical and Aerospace Engineering

Challenges in fabrication and testing have limited the choice of surfaces available for the design of reflective optical systems. Rotationally symmetric conic surfaces are common, but more degrees of freedom are necessary to meet challenging performance and packaging requirements. With support from fabrication technologies developed at the PEC, design of reflective optical systems with non-rotationally symmetric surfaces is investigated. Non-rotational symmetric surfaces correct optical aberrations, especially astigmatism at higher field angles. Issues related to opto-mechanical design, mirror location and mounting are discussed.

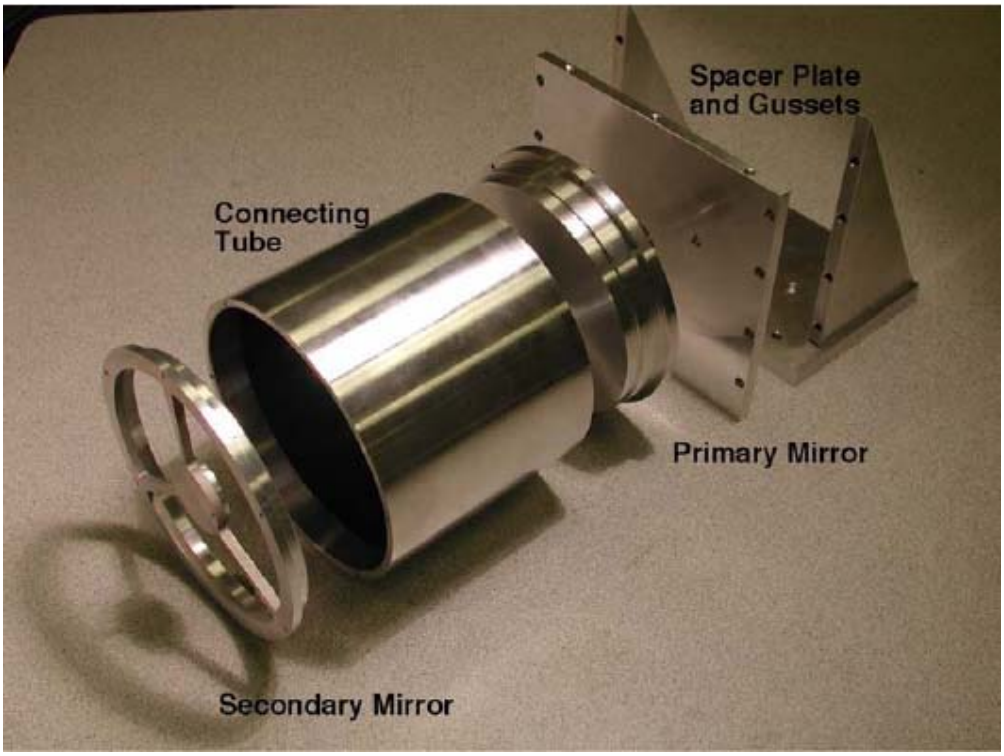

2.1 INTRODUCTION

Optical systems play a crucial role in a wide variety of products from camera phones to seeker missile guidance systems to free-space optical interconnects on computer chips. The field is divided into major categories: Geometric Optics is the study of light without diffraction or interference whereas Physical Optics expands the scope to include diffraction effects. Whereas some optical systems use reflective, refractive and diffractive elements, the emphasis here will be on reflective systems.

2.2 TWO MIRROR TELESCOPE

The goal of the first optical design is to gain familiarity with optical design, fabrication and performance evaluation for telescope systems constructed using reflective mirrors. Because changes are most efficiently made during the design process, an understanding of the whole process (design, fabrication, metrology and assembly) must be addressed and is a key to cost effective deployment of systems. A telescope system using two mirrors was selected for the first prototype because it is the simplest example of a reflecting telescope. The specification of the system are an entrance pupil diameter of 150 mm, effective focal length of 859.872 mm, field of view of 1º, f-number of 5.73, and an image height of 15 mm. The second prototype will be a similar design but using Three Mirror Anastigmat (TMA) design with modified specifications.

The classic Cassegrain uses a two mirror layout that consists of a primary and a secondary mirror. The mirrors are coaxial and each mirror is rotationally symmetrical about this axis. Light enters the system, first encountering the primary mirror, which then reflects the light to the secondary mirror. The secondary reflects light through a hole in the center of the primary to the image plane as shown in Figure 1. The primary mirror aperture is specified by the entrance pupil diameter at 150mm, while the f-number of the primary is specified as f/1; thus, setting the radius of curvature of the primary at 300mm.

2.2.1 OPTICAL DESIGN

The Ritchey-Chrétien telescope differs from the two-mirror Cassegrain prescription such that specific optical aberrations are corrected. In this configuration both aspheres are hyperbolic and correct simultaneously for both spherical aberrations and coma. The Hubble Space Telescope uses a RC design. Similar to the Cassegrain, the Ritchey-Chrétien design is limited by astigmatism at high field angles [1]. Creating and measuring the hyperbolic mirror surfaces was

once considered difficult, but the advent of diamond turning has made the fabrication problems less acute and methods for measurement are now available.

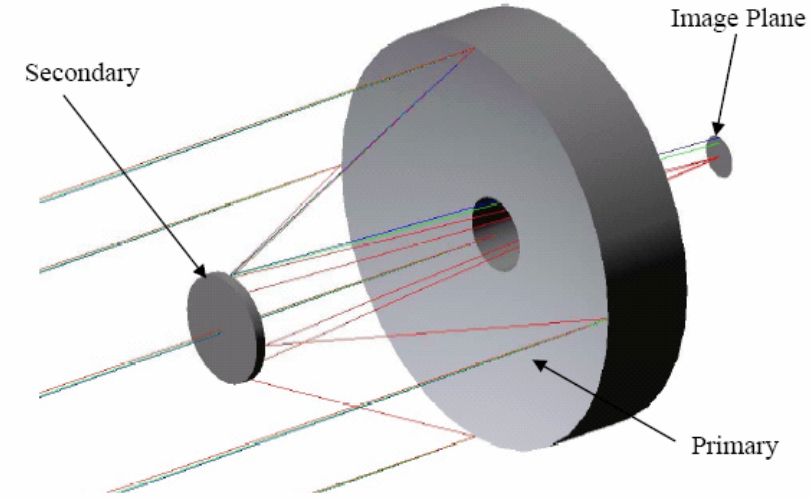

Figure 1: Two mirror optical system

Size and shape

The optical system overall size is determined by optical, fabrication and mechanical design issues. A primary aperture diameter of 150 mm served as the starting point of the optical design. Many of the optical choices are centered on the primary's speed, that is, light gathering ability. The primary is set at f/1; thus, the focal length is 150 mm and radius of curvature is twice the focal length, or 300 mm. Initially, the conic constant was set at -1 (parabola) and allowed to vary. The diameter of the center hole was set to 26 mm.

Specification of the secondary is largely based on its function to reflect light from the primary and to correct the primary's optical defects. Its aperture diameter is solved by the height of the marginal rays reflected by the primary. In accordance with the Ritchey-Chrétien prescription, the conic constant was set for a hyperboloid at -2 and allowed to vary. The radius of curvature was initially set to 90 mm, but was also set to variable.

Mirror spacing is measured as a percentage of the secondary distance from the primary's focal point. Small percentages, below 15%, increase alignment sensitivity and large percentages, above 30%, increase obscuration. Spacing in this system is initially set at 20%. Spacing of the secondary affects the radius of curvature and thereby substantially affecting the focal point of the secondary and thus, the location of the detector. Therefore, small adjustments, 0.25% step size, to spacing is used to finalize the distance from the secondary to the image place.

Optimization

Global system specifications are used in Code V to initialize the system and solve basic system parameters. The entrance pupil is set at 150 mm, or the size of the primary mirror. Analysis wavelength is set at 632.8 nm. Because astigmatism is a function of field height in all two-mirror designs, this system is specified at 1° field angle. Paraxial image solve is enabled such that the image surface is set at the system paraxial image focus, or the point where the rays parallel to the system axis converge.

Optical Research Associates (ORA) provides a standard optimization routine in Code V that is fully customizable. Since reflecting telescopes can be nearly diffraction limited, the error function type is set to RMS wavefront error variance. Third order spherical aberration and third order tangential coma are both targeted to zero. Additionally, the YZ paraxial marginal exit angle between the secondary and the detector is set to 0.0872. This value is calculated by dividing the inverse of the system's f-number by 2. The system f-number is set by a combination of the detector height, field angle, and aperture diameter as shown in equations 1 and 2.

$$\theta_{Paraxial\ Marginal\ Exit} = \frac{1}{2\ f/\#} \tag{1}$$

$$f/\# = \frac{h_{detector}}{\theta_{field}\, d_{aperture}} = \frac{15mm}{\frac{1°}{57.3}150mm} = 5.734 \tag{2}$$

All specifications not explicitly selected are allowed to vary during optimization. The final conic constant of the primary is -1.0195 and the secondary is -2.1666. Radius of curvature of the secondary is 88.1225 mm and the aperture diameter is 38.9395 mm. Distance between the primary and secondary vertices was adjusted by trial and error to accommodate the 44 mm spacing from mount to film plane of the Canon EOS camera used as the detector. The primary/secondary distance was set to 113.625 mm and this made the distance from the secondary to the image plane to be 208.519 mm. The effective focal length of the finalized system is 859.872 mm.

Theoretical Performance

System analysis was performed using tools in Code V to predict the performance of the two-mirror system. The fundamental aberration in a Ritchey-Chrétien (RC) design is uncorrectable astigmatism. Astigmatism occurs when a point source is imaged as two separate lines at different axial positions with an elliptical or circular blur between them [2]. For the rotationally symmetric optical system, astigmatism is zero on-axis and increases with the field angle.

Wavefront Analysis One way to access the errors in an optical system is to plot the wavefront errors over the field of view of the system. Figure 2(a) shows such a plot for the theoretical performance of the RC design over the ±0.5° field of view with the best focus on axis. Note that the smallest error occurs in the center and that the error grows with astigmatism as the field of view gets larger. To minimize the error over the field of view, Code V software creates a best focus for the system – in this case at the 0.35° field angle (70% of the range). Figure 2(b) shows the results with the minimum error now at an intermediate position from the axis to the maximum field angle. The scale of both figures is the same. The maximum error in the on-axis focus is 0.001 waves at the center and 1.199 waves at 0.5°, and for the optimum focus is 0.582 waves on-axis and 0.658 waves at 0.5°.

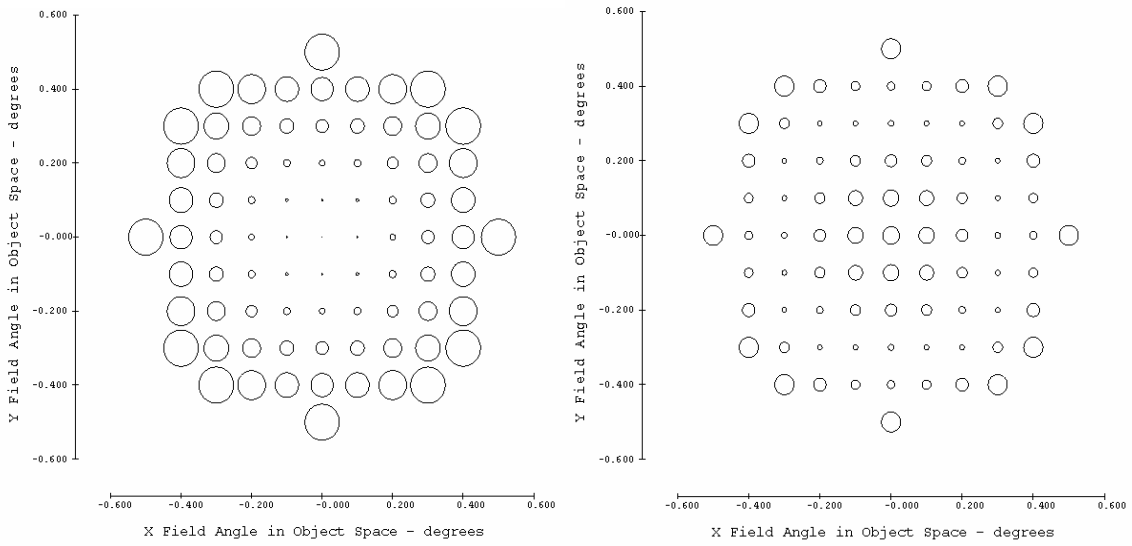

a) Best focus on-axis b) Best focus at 0.35° (70% of max field)

Figure 2: RMS wavefront error map across the field of view of the telescope

Another way to view the system aberration is the departure of the wavefront through the telescope from an ideal spherical wavefront. Code V plot options include presentation of the interferogram fringe pattern for three different field positions with the best focus at 0.35° illustrated in Figure 3. The shapes of the fringes indicate the aberrations present at that region of the system. The only aberration present on-axis is spherical aberration as shown by the circular interference fringes that is caused by the defocus needed to optimize the system over the field of view. The aberrations are smallest at the 0.35° field angle and the fringe pattern is typical of

astigmatism. The interference plot for the 0.5° half-field shows focus and astigmatic errors produce the oval wavefront with more fringes vertically than horizontally.

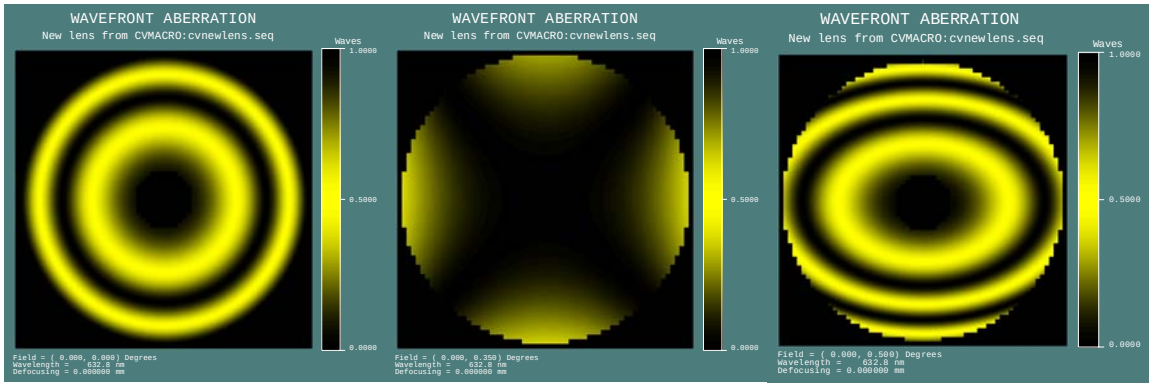

a) Error at 0° b) Error at 0.35° c) Error at 0.5°

Figure 3: Wavefront error for the optimized 2-mirror system at three field positions

Modulation Transfer Function Another measure of the optical quality of the RC telescope is the Modulation Transfer Function (MTF). The MTF is used to determine the frequency response of a system or its ability to render spatial frequencies on the image plane. Characteristic such as sharpness and resolution can be related to MTF. Diffraction sets the upper limit of contrast for all systems and is plotted as the right-most dotted line in Figure 4. This plot gives a modulation value for contrast with 1.0 being perfect black and white boundaries and 0.0 being totally gray as a function of the spatial frequency. The MTF for the RC design displays the best performance at the mid-field point as a result of the focus optimization. The best focus field angle (0.35°) shows 60 cycles/mm at 50% modulation, while the other two exhibit a much lower value, 15 cycles/mm, because of the lack of focus. There are two traces for each field angle that show the MTF along the tangential (solid line) and radial (or sagittal, dotted line).

Spot Diagram Spot diagrams show the ray-based geometrical shape of the image distribution for each field point. A series of rays through that field point will intersect the image plane close to but not at the ideal image spot. The spot diagrams give a good visual impression of image quality and their shape can be used to identify optical characteristics and aberrations. The spot diagram for the best focus position can be seen in Figure 5. The best focus as determined by Code V is at 0.35° field angle. The smallest RMS spot size for this defocus is 8μm at 0.35° and it increases to approximately 47μm fir the full field (0.5°).

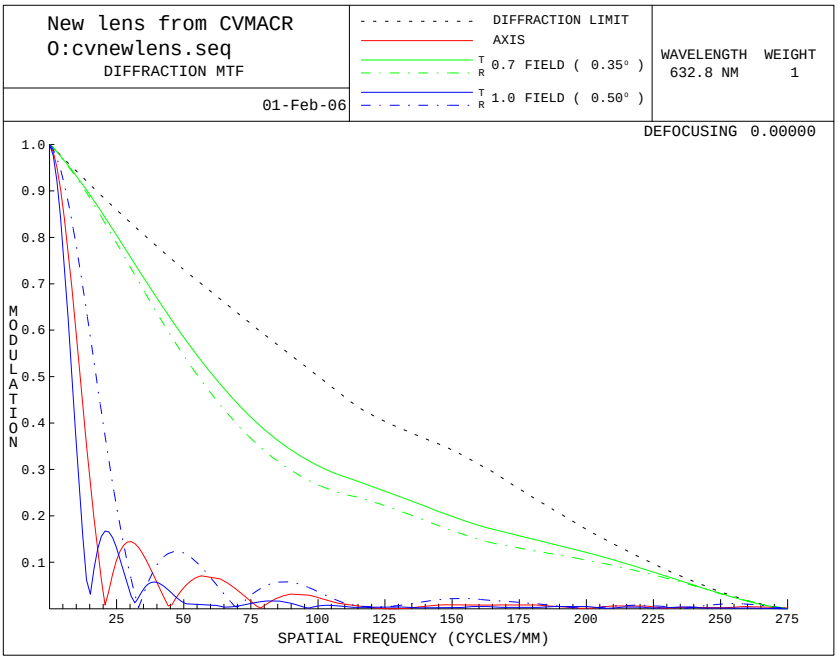

Figure 4: MTF for optimized 2-mirror system presented on-axis and at two locations off-axis (0.35° and 0.5°). Best performance is at the mid position as a result of the focus optimization.

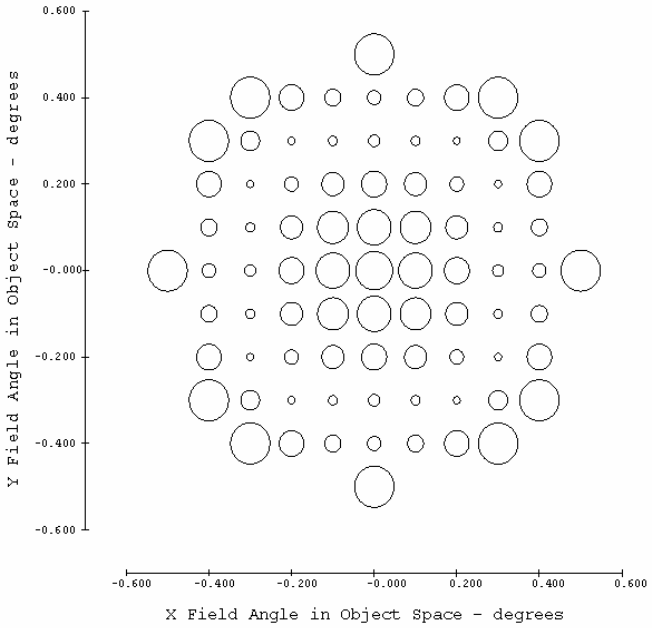

Figure 5: Spot diagram for optimized 2-mirror system

2.2.2 OPTOMECHANICAL DESIGN

The optomechanical design consists of separate primary and secondary optics with a cylindrical tube connecting them. This tube, shown in Figure 6, provides reference surface that locate the two optical surfaces in the axial, radial and tilt directions. The OD of the cylinder is 164 mm. The 39 mm diameter secondary mirror has an average thickness of 10 mm and is supported by three radial struts arms from the outside ring to the mirror. The average thickness of the primary is 27 mm and the OD is 154 mm.

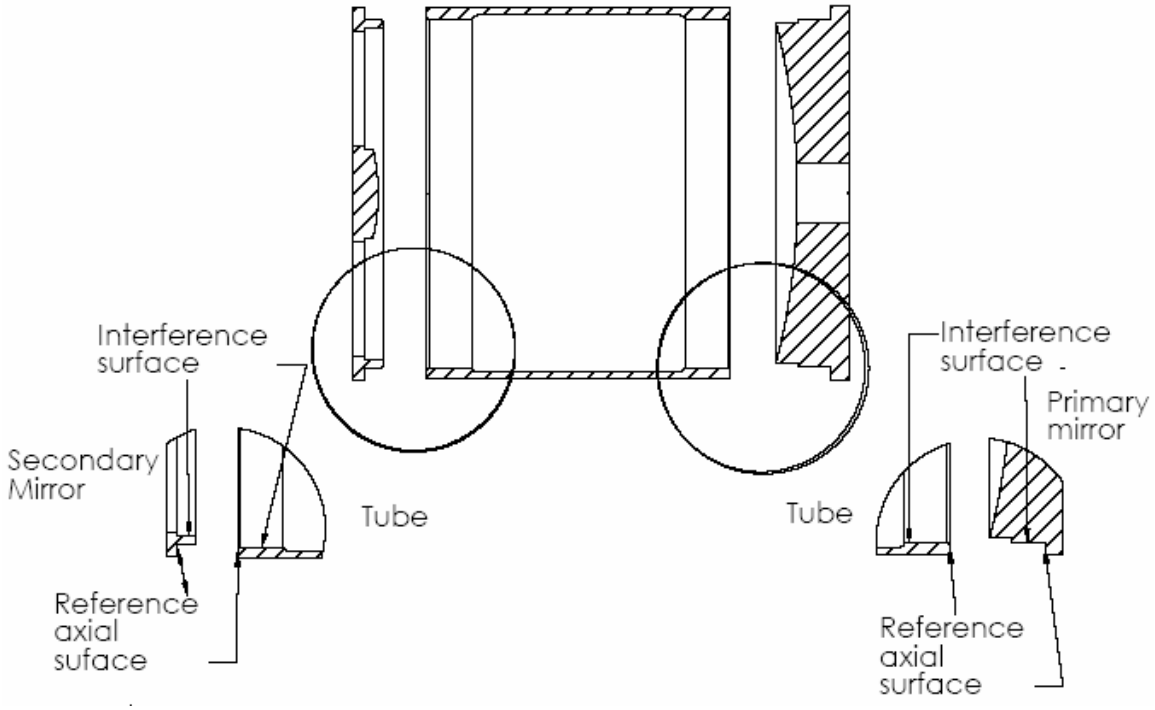

Figure 6: Detail drawing of the telescope

The primary and secondary have a small interference fit to the tube (~6 μm) and three 4-40 screws were employed to hold each in place. The assembly process was to heat the tube by holding it in bare hands to eliminate the thermally interference, inserting the optic into the tube (shown in Figure 7) and then tighten the screws to 2 in-lbs. This torque should produce a force of 100 lbs or 450 N. Because the tube is much stiffer than the optical components, discussed in the following paragraph**,** the application of these three forces on the surface causes distortion to the optical surfaces.

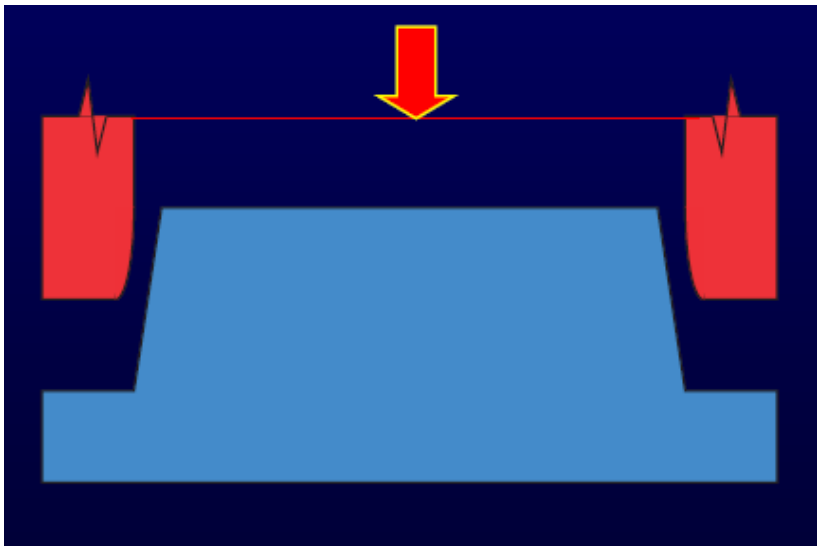

Figure 7: Assembly of optical components into the tube

When the primary is assembled to the tube, the shape of the system will be a function of the shape and stiffness of the mating components. The tube and a circular plate were modeled in SolidWorks/Cosmos to obtain the stiffness of the two components. Both components are analyzed under the same loading-restraint conditions. Distributed load, 100 N, is applied on one end, while the part is restraint on the opposite end. The stiffness of the plate is computed to be 42.83 N/μm, while the tube stiffness is found to be 112.77 N/μm. The tube is more than two times stiffer than the plate; thus, mounting the primary on the tube would deform the primary under the assembly conditions required.

All the components of the telescope are Aluminum 6061-T6. This material combines high strength, low weight, and good machineability with diamond tools, excellent coating adhesion and high resistance to corrosion. Also, by using a single material, no distortion of the components will occur for an environmental temperature change. One problem with 6061 aluminum is the second-phase impurities tend to reduce the surface finish to the order of 10 nm RMS.

Secondary mirror structure

The secondary mirror structure is press fit into the tube with an interference of 6μm applied 5mm from the axial fiducial surface. Since the tube is stiffer than the mirrors, the interference force, 91 lbs, creates a bending moment. This bending moment displaces the secondary mirror 9.26μm away from the primary mirror as shown by the model setup in SolidWorks, Figure 8. This displacement causes focus error in the system, shift in the image plane, as discussed in the metrology section.

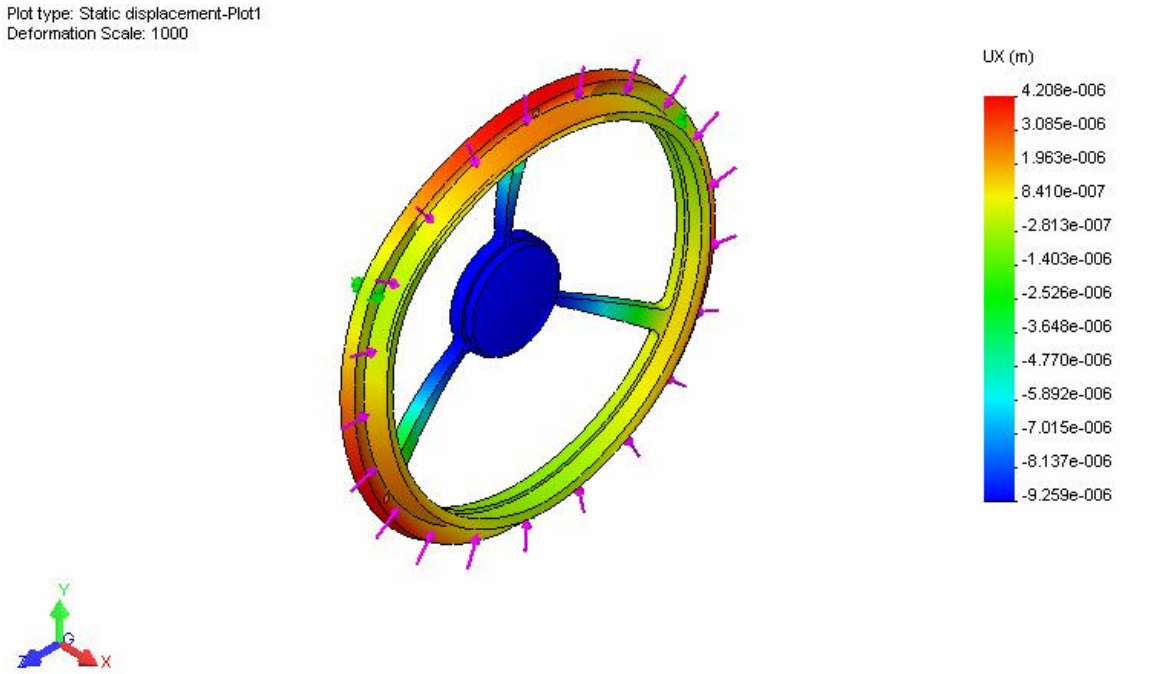

Figure 8: Secondary mirror structure deflection due to mounting onto the tube

2.2.3 ERROR MODELING

Model Dual Pass System

The telescope is going to be measured using the Zygo-GPI laser interferometer as discussed in further sections. The dual pass measurement was setup in Code V to visualize the wavefront error plots generated in the experiment. The wavefront error for this measurement should be twice that of the RC telescope because the wavefront passes through the telescope twice. A schematic of the system is shown in Figure 9. The two telescopes are on top of each other but the optical path in Code V goes from left to right and returns from right to left. A spherical wavefront is generated from the focus point at the left, passes through the telescope and creates collimated light that impinges onto the flat mirror. The light is collimated because the system was designed for infinite conjugates. Light from the mirror is reflected back through an identical telescope and focused onto the original point. To test the system for the 0.35º and 0.5 º fields, the telescope is translated from the nominal optical axis, shown in Figure 9 as the centerline, in the y-direction. The telescope is decentered until the off-axis focus coincides with the optical axis, where each field angle corresponds to a different off-axis focus. Then, the flat mirror is tilted to reflect the collimated light back through the telescope. The wavefront error for the different fields is shown in Figure 10.

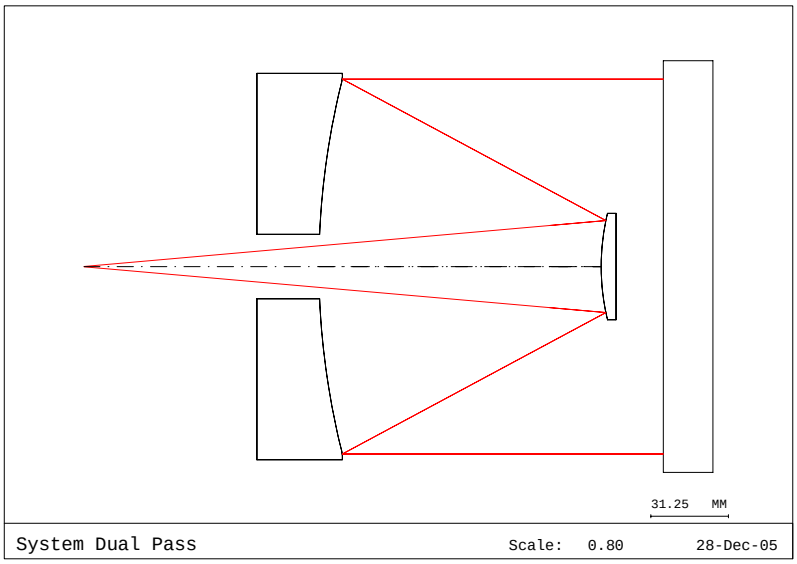

Figure 9: Dual pass setup for telescope testing, showing on-axis rays

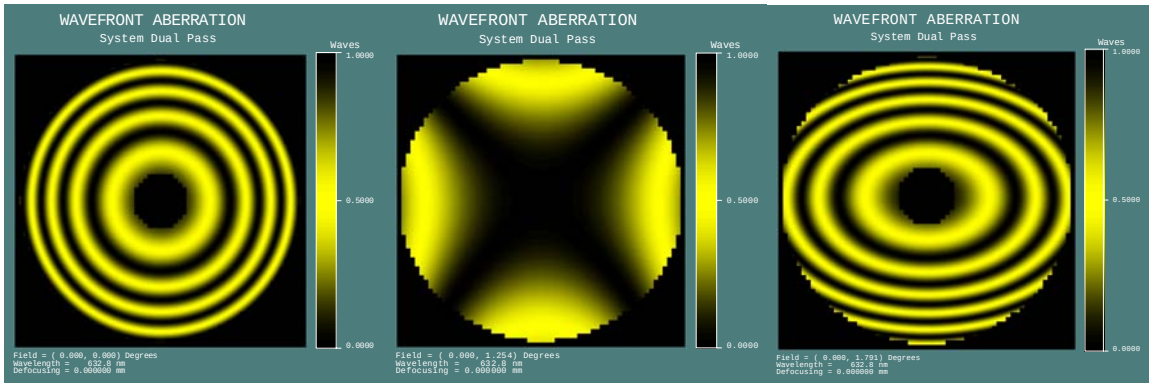

a) Error at 0° b) Error at 0.35° c) Error at 0.5°

Figure 10: Wavefront error for the dual pass model in Code V with best focus at 0.35°

The spherical wavefront passes through the system twice, since there are two telescopes concatenated on top of each other. Therefore, the theoretical wavefront error from the dual pass model, Figure 10, should be double the theoretical system wavefront error, Figure 3. The wavefront error for the 0˚ field shows circular interference fringes, maximum of 4 waves, which indicate that the system is out of focus. Aberrations are minimum at the 0.35˚ field angle where astigmatism dominates the wavefront, peak-to-valley of 1.4 waves. The wavefront error for the 0.5˚ field shows both focus and astigmatic error concluded from the oval interference fringes, maximum of 5.5 waves. Figure 10 shows wavefront errors that are double those of the telescope model in Figure 3.

Aspect ratio

Distortions of the optical surfaces occur when a part is mounted on the vacuum chuck for machining. The parts are modeled as cylindrical plates. The compliance of a cylindrical plate is related to the aspect ratio between the diameter and the thickness. To keep the distortion as small as possible, the aspect ratio should be large. One way to evaluate the effect of a change in either dimension is to consider the simple problem of a plate with diameter *(d)* and thickness *(t)* that is simply supported on the OD and loaded by pressure over the surface. This is analogous to the part being vacuumed onto a chuck but where contact only occurs at the OD. For this condition, the deflection at the center can be written as [3]:

$$\delta_{\max} = 0.7\left(\frac{qr^4}{Et^3}\right) \tag{3}$$

where q is the pressure, r is the outside radius, E is the elastic modulus of the material and t is the plate thickness. Figure 11 shows the deflection of the 150 mm diameter plate as a function of the aspect ratio for a typical vacuum loading of 10 psi (70 kPa). Note that the deflection is not just a function of the aspect ratio but also depends on the radius because the ratio is r^4/t^3. The aspect ratio of the primary is about 5.5 so it will deflect more than 1 μm for the vacuum loading. This turned out to be a problem as discussed in later reports. For the same loading, the secondary mirror (aspect ratio ~ 4) would only have 0.1 μm deflection.

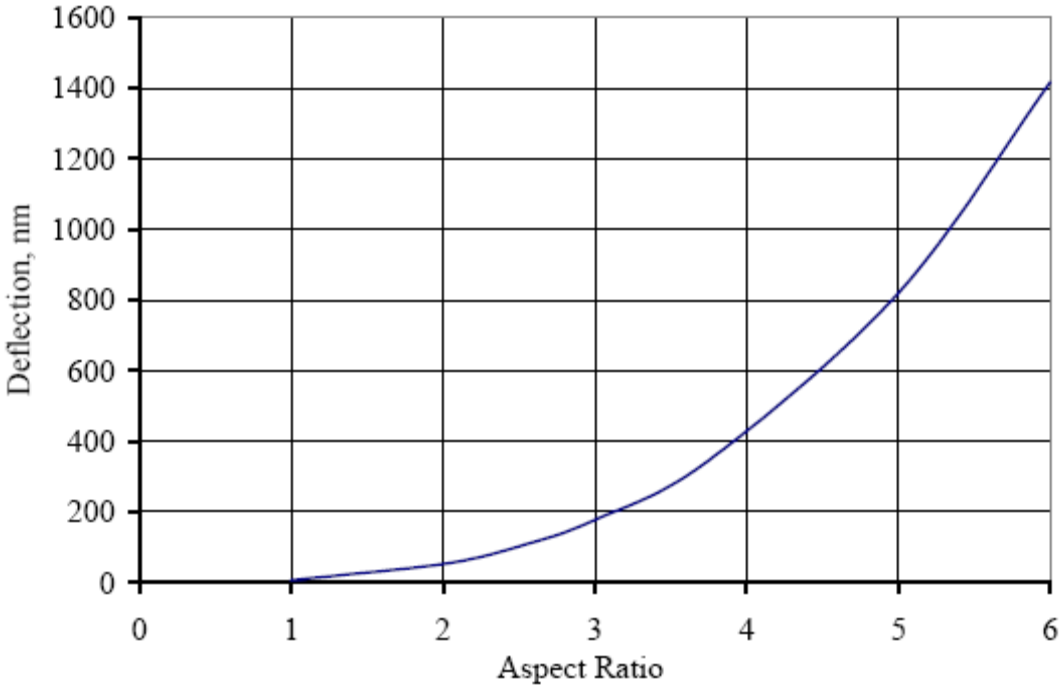

Figure 11: Deflection of a solid 150 mm dia. aluminum plate vs. Aspect Ratio (diameter/thickness)

2.3 THREE MIRROR ANASTIGMAT

For rotationally symmetric systems, there is no astigmatism on-axis. As the image point moves further from the axis, the amount of astigmatism gradually increases. To avoid astigmatism at a single off-axis field angle, unobstructed three mirror telescope is considered. The three mirrors are off-axis conic sections and the system has the following specifications.

2.3.1 OPTICAL DESIGN

The Three Mirror Anastigmat (TMA) is an f/6.139 with an unobstructed 140 mm aperture, and a 1° circular field of view. The three mirrors are diamond turned, aluminum optics that share the same optical axis. These optics are mounted in a one-piece, aluminum telescope housing with fiducial surfaces to reference the optics with respect to each other.

Size and shape

The optical system was designed to improve on the performance of the two mirror telescope. The primary mirror was the corner stone of the design. The state of the art is a primary mirror with an f-number between 0.75 and 1.25. The conic constant was set to -1 (parabola) at the start with but was allowed to vary. The entrance pupil diameter (stop surface) was decentered by 220 mm, setting the f-number of the primary mirror in the range specified above.

The secondary mirror lies on the same optical axis of the primary mirror. The distance between the primary and the secondary is specified to be 260 mm, ensuring the incoming rays to be unobstructed. The radius of curvature was initially set at 400 mm, but allowed to vary in the optimization. Following the initial specifications, off-axis conic sections, the conic constant was initially set to -2 (hyperbolic) and allowed to vary.

The tertiary mirror was placed coplanar with the primary mirror. This might be an advantage where the primary and tertiary mirror could be machined from the same blank. The radius of curvature is calculated in Code V by the YZ paraxial marginal exit angle given in Equation 1. The conic constant is initially set at -2 (hyperbola) and allowed to vary in the optimization. The distance from the tertiary mirror to the image plane is calculated by the paraxial image distance solve. This option sets the thickness to the image surface such that the paraxial marginal ray has a height of zero.

Optimization

The purpose of optimization is to generate the best optical design within a given set of physical and other constraints. The error function combines image error data into a single number that is minimized in the optimization routine. Code V provides four error function types, wavefront error variance is chosen in this case since the system performance will be measured using dual pass interferometer.

The image plane position is constrained to be behind the secondary mirror by at least 25 mm for mounting clearance of the Canon EOS camera detector. The effective focal length and f-number of the system are calculated by the paraxial marginal exit angle reflected from the third mirror using Equations 1 and 2. For this system, the detector and entrance pupil diameter set the f-number at 6.139 and the effective focal length at 859.5 mm. All specifications not explicitly selected are allowed to vary during optimization.

The optimization produces a telescope with improved system performance. The system is evaluated using the field map option. This option presents various analysis results as a grid of field points, helping to visualize the variation of performance across the field of view or image format [4]. Plotting the wavefront polynomial fit for coma and spherical aberration, shows a node for each option that is above the center of the field. A node or an aberration node, in the field of view represents a point where the particular aberration plotted is zero. This is due to the off-axis nature of the system. While the plot for the wavefront polynomial fit for astigmatism shows a node very close to the center. For an unobstructed off-axis system, there are two nodes in the astigmatism plot; the other node is outside the field of view [5]. Constraints are added to the system by placing the single nodes on axis while placing the astigmatic nodes on top and bottom of the field. Running the optimization routine, with the added constraints, leads to degradation in the performance of the system. The degradation is due to the lack of variables that could be manipulated in the optimization routine. Therefore, the older system, without the specified constraints, is restored and the specifications that were allowed to vary are the following.

The 2-D plot of the three mirror anastigmat is shown in Figure 12. The optical specifications of the three mirrors are tabulated in Table 1. Values that are followed with a (v) were allowed to vary in optimization. Distance between the primary-secondary and secondary-tertiary is reset to 270 mm for clearance of incoming beams. The decenter of each surface is solved for in Code V real ray tracing data. The image plane is 294.860 mm from the tertiary mirror to accommodate the 44 mm spacing from mount to film plane of the Canon EOS camera used as the detector. The effective focal length of the finalized system is 859.5 mm. The best focus of the system is 0.140 mm in a direction away from the tertiary mirror.

Table 1: Optical system specifications

	Radius of curvature (mm)	Conic Constant	Aperture Diameter (mm)	Surface decenter (mm)	Distance to next surface (mm)
Primary	-1000	-1.755 (v)	140	220.243	270
Secondary	-587.151(v)	-5.801 (v)	77	105.992	270
Tertiary	-939.433 (v)	-5.197 (v)	70	79.182	294.86

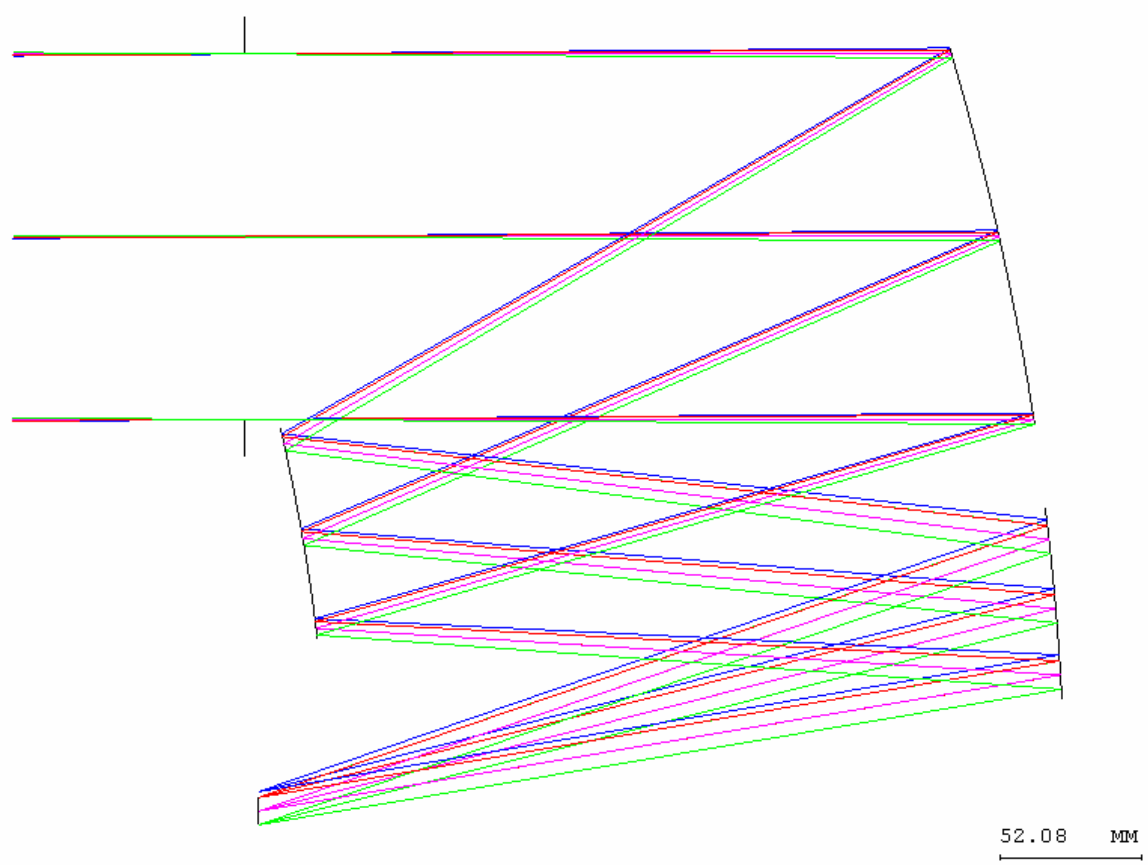

Figure 12: 2D plot of the three mirror anastigmat optical system

Theoretical performance

System analysis was performed using tools in Code V to predict the performance of the three mirror anastigmat. The performance, compared to the two-mirror system described earlier, shows more than three times improvement in the overall system performance illustrated in the following section.

Wavefront Analysis The wavefront error plot over the field of view, Figure 13, gives the best description of the performance of the system. Note that the smallest error occurs above the center of the field, where the minimum error is 0.0328 waves. This is due to the system being off-axis, where aberration nodes are located above the optical axis. The error increases radially outward to reach a maximum of 0.244 waves at -0.5°. The average over the field of view is 0.136 waves compared to 0.6 waves for the RC telescope.

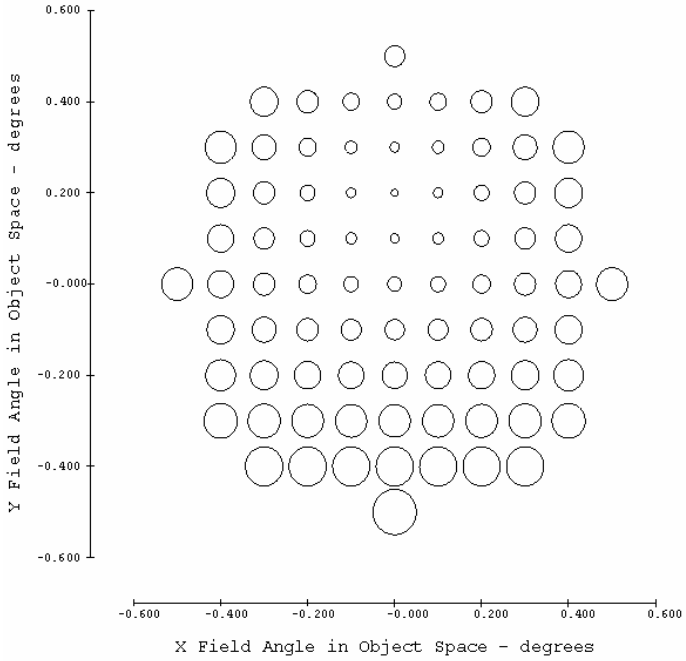

Figure 13: RMS wavefront error across the field of view

Another way to evaluate the performance of the system is to plot the departure of the wavefront through the telescope from an ideal spherical wavefront. The interferogram fringe pattern for three different positions is illustrated in Figure 14. Compared to the two mirror telescope, the three mirror anastigmat is non-symmetric. The wavefront aberration, at 0° field angle, shows a combination of coma and astigmatism, with a peak-to-valley (P-V) of 1 wave. While, the wavefront aberration at 0.35° field angle, is dominated by astigmatism with slight coma effects,

and a P-V of 0.37 waves. The wavefront aberration, 0.5° field angle, exhibits similar behavior to the previous plot, but with a P-V of 0.88 waves. The interferograms show a combination of errors, while the two mirror telescope was symmetric and was dominated by astigmatism and spherical aberration at higher field angles. The magnitude of the aberrations is lower than the two-mirror telescope for each field angle, since aberrations are corrected by the addition of the third mirror.

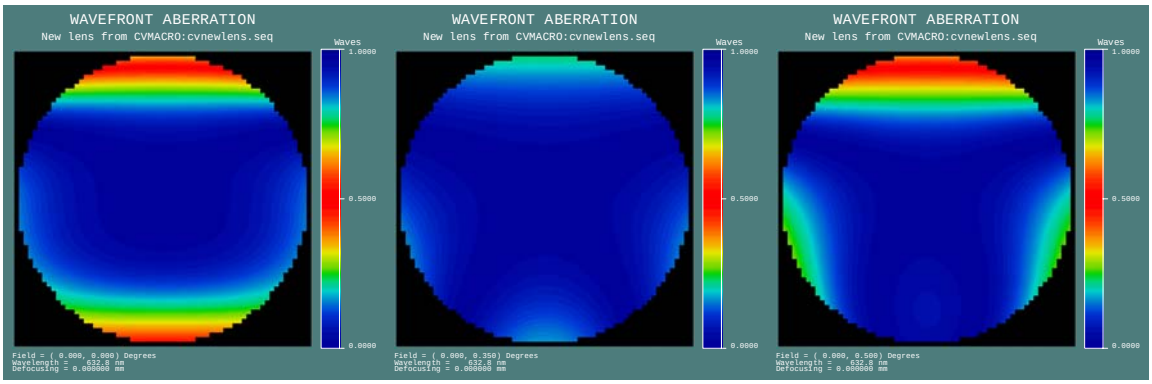

a) Error at 0° b) Error at 0.35° c) Error at 0.5°

Figure 14: Wavefront error for the three mirror anastigmat at three field positions

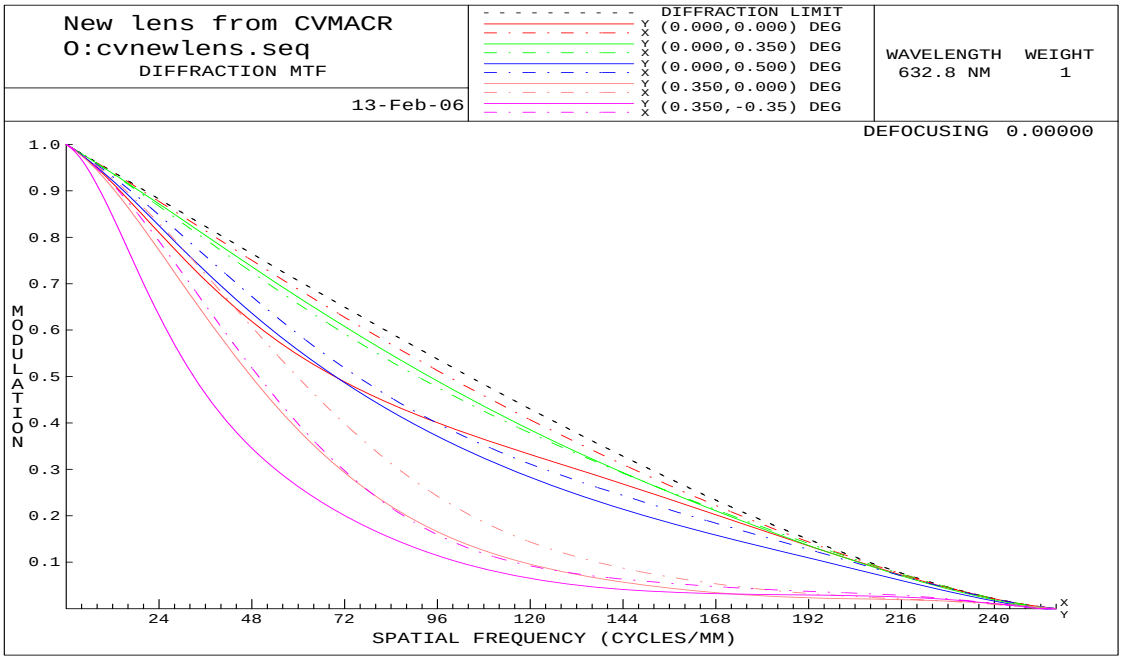

Figure 15: MTF for the three mirror anastigmat

Modulation Transfer function Modulation transfer function is another measure of the quality of an optical system. Diffraction sets the upper limit of the performance and is plotted at the right-most dotted line. The best performance of the system is on-axis where it is almost diffraction limited, or 98 cycles/mm at 50% modulation. While other field angles don't exhibit a sudden drop-off in the MTF found in the RC design; the lowest MTF is at the 0.5° field angle shows 33 cycles/mm at 50% modulation.

Spot Diagram The spot diagram shows the image distribution of a single ray for each field point. The spot diameter for each field point gives a good visual impression of image quality. The smaller the diameter, the better the image quality is at that particular position. The spot diagram of the three mirror anastigmat at best focus position is shown in Figure 16. The smallest RMS spot size is 2.6μm at 0.3°, where the best focus is, and it increases radially outward to reach a value of 18.7μm at -0.5°. The average spot size over the field of view is 9.6μm compared to 25.5μm for the two mirror telescope.

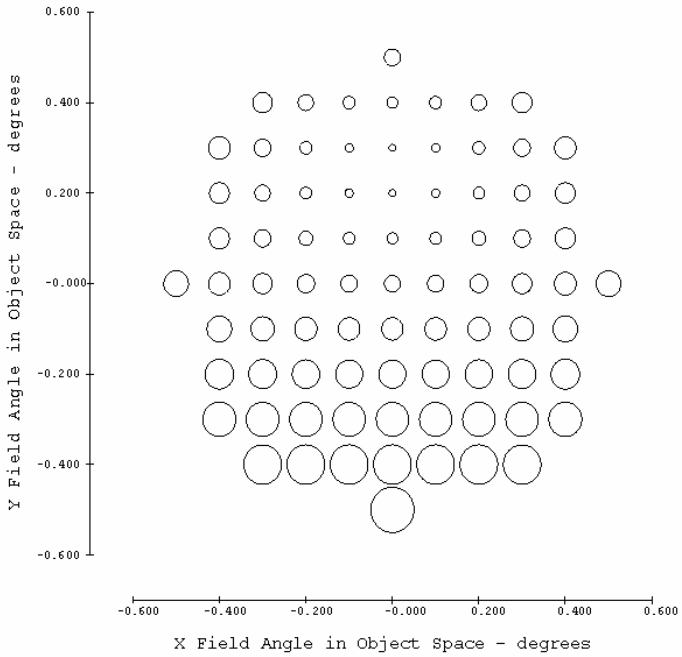

Figure 16: Spot diagram for the optimized three mirror anastigmat

2.3.2 OPTO-MECHANICAL DESIGN

The opto-mechanical design of the three mirror telescope is a snap together aligned telescope with diamond machined aluminum surfaces. The goal is to package the optical elements such

that the appropriate degrees of freedom are constrained but the elements are not over-constrained and thus prone to distortion.

Locational features

The three mirror anastigmat telescope is non-rotationally symmetric. Therefore, each mirror is sensitive to alignment procedure where it should be constraint in six degrees of freedom. The metrology frame is rectangular aluminum housing that would serve as a base to mount the mirrors and camera.

The design of the mirror substrate is crucial in achieving a snap-together telescope. The three mirrors are designed to integrate the same locational and mounting features. Figure 17 shows an optical element with the fiducial and mounting surfaces. To locate the mirror on the metrology frame, six degrees of freedom have to be constrained. The mirror is located in the z-direction using the three mounting pads. The pads constrain the movement in the z-direction and rotation about the x and y axes. These mounting pads provide a precision rotational reference datum that is diamond machined. A precision ground pin and a hole will prevent translation of the mirror in the x and y axes. Finally, a precision ground pin and a slot will prevent rotation of the mirror about the z-axis.

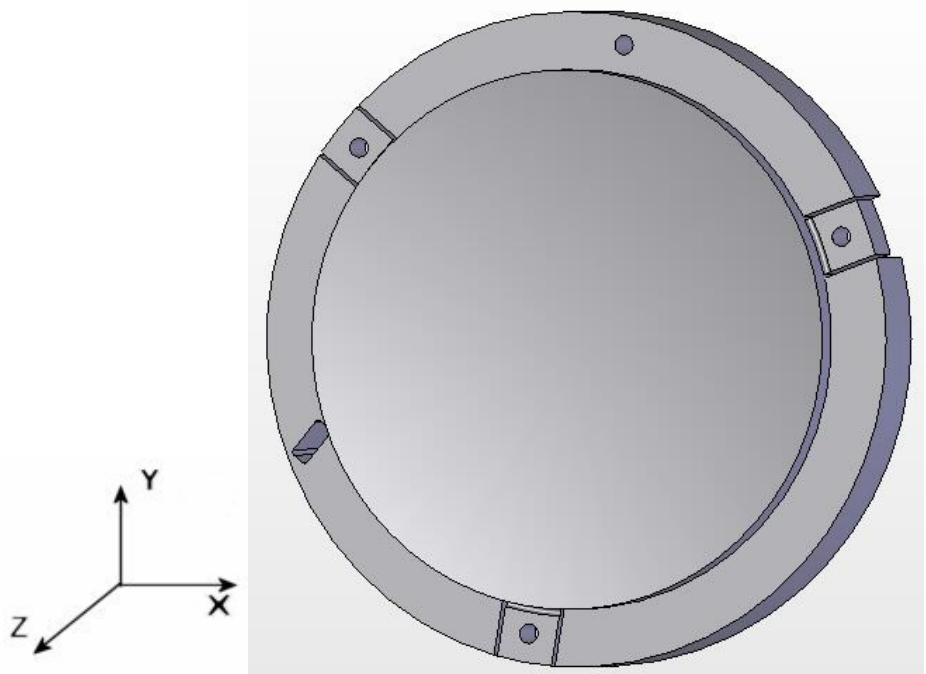

Figure 17: **Primary mirror with precision ground hole and slot, and three mounting flexures**

The mirror blanks will be machined on-axis on the diamond turning machine (DTM). The optical surface has to be tilted to minimize the non-rotational sag. The minimum thickness of each part is based on the aspect ratio experiment described earlier. For example, the primary mirror, Figure 17, has an aperture diameter of 140 mm; the minimum thickness is 28 mm which is the center of the part. Based on the minimum thickness, the thickness of the outer ring is determined accordingly.

The decentered conics will be machined on-axis using diamond turning machine (DTM) with a fast-tool servo (FTS). The optical surface will be decomposed into a rotationally symmetric and non-rotationally symmetric components. The DTM axes create the rotationally symmetric component, while the FTS creates the non-symmetric component. FTS motion is a function of DTM axes position as well as the spindle angular position. Mirrors are tilted with respect to the x-y plane to minimize servo excursion. Table 2 presents the resultant tilt, servo range, and aspheric sag values for each mirror.

Table 2: NRS components of mirrors

	Tilt (degrees)	**NRS range (μm)**	**Ashpere sag(mm)**
Primary	12.163	186.542	2.35
Secondary	9.447	183.466	1.153
Tertiary	4.732	23.526	0.639

The metrology frame, shown in Figure 18, will house the mirrors and camera. The metrology frame is a single piece aluminum structure. The pins will be machined to much tighter tolerances than commercially available. Then, the pins will be lightly press fit on the metrology frame with minimized engagement length to reduce any distortion of the mounting surface [6]. The metrology frame is precision cut for co-planarity of the mirror mounting pads and reference mirror location with respect to each other and the image plane. Surface to surface parallelism is critical to the success of the snap-together alignment philosophy incorporated for the three mirror anastigmat project [7].

Attachment features

The mirrors will be located on the metrology frame using the locational fiducials. Then, the mirrors will be attached using the three flexure arms to minimize optical surface distortions.

The flexure mating surface is offset from the mounting pad plane by 300μm, shown in Figure 19. The flexure surface is offset, not to interfere with the locational procedure of the mirror. The flexure, with 1mm grooves, is designed to displace 300μm, under the screw tightening force, and contact the reference plane of the metrology frame. This mechanism of attaching the mirrors using flexures should minimize the stresses on the optical surface, thus minimizing the optical surface distortions [8].

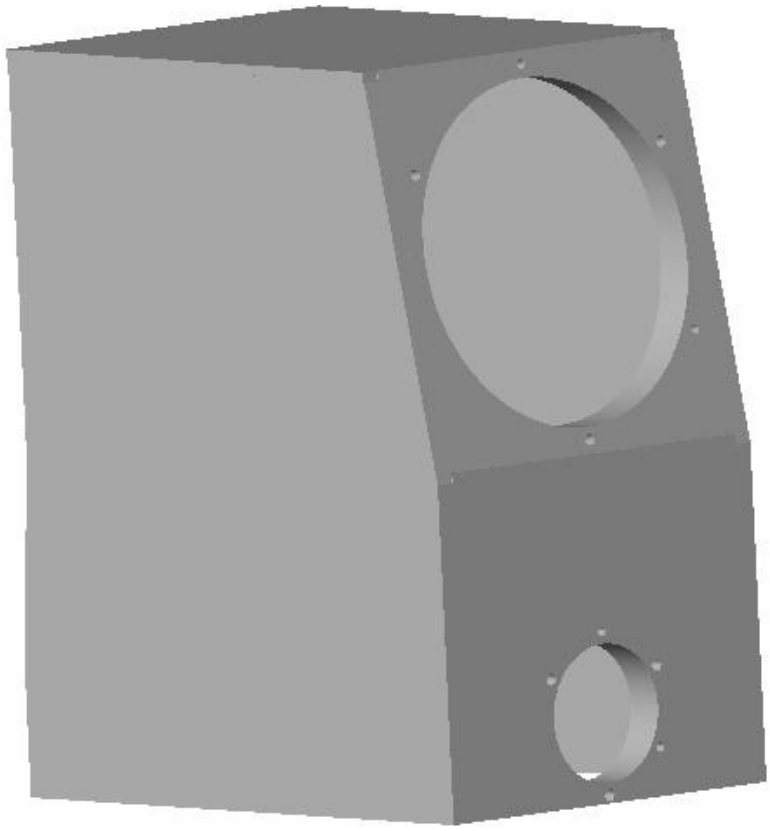

Figure 18: Metrology frame where the mirrors and camera are mounted

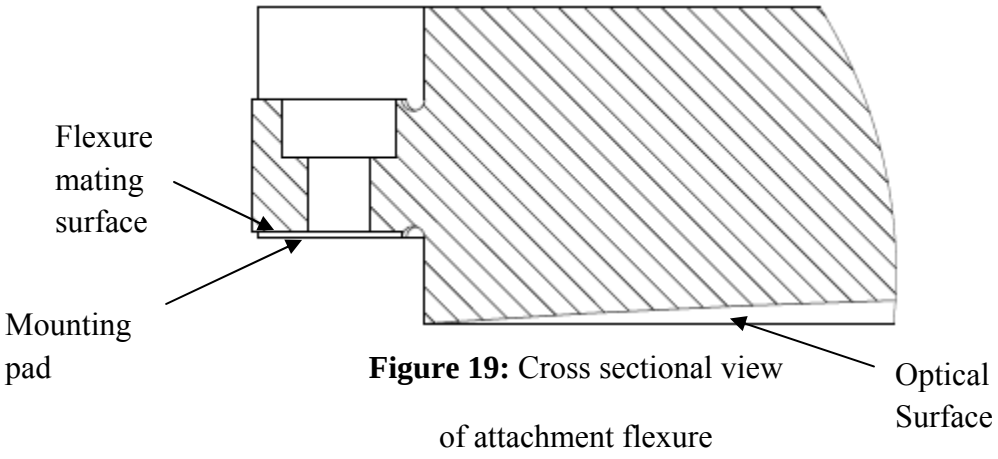

Figure 19: Cross sectional view of attachment flexure

2.4 CONCLUSION

A two mirror axially symmetric telescope has been designed and optimized. Sections 5 and 8 of this report address the fabrication and metrology aspects of this design. The two mirror system suffers from aberrations that increase with field angle and affect the image quality. An unobstructed three mirror telescope has been designed, using off-axis conic sections. The addition of a third mirror reduces the aberrations and improves the image quality. The opto-mechanical design of the TMA followed conventional designs for locating and mounting the mirrors.

Future work includes designing and optimizing an unobstructed three mirror anastigmat using freeform surfaces. With the addition of variables to the optical system, the image quality improves and is diffraction limited. The opto-mechanical design will also be implemented using improved locational and mounting features.

REFERENCES

1. Smith, W.J. “Modern Optical Engineering”. New York, NY: McGraw Hill, 2000.
2. Smith, W.J. “Modern Lens Design”. New York, NY: McGraw Hill, 2005.
3. Roark, R. and Young, W. “Formulas for Stress and Strain”. McGraw Hill, 1975, pg 362.
4. Irving, B. “Code V, Introductory User’s Guide”. ORA, 2004, pg 44.
5. Thompson, K. “Description of the third-order optical aberrations of near-circular pupil optical systems without symmetry”. Optical Society of America, July 2005, pg 1389-1401.

6. Schafer J., “Fundamentals of Single Point Diamond Turning”. ASPE, 2005.
7. Sweeney, M. “Advanced Manufacturing Technologies for Light-Weight, Post Polished, Snap-Together Reflective Optical System Designs”. Proceedings of SPIE, July 2002, pg 144-154.
8. Yoder, P. “Mounting Optics in Optical Instruments”. SPIE Press, 2002, pg 298.

3 SIMULATION OF MANUFACTURING ERRORS FOR FREE-FORM OPTICS

Alex Sohn, Kenneth P. Garrard
PEC Staff
Thomas A. Dow
Professor
Mechanical Engineering

Freeform optical surfaces can be used to control astigmatism at multiple locations in an image. As a result a freeform surface may replace multiple spherical and aspheric reflective components in a complex optical system. Unfortunately, designers have been reluctant to use freeform or even aspheric surfaces in part because they are unable to ascertain the quality of the parts that would be made using diamond turning. Ongoing work in modeling of manufacturing errors in free-form optics will allow the prediction of the quality of optical systems. Limiting factors in machining and assembly are studies and their impact assessed.

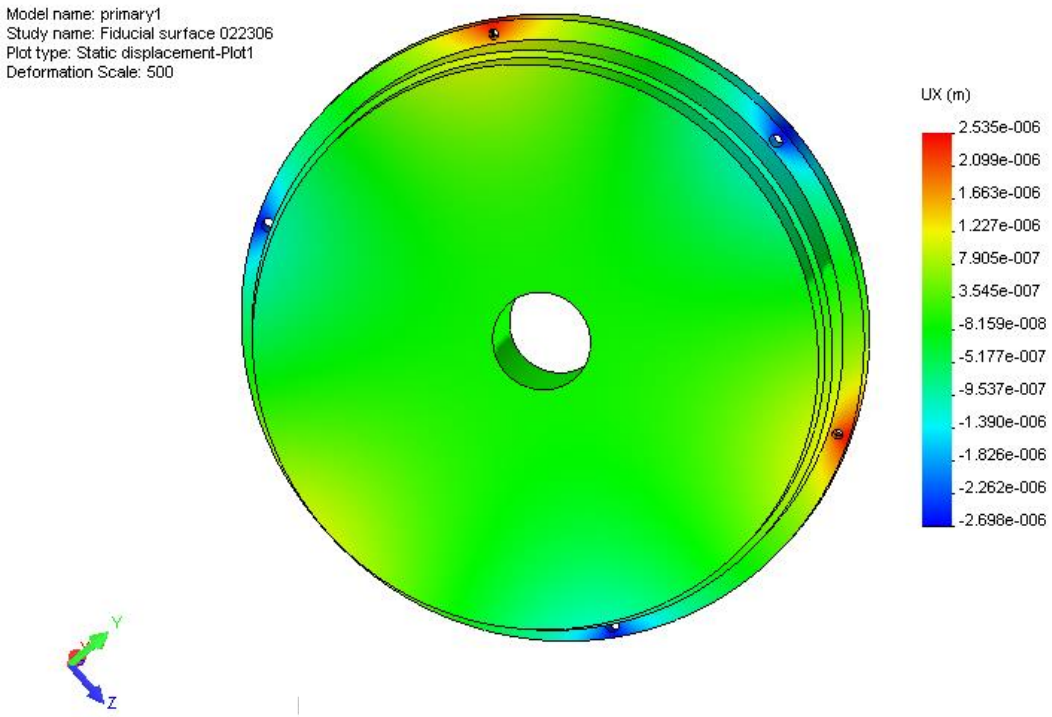

3.1 INTRODUCTION

This is part of an overall effort to predict the errors that will be present in a aspheric or free-form optical system due to machining and assembly processes. A better understanding of these errors and their sources will lead to improved practice in manufacturing and reduce waste in re-processing or correcting flawed systems. Two broad categories of error sources exist: the machining process and the assembly process. In the former, optical surfaces and fiducials are created by machines that may have geometric errors, setup errors or dynamic errors. These cause distortion of the optical surface and lack of knowledge of how the surface is oriented. Assembly errors, falling in two broad categories of stress generation and orientation, also cause distorted and misplaced optical surfaces. Design of fiducials, or orienting features, and mechanical fixturing is key to limiting the impact of these errors. The goal is to design for assembly so that the skill of the assembler becomes less important. As individual errors sources in each of these areas are addressed, their impact on the overall systems can be established to make better performing and more cost-effective optical systems.

3.2 MACHINING ERRORS

Machining errors in diamond turning of free-form optics (specifically those fabricated using a servo axis) falls into two categories: Geometric errors and dynamic errors. Dynamic errors can be estimated by characterizing the dynamic system response of the machining system, inserting those dynamics into a toolpath and thus generating an error profile. Geometric errors are those that are dependent on machining parameters such as tool geometry, axis straightness, scale errors and angular errors (roll, pitch and yaw). Both types of errors can have a significant influence on the final part, though their significance is heavily dependent on the particular part being fabricated. Ultimately, it is the influence of the errors on the optical performance of a system that is of interest. This can be estimated by calculating the surface errors and inserting a simulated, flawed surface into the optical system and observing the change in the optical performance.

3.2.1 DYNAMIC ERRORS

Dynamic error estimation for off-axis conic surfaces and their influence on optical performance has been calculated and is now available in Code V optical design software. These errors are dependent on the measured dynamics of each servo axis. A more responsive axis (higher bandwidth) will exhibit lower dynamic errors, but typically has less range than a more sluggish axis. Dynamic errors are only applied to the non-rotationally symmetric (NRS) portion of the surface determined using decomposition. Each surface point will be shifted in amplitude and

phase and combined with the previously calculated errors to reveal a simulation of what the surface would look like when produced with the method chosen by the designer. Extension of this capability is in progress as discussed in Section 1.

3.2.2 GEOMETRIC ERRORS

Geometric errors can be broken down into two categories: Tool errors and machine errors. Machine errors typically are those associated with straightness, angular, and scale errors in the axes of a machine and must be calculated from measurements of these errors on the machine. Their implementation is very machine-specific and can vary significantly with parameters such choice of tool offset and part mounting method. Axis straightness figures for modern diamond turning machines tend to be less than 300 nm over the entire axis travel. Once again, the influence of these figures on the final part is heavily dependent on part geometry. Smaller components with less sag tend to be affected much less than larger parts. Scale errors can also be significant, though, they also tend to have a smaller influence of parts. Sources of these errors can be things such as polarization mixing in heterodyne interferometers and phase alignment in linear encoders.

Table 1 Sample Tool Error File (TEF)

γ(rad)	R (mm)	Y (mm)
-0.523598776	-0.136574596	0.136974596
-0.436332313	-0.115803313	0.096692213
-0.34906585	-0.093604122	0.063307379
-0.261799388	-0.070544449	0.037074174
-0.174532925	-0.04717713	0.018192247
-0.087266463	-0.02373909	0.006805302
8.32667E-17	-0.0002	0.003
0.087266463	0.02368909	0.006805302
0.174532925	0.04754713	0.018192247
0.261799388	0.070794449	0.037074174
0.34906585	0.093354122	0.063307379
0.436332313	0.115253313	0.096692213
0.523598776	0.136474596	0.136974596

Tool errors

The main body of errors addressed here are associated with the cutting tools. These tooling errors can be classified in to three components: centering, radius error, and edge waviness. While these components are usually presented separately, they are all artifacts of the edge profile

in space. The edge profile, including any imperfections in the tool or its location in space, can be described in the Tool Error File (TEF). The TEF is a series of points in a cylindrical coordinate system with its origin at the programmed tool position. Three columns of data, as shown in Table 1, are generated from a given set of inputs that are either supplied by the user or generated from a database of typical errors. The TEF can be plotted to show a theoretical tool edge in space as shown in Figure 1.

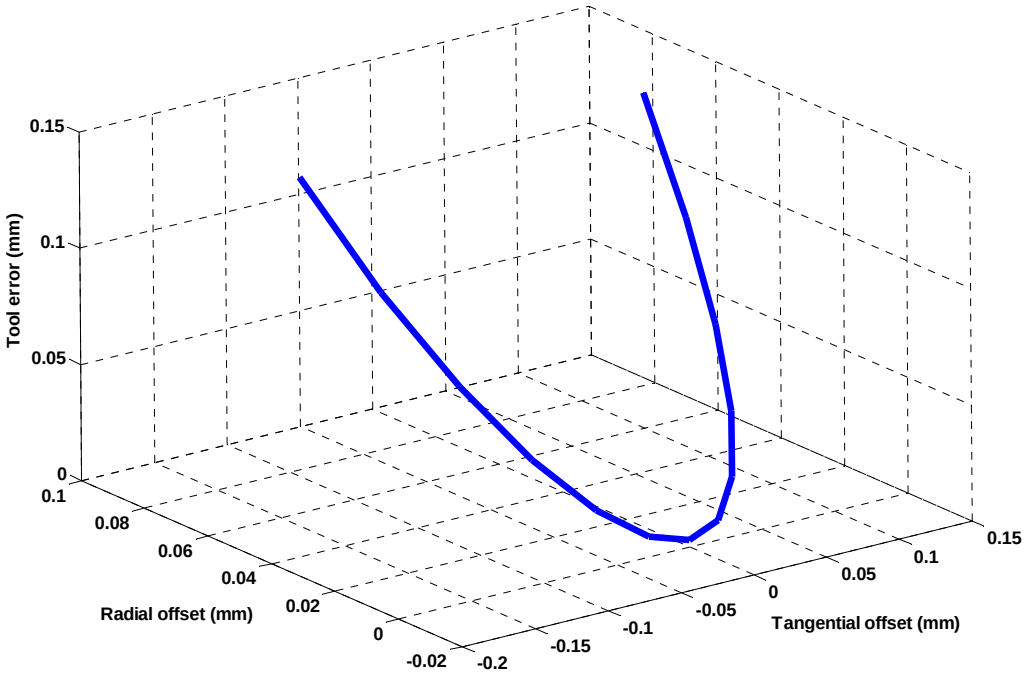

Figure 1. Plot of tool edge error from a sample Tool Error File. Most of the error shown is the result of radius error and rake angle.

The inputs for generating the tool error file are:

- **Base radius**
  R defines the idealized tool shape used in programming the tool path on the machine.
- **X-centering error**
  The tool radius changes by $R_x = \delta x / \sin\gamma$ as a function of the centering error and the tool angle, γ.
- **Y-centering error**
  The y-centering error δy is added to all y-values in the TEF
- **Radius error**
  The radius error δR is a constant that is added to all values of *R* in the TEF.

- **Waviness profile**

The waviness profile is a series of radius errors $w(\gamma)$ that is added to the TEF as a function of the tool angle γ. Since waviness profiles may not be available to the optical designer, sample waviness profiles are available that can be scaled as a function of the specified waviness spec w.

- **Rake angle**
  The rake angle a changes the tool radius as a function of γ: $R(\gamma) = R - R(1-\cos\alpha)\cos\gamma$
  and the vertical position of the tool edge as a function of γ:
  $y(\gamma) = R\sin\alpha\cos\gamma$

Once a tool error file has been compiled, its influence on the part profile to be machined can be determined. This process requires turning the part profile into a series pf data points in cylindrical coordinates with its axis coincident with the spindle axis. Each of these points has an associated surface slope that will determine which tool angle and, hence radius error will be associated with the point on the part's surface. The radius error will then cause an offset of that point in both the normal direction and the θ direction of the part surface. This surface with a modified point profile must then be interpolated back to the point grid to be fed back into CODE V.

Example of a Tilted Flat

A tilted flat is one of the simplest NRS surfaces that can be diamond turned. It is useful to demonstrate some of the types of errors and their impact on the final surface. It can also be used to demonstrate the compatibility of this generalized error estimation scheme with more direct, analytical evaluations that are specific to the surface of interest. For example, looking only at tool radius compensation for a tilted flat, the analytical version of the tool error in the z-direction is:

$$\partial z = \left| r\left(1 - \frac{1}{\cos\gamma}\right)\right|$$

where, γ is the tool contact angle and r is the tool radius. The tool angle is given by

$$\gamma = \tan^{-1}\left(\frac{A}{R}\cos 2\theta\right)$$

where A is the tilt amplitude, R is the radius of the part, and θ is the angular position of the part. Note that this radius error is independent of the radial (x-axis) position of the tool as shown in Figure 2.

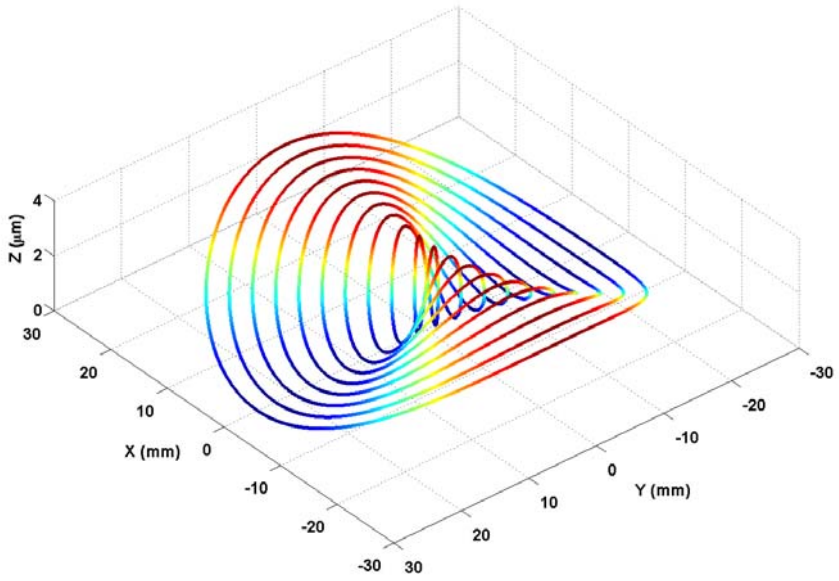

Figure 2. Simulation of radius compensation error on a tilted flat with 4 mm of tilt over a 50 mm diameter aperture using a tool radius error of 500 μm. The total error is 3 μm and it is independent of the radial position.

When only tool radius error is applied to the TEF and the error is evaluated for a tilted flat with the same amplitude, the same result is obtained. While this does not definitively prove congruence between the two methods for obtaining tool errors, it clearly demonstrates compatibility.

Assessing optical impact

It is important to devise a method of not only simulating the errors that occur in machining a free-form surface, but also to addressing the impact of these errors on the overall optical system. In the example of the tilted flat machined with a tool radius error, the resulting optical shape error can be put onto a flat surface in an optical system. The effect of this surface in the system can be evaluated with CODE V. To demonstrate the power of this technique, the error shown in Figure 2 was applied to a fold mirror at the entrance aperture of the Ritchie-Chretien telescope as shown in Figure 3. The

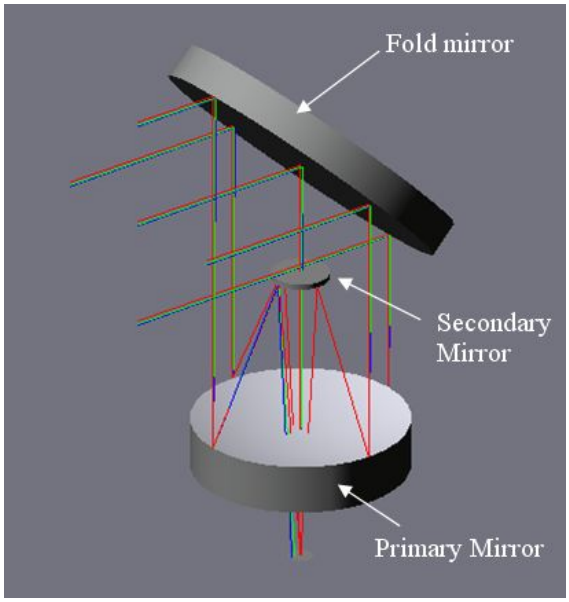

Figure 3. Fold mirror with tool errors in a Ritchie-Chretien telescope

wavefront error in the system is now equivalent to that of the flat as shown in Figure 4.

Of more interest, however, is the impact on optical performance. The error due to the fold mirror can be seen in the field plot shown in Figure 5. It dominates the entire field and eclipses all other errors in the system.

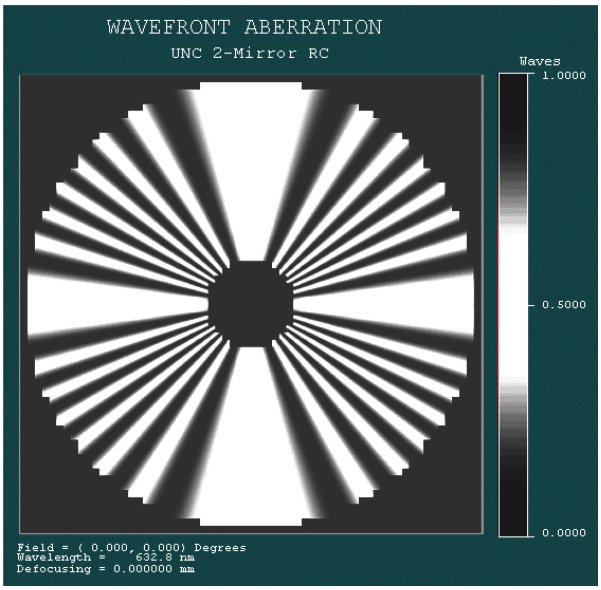

Figure 4. Wavefront error due to tool radius compensation error on the fold mirror in the optical system of Figure 3

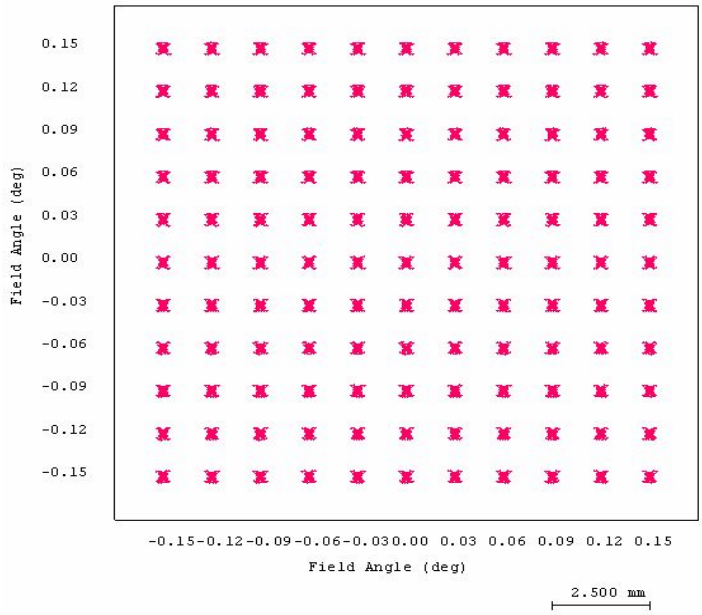

Figure 5. Wavefront error due to tool radius compensation error in a tilted flat. Note that the error is invariant across the field

Now, the error in tool radius can be evaluated based on their optical performance. Measuring tool radius is something that is typically difficult to high accuracy. Different radius errors can be evaluated and their optical impact assessed. When the radius error is reduced to 50 μm, the wavefront error is now reduced to less than one wave as shown in Figure 6 but more importantly,

the impact on the field aberrations is now minor compared to other aberrations in the system shown in Figure 7.

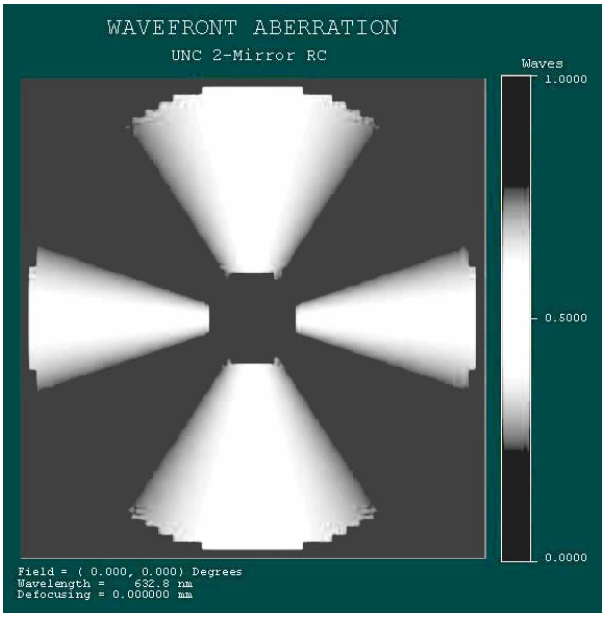

Figure 6. Wavefront error in the optical system when the radius compensation error is reduced by one order of magnitude as compared to Figure 4

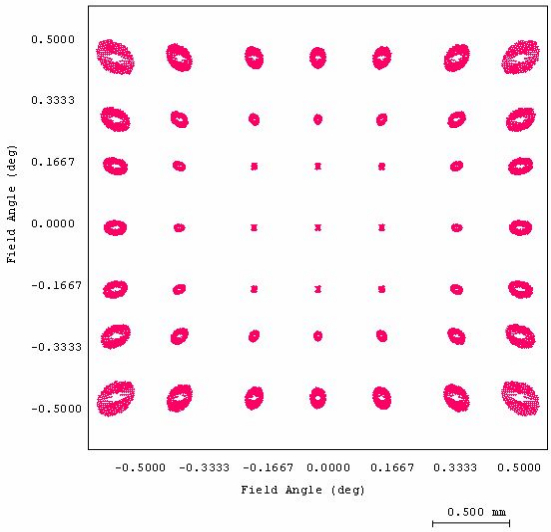

Figure 7. After reduction of the tool radius error, the aberrations in the system are now dominated by the inherent geometry and not the error in the tilted flat. Note the scale is less by a factor of 5 from that in Figure 5.

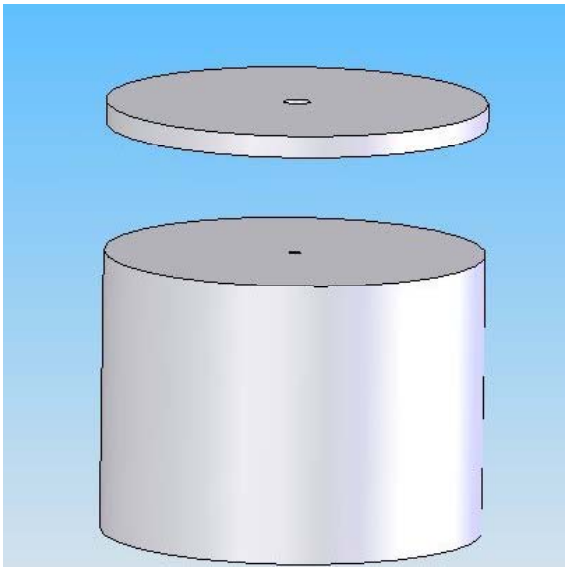

Figure 8. Simple model used for analyzing distortion due to stress resulting from a single bolt. The bolt itself is omitted.

3.3 ASSEMBLY ERRORS

In addition to errors in the optical components themselves, significant perturbations due to assembly errors often occur. These fall into two broad categories of location errors and distortion due to induced stress. Location errors result from misplacement of fiducial surfaces in bolt-together assemblies or misalignment during the assembly process. Oftentimes, fiducials can be difficult to locate since they commonly take the form of pins and clearance holes. Locations of these features are limited by how well their locations can be measured by a coordinate measuring machine, which normally have uncertainties in the 5 to 10 μm range. Additionally, holes or slots that pins are to mate with either require some clearance, which provides uncertainty in location, or if pressed into place, create stress, which can deform both the metrology frame and the optical component.

Another source of localized stress causing distortion are fasteners. The most common type of fastener is a bolt. Localized stresses can be high, but stress decreases rapidly as a function of distance from the fastener location. The impact on the optical system is, however, difficult to ascertain analytically, so modeling using finite element analysis (FEA) is required.

3.3.1 ANALYSIS OF BOLT STRESSES

The initial analysis addresses the simplest case: two parts attached with a single bolt #4-40 screw (2.54 mm dia) that is torqued to 1 in-lb (0.113 N-m). This is illustrated in Figure 8. The torque/expression is:

$$T = Kd_m F_p \qquad (1)$$

T = Applied Torque (N-m)
F_p = Desired bolt Preload (N)
d_m = Mean diameter of thread (m)
K = Bolt Constant, nominally 0.2

Solving for Force (F_p), the applied force is 220 N. The plate in Figure 8 has a diameter of 100 mm and a thickness of 6 mm. Initial difficulties were encountered with meshing the threaded holes. Meshing failed in all cases until the cosmetic threads were replaced by simple holes. The bolt itself is not modeled in this case, since we are only interested in the effects of the force it applies. Thus, it is modeled as being rigidly attached to the bore of the hole and applying a force over the counterbore area i.e. under the head. The solid model was created in SolidWorks and the FEA was performed in COSMOS. The results shows a large amount of localized stress, in excess of 10 MPa, present in the material being compressed by the bolt. However, since the stresses decay rapidly with distance away from the bolt, their influence is small, though not insignificant. Figure 9 shows displacement of the material as modeled. While maximum displacement is limited to 80 nm, considering the minimal amount of applied torque, this comes very close to being significant in an optical system.

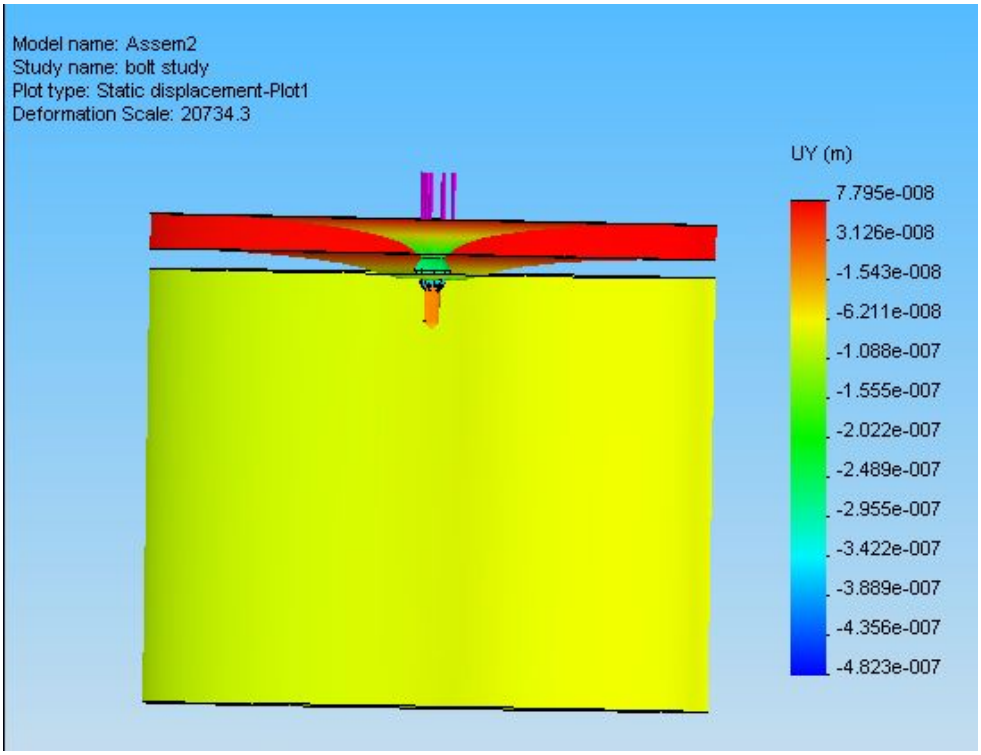

Figure 9. Distortion due to single bolt. Note that the plate distortion actually separates the plate from the bulk, though by only 80 nm.

3.3.2 ANALYSIS OF DISTORTION IN AN OPTICAL SYSTEM

The mirror-tube assembly of the Ritchie-Chretien telescope was distorted as a result of the 3 screws that attached it to the tube. One third of the geometry of the assembly is shown in Figure 10. There are three holes in the primary mirror periphery and screws attach the mirror to the tube. The secondary is attached to the other end of the tube and both spaced and aligned the two mirrors. The analysis was performed with a 220N applied force at each hole with each of the three threaded holes fixed as shown in Figure 12.

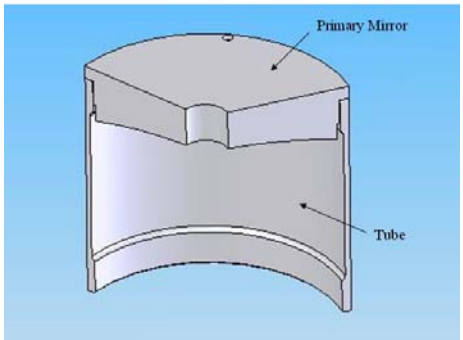

Figure 10. One third of the primary mirror and tube of the two mirror telescope analyzed for distortion.

Optical Distortion

The fiducial surface (flange) on the outer edge of the primary mirror is used to attach the mirror to the tube. The measurements of the primary flange from Section 8 are reproduced in Figure 11 and 12. The tube has about ± 1 μm of variation with two high spots and two low spots. The flange has a similar shape (but moved in phase) but with about double the amplitude.

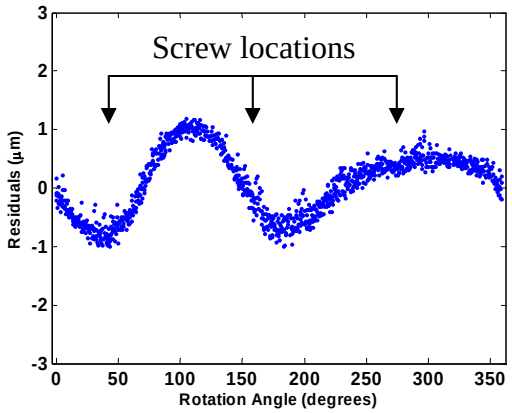

Figure 11. Tube primary end fiducial surface rotary measurement data

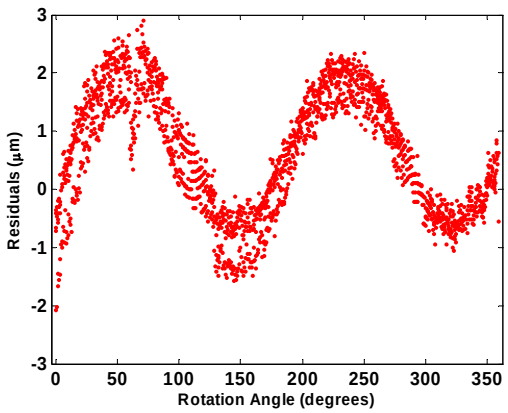

Figure 12. Primary mirror fiducial surface rotary measurement data

If these two surfaces were put together, the screw would be able to deflect the primary mirror about 1 μm before it contacted the tube. Since the tube is stiffer than the mirror and much stiffer than the mirror flange, the distortion of the mirror will be caused by the force applied to the flange.

Calculating Deformation

To verify this assumption, the mirror flange and the tube were loaded individually with a 220 N load applied at each of the 6 screw holes around the periphery of each component. Three of the screws are loaded from the left and the others are loaded from the right. The deformation of the outer flange of the primary, the outside of the mirror surface and the tube are shown in Figure 13.

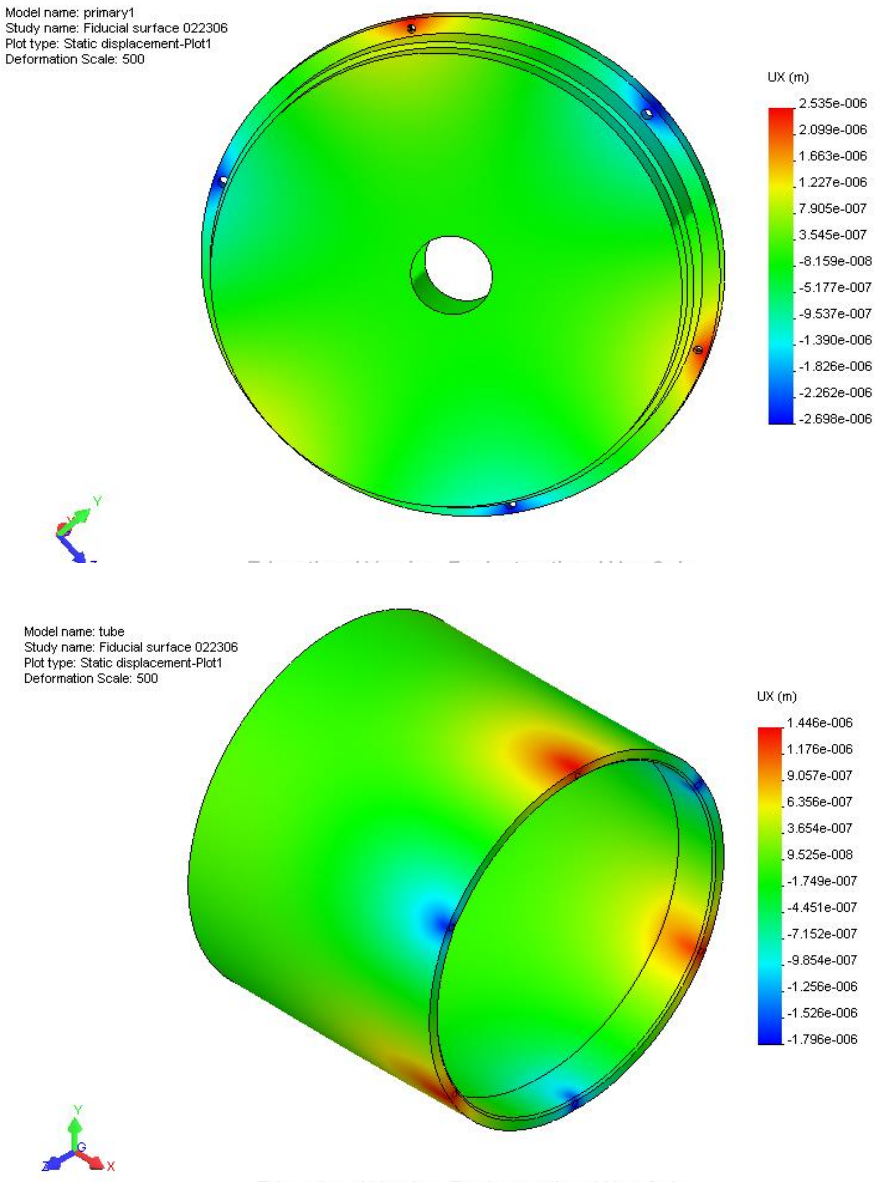

Figure 13. Distortion diagrams of the primary (top) and the tube (bottom). Forces are applied at six screw holes with load on every other screw in the opposite direction.

The detail of the distortion of the primary is shown in Figure 14. With the 220 N load applied, the outside edge of the primary mirror surface moves ± 1 μm but the much more flexible fiducial surface moves ± 2.5 μm. This displacement is approximately that needed to bring the flange in contact with the tube from the traces in Figures 11 and 12. Under these conditions, the face of the mirror at the OD would deflect about 1 μm at each screw. The assembled mirror would then exhibit a three-fold symmetry as is shown in the wavefront error for the assembled mirror in Figure 14.

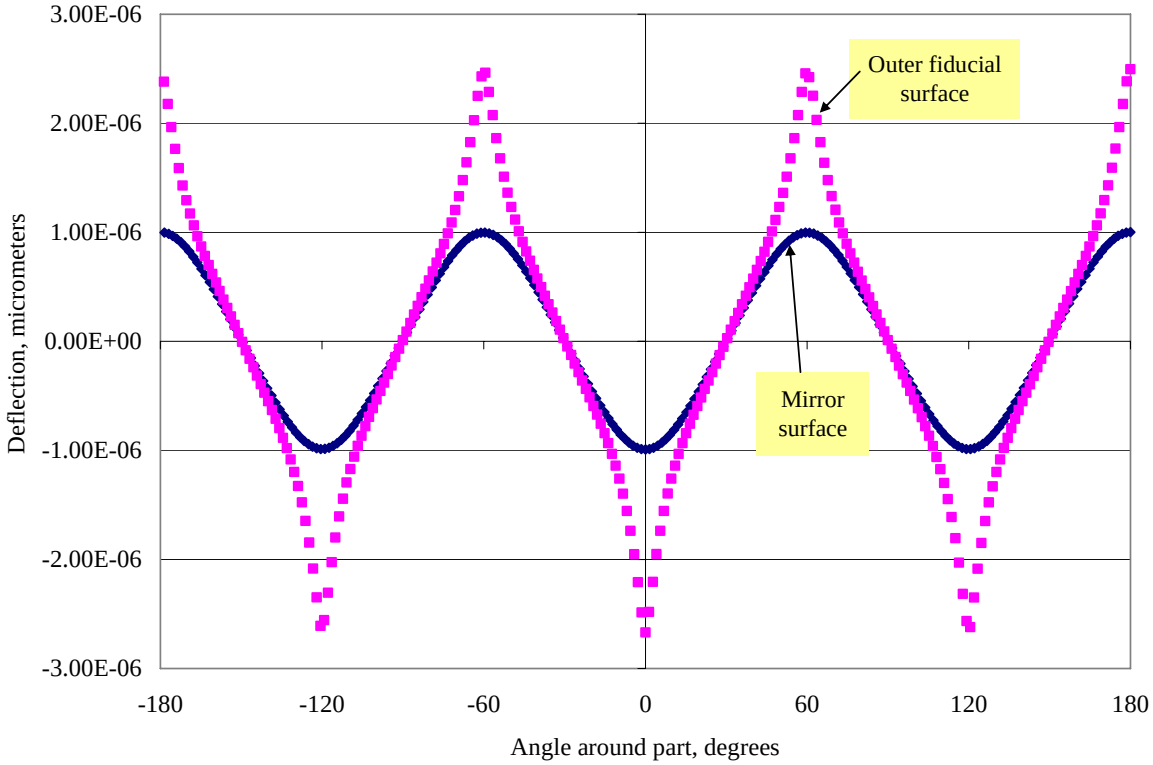

Figure 14. Deflection of the primary mirror at the fiducial surface and edge of mirror.

A close up of the mirror surface emphasizing the deflection due to the screw forces is presented in Figure 15. The range of the color contours on this picture was limited from zero to the maximum at the edge of the mirror to emphasize the distortion of the mirror. It would limit the deflection in Figure 14 to positive values on the mirror surface curve. But this image makes and excellent comparison with the wavefront measured on the assembled telescope. When the primary and secondary are attached to the tube and the telescope measured in a dual-pass configuration, the result is shown in Figure 16 (see Section 8 for additional details on this measurement). The telescope shows 1.7 μm of error and the shape and magnitude are similar to the prediction in Figures 14 and 15 which would estimate the error as 1-2 μm.

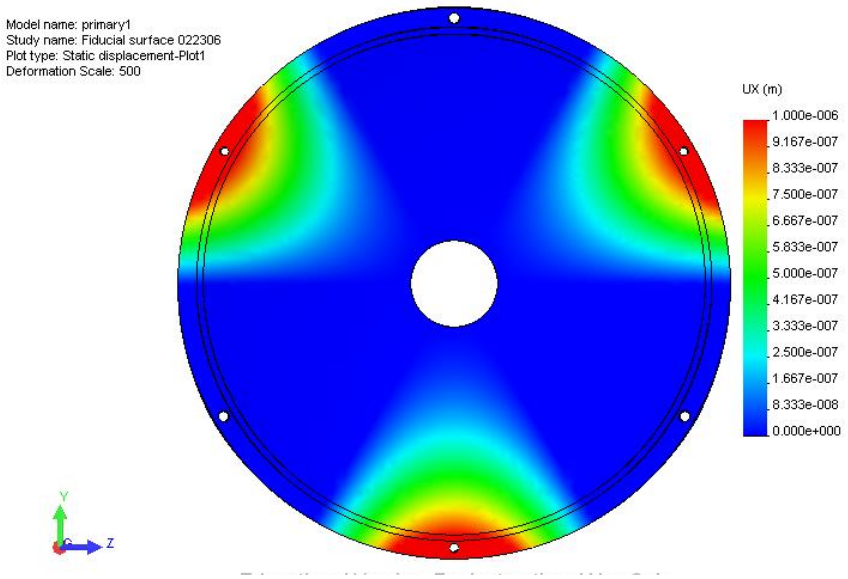

Figure 15. Predicted mirror deflection due to screws in the fiducial surface.

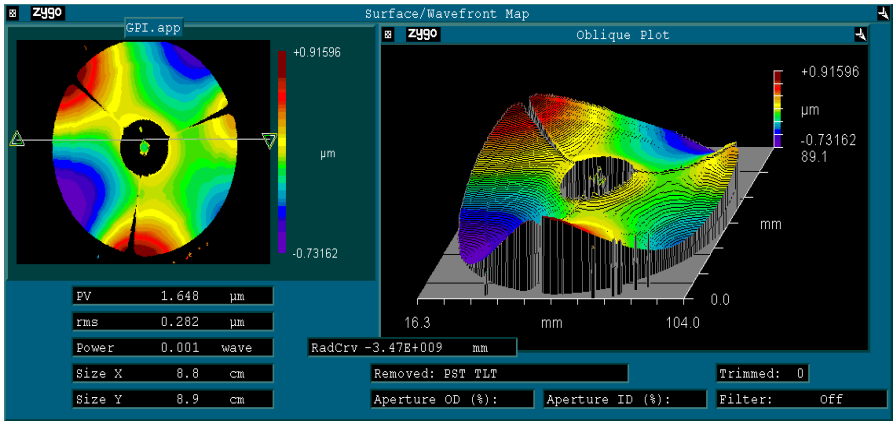

Figure 16. Measured wavefront error for the assembled two-mirror telescope.

The problems with this design of the mirror mount were the lack of flexibility in the mount of the primary mirror to the tube and the high aspect ratio (diameter/thickness) of the primary mirror blank. Each of these factors lead to errors in the fiducial surface distorting the mounting surfaces and transferring that distortion to the mirror surface. The next generation of mirror mounts designed for the three-mirror design, will address this issue more carefully.

3.4 CONCLUSION

A method for evaluating tool errors in diamond turning free-form optics that is applicable to a wide range of surface geometries has been demonstrated. This method is intended to aid designers in evaluating the manufacturability of freeform optics through feedback to Code V optical design software. The example of a tilted flat has shown that the errors evaluated from a

closed form agree with those obtained through the tool error file application to an arbitrary surface. Also, a method of determining the impact of bolt stresses and mounting features on an optical system has been demonstrated. In some systems, particularly those intended to withstand high accelerations, higher bolt stresses are likely to be encountered. In those cases, this modeling method may be used to design isolating flexures or increase stiffness to minimize the impact of the bolt stresses.

4 LIVE AXIS TURNING

Nathan Buescher
Graduate Student
Thomas Dow
Professor
Department of Mechanical and Aerospace Engineering

An emerging trend in optical design is the use of freeform optical surfaces that are non-rotationally symmetric. When such surfaces are included in an optical system, the complexity, bulk and weight of the system can be reduced at the same time the performance is improved. However, the production time for these parts is often excessively long due to their complex shape and the slow response speed of a typical diamond turning machine. One way to speed up the process is to add a lightweight fast tool servo that will respond more quickly to the changing shape of the surface. The goal of this project was to develop a new FTS design (called Live-Axis Turning) with increased stroke while retaining the surface finish of current diamond turning processes. This design takes advantage of advances in lightweight materials, air-bearing design, linear motors, high-resolution encoders and control algorithms to increase the velocity and range of tool motions. The goal of optical fabrication at 4 mm displacement and operating frequency of 20 Hz was not realized due to slide mass and encoder resolution. Form error was less than 1% (displacement of 2mm @ 8.3 Hz) and the average surface finish was 16 nm.

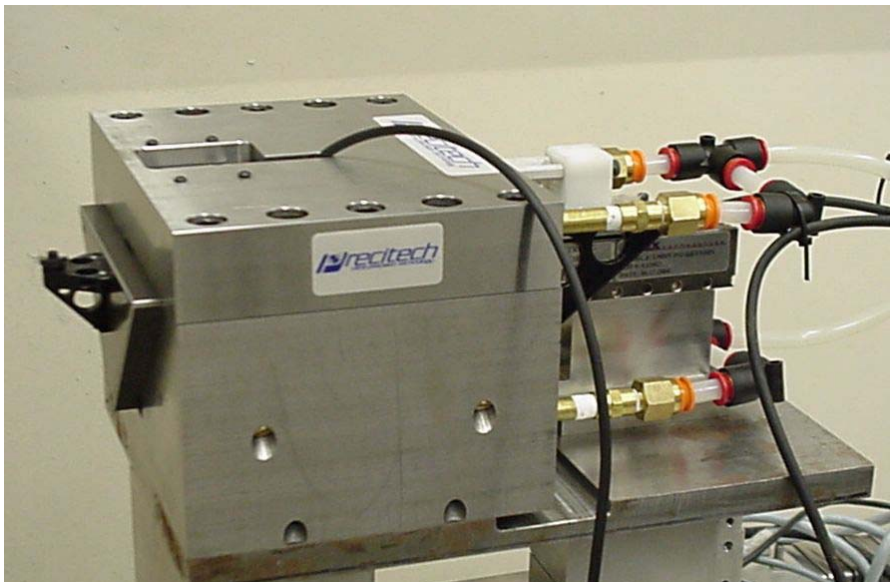

4.1 INTRODUCTION

Diamond turning has revolutionized optical fabrication because of its ability to accurately and rapidly create spherical and aspherical optical surfaces as well as the mechanical features needed for alignment. An emerging trend in optical design is to use optical surfaces that are non-rotationally symmetric (NRS) or freeform. When such surfaces are included in an optical system, the complexity, bulk and weight of the system can be reduced while the performance is improved. However, the manufacturing process remains controversial [1]. Some organizations use a flycutter on a 3 axis machine and raster scan this tool over the surface with x, y and z commands. To create optical surface finish on the surface, the upfeed and crossfeed rates must be kept small resulting in long fabrication times (more than a day) and the possibility of thermal drift. Others have dithered the slides of a precision lathe with linear motor drives to move the tool as a function of radius and part rotation. However, the slide weight of several hundred pounds reduces the possible speed of part rotation and again leads to long fabrication times.

Another approach is to decompose the optical shape into rotationally symmetric and Non-Rotationally Symmetric (NRS) components [2]. For most optical surfaces, this decomposition results in a much smaller NRS amplitude leading to the use of an auxiliary small-displacement (and therefore fast) actuator to add the NRS component to the larger asphere. This decomposition is computationally intensive (especially for non-conic freeform surfaces) and must also include compensation for the tool nose radius. As a result, it is not utilized to fabricate optical surfaces outside the activities of the PEC. This is unfortunate because it has broad application such as the fabrication of off-axis conics on center.

For example, Figure 1 shows the process of machining an off-axis segment of a parabola with the segment axis on the center of the lathe. The parent parabola and the off-axis segment of that surface to be machined are shown in Figure 1(a). If this segment is moved to the center of rotation and tilted so that the normal vector at its center is along the spindle axis of a DTM, the resulting surface can be divided into the rotationally and non-rotationally symmetric components shown. By using the axes of the DTM to produce the rotationally symmetric component (in this case a little over 2 mm) while simultaneously using a FTS to create the non-rotationally symmetric component (here approximately 40 μm), the shape of the off-axis parabola can be produced. The NRS component results from a different radius of curvature in the circumferential direction at the inner and outer radius of the segment. The bulk of the shape will be the local curvature of the parabola at the center of the segment and the FTS will add (or subtract) the changes due to the radial extent of the segment. The segment illustrated in Figure 1 is 100 mm in diameter but its center is 300 mm offset so it would require a swing of 400 mm radius (800 mm diameter) to machine the optic on axis. There are few, if any, diamond turning machines available that can swing a part that large.

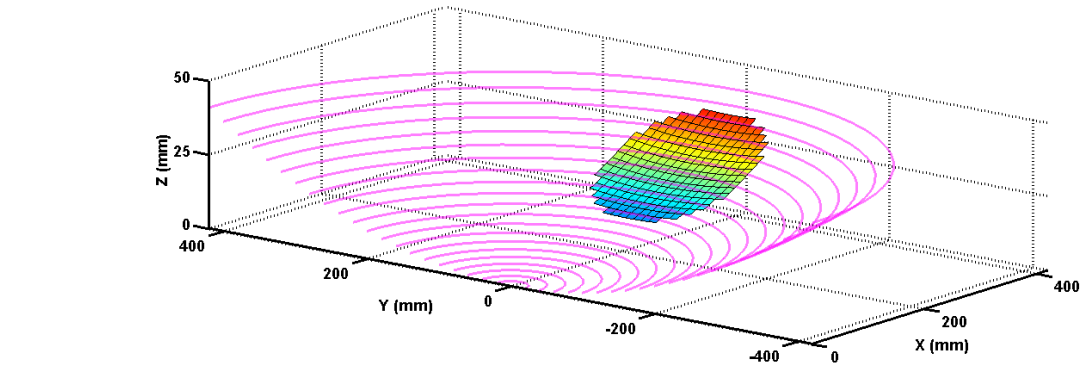

a) Parabolic surface (R=2159 mm) and off-axis segment (100 mm diameter offset 300 mm)

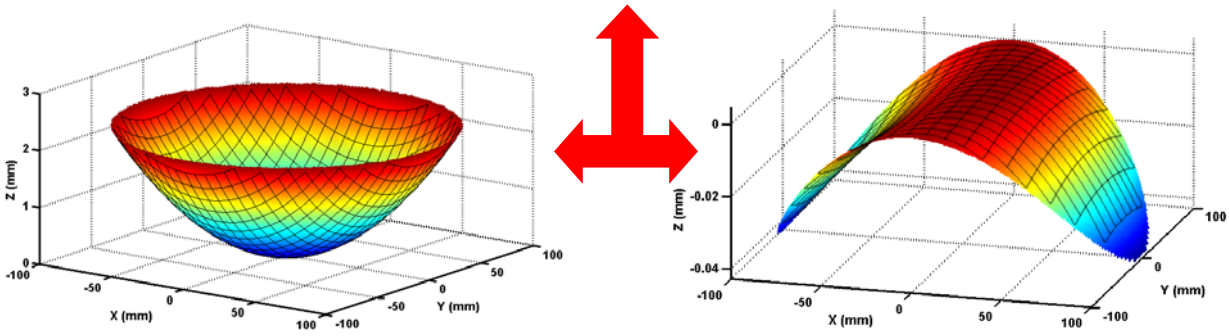

b) rotationally symmetric component

c) non-rotationally symmetric component

Figure 1. The off-axis segment of the parent parabola can be moved to the center, tilted and decomposed into the rotationally and non-rotationally symmetric components

Currently available fast tool servos fall into two main categories: piezoelectric or motor driven servos. The piezoelectric type is again subdivided into direct piezoelectric drives and mechanically amplified drives. The motor drive systems are subdivided into rotary motion and linear motion.

Piezoelectric The advantages of a piezoelectric actuator are a stiff structure with high force capability and bandwidth but the disadvantages include small range of operation (0.1% strain), hysteresis and heat generation. The range limitation can be overcome to some extent by using mechanical magnification but this reduces the stiffness and bandwidth. The direct drive type can have a range of operation from a few μm to 50 μm with bandwidth up to several KHz and the mechanical magnification can increase that by nearly an order of magnitude to over 500 μm, but at the cost of a drop in bandwidth to a few hundred Hz.

Electric motor drive The motor driven systems are quite different. They use Lorentz force motors and can be a normal rotary motor with the tool on the swingarm (ref) or a linear motor or voice coil supported by a air-bearing or flexure. Several manufacturers produce this type of actuator but the range of motion is limited to about 1 mm.

The goal of this project was to develop a new FTS design with increased stroke that would allow the fabrication of optical quality surfaces at high bandwidth. The Live-Axis Turning (LAT) system takes advantage of recent advances in air-bearing slide design, linear motors, high-resolution encoders and control algorithms to increase the velocity and range of tool motion and demonstrate a commercially viable device that will extend the capability to fabricate high-quality NRS optical surfaces. The goal was to create a tool axis capable of fabricating optical surfaces with a stroke of 4 mm displacement operating at 20 Hz.

4.2 ACTUATOR DESIGN

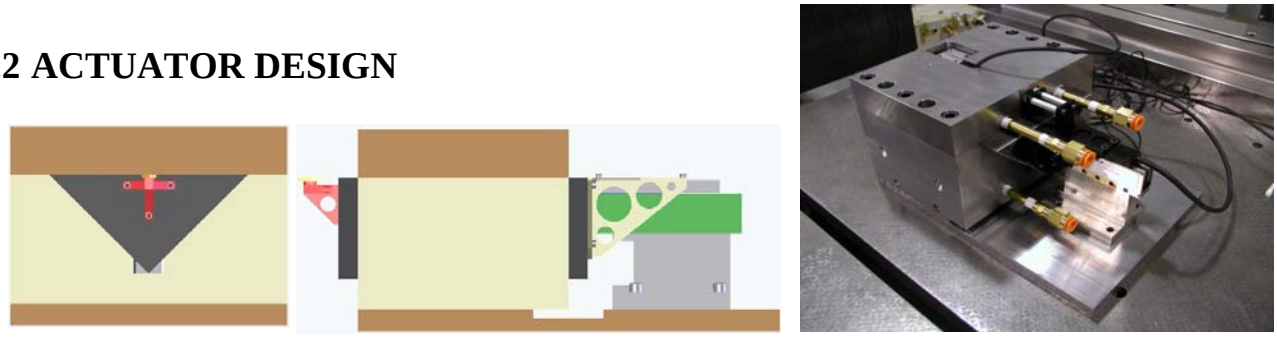

Figure 2. Front and side view drawings of the LAT and a photograph of the finished system

The LAT axis is a light-weight, air bearing, linear motor driven slide that has a range of motion of 25 mm. The piston is a triangular cross-section and is fabricated using lightweight aluminum-honeycomb construction. It is supported on each side by air bearings and driven by a linear motor. A holder for a diamond tool is attached to the front of the slide. A drawing and photograph of the LAT system is shown in Figure 2.

Piston Design The main challenge was to create a stiff, lightweight tool holder to support the tool in 5 degrees of freedom while allowing it to move along a single linear axis. The solution was a triangular shaped piston riding in a linear air-bearing. Different piston cross-sections and lengths were studied to find a design that would be both light and stiff with high natural frequencies in the critical directions. The piston was fabricated using sheets of aluminum honeycomb with face and end sheets glued together, anodized and lapped flat. The properties of the honeycomb sheets were calculated and measured, and a model for the piston properties based on modulus and density was constructed. To select an optimum cross-section shape, finite element models were created for different cross-section shapes including a box, a V, and a triangle. The properties of interest were the bending stiffness, mass, first natural frequency, center of gravity, location of the linear motor and location of the position sensing encoder. Piston length is another important design issue because the air-bearing performance improves with increased length but the structural stiffness decreases. After analyzing the changes in natural frequency and the rate of change of air-bearing stiffness with bearing length, a 180 mm slide was selected. Table 1 shows the results of the predicted and measured structural properties

of the triangular piston. The predicted mode shape of the first natural frequency was a twisting motion around the central axis of the triangle and the second was a bending mode perpendicular to the central axis as shown in Figure 3.

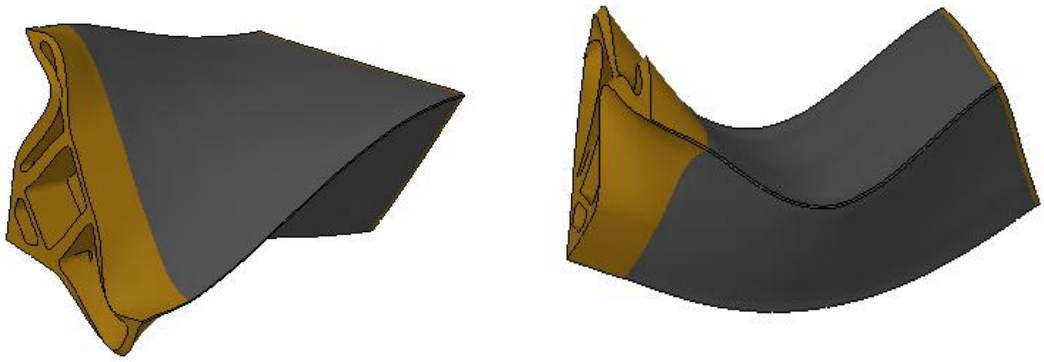

Figure 3. FEM results showing the twisting mode (ω_1, left) and the bending mode (ω_2, right) for the final triangle design.

Table 1. Structural properties of LAT piston

	Weight, gm	ω_1, (Hz)	ω_2, (Hz)	ω_1/ω_2
Predicted	445	3950	5110	0.77
Actual	517	3540	4660	0.76

The finished LAT piston is shown in Figure 4. The actual structural properties were determined by supporting it in foam rubber, installing small accelerometers on the face and tapping the structure with an instrumented hammer. The relative phase and amplitude of the accelerometer outputs was used to indicate the mode of motion and the frequency indicated the natural frequency.

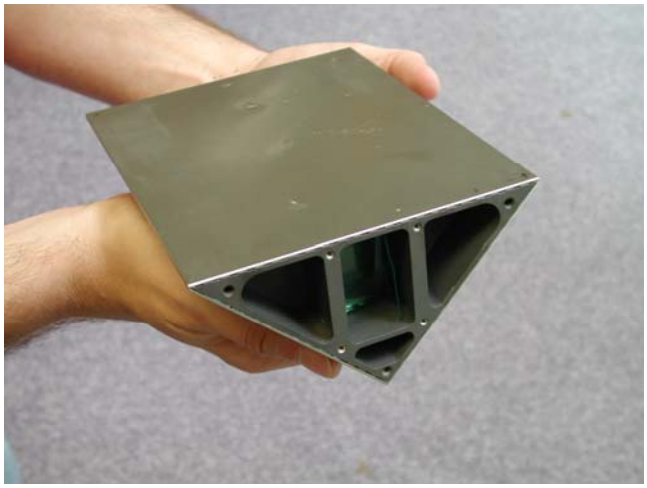

Figure 4. Photograph of LAT piston showing end cap with clearance for the linear motor

The design process described above produced a rather large piston when compared to the size of the diamond tool ((a few mm) and the stroke of the actuator (25 mm). The piston is 140 mm wide at the top, 100 mm on the two sides and 175 mm long. The weight (complete with motor is 665 gm) is large enough that significant inertial force is transmitted to the support. Future designs will need to significantly reduce the size and mass of the piston.

Linear Motor A brushless linear motor was chosen for its smooth motion characteristics, light weight, high accuracy, repeatability, high acceleration capabilities and stiffness. The force needed to drive the piston (M=0.665 Kg) at target motion (2 mm amplitude at 20 Hz) is 21 N. The Airex Linear Motor P12-1 chosen has a motor constant of 8.4 N/amp and when coupled with an Elmo Cello amplifier produces 28 N cont. (56 N peak). The motor adds 100 g to the moving mass of the piston but can produce peak acceleration up to 8 g's.

Motor Amplifier The Elmo Cello 3/100I is a pulse width modulated (PWM) motor amplifier with a switching frequency of 22 KHz. It takes a voltage command based on the amplitude of the control algorithm in the UMAC and converts it to a scaled current sent to the motor. This particular amplifier has a continuous current output of 3.3 amps and a peak current of 6.6 amps. The amplifier also controls the motor commutation by sending the commanded current to the motor in three phases 120º apart. To do this, the amplifier needs to know the location of the slide, so the encoder signal was split and sent to both the amplifier and the UMAC interpolator.

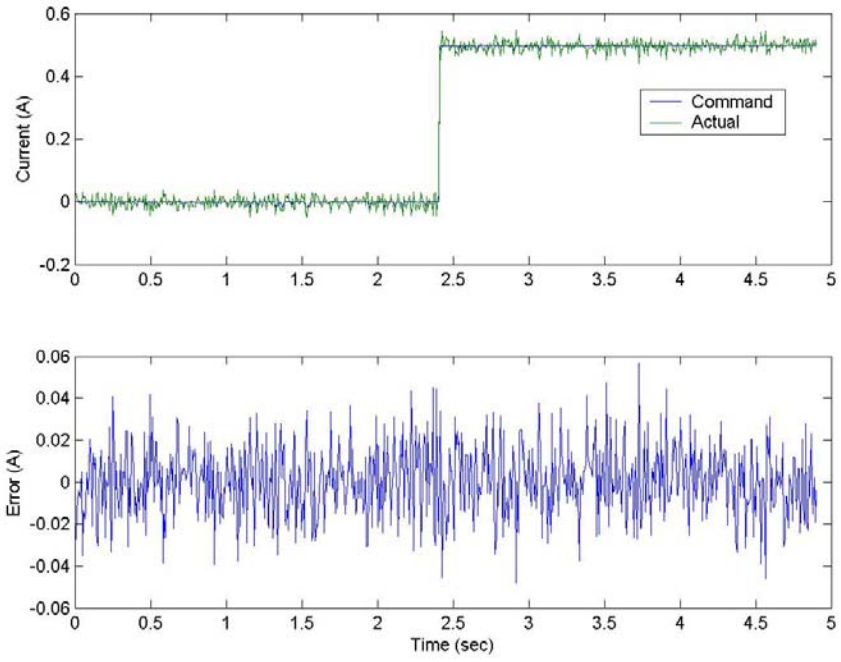

Figure 5. Amplifier response to a closed-loop step command.

Because the dynamics of the amplifier were assumed to be much faster than those of the motor, it was modeled as a unity gain in the control block diagram. To verify this assumption, a current input command was sent to the amplifier in closed-loop mode and the current output was recorded with the amplifier software tools. Since a manual tuning feature was not available during the amplifier setup, the controller gains were obtained through the amplifier software's auto-tune process. The amplifier's response to a step command is shown in Figure 5. The plot shows a PV current error of roughly 0.08 Amps and an RMS value of 0.0167 Amps. This corresponds to a peak force of 0.67 N (0.14 N RMS). This noise has been traced to the 24 V power supply for the amplifier but it is not clear if that is the origin.

Linear Encoder The Renishaw RGH24B steel-tape, linear encoder (20 μm period) provides position feedback to the controller and motor commutation information to the amplifier. The read-head is attached to the structure of the bearing. The tool is in line with the linear encoder so there is no Abbe offset in the position measurement. The 1 V P-P sinusoidal output is interpolated by the UMAC into 4096 counts per period, giving it a theoretical resolution of 5 nm. Unfortunately, a noise level of 2.5 mV on the sine wave signal reduced this resolution to approximately 50 nm.

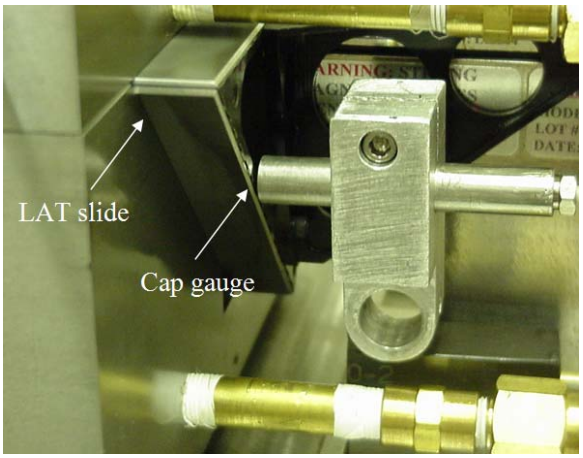

Figure 6. Cap gage location for position sensing

This noise was responsible in part for the surface finish problems using this LAT prototype. The problem with the encoder was identified by using an external position sensor (capacitance gage) looking at the end of the piston as illustrated in Figure 6. Figure 7 shows the position of the stationary slide (controller holding position) as read by the encoder and the capacitance gage. The motion seen by the encoder is significantly larger than the external sensor and the noise will excite the control system.

The data from both the cap gauge and the LAT encoder show the presence of 400 Hz and 1000 Hz frequencies, although neither accounts for more than 30% of the motion. These frequencies are likely higher frequencies aliased by the sample rate (2.25 KHz). Very low frequencies (< 1 Hz) have also been observed on the surface and their source is unknown.

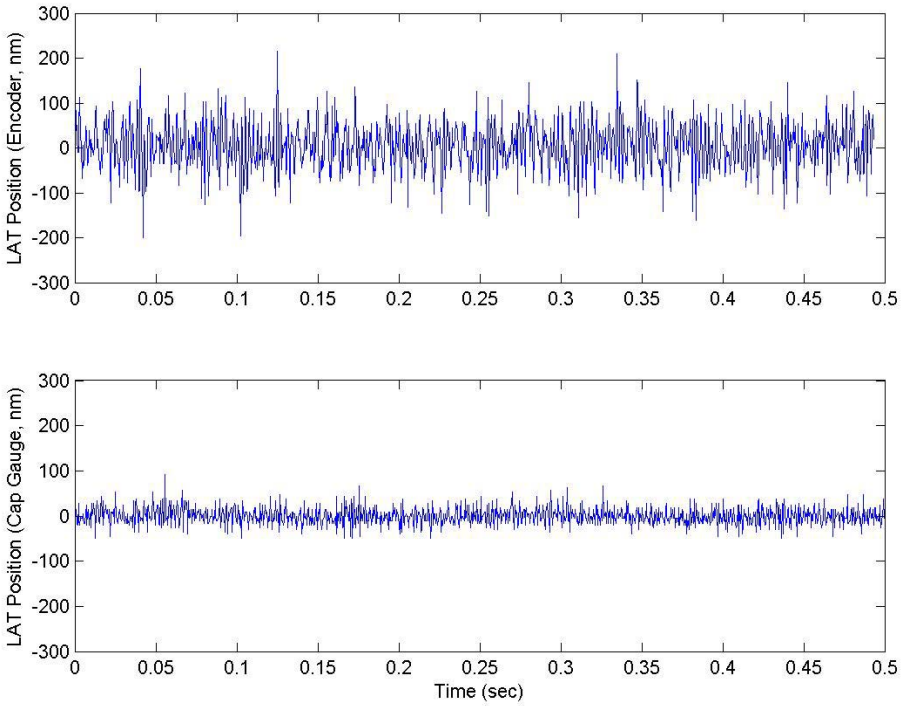

Figure 7. LAT position as measured by the Renishaw encoder (top) and a Cap gage (bottom)

Air Bearing The triangular piston is supported by a 90º v-block base assembly and a flat top as shown in Figure 1. The base assembly has an air bearing designed by Precitech that incorporates innovations in both the design and fabrication procedure. The bearings in the base assembly were optimized for stiffness and damping in the frequency range of the first dominant vibration mode. Static stiffness measurements were made by loading the piston in the vertical direction (300 N/μm) and at one edge (0.2 Nm/μ rad). Air flow with 80 psi applied to the bearing was 90 liter/min with an initial clearance of 45 μm.

4.3 EXPERIMENTAL APPARATUS

The LAT axis mounted on the z-slide of the Nanoform 600 DTM is shown in Figure 8. The microheight adjustor used to provide fine adjustment of the tool height was not installed when this photograph was taken. The Nanoform machine has a large swing to fabricate 600 mm diameter optics and the LAT must be raised well above the z-axis to center the tool. The LAT has also been installed on the ASG-2500 DTM which has a smaller swing and it is a better fit. Because of the 25 mm range of the actuator, it could also be installed with only a spindle mounted on a perpendicular axis. The results presented here are for the Nanoform installation but future experiments will be done on the ASG.

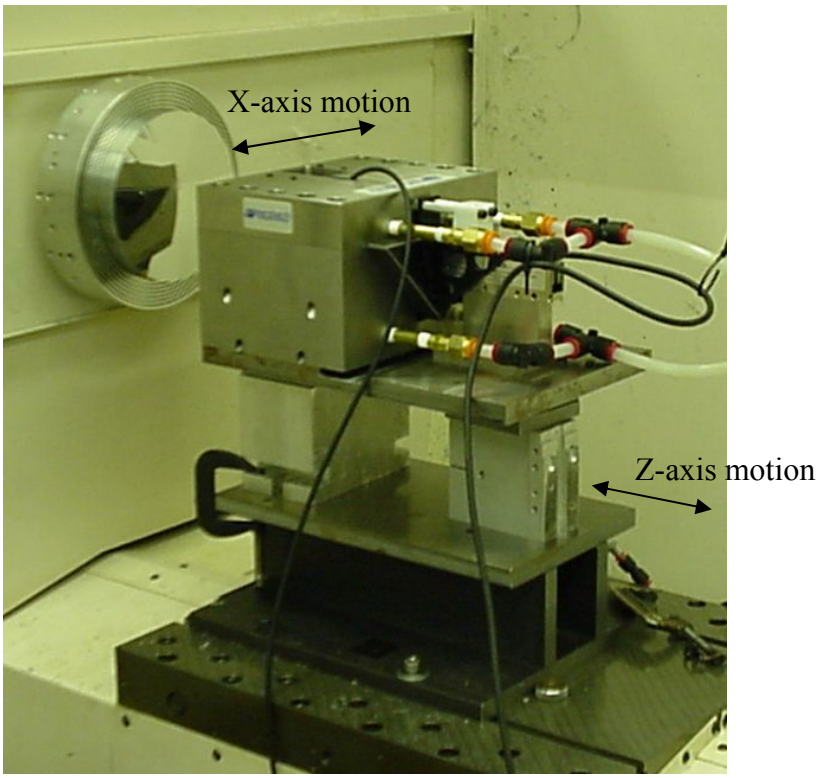

Figure 8. LAT shown in a temporary mount on the Nanoform DTM before the micro-height adjustor was attached to the front to center tool.

4.3.1 DYNAMIC TESTING

One major concern in attaching the LAT system on top of, and aligned with, the Z-axis of the Nanoform 600 DTM was the effect it would have on the motion of the Z-axis. Initial estimates showed that the impact on the Z-axis would not be significant due to the high stiffness of the Z-axis and the small moving mass of the LAT axis compared to the Z-axis. The stiffness of the ball-screw driven Nanoform 600 slide is 60 N/μm and the dynamic displacement of the 300 lb z-axis excited by the LAT motion (piston moving at 2 mm amplitude and 20 Hz) is estimated to be about 350 nm. If this deflection only occurred at the excitation frequency (as it would with a linear system), the result would be an small reduction in the amplitude of the servo motion (~.02%) and that reduction could be compensated with increased gain. However, the low frequency servo motion excites the Z-slide at its natural frequency (120 Hz) as shown in Figure 9. The relative motion of the Z-slide at its 120 Hz natural frequency (± 200 nm) is larger than its motion at the excitation frequency of 20 Hz (±150 nm). Such high frequency disturbances have a deleterious effect on the surface finish and some remedy must be developed to reduce this effect. Several ideas including counter-balance masses and tuned dampers will be examined in a later phase of the project.

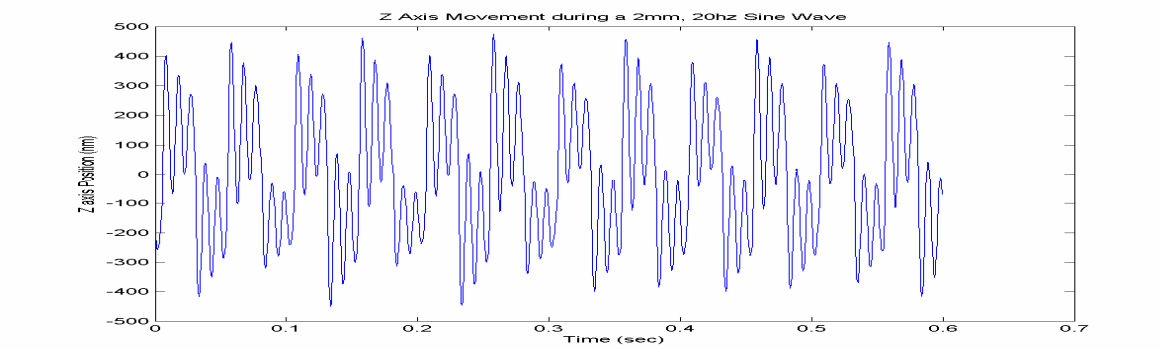

Figure 9. Motion of the Z-axis of the DTM as measured by the laser interferometer with the LAT moving in a sine wave motion of ±2 mm at 20 Hz

4.4 CONTROL SYSTEM DEVELOPMENT

The LAT system was integrated into the Nanoform 600 diamond turning machine for the machining experiments. The machine controller, a Delta Tau Turbo UMAC, allowed this new axis to be added to the system without compromising performance or flexibility. The existing user interface was used to input the commands to the LAT slide and evaluate the motion of the tool with respect to the commanded position.

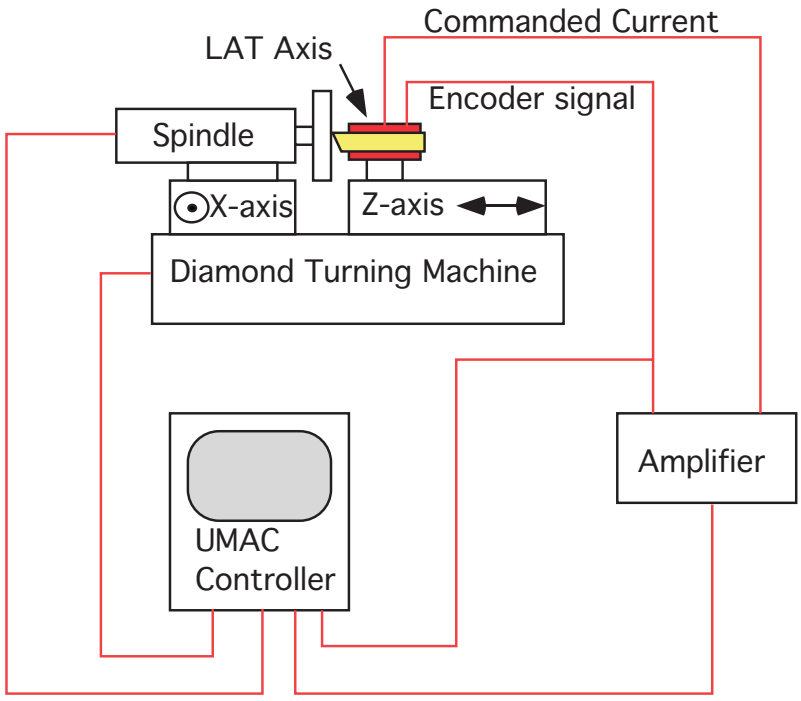

Figure 10. Diagram of general control system layout

As shown in Figure 10, the UMAC controller on the DTM controlled the LAT axis as well as the other linear axes (X and Z) and the spindle. This setup, as opposed to one where a separate system controls the LAT axis, was chosen to simplify the integration problems. The controller for the LAT axis must know the positions of the other axes, including the spindle, in order to produce the commands for a freeform optical surface. The other reason for using the Delta-Tau UMAC is that a high-resolution encoder interpolator accessory board was available on the controller. The 2.25 KHz UMAC cycle update was deemed acceptable for controlling a system with an expected closed-loop natural frequency of less than 1/10th of the controller frequency. Finally, the UMAC includes all the trajectory generation code necessary for specifying a toolpath for the LAT axis.

Open loop testing was first performed to characterize the system and to create a model to study potential control algorithms. Since the LAT system has a mass driven by a linear motor with little or no friction from the air bearing, a sinusoidal current input (force) signal is expected to produce an decreasing output amplitude (40 dB/decade) with a constant 180° phase shift. The measurement confirmed this result and indicated no mechanical resonances at frequencies below 1000 Hz.

Closing the control loop involved tuning the controller to produce the best possible response without going unstable. Initial loop tuning was performed using step function testing to minimize rise time while maintaining a damping coefficient of approximately 0.3. Proportional, derivative, and integral gains were all optimized to achieve this goal. Additionally, acceleration and velocity feed-forward gains were optimized to achieve the best possible following error in a parabolic move command.

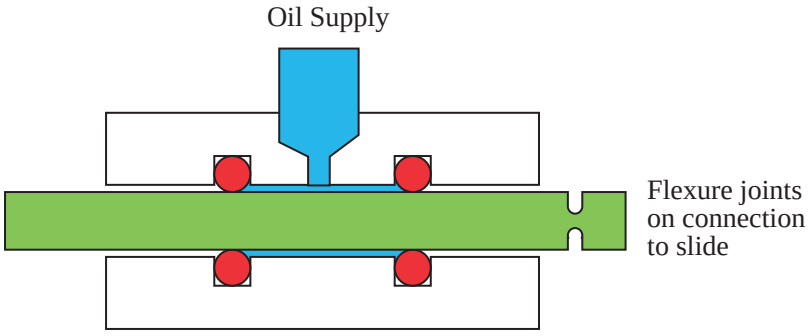

Figure 11. Damper attached to rear of LAT axis

The issue of low damping in the air bearing was considered a potential problem. As a result, an effort was made to include external damping to the slide in the form of a fluid bearing. The idea was to create a damper that was hydrodynamic and therefore only proportional to the velocity

and not a friction damper that would introduce hysteresis non-linearity to the system. A sketch of the design is shown in Figure 11.

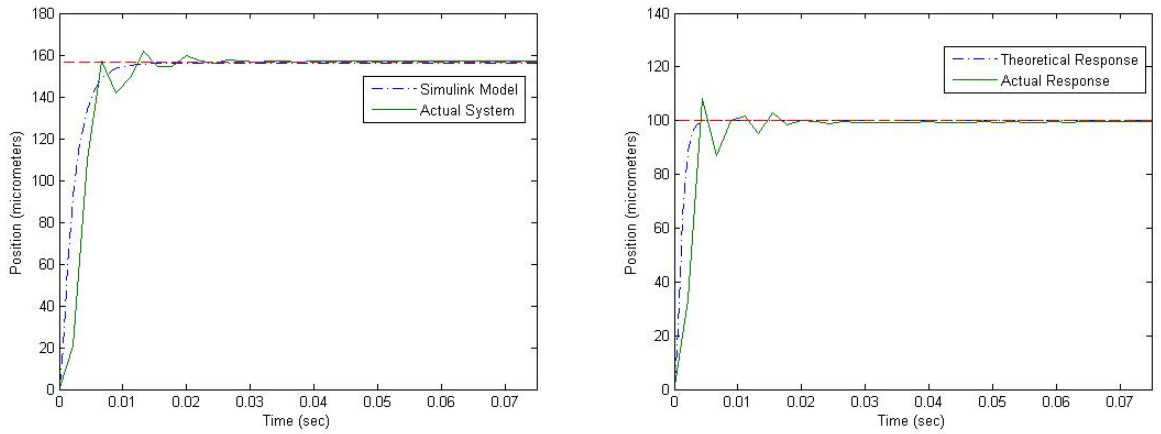

Figure 12. Step response for LAT without (left) and with (right) damper

Figure 12 shows the response of the LAT to a 160 μm step command without and with the damper. Each was tuned to optimal response and this tuning resulted in larger gains for the damped case which produced faster response from both the model and the actual system. In addition to the faster response, the damped system also had a higher frequency in the response of 200 Hz compared to the 160 Hz present in the undamped system. This is to be expected since the higher gain should produce a stiffer system and therefore a higher natural frequency. The gains for the two systems are shown in Table 2.

Table 2. Gains used in the UMAC controller for the LAT axis (sample time = 442 μsec)

Gain	Undamped System	Damped System
Proportional	400,000	700,000
Integral	10,000	10,000
Derivative	805	400
Velocity Feedforward	805	400
Acceleration Feedforward	700	440

4.5 MACHINING EXPERIMENTS

Two sets of cutting tests were performed: machining a flat surface and machining a tilted flat.

Flat Surface The flat was machined to test the ability of the LAT axis to hold position while machining. The flat was cut at 500 rpm with a 1 mm/min feedrate (2 μm/rev) and 5 μm finish pass depth of cut. The Scanning White Light Interferometer (SWLI) measurement in Figure 13 show a 50 X 70 μm patch representing approximately 35 tool passes with a surface finish of 16 nm (Ra).

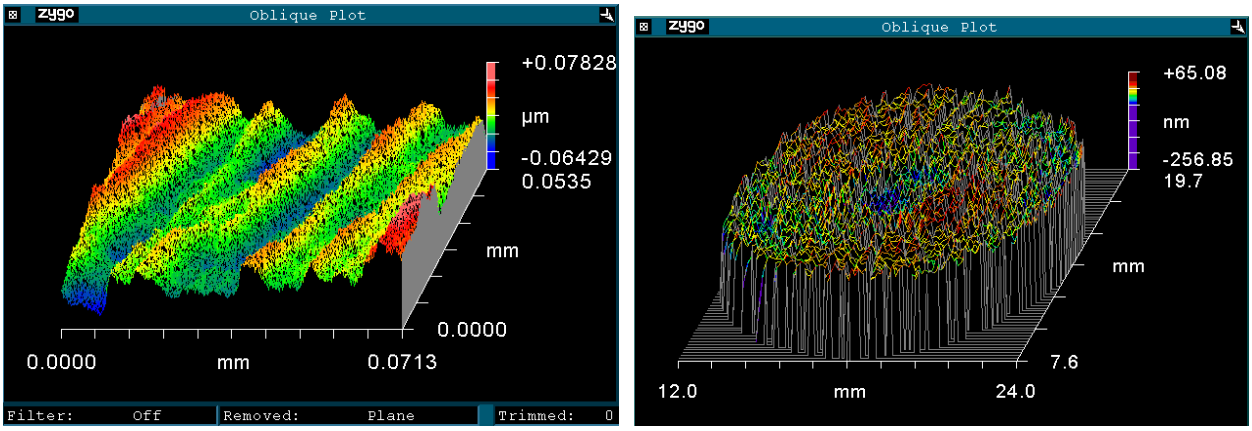

Figure 13. SWLI image of surface finish (Ra=16 nm) and overall figure error (λ/2) of 12 mm diameter copper flat.

Figure 13 also shows a Zygo laser interferometer image of the entire part. The figure shows the part's deviation from a perfect flat. The PV form error over the entire part is 321 nm (Ra 27 nm), which is less than ½ wave. This value is very close to the observed PV motion of the slide during position holding and thus is the limiting factor in achieving better finishes.

Tilted Flat A second experiment involved the creation of a tilted flat. The LAT slide moves the tool in a sine wave with one cycle per rotation of the part. As the tool moves from the OD to ID, the amplitude will decrease linearly to create a flat surface that is tilted with respect to the spindle face. This experiment exercises the full range of motion of the tool servo but creates a surface that is easy to measure and interpret. A number of different samples were created in plastic and aluminum. The range of amplitude was from ±1 to ±2 mm at a range of frequencies from 5 to 20 Hz.

The results from an aluminum workpiece are shown in Figure 14. The surface finish is shown on the left and the figure error through the center of the part is shown at the right. The 25 mm diameter surface was machined at a fixed speed of 300 rpm, 2.5 mm/min feedrate (5 µm/rev), 5 µm final pass depth of cut and ± 1 mm tilt. The surface finish shown in Figure 14 is 20 nm Ra. The figure error through the center of the tilted flat (which should be parallel to the base and thus zero) is tilted as shown at the right in Figure 14 and the maximum error is about 70 µm. Clearly this could be smaller (± 5 µm) if the tilt were removed but the error shown has been related to a non-linearity in the actuator.

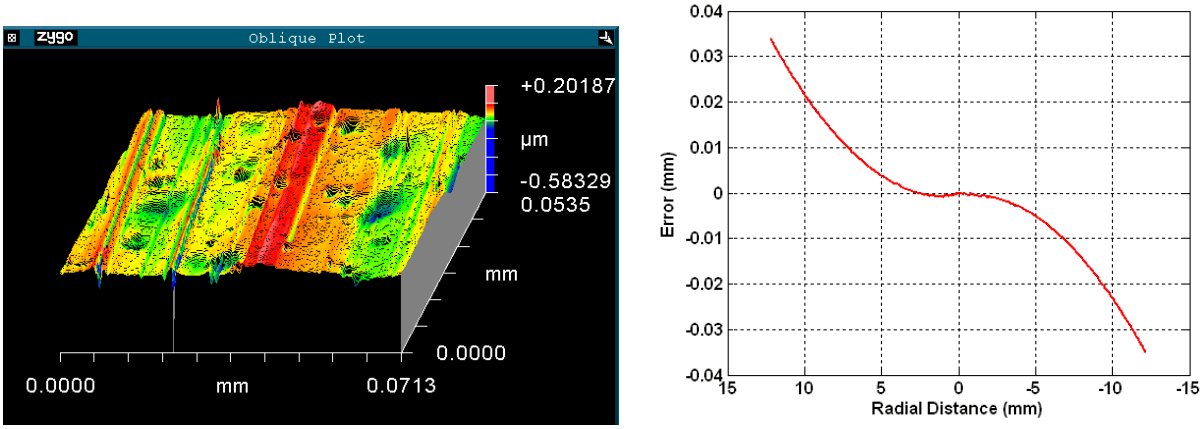

Figure 14. Surface of the aluminum tilted flat measured by the SWLI (left) and error through the center of the flat measured on a Talysurf (right)

Figure 15 shows a model of the tilted flat (left) and the error attributable to a phase angle (right) that is a function of the speed of the LAT axis. Such an error has been observed in other long range actuators such as the piezoelectrically-driven Variform. The image at left is the tilted flat showing the ±1 mm tilt in the x direction. The right image is the error between the perfect tilted flat and a tilted flat with an assumed linear change in phase with velocity - the maximum being only 2º at the OD. Note that the error is largest in a plane that is at right angles to the tilted surface. This is because the error is proportional to velocity which is 90º out of phase with the displacement. While this error is large, once it is identified, the input signal can be modified to take into account the dynamics of the actuator and reduce the value significantly [3].

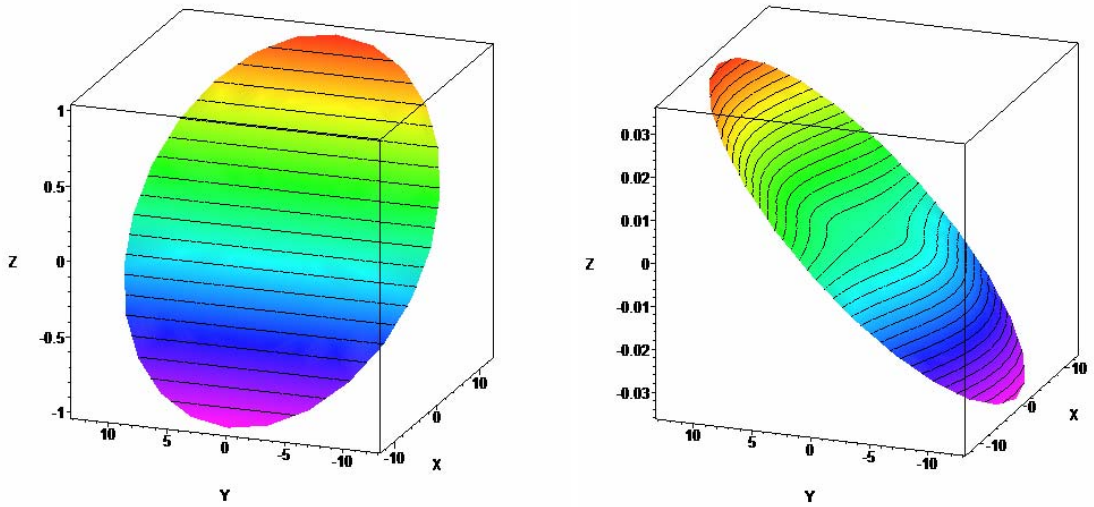

Figure 15. Error due to a linear change in phase with amplitude with a maximum of 2º at OD

4.6 CONCLUSIONS

The surface finish and figure error for the prototype LAT actuator are not acceptable for finish machining of optical surfaces. A number of concerns have been identified and solutions to those should improve the performance. These concerns and techniques to address them are:

- **Vibration of machine axis –** The mass of the LAT axis running at 20 Hz excites the natural frequency of the Z slide of the Nanoform DTM. At the maximum amplitude of interest (±2 mm), the motion of the DTM slide is ±400 nm. During the experiments discussed here, the amplitude of the LAT motion has been reduced to alleviate this effect. An obvious solution to this problem is to reduce the mass of the slide (next generation design) or another is to add a second mass to counter balance the slide mass or to do both.
- **Encoder noise and resolution –** The long-range, high speed LAT axis is a challenge for a linear encoder because the data rate cannot exceed the clock of the encoder electronics. The 20 μm period of the Renishaw steel tape is relatively long and, coupled with noise on the sine waves, reduces the resolution to greater than 50 nm. A comparison between the encoder and an external capacitance gage showed twice the noise on the encoder. The solution for this prototype is to add a laser interferometer with high-resolution, parallel-data position feedback as shown in Figure 16. For the next generation LAT, a shorter period glass scale will be used.

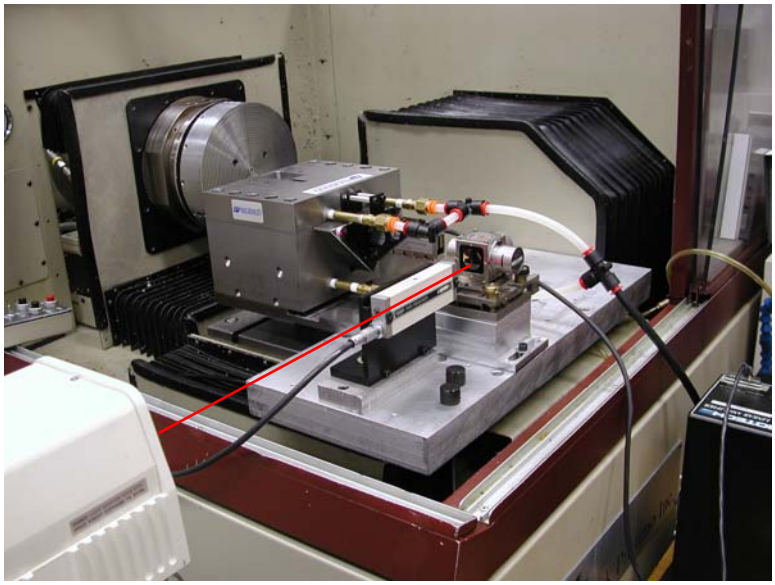

Figure 16. LAT installed on the ASG DTM with laser interferometer for position feedback

- **Noise in PWM amplifier** – The Pulsed Width Modulated power supply for the LAT motor has significant noise and this can excite the slide and degrade the surface finish. The amplitude of this noise is on the order of 0.5 N force and this will certainly effect the surface finish. A linear amplifier will be substituted.

- **Non-linear slide motion** – A non-linearity has been identified in the LAT slide; that is, the phase angle (following error) is a function of the speed of the slide. This creates a relatively large error for a small phase angle. However, with an understanding of the source of the error, it can be compensated with a modified input signal.

4.7 FUTURE WORK

4.7.2 TECHNICAL CHALLENGES

To further develop the LAT process, several specific technical challenges have been identified and will be addressed in a new 3-year project funded by NSF.

- **Form Error** Diamond turning has evolved based on the concept of stiff, straight, slow linear slides and accurate air-bearing spindles. By taking advantage of the repeatability of these components, the tool can be positioned with high accuracy and the surface shape can be created with form error less than a few hundred nanometers. This process is ideally suited (and was developed) for rotationally symmetric surfaces such as spheres or rotationally-symmetric aspheres. However, for freeform surfaces a new fabrication process must be developed to produce the desired shape.
- **Surface Finish** Simple theoretical relationships between machining parameters (spindle speed, axis velocity) and tool geometry can be used to estimate surface finish. However, other factors such as tool waviness, tool wear, material properties, position disturbances and machine vibrations can degrade the surface finish beyond that required for optical surfaces.
- **Disturbance Rejection** A machining process seeks to move the tool and/or work in a prescribed path to create the desired shape. Any variation in the tool force will create a disturbance in the tool position that must be overcome by the stiffness of the machine or the control system. Because disturbance induced errors will appear in the final optical surface, it is critical that their effect be minimized.
- **Dynamic Forces** A turning operation is an efficient way to create an optical surface, but for a NRS surface the tool axis must change directions at least twice per revolution of the spindle. The forces required to accelerate and de-accelerate this axis must be generated and controlled or surface fidelity will be corrupted. Heating within the actuation mechanism may also become a source of error.
- **Motion Planning** Advanced algorithms must be developed to decompose the freeform surface geometry into synchronized, relative motion commands for the machine axes.

4.7.2 PLAN OF WORK

The research plan is designed to address the technical challenges discussed above. It defines three tasks that will build the scientific foundation for this new machining technique. The plan

presented includes servo and controller development as well as machining experiments to verify the quality of the freeform surfaces produced.

Task 1 – Live Axis Turning Development

A new LAT axis will be designed and constructed that meets performance specifications. Control strategies will be developed and implemented to effectively position the high-bandwidth, lightly-damped actuator.

Task 1 (a) – Evaluation/Tuning of Prototype LAT The prototype system will be used to define the key parameters that influence the LAT performance (e.g. piston natural frequency, mass, air bearing stiffness, encoder resolution, controller update time) and create merit functions for continued development.

Task 1 (b) – Develop Piston Material Alternative structural materials for the LAT axis slide will be evaluated. Stiffness/weight ratio will be important but size, relationship to air bearing stiffness and manufacturing cost must also be addressed.

Task 1 (c) – Create New Design Based on the evaluation of the prototype performance and the candidate piston materials evaluated, a new LAT will be designed and built.

Task 2 – Motion Planning for Freeform Surfaces

In the past, freeform surfaces were dealt with on an ad hoc basis and a specific solution was produced for each machining operation. A comprehensive representation of synchronized motion paths for freeform surfaces will be developed.

Task 3 – Optical Fabrication

The capability of the LAT system will be demonstrated by fabricating optical surfaces such as flats, tilted flats, off-axis conics machined on-axis and biconic surfaces. This will be an iterative design process to optimize the key system components.

REFERENCES

1. K.P. Garrard, A. Sohn, R.G. Ohl, R. Mink, V.J. Chambers. Off-Axis Biconic Mirror Fabrication. Proceedings of the Third International Meeting of the European Society for Precision Engineering and Nanotechnology (EUSPEN), 277-280, (2002).
2. K. Garrard, T. Bruegge, J. Hoffman, T. Dow and A. Sohn. Design tools for freeform optics. Proceedings of the SPIE, 5874, (2005).
3. W. Panusittikorn, K.P. Garrard and T.A. Dow. Error Compensation via Command Signal Deconvolution. Proceedings of the Nineteenth Annual Meeting of the ASPE, 34, 201-204, (2004).
4. Montasanti et al. Rotary FTS. ASPE Proceedings

5 DIAMOND TURNING OF OPTICAL SURFACES AND FIDUCIAL FEATURES

D. Lucas Lamonds
Graduate Student
Thomas Dow
Professor
Department of Mechanical and Aerospace Engineering

Diamond turning (DT) has revolutionized the fabrication of lightweight optical surfaces for consumer, defense and science applications such as contact lenses, forward-looking infrared radar and infrared spectrometers. It has made this impact not only because it can accurately and rapidly fabricate diffractive, refractive and reflective optical surfaces, but because it can create reference features tied to the optical surfaces to guarantee optical alignment. An emerging trend in optical design is the use of Non-Rotationally Symmetric (NRS) surfaces to reduce complexity, bulk and weight while improving optical performance. This section reports on the details of machining the two-mirror Richey-Chrétien telescope described in Section 2. The mirrors are concave and convex hyperbolic shapes machined from 6061-T6 aluminum bar. A thin tube provides a fixed distance between the fiducial surfaces on the mirrors and aligns them to create collinear optical axes. The steps to create these components are discussed. In addition, the plan for the next telescope, a three-mirror antastigmat, is presented. These mirror surfaces will require the use of a fast tool servo to create the necessary NRS optical elements.

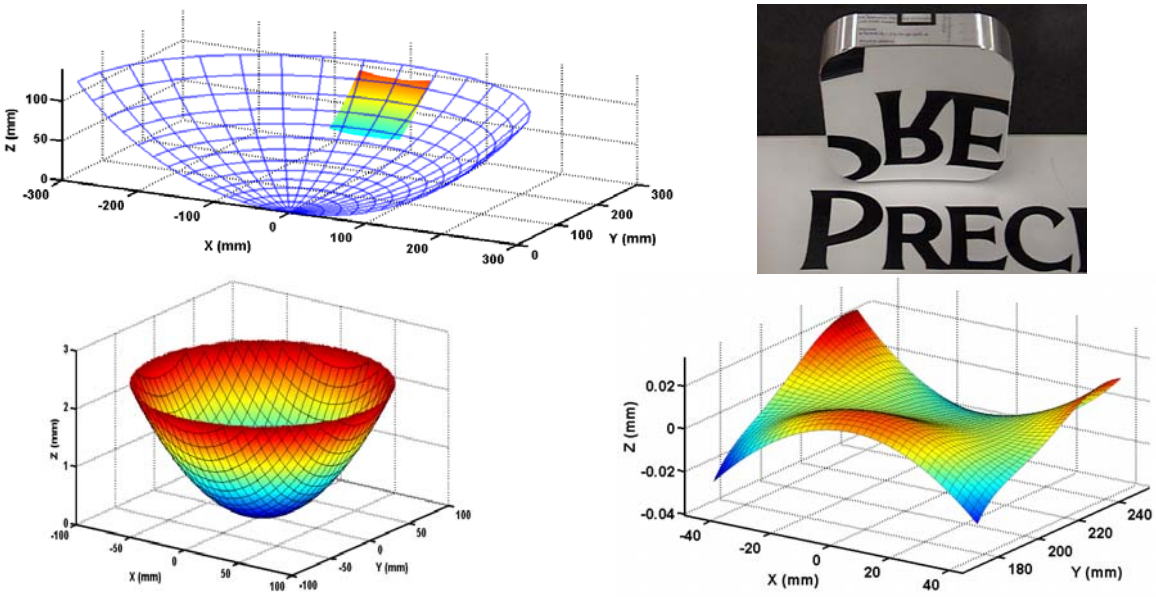

5.1 INTRODUCTION

Diamond turning is a standard technique for creating rotationally symmetric reflective optical surfaces. The workpiece is mounted on a rotating spindle and the diamond tool is moved along a path in space equal to the cross-section shape of the surface to be created. The rotating spindle of the Diamond Turning Machine (DTM) turns the tool path into a three dimensional surface. The Richey-Chrétien telescope that was fabricated consists of a concave, hyperbolic primary, a convex hyperbolic secondary and a thin tube connecting them. The components are shown in Figure 1. In addition to the two optical elements and the tube, a mounting plate to attach an SLR camera to the telescope and a mounting bracket are shown.

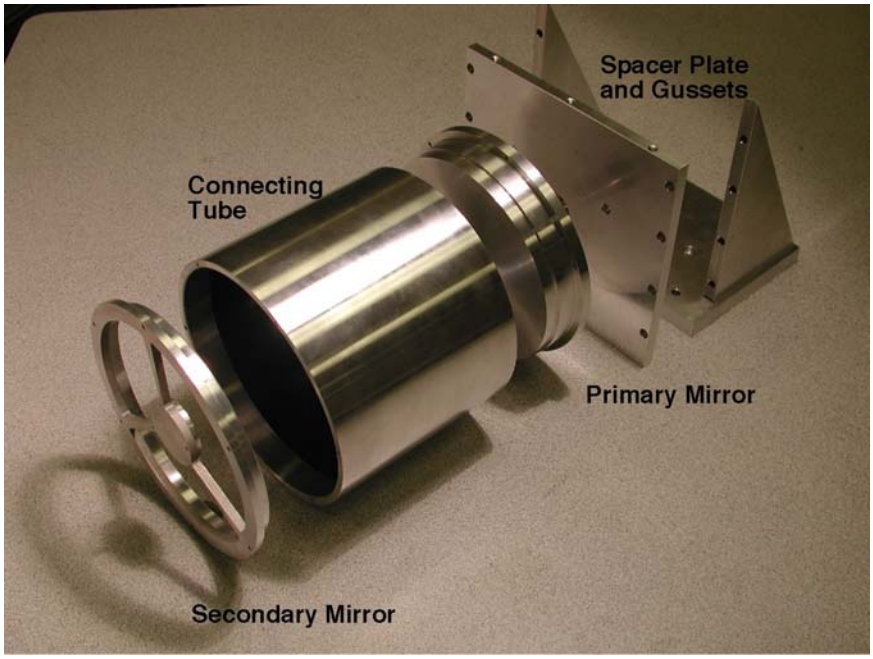

Figure 1: Rough machined components of the two-mirror telescope.

To create the optical surfaces, the tool moves through the path defined by the 2D shape of the hyperbola with some minor corrections based on the shape of the diamond tool used for the machining process. The geometry of the machine slides (straightness and squareness) as well as the control system that coordinates their position determines the form error of the optical shape. The radius of the diamond, the speed at which it is fed across the part and the workpiece material determine the surface finish.

Fiducial surfaces are used to locate the two mirrors with respect to each other based on the optical design specifications. In this case of the two mirror system, a step on the outside of the mirror locates one end of the tube while a step on the OD of the secondary support locates the other. The length of the tube controls the mirror spacing through the relative location of the step

on the primary to the apex of the hyperbola and the distance from the step on the secondary to the apex of that mirror. Setting these distances is done using the high-resolution distance measuring laser interferometer on the slides of the DTM.

This section of the report describes the fabrication of the telescope designed in Section 2 and measured in Section 8.

5.2 FABRICATION OF TWO MIRROR TELESCOPE

5.2.1 MATERIAL PREPARATION

Rough Machining

The telescope components shown in Figure 1 were rough machined with allowances for final machining on the optical and fiducial surfaces. All of these surfaces had a minimum of 150μm of extra material to be removed during final machining. The optical surfaces were machined to the best fit spherical equivalents. The primary and secondary mirrors each have a tapered section that will press into the tube.

Stress Relief

To reduce residual stress introduced during the rough machining process, the components were heat-treated. The procedure was as follows:

- Cool the parts to -100º F for one hour at a natural rate, then return to room temperature in a still, ambient atmosphere
- Heat the parts to 300º F at a natural rate for 2 hours and cool in the still, ambient atmosphere
- Repeated previous steps once

Material Hardness

The hardness of the system was measured following the stress reduction heat treatment process. A Vickers indenter (pyramid shaped diamond with 136° included angle between the faces) was used for the experiments. Vickers Hardness Number (VHN) is a function of the load, P (kg), and the diagonal of the indentation, d (mm), as described in Equation 1. All tests were performed using a 1 Kg load.

$$VHN = \frac{1.72P}{d^2} \quad (1)$$

Three pieces were tested: the heat treated spacer and two reference specimens of 6061-T6. The indentation lengths were measured with the New View White Light Interferometer via an interferometric image and again utilizing the New View translating stage and a cross hair on the video output. The average distance was used to calculate the VHN. The resultant distance and VHN are found in Table 1.

Table 1: Vickers Hardness Values

Sample	d (mm)	Hardness (VHN)	Hardness (GPa)
Spacer	0.125	110	0.110
Reference 1	0.139	90	0.90
Reference 2	0.126	108	0.108

The hardness of 6061-T6 Aluminum is 107 VHN or 95 Brinell hardness [7]. Both the spacer and reference 2 are close to this value. Reference 1 is lower, however none of the samples approach the hardness of untempered 6061: 30 Brinell hardness. Based on the results shown in Table 1, the heat treat process used to reduce residual stresses created during the rough machining had no effect on the hardness of the optical surfaces.

5.2.2 DTM SETUP

ASG 2500 Geometry

The fabrication of axisymmetric, Richey-Chrétien optical systems can be carried out using a Diamond Turning Machine (DTM) as shown in Figure 2. The optical axis of each element is collinear and as a result, each can be made using the face of the vacuum chuck as a reference surface and the spindle axis as the optical axis. The process begins with the primary mirror that is vacuumed to the spindle and the flat fiducial surface is machined on the face along with the optical surface. The distance between the fiducial surface and the apex of each optical surface is set during the machining process. The tube is then machined and its length and parallelism of the faces aligns the two optical elements. Finally the secondary is machined including a flat fiducial surface and the optical surface. As with the primary, the relative distance between the fiducial and the optical surface along with the length of the tube sets the spacing. While the tube shown in Figure 2 is only one way to create the spacing between elements, it is a good illustration of the technique to design and build these optical systems.

The fabrication capability of a modern DTM allows the optical elements illustrated in Figure 2 to be machined with a tolerance of $\lambda/4$ (150 nm) on the flatness and shape of the optical and

fiducial surfaces and diameters and lengths can be fabricated to a tolerance of ±1 μm. Machining errors of this magnitude have a negligible effect on the optical performance of the system.

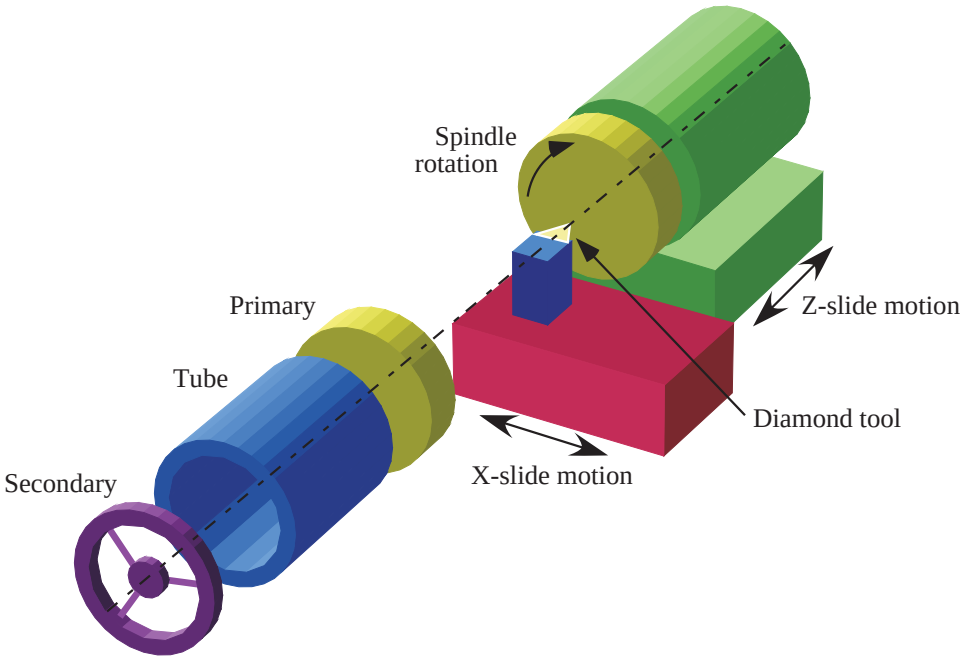

Figure 2. Fabrication of Richey-Chrétien telescope components on a diamond turning machine

Tool Setup

The DTM X-axis table provides room for multiple tool holders. To create both the optical surface and the fiducials in one setup, two tools were used: a large nose radius (3.135 mm) to create a low roughness on the optical surfaces with shorter machining times and a small radius tool (0.1057 mm) to create the sharp corners needed for the fiducial features. Since it is important to know the location of the tool in both the X and Z directions, each tool must be setup to find their location in X, Y and Z.

Finding tool center is a multi-step process that takes considerable time. There are a number of different techniques that have been proposed and used to "center" a tool. The one used here was to machine a small convex sphere on a test part and measure its sphericity in the laser interferometer. The goal is to place the apex of the tool (X=Y=0) at the center line of the spindle. If the tool is low or high (Y direction), a center defect will be created and the micro-height adjustor can be used to center the tool in Y. If the tool is sweeping out a circular path from some value of X to X=0 and it stops short of center (or goes beyond center) the interferogram will have a characteristic shape. Based on the results of the measurements, the X value is offset toward or away from the spindle center until a perfect sphere is created. At that

point, the tool location is known. Figure 3 shows the larger tool being centered with respect to the spindle centerline. After each tool is centered with respect to the spindle axis (X and Y), each was used to touch the face of the vacuum chuck to define a common Z reference. Note that the small radius tool is tilted so that it can machine the OD and face of the primary and secondary as well as the face and ID and face of the tube. The location of the two tools on the X slide must also allow each to cut its respective surfaces without interference of the other tool with the part.

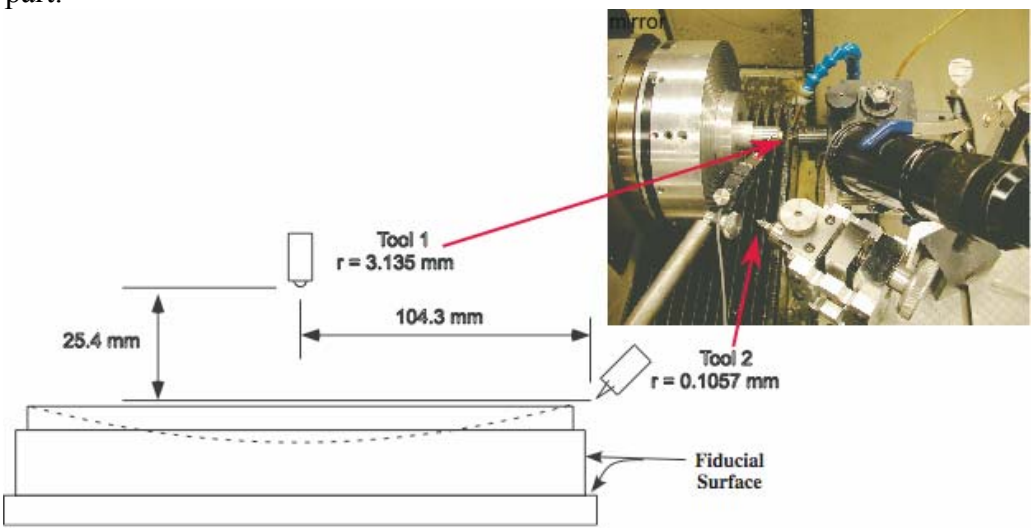

Figure 3. Tool layout on the DTM showing relative location of the two tools

Feed Rate and Spindle Speed

Feed rate and spindle speed are selected based on the desired surface finish, machining time and the characteristics of the spindle. The theoretical surface finish is calculated with a parabolic approximation of the tool shape using the feed rate (f=feed/rev) and the tool radius (R_t).

$$PV = \frac{f^2}{8R_t} \tag{2}$$

Smaller federates and larger tool radii will improve the finish. However, there is a limit based on the asynchronous vibration of the spindle, the tool sharpness and the material to be machined. Asynchronous spindle vibration will change the tool position from one revolution to the next at any angular position across the face of the part and thus influence the measured finish. The tool edge sharpness will affect the minimum chip thickness and can increase the roughness. Finally, the material structure (second phase particles in 6061 Al) will create imperfections that will degrade the surface finish.

For the proposed mirror surfaces, a spindle speed of 530 rpm was selected (minimum asynchronous error motion), feed rate of 2 mm/min for the primary, 1 mm/min for the secondary, and a tool nose radius of 3.135 mm. For this combination the theoretical PV surface roughness

will be less than 1 nm. The machine has created surface finishes on this order but not on 6061-T6 [5]. The actual surface finish was on the order of 6 nm RMS due to the issues discussed above. The machining time for the finish cut was approximately 30 min. for the primary and 20 min. for the secondary.

5.2.3 CONTROLLER PROGRAMMING

Number of Points

The hyperbolic surfaces of the primary and secondary mirrors are created with a programmed path that consists of a series of X, Z commands. As a result, the controller commands a series of straight lines that approximate the hyperbolic shape. If the acceptable deviation between the straight lines and curve is 1 nm, Equation (3) can be used to calculate the acceptable distance between points (d_p) for the primary mirror in Equation (3). The width of the primary mirror is 62 mm, which yields 1266 X, Z points. Employing the same method for the secondary mirror yields 735 X, Z points.

$$d_p = \sqrt{(PV) * 8 * R} = \sqrt{(1 \text{ nm}) * 8 * 300 \text{ mm}} = 48.9 \ \mu\text{m} \quad (3)$$

Tool Radius Compensation

The shape of the diamond tool must be considered when cutting non-flat surfaces. For a circular tool cross-section, the theoretical tool center traces out a path that is offset from the cutting edge by the radius of the tool. The direction of this offset is perpendicular to the slope of the surface at the point of contact. The programmed tool path can be corrected for the finite radius of the tool by 1) finding the normal vector at each point in the path and 2) offsetting the axes locations by the tool radius along this vector (in the correct direction). Normal vectors can be found analytically for many surfaces or estimated numerically for a closely spaced path of discrete data points. The offsets are simply the product of the tool radius with the sine (for X) and the cosine (for Z) of the normal angle. The sequence of corrected points defines the path of the tool center. This process is illustrated in Figure 8 where the upper curve in each plot labeled “Tool Path” (i.e., the tool center) is at a constant offset (the tool radius) from the hyperbolic surface swept out by the tool edge during machining.

Axes following error

The programmed tool path for the hyperbolic mirrors with correction for the tool radius was input to the controller. To check for error in this path, the trajectory following capability of the

ASG 2500 DTM was evaluated while running the primary and secondary hyperbolic mirror finish pass motion programs. Data was recorded by the controller every 32nd iteration of its 500 Hz servo loop (i.e., 15.625 Hz or 64 msec/sample). The finish pass cross-feed rates for the secondary and primary mirrors were 1 and 2 mm/min, respectively. Approximately 30,000 data points were collected for the primary mirror motion program and 22,000 data points for the secondary mirror. Each sample contains the commanded positions of the X and Z axes, their actual positions as measured by the laser interferometer and the servo loop voltage commands sent to the pulse width modulated motor amplifiers. Each axis of the DTM vibrates at its natural frequency (Z axis with spindle is 61 Hz and X axis is 89 Hz) with an amplitude of about 30 nm. This aliased high frequency vibration was removed from subsequent plots with a 100 point running average filter.

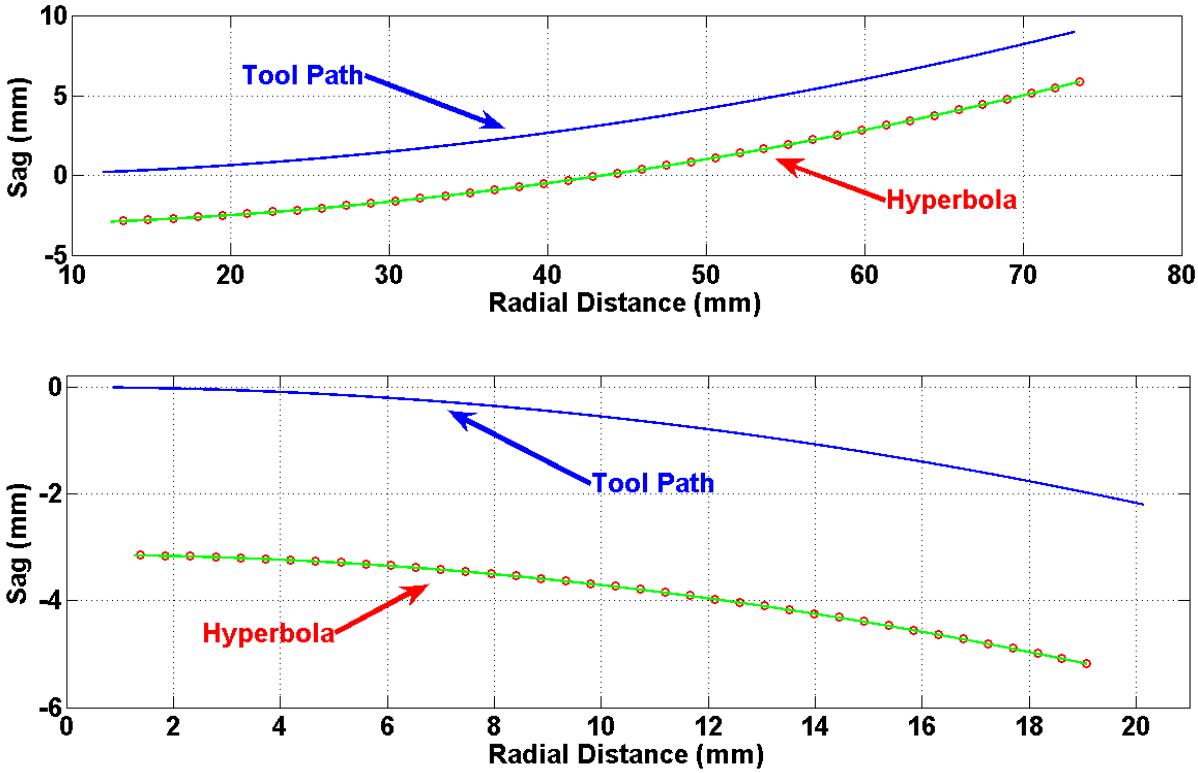

Figure 4. Primary (upper) and secondary (lower) mirror motion paths and desired surface.

The error in tool trajectory for each mirror is a combination of the X and Z positioning errors. To evaluate this error, X and Z axis positions were compared with the ideal trajectory in Figure 4. The commanded tool path (and presumably the resulting motion of the axes) was compensated for tool radius as discussed previously. The direction of the offset is determined by whether the shape is a concave or convex. Therefore, to compare the actual motion to the desired, the recorded data was uncompensated for tool radius by applying a radius compensation algorithm with a reversed shape parameter. Then for each X position in the data stream a sag value on the desired hyperbola was generated and the sag error was calculated. Figure 4

compares the primary and secondary recorded tool positions with the desired hyperbolic shapes. The upper curves are the recorded tool paths as measured by the laser interferometer. The same data *uncompensated* for tool radius is shown as dots and the desired hyperbola is the solid line that passes through the dots.

Figure 5 shows the difference between the dots and the solid lines that pass through them from the two plots in Figure 4. This difference is the sag error versus radial distance. For the primary mirror the PV motion path error is 6.75 nm (2.4 nm RMS) and for the secondary mirror the error is 12 nm PV (2 nm RMS). For both mirrors, the actual tool motion is close enough to the programmed tool path to create no optical errors.

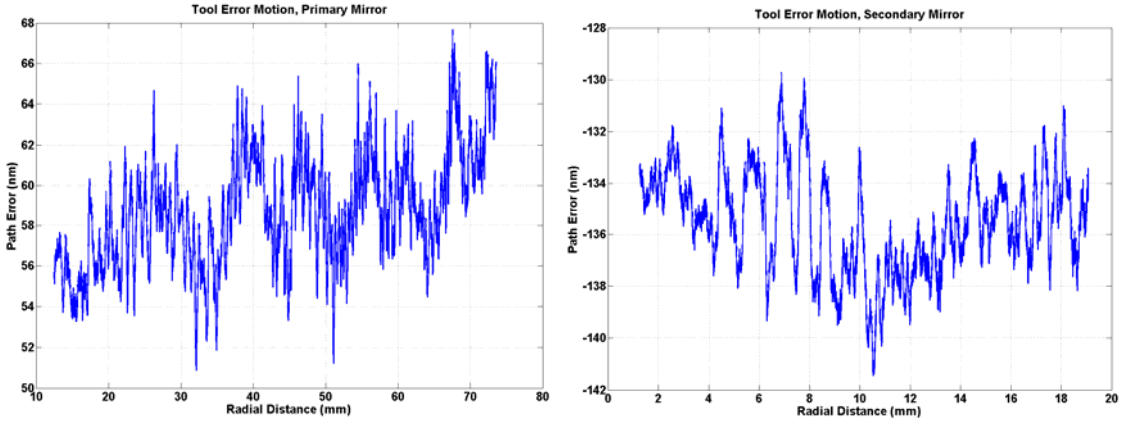

Figure 5. Primary (left) and secondary (right) mirror motion path error

5.2.4 MACHINING STEPS

The diamond turning machine used for machining the optical surfaces and fiducials is equipped with hydrostatic oil bearing slideways with laser interferometer position feedback (2.5 nm resolution), ball screw drives, air bearing spindle with angular encoder (20,000 points/rev) and a vacuum chuck to hold parts to the spindle.

Vacuum Chuck Flatness The face of the vacuum chuck was used in the machining process as the reference surface for relative position of the optical and fiducial surfaces. It was faced off prior to final machining of the optical surfaces and was assumed to be flat. Figure 6 shows the flatness of the chuck around the periphery measured with an electronic indicator. Comparing the slope of the flat and tapered face, the relative angle is about 2 arc-seconds. This is a result of not calibrating the yaw correction built into the machine tool controller as discussed later in this

section. The surface of the chuck was cone shaped with a peak in the center of about had a taper of about 710 nm. This will affect the flatness of the mirrors.

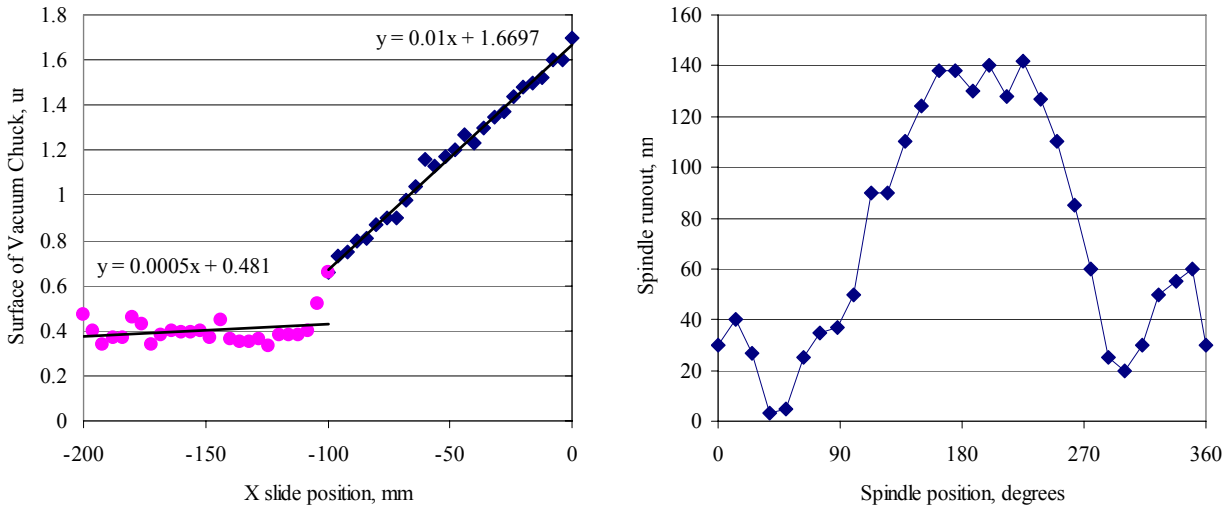

Figure 6. Vacuum chuck face flatness and axial runout

Axial Runout of Vacuum Chuck The axial runout of the chuck was also measured with an electronic indicator with the spindle rotating at low speed and is shown in Figure 6. The indicator was 80 mm from the center of the spindle. The runout is very low (140 nm) which should produce a λ/4 optical surface if the yaw error is corrected.

Primary Back

The back of the rough machined primary mirror was diamond turned to create a flat reference surface for attaching to the vacuum chuck. A small flat ring was first cut into the rim of the optical surface to create a chucking surface. When this component was vacuumed to the chuck, the support at the edge would cause it to take on a concave spherical shape. If machined and removed from the chuck, it would be a convex shape. To counteract this effect, the deflection was calculated (~1 μm) and the back was machined with a concave radius with a sag equal to 1 μm. When the back was measured, this was not enough and it was done again. The final shape of the primary found in Section 8 however, shows convex shape with about 1 wave (0.6 μm) from flat. Also, a non-rotationally symmetric shape remained with PV of 1 wave when the rotationally symmetric shape is removed with the interferometer software. The lack of vacuum chuck flatness discussed above may be have influenced this result.

Primary Mirror Surface

The programmed path of x,z commands are based on the mathematical description of the optical surface. The optical surface is a hyperbola with a k=-1.0195, a base radius of 300 mm, an OD of 150 mm and a 26 mm hole in the center. Because there is a hole in the center of the mirror, a

rubber plug was used to create a seal for the vacuum chuck. The surface was first rough machined to the desired hyperbola shape with the 0.1 mm tool and was finished using the 3.135 mm tool with increasing depth until the surface was completely machined. At this point, the apex to chuck distance was 22.571 mm. The designed distance was 22.5 mm; however, tool wear concerns when cutting 6061-T6 aluminum dictated the decision to cease machining. Fiducial step to apex height remained unchanged. The cutting paths are seen in Figure 7.

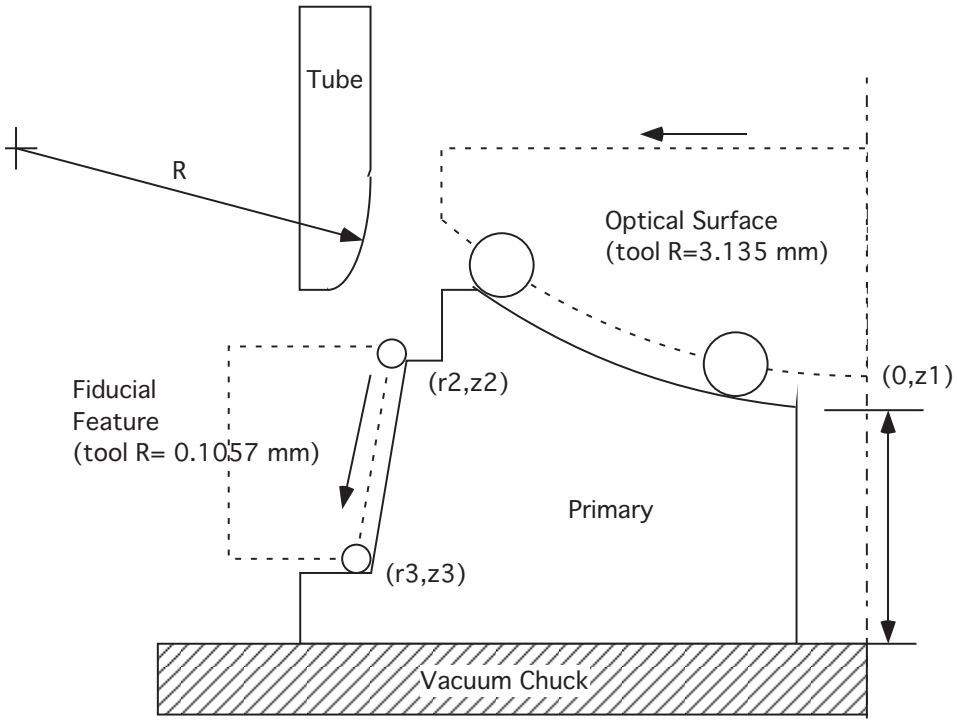

Figure 7. Primary optical & fiducial cutting paths.

Unfortunately, the tool radius was input to the controller as 3.125 mm instead of the actual value of 3.135. As a result, sag in the primary was reduced by 300 nm or the radius of the parabola was increased. This should have a minimum effect on the performace but is partly responsible for the difference between the focal point in the model and that measured in Section 8.

The fiducial feature that transfers the primary optical shape to the secondary is a step on the OD that mates with the tube as seen in Figure 7. The crucial features of this fiducial are the taper angle (1^o), the diameter and the axial distance to the back surface of the mirror. These features were machined with the 0.1057 mm diamond tool which was set to Z reference by using this tool to face the vacuum chuck prior to final machining.

Secondary

The secondary mirror is another hyperbolic surface but is much smaller than the primary (~40 mm diameter) and is convex rather than concave. The optical surface is supported on three arms that extent to a ring that mates with the tube via the same interference fit method as the primary. As with the primary, the optical surface and the fiducial stops are machined on the DTM. To vacuum this mirror to the spindle, a thin plate was used to seal the area between the outside ring and the optical surface (the thin plate contacted on the support arms). The machining process for creating the optical and fiducial surfaces was the same as described on the primary mirror.

The rough machined secondary was measured on the CMM and back face of the mirror was about 20 μm above the outer ring and is shown in Figure 8. A force experiment was performed to measure the motion of the optical surface when the secondary is vacuumed to the chuck. This result verified the CMM measurement. The key distance is from the apex of the hyperbola to the fiducial surface. When loaded by the vacuum chuck, this distance is 20 μm closer than in the unloaded condition. Therefore the controller was programmed to compensate this deflection by cutting the optical surface 20 μm deeper with respect to the fiducial surface than designed.

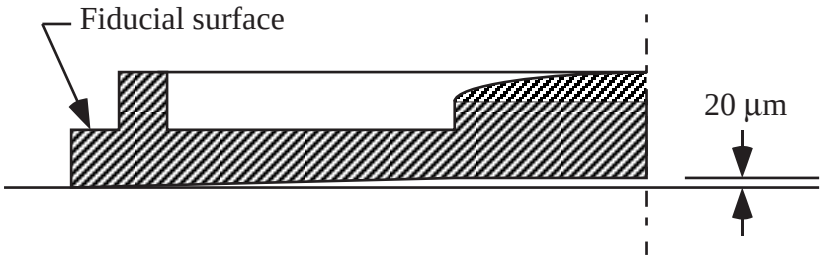

Figure 8. Cross section of the secondary mirror through one of the three support arms.

Tube

The connection between the primary and secondary mirror is established by the tube. It sets the axial spacing as well as aligning the two optical axes. The ID of each end includes a radial interference fit surface with an axial seating surface. These surfaces mate to the primary and the ring on the outside of the secondary. To machine the tube, it was attached to a flat plate using the 3, #4-40 threaded holes in each end as shown in Figure 9. This plate mounted to the vacuum chuck and the 0.1 mm tool was used to machine the IDs, end faces, and OD references. The process was as follows:

1. Machine flat at on exposed end face
2. Invert tube
3. Machine primary fiducial surfaces
4. Machine centering reference on OD
5. Machine tube end symbol on OD
6. Invert tube
7. Center tube with OD reference
8. Measure plate to tube end distance
9. Machine secondary fiducial surfaces

Figure 9. Machining tube in DTM

Spacer

The distance between the back surface of the primary and the camera body is set by the spacer. It is connected to the primary with three machine screws and thin spacers that act as a semi-kinematic mount. As a reference surface for both the camera and primary, the thickness of this plate provides the most versatile adjustment for focus.

5.2.5 Fiducial Feature Fidelity

The spacing of the three main components of the telescope - primary, secondary and tube - were measured using the Brown & Sharpe CMM. These measurements were made with and without the mirror attached to the tube. The results are intended to see if any of the components are distorted during assembly. The measurement details are illustrated in Figure 10 and presented in tabular form in Table 2 and 3.

Figure 10 shows the primary, the tube and the secondary and the distances measured. The procedure was to measure each optical component both alone and assembled onto the tube. For example, the primary axial fiducial was measured as it rested on the granite flat of the CMM. 18 points were measured and the average is the distance A shown in Table 2 to be 7.558 mm.

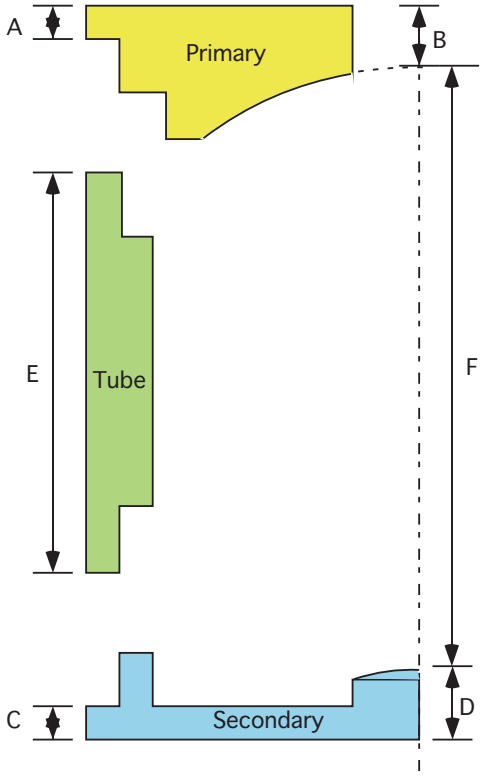

Figure 10. Fiducial Features on two-mirror telescope

Table 2. Fiducial Spacing Measurements

Dimension	Actual (mm)	Variation (mm)	Desired (mm)	Error (μm)
A	7.558	±.0025	7.571	-13
B	22.566	±.0035	22.571	-5
B-A	15.008	-	15.000	-8
C	5.015	±.0125	5.000	15
D	10.788	±.0005	10.775	13
D-C	5.773	-	5.775	-2
E	134.392	±.0005	134.400	-8
E+C-D	128.619	-	128.625	-6
E+A-B	119.384	-	119.400	-16
F	113.611	-	113.625	-14

Next the hyperbolic surface of the mirror was probed with enough points to estimate the apex height B. The difference between these heights is the distance from the fiducial surface to the apex, B-A = 22.566 mm. This is very close to the intended spacing of 22.571 mm. The primary mirror was then assembled to the tube and the distance from the top of the tube to the apex of this mirror was measured to be 119.447 mm. This distance was compared to the individual parts or A+E-B = 119.379. This shows that the apex surface moved 68 μm toward the secondary as a result of the assembly process. The secondary mirror assembly was measured in the same way as the primary described above. In this case, the apex of the secondary moved 40 μm away from the primary.

Table 3. Assembled Spacing Measurement

Dimension	Actual (mm)	Variation (μm) Flatness / Apex	Desired (mm)	Error (μm)
Tube to secondary apex	128.658	3 / 2	128.617	41
Tube to primary apex	119.447	10 / 18	119.392	55
Apex to apex	113.713	-	113.625	88

The calculated apex to fiducial measurements, combined with the tube length, yields the total system spacing. Unfortunately, during assembly, the primary moved away from the secondary and the secondary moved away from the primary to increase the spacing. This value, shown as F in Figure 10 and Table 2, is larger than desired and this will have an impact on the focus point of the compared to the optical design.

5.3 FORM ERROR CAPABILITY OF THE DTM

The measurements of the surfaces created for the two-mirror design showed some problems with the setup of the ASG diamond turning machine. The spindle flatness was a key parameter that influenced the shape of the primary mirror. Over the past 20 years, a number of experiments have been performed to study the errors in this machine. This section summarizes some of that data and verifies the machine capability. The goal was to determine that capability of the DTM to fabricate a flat and spherical surface and determine the peak to valley (PV) form error. The goal is to make a surface equal to or less than λ/4 (0.25 wavelengths HeNe ~150 nm). Thermal expansion of work pieces due to handling contact was studied along with spindle expansion due to transient heating effects of startup.

5.3.1 DTM ERROR BUDGET

An error budget was completed on the ASG 2500 DTM in 1991 [3]. To create high quality optical surfaces, repeatable errors in the machine must be compensated. Such error sources are induced through the lab environment, machine, material and startup conditions.

Environment

The labs at the PEC are designed to provide an environment conducive to high precision machining. Temperature stability is critical for dimensional stability and the actual temperature in each laboratory room is 20 ± 0.05 ºC [1]. The laser interferometer system used on the ASG is open to the ambient air so it is sensitive to temperature changes as well as humidity, barometric pressure and carbon dioxide content. The floor of each lab is a concrete slab that is suspended by a specially designed rubber vibration isolation device. The first natural frequency of the system is approximately 12 Hz and it will attenuate higher frequency excitation.

Slide Straightness and Compensation

Each axis has 5 constrained degrees of freedom: straightness in the vertical and lateral direction plus the angular motions of roll, pitch, and yaw. Because the geometry of the ASG 2500 is designed to reduce Abbe offsets and error motions, these can be reduced to three error motions [2]. X-axis straightness contains lateral and vertical straightness plus roll, pitch and yaw. The Z-axis straightness contains the same components except it excluded Z-axis yaw error, which is discussed later. Straightness measurements were recorded using a Zerodur straight edge supported by a custom fixture. The fixture allowed use of the ‘reversal’ technique such that the errors in the straightedge can be eliminated in the reported slide errors.

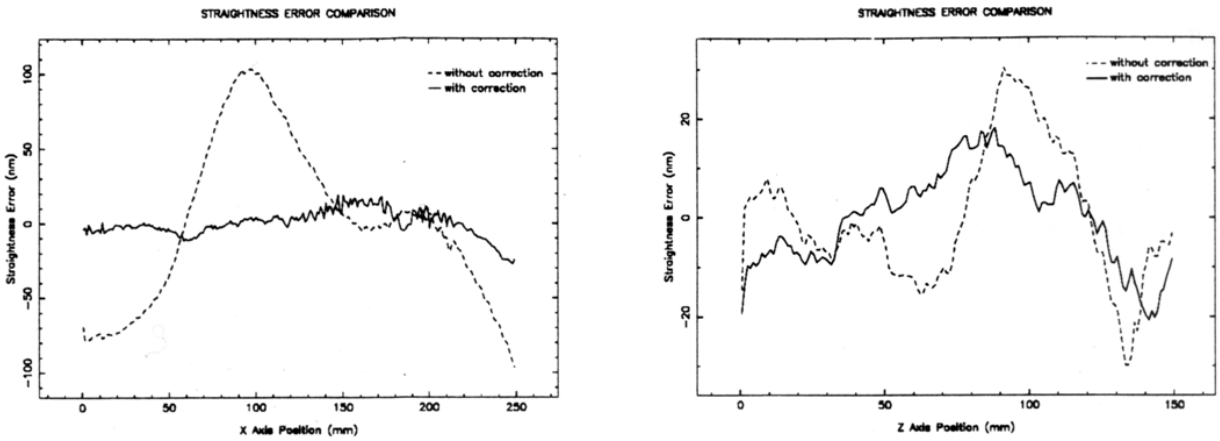

a) Z straightness of X slide b) X straightness of Z slide

Figure 11. X and Z Axis Straightness (note scale difference) with and without compensation from the orthogonal slide. [2]

Error shapes for each axis error were repeatable with a $\pm 3\sigma$ variation of approximately 20 nm. The X axis shows a peak to valley (PV) error of 200 nm over its entire 250 mm travel [2] with features that indicate the pitch of the ball screw drive system. The Z-axis shows a PV error of 60 nm over its 150 mm travel [3]. Error maps were created from these measurements for the ASG controller in the form of lookup tables. Figure 11 shows that straightness using automatic compensation from the lookup tables of both axes is 40 nm PV.

Spindle Growth

Heating effects caused the spindle of the ASG 2500 to grow in length (Z-direction) when started from a standstill at room temperature [4]. Several long term tests determined the time required to achieve steady state operation and transient effects caused by the stopping and restarting of the spindle. Transient effects were modeled around typical operating conditions such as part measurement, tool changes and setup routines. Results indicated that at 1000 rpm the spindle takes 8 to 12 hours to reach a steady state growth of 1500 nm. Cycling tests revealed that once the spindle is restarted at 1000 rpm, it requires a re-stabilization time equal to the time it was not operating.

5.3.2 DIAMOND TURNED FLATS

A series of experiments were conducted to measure the capability of the DTM to machine a flat surface as shown in Figure 12. The programmed path is shown where the tool moves through a rectangular path. The cutting leg of the rectangle is started beyond the OD of the part and moves to the center. A stream of oil, directed at the tool and spraying from the OD towards the center

of the part was used to remove chips. Spindle rotation was 500 rpm ccw. The diamond tool used has an approximate radius of 5.45 mm and the cross-feed rate was set at 5 mm/min. A 10 to 15 µm depth of cut (DOC) roughing pass was performed followed by a finishing pass of 2 µm depth of cut (DOC).

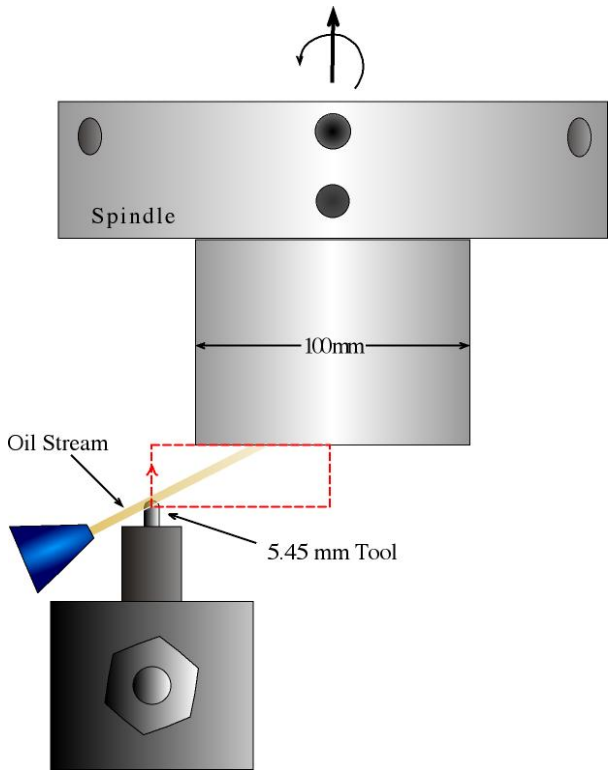

Figure 12. Tool Motion and Oil Spray for Flats

The flats were machined in 6061-T6 aluminum alloy with a diameter of 100 mm and a thickness of 75 mm. The aspect ratio (diameter/thickness) of this workpiece is 1.33, which is much larger than the mirror blanks discussed earlier in this section and should cause no distortion in the finished surface as a result of non-flat vacuum chuck.

Yaw Error and Compensation

The change in the yaw of the Z-axis as it moves has a significant effect on surface form error [3]. Measurements revealed that the axis yaws nearly linearly and the magnitude is 1.6 arcsec over its entire 150 mm length. The change in yaw error is repeatable so it can be compensated in real time according to the expression:

$$Z_{comp} = \left(X_{pos} - X_0\right)\left(\delta_{slope} Z_{pos} + Slope_0\right) \tag{3}$$

where ($X_{pos} - X_0$) is the X distance from the spindle rotation axis, δ_{slope} is the linear change in slope along the Z axis (1.6 arcsec./150 mm)and the intercept is $Slope_0$ (yaw magnitude at a Z = 0) [3]. The intercept may vary, as the spindle can be unbolted and its angular orientation changed. For this reason, measurements and test cuts were performed to find this intercept. The position measuring system on the Z-axis has an Abbe offset ($X_{pos} - X_0$) from the location of the center line of the spindle to the laser retroflector. The effects of the Abbe offset is negligible when performing an operation where the Z axis is held constant; however, any operation where the Z axis moves will be affected. Measurement of the Abbe offset and modification to linear yaw compensation equation are discussed and used to create a controller program to compensate for this effect.

Flat Test Results The results of 16 machining tests used to find the yaw error compensation values are shown in Table 4. The Z-axis coordinate is the absolute position of the Z-slide during the cut. It also serves as an intercept for automatic yaw compensation. The surface profiles were measured on the Zygo GPI and the PV surface is the total peak to valley measurement over the 100 mm diameter of the part including any non-rotationally symmetric features. PV Trace a single trace across the entire 100 mm diameter of the work piece at an arbitrary location. An example of the measurement of a 6061 aluminum flat is shown in Figure 13. The figure at left is the top down view of the entire part showing the machined shape. The surface is flat but the center is lower than the edges. The PV is 170 nm or approximately λ/4. The trace along the line in the top view is shown at the right. The profile is more obvios and the PV is 148 nm. For Tests 1-4 the motion of axis was manually changed to reduce the cone error. Starting at Test 5, the automatic compensation routine was activated and the linear intercept values are seen in last column.

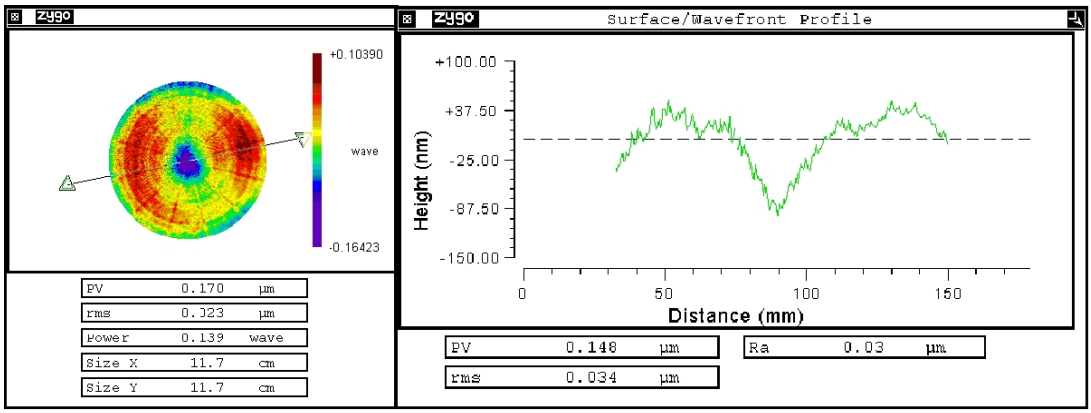

Figure 13. Example trace of 6061 aluminum flat machine on the DTM

Table 4. Results of machining tests to produce flat specimens

Test No.	Z axis coordinate (mm)	PV Surface (nm)	PV Trace (nm)	Manual Compensation (nm)	Auto Compen (slope , intercept) (arcsec., mm)
1	1.19852	250	150	600	no yaw
2	1.19852	207	121	600	no yaw
3	1.19852	201	107	600	no yaw
4	1.19852	184	105	600	no yaw
5	1.19852	200	184	-	1.03, 1.2
6	1.19852	250	193	-	1.03, 1.2
7	1.19852	160	-	-	1.03, 1.2
8	1.19852	290	162	-	0.7, 1.2
9	1.19852	300	-	-	0.7, 1.2
10	1.19852	290	-	-	0.7, 1.2
11	1.19852	220	125	-	0.7, 1.2
12	20	316	193	-	0.7, 1.2
13	20	203	162	-	0.7, 1.2
14	20	202	99	-	0.7, 1.2
15	20	186	100	-	0.7, 1.2
16[1]	26.614	134	78	-	0.7, 1.2

Tests 1-4 Manual Compensation

Z-axis yaw leads to a cone shaped feature in the flat that may be concave or convex. Initially, manual modification of the part program was used to remove cone shape caused by the z-axis yaw. The path was modified to create an inverse of the measured shape. The results of these tests indicated that the yaw at Z = 1.2 mm was 10 μrad (2 arcsec.) or 600 nm at a radius of 60 mm.

Tests 5-16 Automatic Compensation

Based on the results of the manual compensation tests, the ASG 2500 automatic compensation routine was implemented to correct for Z-axis yaw. The intercept for the yaw compensation routine was calculated from the results of the manual compensation experiments. The first estimate for the intercept were yaw = 1.03 arcsec. at Z = 1.2 mm. Tests were conducted and the

[1] Test 16 was an 1100 aluminum specimen - the rest of the specimens were 6061 aluminum

shape of the cone went from convex during manual compensation to concave during automatic compensation. The intercept was then changed to yaw = 0.7 arcsec. at z = 1.2 mm, which gave the initial convex shape.

To prove the robustness of automatic yaw compensation the tool was moved such that Z = 20 mm for a series of tests. The compensation expression is the same as was used in Tests 8-11 which were machined at Z = 1.2 mm. The results at Z = 20 mm have error magnitudes like the tests at Z = 1.2 mm and were similarly convex.

1100 Aluminum Workpiece

During preparations for a surface finish test, a sample of 1100 aluminum was used to fabricate a reflective flat indicated in Table 3 as Test 16. The process differed in that it had a spindle speed of 530 rpm, a tool radius of 5.45 mm and a 1 μm depth of cut. Z-axis position was 26.614 mm. The final automatic compensation settings were used, there were two roughing passes before the final and the spindle had been running for more than 24 hours. The error level, as shown in Table 3, was smaller than with the 6061 tests.

5.4 SURFACE FINISH

Previous work by Drescher [5] addressed the surface finish capabilities of the ASG-2500 and the relationship between tooling forces, machine vibration and surface finish. He found motion between the tool and spindle was caused by the z-axis. The only way to eliminate this vibration was to shut off the oil flow to the Z-slide and let it rest on the machine base and turn off the z-axis controller. Only then was the predictive model accurate when inputting cross-feed rate, nose radius, depth of cut, and edge sharpness.

DTMs commercially available in the 1990s, like the ASG 2500, are typically equipped with oil hydrostatic bearings, ball screw drives, air bearing spindles, and laser interferometers for feedback [6]. These machines can create surface finishes in 6061 aluminum of approximately 40 nm PV and 6-7 nm RMS, which is useful for the near infrared spectrum. Newer machines with linear motors, high-speed spindles can produce smoother surfaces especially if a single phase material such as pure aluminum plating (Alumaplate ®) is used. A surface finish approaching 1 nm RMS has been reported [6]. These mirror surfaces are adequate for use in the visible light spectrum.

5.4.1 TWO-MIRROR 6061-T6

Optical surfaces and structural members in the two-mirror telescope were created entirely from 6061-T6 aluminum alloy. The disadvantages of this material were discussed previously in the two-mirror section of this report, specifically: high hardness and high levels of particulate impurities.

Both surfaces were cut on the ASG-2500 DTM using a 3 mm nose radius diamond tool and 530 rpm spindle speed. Because the primary was much larger than the secondary; different cross-feed rates were used for the primary (2 mm/min) and secondary (1 mm/min). This gives theoretical RMS surface finish of the primary of 0.19 nm while the actual was 5 nm [Section 8]. Theoretical RMS of the secondary is 0.05 nm while actual was 4 nm. Both surfaces show little indication of the feed rate of the diamond tool.

5.5 CONCLUSIONS

The study of diamond turning for fabricating optical and fiducial surfaces is an important area of research related to the production of high-quality optical systems for civilian and military applications. This section discussed the generation of the hyperbolic mirrors for the Ritchey-Chretien telescope as well as the general capability of the ASG diamond turning machine to generate optical quality surfaces.

Hyperbolic Mirrors The steps needed to create the hyperbolic optical surfaces are described as well as the related fiducial surfaces that dictate the spacing of the mirrors. Multiple tools were needed to create both types of surfaces and each was centered with respect to the X, Y and Z axes. The capability of the machine to create assembled features is discussed and spacing on the order of 10 μm is possible.

Flat Surfaces A number of diamond turned 100 mm diameter flats were machined on the ASG-2500. These surfaces have PV form fidelity below λ/3 (211 nm) often falling below the λ/4 (158 nm) threshold. All linear traces of the surface fall below λ/4 and often fall below λ/5 (127 nm). Yaw errors of the Z-axis are dominating error in optical flat fabrication with the ASG-2500. The straightness errors of the X and Z axes are corrected by lookup tables in an automatic compensation routine as is the Z-axis yaw.

The consistency in the results above was not achieved until thermal allowances were observed. The aspect ratio of the part gave it high sensitivity to temperature changes such that a 75 mm long part made from 6061-T6 aluminum alloy will expand 1770 nm per ºC. It is absolutely necessary to utilize thermally isolating gloves, have minimal contact with the work piece and confine it to a tightly controlled environment. Also, "warm up" of the spindle must be complete before attempting to diamond turn an optical surface.

Surface Finish Diamond turned surfaces created with the ASG-2500 seem to approach a lower boundary in both RMS and PV measurements of surface finish. The RMS minimum is approximately 6 nm, which is adequate for infrared imaging systems and approaching the maximum for visible light.

5.6 FUTURE WORK

5.6.1 THREE MIRROR ANASTIGMAT

A three-mirror anastigmatic (TMA) telescope is currently being designed. If off-axis conic or NRS conic shapes are needed for this system, the fast tool servo will be needed. New processes will be developed to fabricate the mirror surfaces and fiducials.

Like the two-mirror system, the TMA will utilize a bolt together design. Each mirror will have six degrees of freedom: x, y, and z position with roll, pitch and yaw. Proper constraint of each will be achieved through fabrication of a high precision fiducials on metrology frame. Fly cutting and precise fixtures will be necessary, so a single setup and single tool set are envisioned. The Rank Pneumo Nanoform 600 DTM will be used for the fabrication of the metrology frame as it is fitted with a Moore Nanotech System y-axis (vertical displacement) and a C-axis spindle.

REFERENCES

1. Moorefield II, G.M. and T.A. Dow. Error Budget for Diamond Turning Machine. Precision Engineer Center 1989 Annual Report, 7, 65-70, (1989).
2. Moorefield II, G.M. and T.A. Dow. Error Budget for Diamond Turning Machine. Precision Engineer Center 1990 Annual Report, 8, 239-261, (1990).
3. Miller, M.H. and T.A. Dow. Enhancements to Three Axis DTM Controller. Precision Engineer Center 1991 Annual Report, 9, 265-278, (1991).
4. Hubbel, P., G.M. Moorefield II and T.A. Dow. DTM Metrology. Precision Engineer Center 1991 Annual Report, 9, 83-107, (1991).

5. Drescher, J. and T. Dow. Tool Force and Surface Finish Aspects in Diamond Turning of Ductile Metals. Precision Engineer Center 1991 Annual Report, 9, 109-138, (1991).
6. Schaefer, J.P. Progress in Precision – Single Point Diamond Turning (SPDT) of Optical Components, Presented at APSE 2002 Spring Topical Meeting on Progress in Precision, (2002).
7. Matweb Material Property Data. Blacksburg, Virginia. http://www.matweb.com
8. Sphericity and radius of curvature metrology. Tucson, AZ. http://www.phase-shift.com/products/interferometer-sphericity.shtml.

6 MICROMACHINING USING ELLIPTICAL VIBRATION-ASSISTED MACHINING (EVAM)

David E. Brehl
Graduate Student
Alexander Sohn
Precision Engineering Center Staff
Thomas Dow
Professor
Mechanical & Aerospace Engineering

The goal of present research is to extend the Ultramill EVAM tool's capabilities so that it can become a practical means of making functional microdevices. To improve surface finish over previous work, an oil-bearing Y-axis with increased stiffness in the Z-direction replaced the original air-bearing unit, leading to improvement in PV and RMS finish by nearly a factor of 2. Additional detailed investigation of upfeed feature generation is described, showing that further improvement in surface finish depends on identifying and reducing tool / work relative vibration in the Z-direction. The range of materials successfully machined by the Ultramill is expanded to include stainless steel, with fabrication of submillimeter-scale binary-feature parts. The next activity for Ultramill development is described, creating a groove pattern at precise locations on a MEMS component. Challenges for this project include making 1:1 aspect ratio grooves with steep sidewalls, a feature scale of less than 5 μm and achieving precise XYZ tool location relative to a fiducial on the part. Conceptual solutions are proposed for these issues.

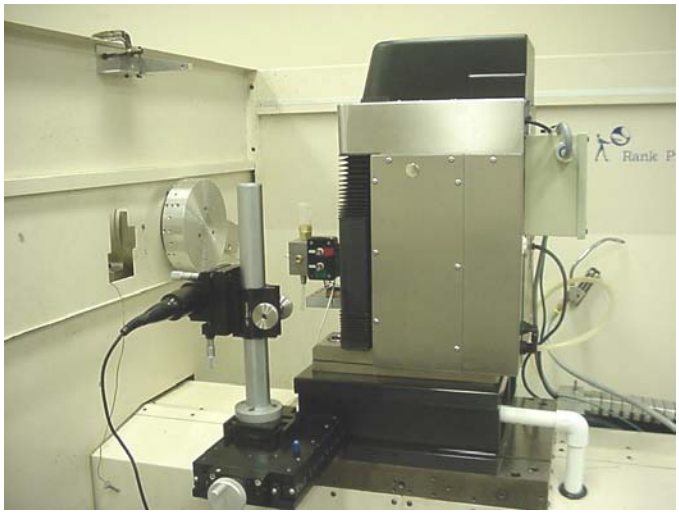

6.1 INTRODUCTION

Microstructures can be defined as fabricated features with critical dimensions in the range 1 to 100's of μm. They can be functional small-scale devices in themselves, or features of a large structure. Microstructures can also take the form of ultraprecision molds and dies used in mass replication methods like injection molding and hot embossing. Effective microstructure creation is essential to the success of miniature integrated systems such as micro-electromechanical systems (MEMS), micro-optoelectronics systems (MOEMS), and biomicrofluidic "lab-on-a-chip" packages.

The Ultramill is a precision cutting tool using "elliptical-vibrated assisted machining" (EVAM). It avoids many of the issues associated with other methods for micro-device fabrication. In EVAM, a piezoelectrically-driven toolholder moves the tip of a diamond cutting tool in an elliptical path at frequencies of 1 to 4 kHz. This elliptical tool motion is superimposed on the feed motion of the workpiece. Potential advantages of the Ultramill EVAM process are:

- Optical quality surface finish
- 3-D features at micrometer scale, with sub-micrometer tolerance
- Near-zero burr at the edges of cuts
- Large range of materials that can be machined
- Extended diamond tool life when used to machine ferrous and brittle materials

The Ultramill has been used at the PEC to create binary micro-structures in copper [1]. These included the PEC's Angstrom symbol logo shown in Figure 1 at sizes of 1mm square and 200 μm square. This demonstrated the potential for the Ultramill to create microstructures of arbitrary geometry and smaller than 200 μm overall size. However, significant development is necessary for EVAM to be useable in fabricating functional microstructures. The goal of the present research is to extend Ultramill capabilities in several areas:

1. Improving surface finish – The Ultramill initially achieved surface finishes of 15-25 nm (RMS). This is acceptable for some applications, but marginal for optical purposes. In any case, it is considerably worse than EVAM's theoretical capability. These larger-than-expected surface finishes are partly attributed to Z-direction vibration caused by the diamond turning machine's original air-bearing Y-axis. Using an axis with stiffer hydrostatic oil bearings for the slideway was expected to address this. Detailed investigation was undertaken into how the EVAM process caused formation of surface features. Process improvements were also identified that could lead to further reductions in surface roughness.

2. Materials – Steel, and stainless steel in particular, are of interest for use in micro-molding, micro-optics, and applications where a hard or chemical resistant material is needed. Machining experiments were conducted using the Ultramill to make features in stainless steel.

3. Complex and/or high-aspect ratio features – Binary features made to date are low-relief, with shallow, curving walls due to the use of round-nosed tools. The smallest single feature achieved is 15 µm wide. Functional micro-structures frequently require high aspect ratios, straight vertical walls, and micrometer-scale features. Features may need to be located precisely when the Ultramill is used as a value-added process on partially-finished part. A project was proposed that would be a next step from the binary features made to date: machining a groove pattern with steep wall profiles, sinusoidal cross sections, 1:1 aspect ratio, and 3 µm minimum feature width, onto a micro-relay element. Detailed analysis of fabrication issues enabled proposed solutions which will be tried in the near future.

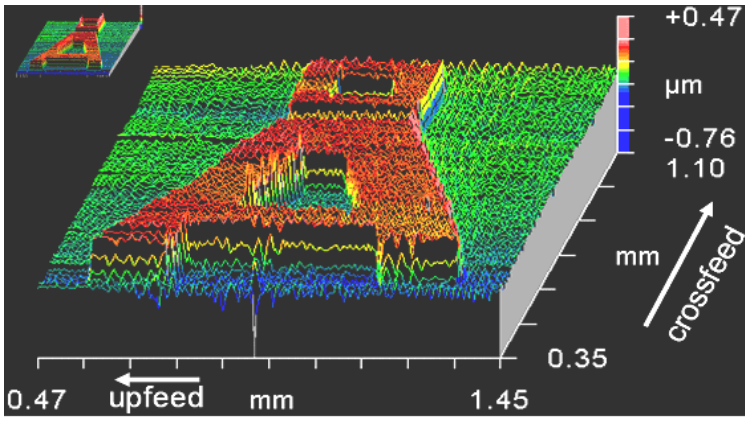

Figure 1. Angstrom symbols cut with 1 mm nose radius tool (main image) and 50 µm nose radius tool (upper left) shown at the same magnification [1].

6.2 PROCESS DESCRIPTION AND EQUIPMENT

6.2.1 EVAM PROCESS

Figure 2 depicts the Ultramill elliptical tool-tip motion generated by a pair of piezoelectric actuators. Sinusoidal voltage signals, 90 degrees out of phase, are supplied to the two parallel actuators. The linear motion of the actuators is converted to an elliptical tool motion by means of a mechanical linkage that is part of the toolholder design. The ellipse dimensions can be varied by changing the amplitude and relative phase of the voltage signals applied to the piezo stacks.

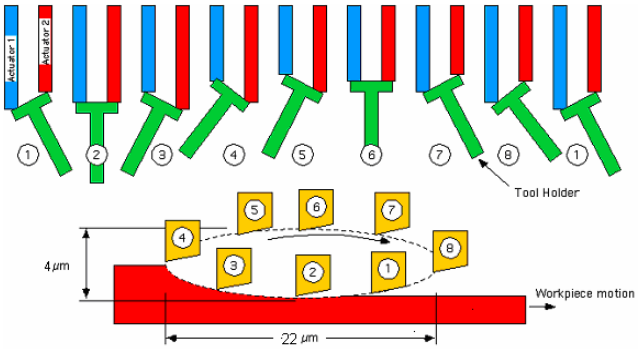

Figure 2. Ultramill Vibration-Assisted Machining Concept

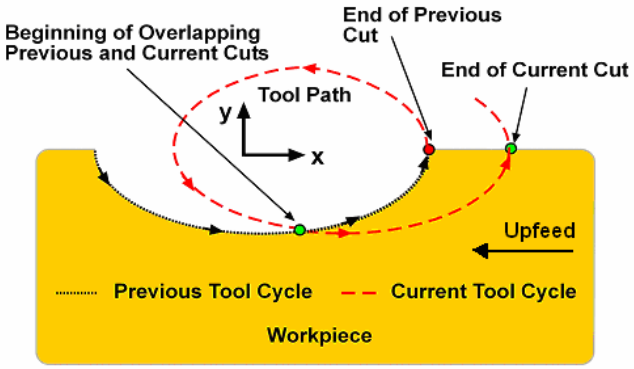

Figure 3. 2 cycles of tool motion, superimposed on work feed

Figure 3 shows two cycles of the elliptical tool path, superimposed on the workpiece feed motion. The periodic entry and exit of the tool from the work creates cusp-like features regularly spaced in the upfeed direction. Short, discontinuous chips are created when the depth of cut (DOC) is smaller than the semi-minor axis of the toolpath ellipse. For this condition, the tool tip exits the workpiece before its motion reverses relative to the work feed, and so the chip end is cut cleanly from the material instead of remaining attached. This results in near-zero burr at the edge of the cut.

6.2.2 EQUIPMENT

Figure 4(a) is a cutaway view of the Ultramill. It shows the two piezoelectric actuator stacks and the ceramic toolholder, to which the diamond tool is cemented. The piezo stacks are housed in a steel chamber. A dielectric heat transfer fluid circulates through the chamber to cool the stacks. A titanium diaphragm (not visible in the figure) provides fluid sealing around the toolholder, and exerts the required preload force on the piezo stacks.

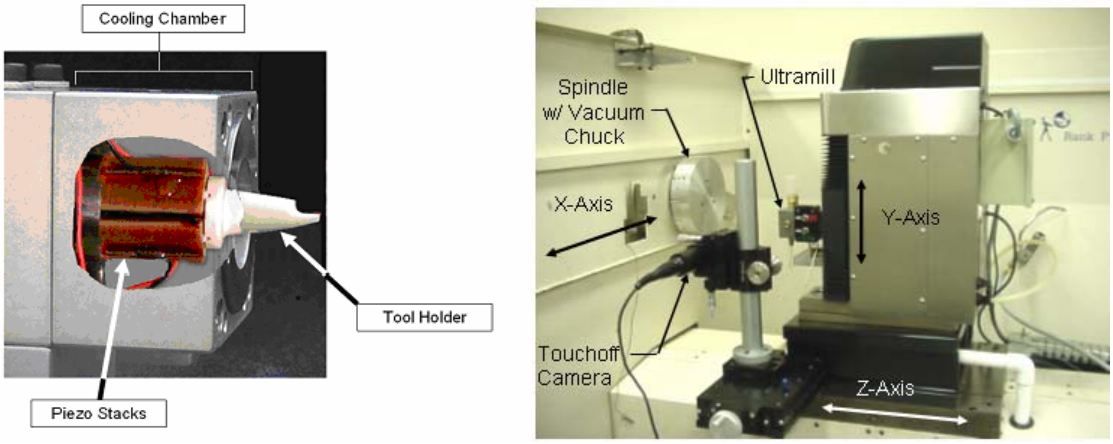

(a) Cutaway view of Ultramill (b) DTM with oil-bearing Y-axis

Figure 4. Ultramill EVAM tool and Nanoform diamond turning machine (DTM)

Figure 4(b) shows the Ultramill installed on the PEC's Nanoform 600 diamond turning machine. (DTM). The Nanoform provides 3-axis X-Y-Z motion for raster machining (the spindle is currently locked when using the Ultramill). Following an upgrade in August 2005, all three axes now possess hydrostatic oil bearings and nanometer-accuracy positioning ability. Laser interferometers give position feedback information for the X and Z axes, while a linear encoder is used by the Y-axis. A UMAC controller provides motion and control commands to the Nanoform axes. The UMAC interface was upgraded in 2005 to permit use of standard CNC 'G'and 'M' codes. A vacuum chuck on the spindle face holds the workpiece during machining. A video microscope camera provides a view of the tool rake face and the work surface, to facilitate touchoff.

6.2.3 Y-Axis Upgrade

The original air-bearing Y-axis was in place when the Angstrom symbols (Section 6.1) and Thunderbirds (Section 6.4) were machined. It is theorized that vibration of this Y-axis, in some combination with the Z-axis, was responsible for much of the surface roughness in these parts. Brocato studied the effect of axis vibration on surface finish of parts made with the air-bearing Y-axis [1]. The Z, X, and spindle amplitudes were found to be much less significant than those for the Y-axis, by nearly an order of magnitude. Spatial frequencies were determined for upfeed surface profiles on test flats. The two most significant component frequencies were very close to the resonant Z-direction frequencies determined for the Y- and Z-axes.

The air-bearing Y-axis was replaced with a new axis from Moore Nanotechnology Systems. The Moore axis uses a hydrostatic oil bearing for the slideway. This axis also features a linear motor drive. With encoder interpolation carried out by the UMAC controller, the new axis can achieve

step sizes of approximately 1.1 nm, compared to 40 nm resolution for the air-bearing axis. In place of the airpot weight compensator on the air-bearing axis, the Moore axis uses a closed-loop electro-pneumatic compensation scheme. The stiffness of the oil-bearing axis in the Z-direction was stated by the manufacturer to be approximately 2.5 million N/m. This compares with Brocato's estimate for the air-bearing axis' Z-direction stiffness of 500,000 N/m. Table 1 shows the improvement in upfeed surface roughness obtained by switching to the stiffer oil-bearing axis.

Table 1: Surface Comparison for Oil-Bearing and Air-Bearing Axis Slides

Axis	Oil- bearing	Air-bearing
Material	hard-plated copper	hard-plated copper
Part Description	test groove	small angstrom symbol [2]
Tool Nose Radius	1.0 mm	.050 mm
Machining Conditions	22 µm x 4 µm elliptical path, 1000 Hz elliptical frequency, 0.5 mm / s upfeed velocity	
Upfeed Finish, PV	48	91
Upfeed Finish, RMS	8	19

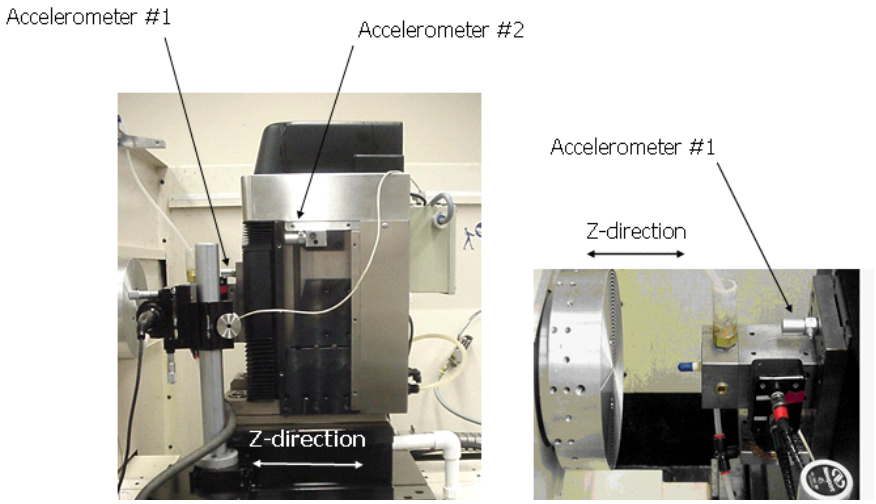

Figure 5. Accelerometer locations for hydrostatic oil bearing Y-axis response

The response of the oil-bearing Y-axis was characterized with the Ultramill as an excitation source. Accelerometers were installed on the moving slide (Accelerometer 1), and on the axis frame (Accelerometer 2), oriented to sense Z-direction acceleration. See Figure 5. Acceleration

data was collected by oscilloscope with the Ultramill operating at its normal machining condition used to date (frequency, 1000 Hz, nominal tool ellipse dimensions, 22 μm x 4 μm). Z-direction displacement of the Y-axis was not measured, because it was expected to be smaller than 50 nm, which is the resolution of available capacitance gauge systems.

Figure 6 is an oscilloscope trace for Accelerometer 1, showing Z-direction acceleration of the Y-axis slide. Acceleration peaks are visible every 0.001 s, corresponding to the 1000 Hz Ultramill frequency. The peak acceleration amplitude shown is 0.32 G. For a sinusoidal response, displacement can be obtained by twice integrating the acceleration:

$$\begin{aligned} \ddot{z}(t) &= -\omega^2 * A * \sin \omega t \\ \dot{z}(t) &= \omega * A * \cos \omega t \\ z(t) &= A * \sin \omega t \\ \omega &= 2 * \pi * f \end{aligned} \qquad (1)$$

where A is the maximum displacement amplitude, f is the operating frequency of the Ultramill in Hz, ω is the angular frequency, and $z(t)$ and its first two derivatives are displacement, velocity, and acceleration in the Z direction.

For the observed maximum accelerations of 0.32 G in Figure 6, the peak displacement using Equation (1) is 81 nm. However it is obvious from the plot that multiple frequencies are interacting, that the acceleration deviates considerably from a pure sinusoid, and that it would be difficult to accurately calculate the axis displacement from the acceleration response. The value found using Equation 1 is at best indicative of the displacement range. The displacement will need to be measured directly, by a very high resolution non-contact method such as the Angstrom Resolver or a nanometer-resolution capacitance gauge system.

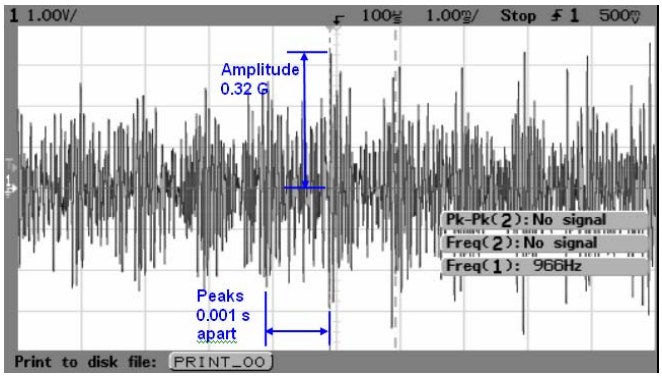

Figure 6. Acceleration response of hydrostatic oil-bearing Y-axis, for Ultramill operation at 1000 Hz and 22 μm x 4 μm ellipse

Accelerometer 2, attached to the axis frame, recorded insignificant accelerations on the order of a few milli-G when the Ultramill was operating, or less than 1% of that recorded on the slide. The hydrostatic bearing is therefore shown to be highly effective at vibration absorption between the slide and axis frame.

The impulse response of the axis was checked by tapping the slide with a small hammer, while the Ultramill was turned off. From the accelerometer response (not shown here), the Z-direction natural frequency of the oil-bearing Y-axis was estimated to be 8-10 kHz. On Figure 6 the slower-frequency Ultramill excitation is seen to be interacting with the higher natural frequency of the axis.

6.3 SURFACE FINISH

The generation of surface features by EVAM was investigated in detail. The purpose was to identify process improvements that could lead to further reductions in surface roughness, beyond that obtained by upgrading the Y-axis to an oil-bearing slide for greater stiffness in the Z-direction.

6.3.1 THEORETICAL SURFACE FINISH

Surface finish in EVAM has two components. The upfeed component is created by the elliptical tool motion superimposed on the work feed. The crossfeed component is caused by the round-nosed tool being incrementally moved after each raster pass. Crossfeed surface roughness is not discussed here since the variables affecting it are the same as for conventional diamond machining.

The theoretical peak-to-valley surface finish in the upfeed direction, PV, is calculated by:

$$PV = \frac{b}{8 * a^2} * (F_{up})^2 \qquad (2)$$

$$F_{up} = \frac{V_{up}}{f} \qquad (3)$$

where a and b are respectively the semi-major and semi-minor axes of the tool ellipse, f is the elliptical frequency of the tool and V_{up} is the upfeed velocity of the workpiece. F_{up} is the upfeed, the distance the EVAM ellipse advances relative to the workpiece in one complete cycle. F_{up} also expresses the expected upfeed distance between consecutive features in the workpiece, and can be used to relate machining results for different combinations of upfeed velocity and elliptical frequency.

6.3.2 SINGLE-GROOVE MACHINING TESTS

Single-groove machining tests were performed with a 1 mm nose radius tool, to evaluate the surface roughness with the new hydrostatic oil-bearing Y-axis. Figure 7 shows the part design used for these trials. This layout enabled upfeed surface roughness to be assessed as a function of both upfeed velocity and depth of cut.

In each part, a square foreground was first cut by the Ultramill, to provide a constant-depth reference surface. The 3 mm long grooves were then machined into it. By cutting the grooves into a machined surface instead of directly into the workpiece, it was possible to eliminate part-to-part depth variations that could arise from inconsistencies when touching off. Grooves were machined for a range of upfeed from 8 μm/cycle to 1 μm/cycle, or less in several instances. At each upfeed, grooves were machined at either 2 or 3 depths of cut, ranging from 1 μm to 2.5 μm. The grooves were sufficiently long so that in all cases the X axis was able to accelerate to the programmed upfeed velocity. The machining time for a groove was on the order of seconds, so temperature variations of the piezoelectric stacks would not play a part in groove roughness. Similarly, by machining grooves of varying depths adjacent to one another, stack temperature transients would have minimal opportunity to affect DOC compared to the programmed value.

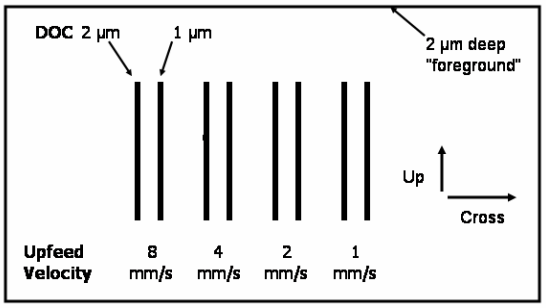

Figure 7. Part design for single-groove tests

Four parts were made, 3 in hard-plated copper and one in 1100 aluminum. Two copper parts and the aluminum part were made, then the tool was relapped by the manufacturer due to concern it might not be sharp. The final copper part was cut after the tool was relapped. The machining frequency in all cases was 1000 Hz, with a 22 μm x 4 μm ellipse.

6.3.3 UPFEED SURFACE FINISH

Upfeed surface finish was measured for each groove, using the Zygo New View white-light interferometer. Two or three measurements were made on each groove, at random locations in the central (constant-velocity) region. Figures 8 thru 11 show peak-to-valley (PV) surface finish versus upfeed, $F_{up,}$ for several test cases. The "theoretical surface finish" plotted on the figures is the minimum PV roughness using Equation 2.

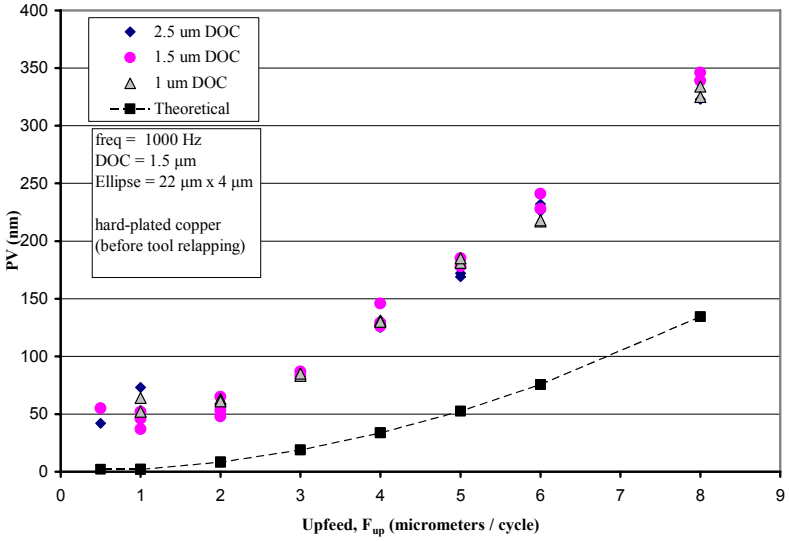

Figure 8. Effect of depth of cut on upfeed surface finish (PV). Theoretical finish from Equation 2.

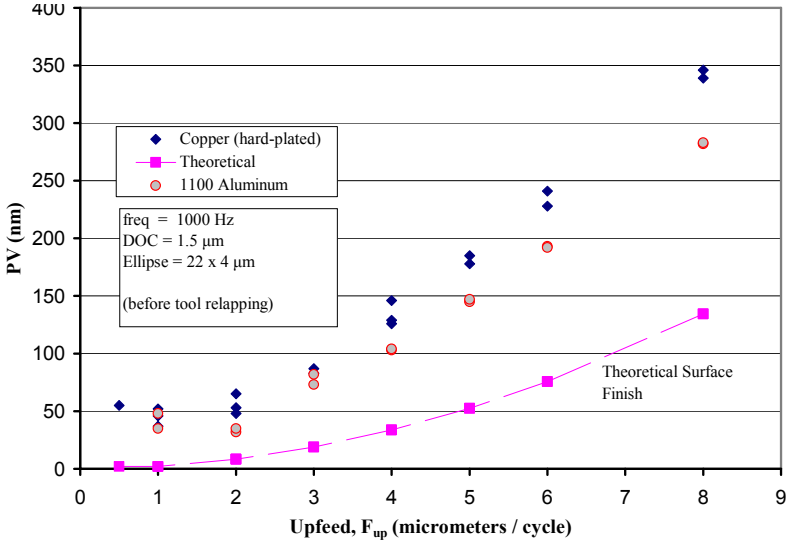

Figure 9. Comparison of upfeed surface finish (PV) between hard-plated copper, and 1100 aluminum. Theoretical finish from Equation 2.

Figure 8 shows the impact of varying DOC on PV surface finish in hard-plated copper. Figure 9 compares PV surface finish, at a single DOC, between the hard-plated copper and 1100 aluminum. Figures 10 and 11 show PV surface finish in hard-plated copper before and after the tool was relapped.

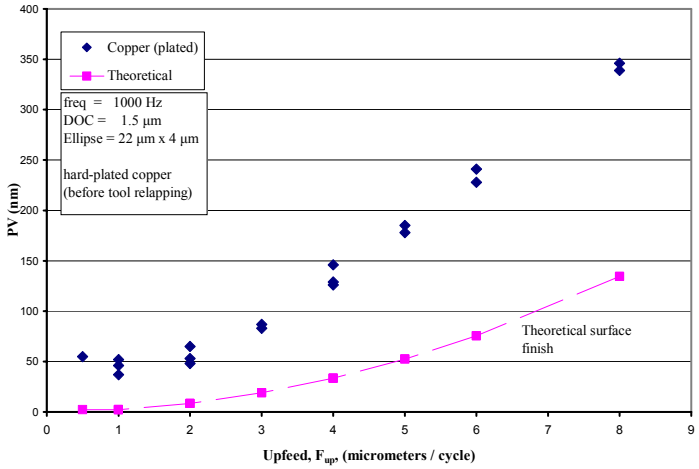

Figure 10. Upfeed surface finish (PV) vs. upfeed (before tool was relapped). Theoretical finish from Equation 2.

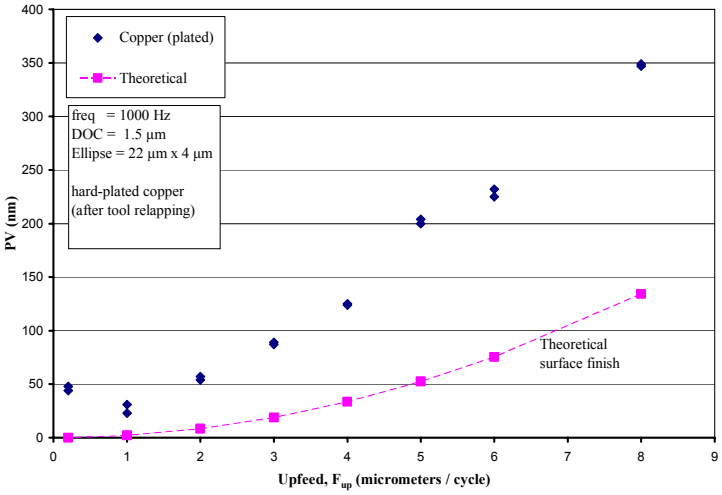

Figure 11. Upfeed surface finish (PV) vs. upfeed (after tool was relapped). Theoretical finish from Equation 2.

In Figures 8 to 11 the following significant results are observed:

- For all cases, the actual machined PV finish exceeded the theoretical finish predicted from Equation 2, by a considerable margin.
- The PV surface finish fell into two regimes. When the upfeed was greater than 2 μm/cycle, the PV finish increased with larger values of upfeed. Below 2 μm/cycle, the finish remained in a range of 40 nm to 60 nm, independent of the upfeed.
- Finish was unaffected by DOC across the range 1.0 μm- 2.5 μm.
- Finish for 1100 aluminum was, close to that for copper, despite its relative softness and low yield stress. At upfeed greater than 2 μm/cycle, the PV finish was 75-80% of that for copper, and was the same as copper for upfeed less than 2 μm/cycle.
- Relapping the tool had no effect on surface finish.

The tool was relapped because the excessive PV surface roughness, compared to theoretical values, was initially thought to be caused by wear or damage on the cutting edge. No attempt was made to measure the edge radius between the rake and flank faces due to the difficulty of obtaining an accurate value for this dimension, which on a sharp tool can be smaller than 50 nm. Therefore it is unknown whether relapping actually changed the sharpness of the tool, or if it was worn to begin with. Chardon Tool, the manufacturer, inspected the tool cutting edge using high-power optical microscopy, before and after the relapping. They too were not equipped to measure the edge radius, but made a qualitative evaluation that the tool was in good condition before it was refurbished. The lack of improvement in surface finish after relapping may simply indicate that the tool was sharp from the start.

The elliptical tool path was evaluated to be certain that it matched the assumed dimensions (22 μm x 4 μm). Negishi replaced the diamond tool with a reflector, and measured the tool path optically using a Dual Angstrom Resolver system [2]. This was not practical in the current instance, since a tool was already cemented to the toolholder. Several indirect methods were used to build confidence that the tool ellipse was as assumed. DC voltages were applied to the Ultramill piezo stacks, and static deflection of the tool measured using a Federal gauge: tool deflection was in the correct direction, and by the expected amount for the applied voltage. The power amplifiers that supply sinusoidal voltage signals to the piezos were checked via oscilloscope, and determined to be correct for frequency and amplitude through 2000 Hz. The output of the signal generator used to create the front-end sinusoidal input was checked, and found correct for frequency, amplitude, and phase. Finally, the entrance and exit regions of grooves were measured using both white-light interferometery, and an Atomic Force Microscope (AFM). When cutting the test groove, the tool was plunged into or extracted from the workpiece at zero upfeed velocity. The profile at the end of the groove should therefore indicate the path

followed by the tool cutting edge. An AFM was used to supplement the interferometer because it is more capable of measuring a steeply-inclined surface. Figure 12 shows the exit region profile of a groove, plotted from interferometer data using the SLICER program described in the next section. The intended tool ellipse is superimposed upon it. The accompanying AFM profile confirms that the spiky features on the vertical segment of the interferometer profile are indeed artifacts. It is concluded that the Ultramill tool path is close to its intended shape based on the excellent agreement between the ellipse and the exit profile, and the lack of contrary evidence from the equipment checks described above.

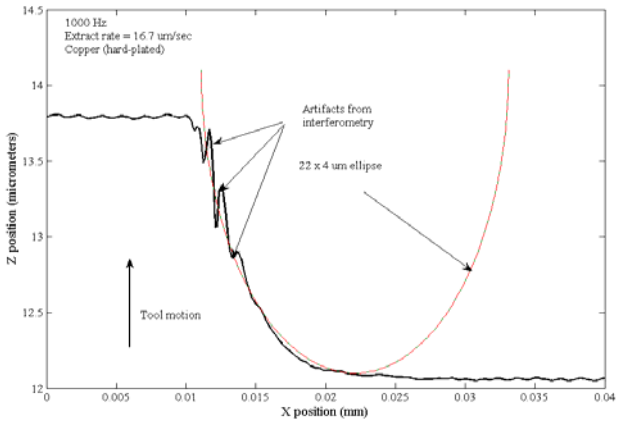

(a) White-light interferometer data replotted using SLICER program

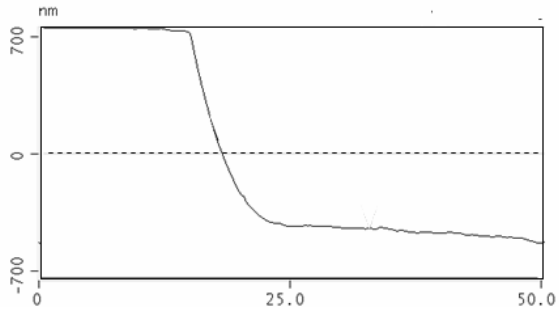

(b) AFM profile

Figure 12. Groove exit region. The machined surface profile closely matches the shape of the assumed toolpath ellipse. AFM profile confirms the absence of real features at location of artifacts in the interferometry data.

6.3.4 UPFEED SURFACE PROFILES

Figure 13 shows surface profiles for grooves machined at upfeeds of 8, 4, 2, 1, and 0.2 μm/ cycle. These profiles were generated by exporting surface metrology data from the Zygo New View white-light interferometer to SLICER, an in-house MATLAB program [3]. SLICER

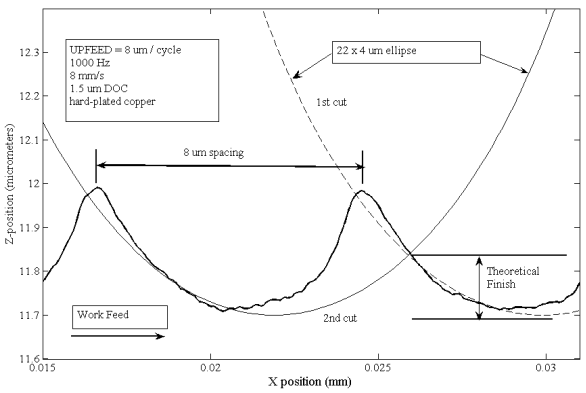

(a) Upfeed = 8 μm / cycle

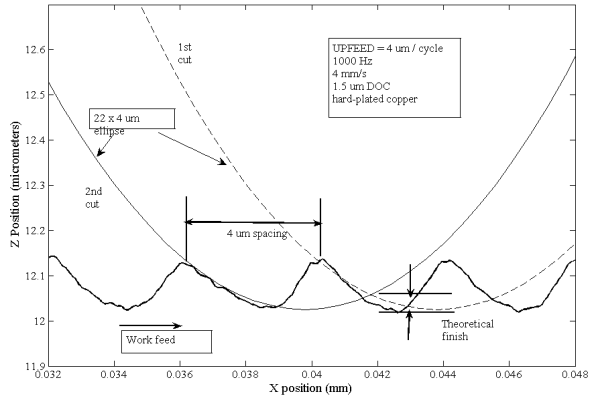

(b) Upfeed = 4 μm / cycle

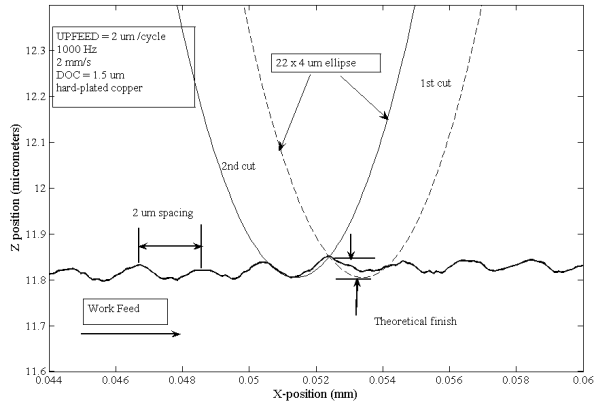

(c) Upfeed = 2 μm / cycle

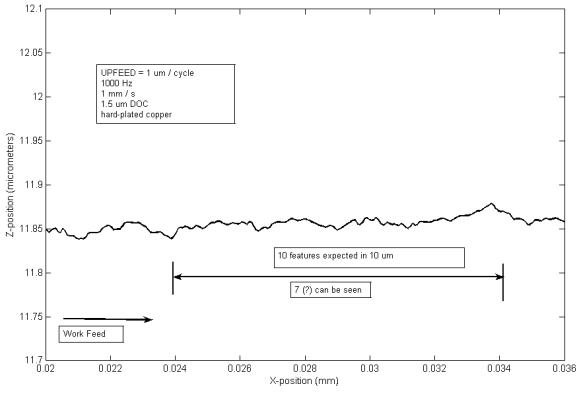

(d) Upfeed = 1 μm / cycle

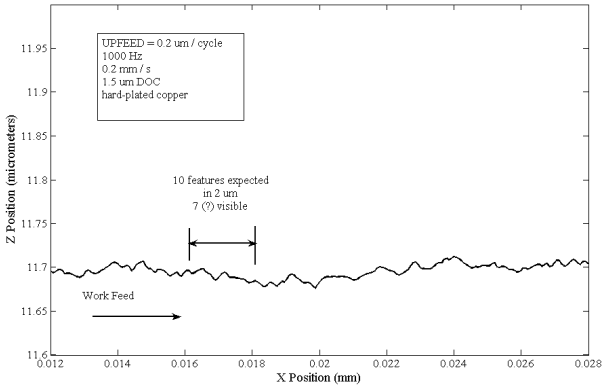

(e) Upfeed = 0.2 μm / cycle

All parts made in hard-plated copper
f = 1000 Hz
DOC = 1.5 μm,
Machining ellipse = 22 μm x 4 μm

Figure 13. Upfeed surface profiles. White-light interferometer data replotted using SLICER program. All profiles are at same horizontal scale. Vertical scale on (d) and (e) exaggerated by a factor of 2.

permits 2-D profiles to be drawn with greater location accuracy on the part, and with more flexible control of scaling, than can done with the New View. The profiles in Figure 13 are all drawn on the same horizontal scale. The vertical scale in Figures 13(d) and 13(e) is exaggerated by a factor of 2, compared to the profiles at larger upfeed.

For upfeed from 8 µm/cycle down to 2 µm/cycle (Figures 13(a)-(c)), the cusp-like EVAM surface features are clearly visible, and are spaced periodically at the predicted upfeed interval. Their height decreases as upfeed grows smaller. The features generally have a regular, repetitive appearance, although some irregularity is visible in the profile for 2 µm / cycle.

In the last two profiles, for upfeed of 1 and 0.2 µm/cycle, the EVAM features can no longer be distinguished (Figure 13(d)-(e)). For example, over a 10 µm distance, in Figure 13(d), 10 features should be visible at a regular spacing of 1 µm. But it is difficult to even identify features: the statement on the figure, that 7 can be discerned, is subjective.

These profiles explain the shape of the measured PV versus upfeed data. See Figure 14 for example, which repeats Figure 11 from Section 6.3.3. When upfeed is large, for example 8 µm/cycle, the features are large and regular as in Figure 13(a). This results in a high value for PV roughness. As upfeed is decreased, the features become smaller and more closely spaced and the PV finish grows smaller as well (Figure 13(b) and (c)). Below 2 µm/cycle, the features can no longer be detected and the surface profiles are irregular with small amplitudes that do not seem dependent on the value for upfeed, as shown by Figures 13(d) and (e). This corresponds to the portion of Figure 14 where upfeed is less than 2 µm/cycle, and where PV surface finish stays within the range 40 nm to 60 nm.

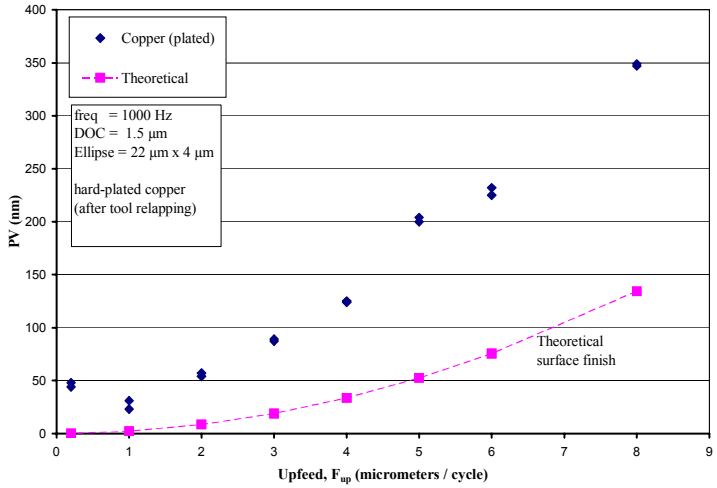

Figure 14. Upfeed surface finish (PV) vs. upfeed (after tool was relapped). Theoretical finish from Equation 2. (Repeat of Figure 11)

6.3.5 ANALYSIS OF SURFACE FINISH RESULTS

Surface roughness for upfeed less than 2 µm/cycle Most Ultramill machining takes place at upfeed velocities slower than 2 mm/s, to minimize upfeed surface roughness while using an elliptical frequency of 1 to 2 kHz.. In microstructure fabrication, where individual axis moves might measure only tens of micrometers, the acceleration of the X-axis can make it not meaningful to program velocities faster than 0.5 mm/s. At an elliptical frequency of 1000 Hz, this corresponds to an upfeed of 0.5 µm/cycle. Factors affecting surface finish in this upfeed range need to be well understood in order to enable creation of optical quality small-scale structures.

The profiles in Figure 13(d)-(e) have the appearance of high-frequency, small-amplitude signals superimposed onto low-frequency, large-amplitude vibrations. Autocovariance plots generated on the Zygo interferometer are shown in Figure 15 for these profiles. A periodic pattern with a frequency of 10 Hz (after conversion to the time domain) appears in the 1 µm/cycle plot and is confirmed at 0.2 µm/cycle. From the available data, it is not possible to establish whether this is caused by a 10 Hz vibration, or a beat-type phenomena (for example, a 990 or 1010 Hz vibration interacting with the 1000 Hz Ultramill frequency). The source of this vibration has not been identified.

As discussed in Section 6.3.3, the surface finish stays roughly constant when upfeed is smaller than 2 µm/cycle. From the preceding analysis, it is inferred that during machining there is a tool/workpiece vibration with an amplitude of <50 nm. With upfeed larger than 2 µm/cycle, the features created by the Ultramill are tall enough that they mask this vibration. For upfeed smaller than 2 µm/cycle, the vibration amplitude is larger than the individual feature heights, so it dominates in establishing the surface profile. Since the vibration appears to not change with

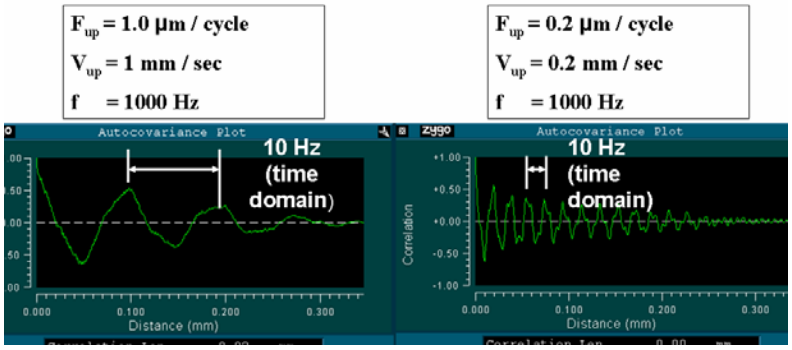

(a) Profile shown in Figure 13(d) (b) Profile shown in Figure 13(e)

Figure 15. Autocovariance for grooves cut at upfeed of (a) 1 µm/cycle (b) 0.2 µm/cycle

upfeed, no further reduction in surface finish occurs below 2 μm/cycle. Reducing the vibration can therefore be expected to result in proportionate improvements in surface finish.

Surface roughness for upfeed larger than 2 μm/cycle To gain insight into the processes associated with creating EVAM features, surface profiles were examined for grooves cut with upfeed as large as 8 μm/cycle. As the upfeed increases above 2 μm/cycle, the features become progressively larger and spaced more widely, allowing more details to be seen.

An attempt was made to explain why the actual peak-to-valley surface finish consistently exceeds the theoretical PV predicted by Equation (2), using the concept of "minimum chip thickness". When turning ductile materials it has been noted that there is a minimum achievable chip thickness, established by material properties (hardness and elastic modulus) and tool sharpness and geometry. This phenomena results from elastic compression of the work material as it passes underneath the tool cutting edge and wear land, and then rebounds after the tool passes. The minimum chip thickness produces a corresponding feature in the work, termed the *spansipfel.*

Figure 16 illustrates how this concept might be applied to generation of EVAM surface features. In Figure 16(a), the tool is beginning to cut upward into the surface left from the preceding pass. In Figure 16(b) the tool has completed its upward cut, leaving a new surface including a *spansipfel.* If the upfeed distance is short relative to the *spansipfel height,* on the next downward pass, the tool cuts off the top portion, Figure 16(c). This leaves a feature shorter than the initial *spansipfel*, but taller than the theoretical value based the toolpath geometry, Figure 16(d). Figure 16(e) shows what happens when the upfeed is sufficiently large for the tool to clear the *spansipfel* made on the previous pass. In this case, the final surface consists of a line of *spansipfels* in the upfeed direction, and the PV surface roughness is simply their height.

Simulated surfaces were generated by plotting the toolpath as a function of time, and applying the model depicted in Figure 16 for a range of assumed minimum chip thicknesses. Figure 17 compares the predicted surface finish for a minimum chip thickness of 200 nm to actual results for 1100 aluminum. Good agreement is obtained over most of the range for upfeed, except at the high end. With upfeed of 8 and 6 μm/cycle, the tool missed the *spansipfel* on the next pass as depicted in Figure 16(e). For an upfeed of 4 μm/cycle and smaller, the tool trimmed the *spansipfel*, as in Figure 16(d).

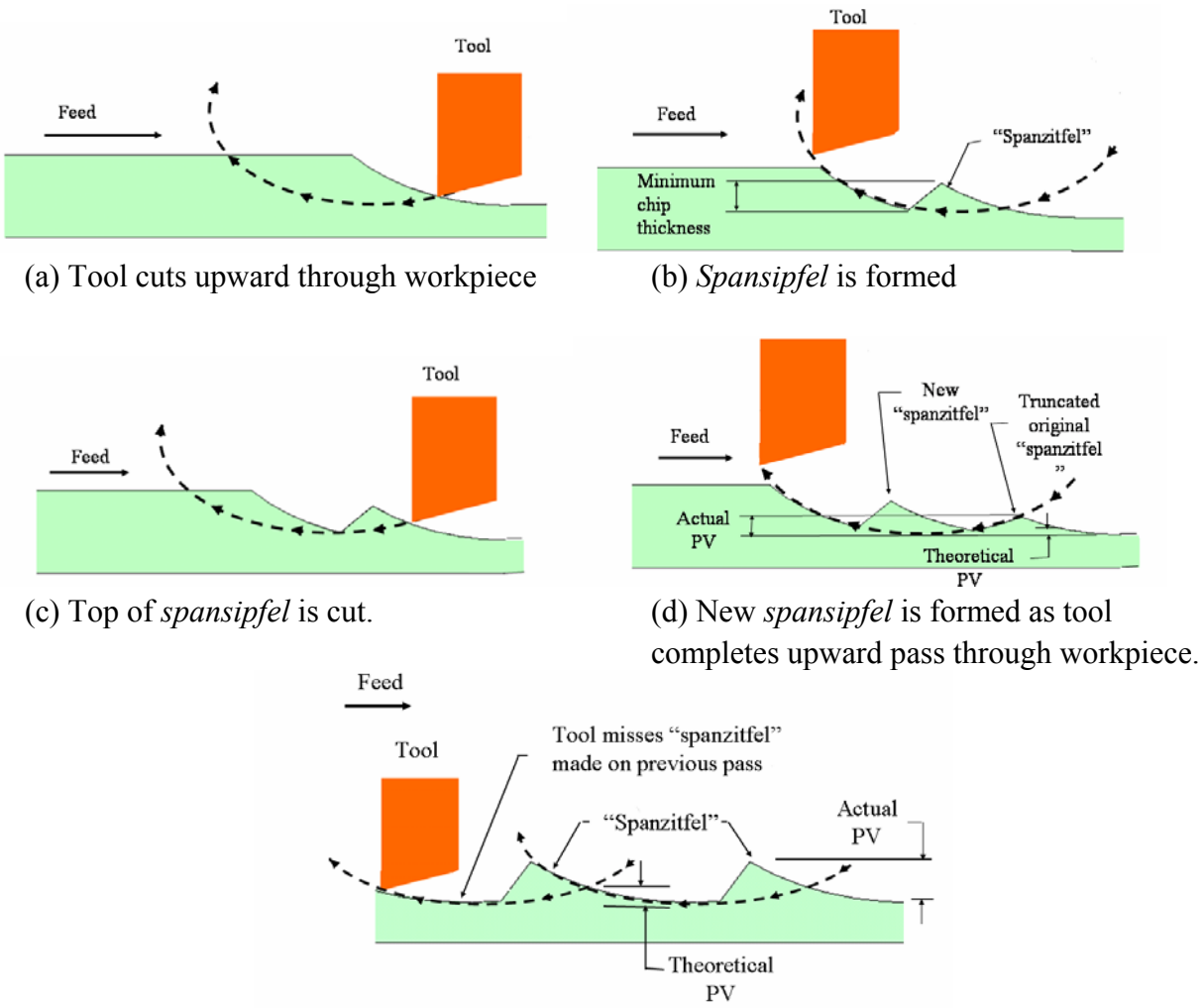

(a) Tool cuts upward through workpiece

(b) *Spansipfel* is formed

(c) Top of *spansipfel* is cut.

(d) New *spansipfel* is formed as tool completes upward pass through workpiece.

(e) When upfeed is large enough, tool clears the *spansipfel* created by the preceding pass.

Figure 16. Surface feature generation using the "minimum chip thickness" hypothesis.

While it is thus possible to create a simulation consistent with machining results, there are at least two potential problems with the hypothesis. First, is the assumed value of minimum chip thickness of 200 nm realistic? For conventional diamond turning, Arcona reported a minimum chip thickness for electroless nickel of 40 nm to 220 nm, increasing with greater tool wear [4]. As noted in Section 6.3.3, relapping the tool had no effect on surface finish here, so the finish is either not strongly dependent on the tool condition, or the measured surfaces are being created with a sharp tool. More notably, Negishi created discontinuous aluminum chips using the Ultramill that he estimated were only 10 nm minimum thick, based on their "transparency" in

SEM images [2]. However he did not report the alloy that he used, which might have

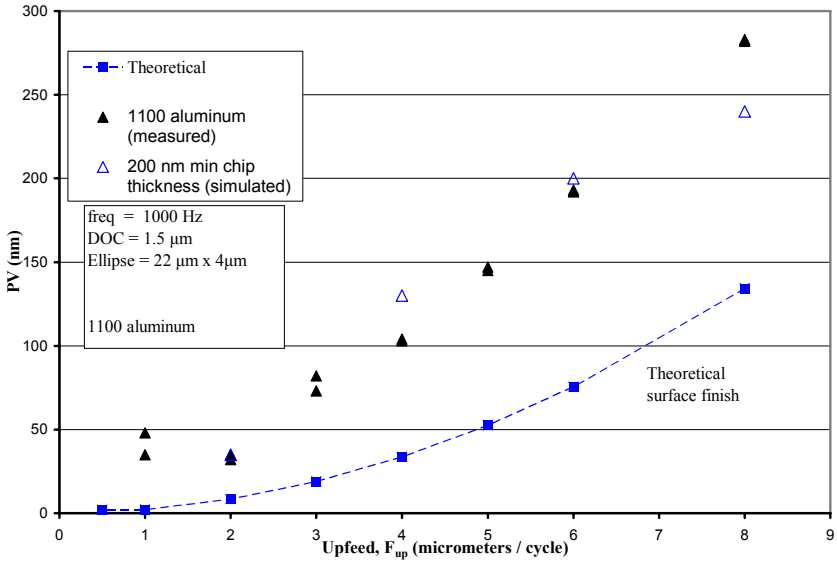

Figure 17. Simulated surface finish (PV) using the minimum chip thickness hypothesis, compared to results from machined grooves. Theoretical finish from Equation 2.

considerably different properties from the 1100 aluminum material. But there is a significant inconsistency between 10 nm observed minimum chip thickness and 200 nm required by the model. This creates doubt about the usefulness of the minimum chip thickness hypothesis for explaining the observed surface roughness, at least as the sole mechanism.

A second problem is the lack of an identified mechanism that requires a 200 nm minimum chip thickness, producing an associated tall feature, on the first cutting pass. But then on the following pass allows the top of the feature to be cut off, producing a much thinner chip. As of this writing, the insight needed to resolve these questions has not been obtained.

6.3.6 SUMMARY AND RECOMMENDATIONS

The best surface finish which can be presently achieved with the Ultramill is 40-60 nm PV, in plated copper and soft aluminum. As a comparison, Shamato *et. al.* reported 40 nm PV roughness in a hardened die steel using EVAM at ultrasonic frequencies [5].

At upfeed values typically used in microstructure fabrication, roughness appears to be caused by small-amplitude vibration that dominates the surface profile. A priority task toward improving surface finish is to identify the sources of this vibration, and to reduce it.

When upfeed is larger than 2 μm/cycle, regular surface features are seen at the expected spacing, but with much larger peak-to-valley measurements than predicted by theory. No satisfactory explanation has been found. A hypothesis based on "minimum chip thickness" was proposed, but has not been verified. Another suggestion is that the Ultramill is compliant in the upfeed direction, so that the cutting forces distort the tool path during the portion of the cycle when the tool is in contact with the workpiece. This also should be investigated as part of any effort to improve surface finish.

6.4 STAINLESS STEEL MACHINING

Stainless steel is one of the materials used for molds and dies for micro-injection molding and hot embossing. It also has other potential micro-device applications, owing to its strength, hardness, and corrosion resistance. However, as is the case for other ferrous materials, diamond tools have limited life when stainless steel is machined by turning conventional methods.

Two tests were carried out on stainless steel workpieces using the Ultramill:

- Creating a microstructure in Stainless Steel (17-4 PH SS) using EVAM.
- Obtaining diamond tool wear data for SS machining

6.4.1 MATERIAL AND SETUP

The material used in the tests was 17-4PH stainless steel, a precipitation-hardening stainless steel with approximately 0.07% carbon. It was supplied in the annealed state with a published hardness of RHC 34 [6]. The raw material was received as 3/4" round bar which was turned to approximately 1/2" diameter to fit the workholder and cut into 1" long pieces. The ends of these pieces were faced flat and then surface ground smooth (the surface grinding was not done on the piece used for wear investigation).

6.4.2 MICROSTRUCTURE DESIGN AND FABRICATION

The "Thunderbird" from the Sandia logo was chosen as the microstructure to be fabricated. Figure 18 is a sketch showing the main features of the part. The overall size of the raised feature is approximately 0.91 mm x 0.78 mm. It is 0.5 μm high relative to the background. The background itself is 2.5 μm deep. The ground steel surface gave only a diffuse reflection and made it difficult to confirm touchoff of the tool to the surface. For this reason, a foreground

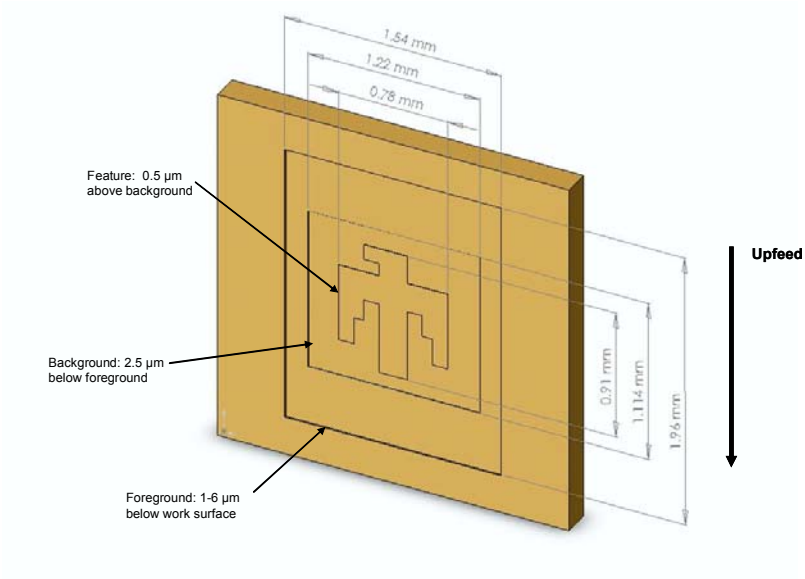

Figure 18. Thunderbird part design

Table 2. Machining parameters for Thunderbird microstructure

EVAM Freq.	Hz	1000		
Stack Voltage	Volts, pp	400		
Ellipse Size	µm	22 x 4		
		Fore-ground	**Part**	**Back-ground**
Upfeed Velocity	mm/s	2.5	0.5	0.5
Depth of Cut (actual)	µm	~ 6	2.0	2.5
Theoretical Finish	nm, PV	12	0.5	0.5
Index Feed, F_i	µm	2.5	0.5	0 .5
Crossfeed Increment, F	µm	12.0	4.0	4.0
Theoretical Finish	nm, PV	18.0	2.0	2.0

was machined first to create a flat surface at a constant depth to begin the Thunderbird fabrication. The planned depth of the foreground was 1 µm but recurrent difficulty when touching off led to actual depths of up to 6 µm.

The machining parameters are shown in Table 2. To reduce machining time, and to provide a contrasting textured surface, the foreground was cut at a higher upfeed velocity and larger crossfeed increment. The diamond tool had a 1 mm nose radius, 0 degree rake face, and 10 degrees clearance angle. It was reconditioned and lapped prior to use on this project,

to assure a sharp edge. Lubrication was by mineral spirits manually applied to the workpiece (i.e. batch deposition, not continuous flow). The original air-bearing Y-axis was in place when these parts were made. Three "Thunderbirds" were machined, 2 with a foreground. Machining time per part was 29 minutes (foreground 7 minutes, feature 22 minutes).

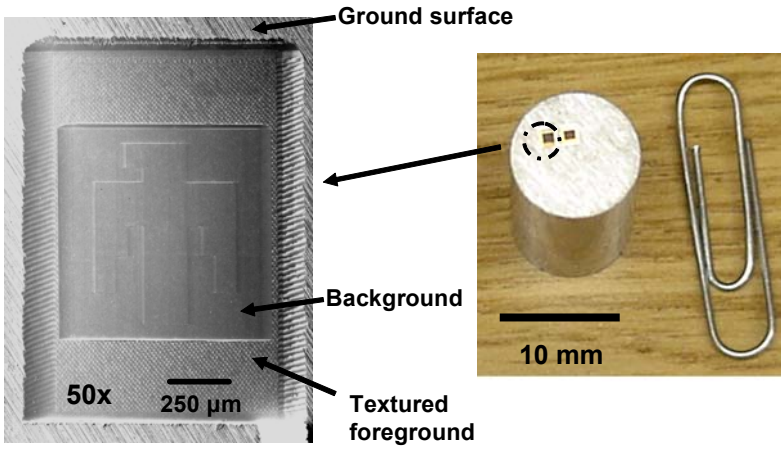

Figure 19. Thunderbird machined in 17-4PH stainless steel

Figure 19 shows an SEM image of one of the Thunderbirds. The difference in finish between the surface-ground raw material, foreground, and background and feature, is clearly visible. Figures 20 to 22 show white light interferometry of the Thunderbird surface. Figure 20 is an oblique view of the feature showing the length, width and depth (1.8 x 1.4 x 0.5 mm). Figure 20 shows a trace along the upfeed direction, with a PV surface finish of 60 µm and an RMS of 14 nm. This is a good surface finish but it should appear as a series of cusps with a spacing of 0.5 µm and a height of less than 1 nm. The profile shows much larger features that have been attributed to the vibrations of the air-bearing vertical slide. Figure 22 shows a similar trace but along the cross-feed direction of the Ultramill. Note the slightly larger vertical scale than in Figure 21. The profile shows a PV roughness of 157 µm and RMS finish of 24 nm. These profiles are typical of the surface of the three Thunderbird parts.

The upfeed and crossfeed surface finishes for the Thunderbird are comparable to the finishes achieved when machining copper using EVAM. For example, the large Angstrom symbol was also machined with a 1 mm nose radius tool. It had a surface roughness of 32 nm RMS (upfeed) and 26 nm RMS (crossfeed). Between the copper and stainless experiments the air-bearing Y-axis was reassembled to reduce the air film thickness and improve its stiffness. As a result, the numerically-superior finishes reported for 17-4PH may be the result of the different dynamic system and not any inherent machinability advantage.

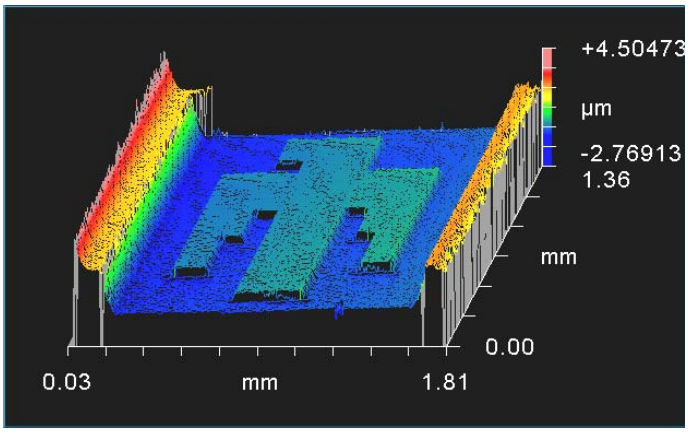

Figure 20. Oblique interferogram of Thunderbird feature

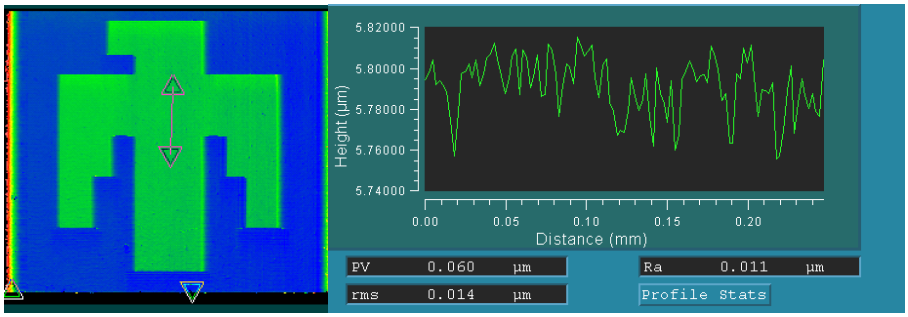

Figure 21. Interferogram showing surface finish of feature in upfeed direction (14 nm RMS). Upfeed spacing is 0.5 µm is too small to see on this profile which is 250 µm long

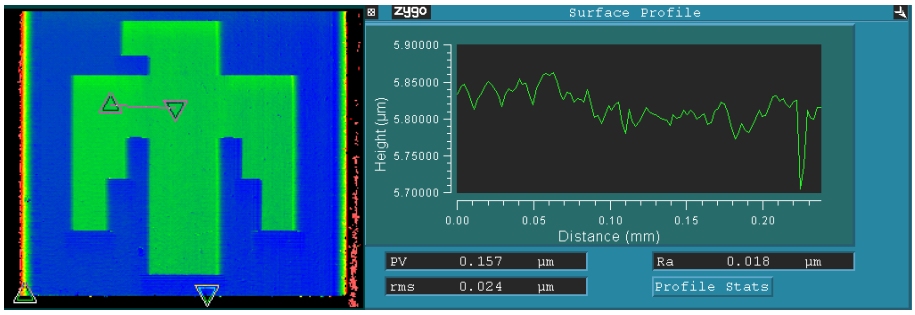

Figure 22. Interferogram showing surface finish of feature in crossfeed direction (24 nm RMS), Cross feed spacing is 4 µm which is too small to see on the profile which is 250 µm long.

The significant difference in surface finish, between observed values and theoretical prediction (see Table 2) is believed to be due to the low stiffness of the air-bearing Y-axis, which resulted in significant vibration of the slide in the Z-direction.

6.4.3 TOOL WEAR EXPERIMENT

Wear was to be evaluated by machining repetitive raster passes and accumulating distance on the tool. The 1 mm nose radius tool from the Thunderbird fabrication was used for the wear tests, after the microstructures had been machined. The tool was to be imaged at intervals (nominally 5, 10, 20, 50, and 100 meters of accumulated machining distance), to capture the onset and progress of wear on the tool edge. The wear testing was conducted with parameter values shown in Table 3.

Table 3. Machining Parameters for Tool Wear Test

EVAM frequency	1000 Hz
Stack Voltage	400 Vpp
Ellipse Size	22 μm x 4 μm
Upfeed velocity	3.0 mm/s
Depth of cut (programmed)	2.5 μm
Theoretical finish	1.8 nm, PV

However after only 6 meters cumulative distance, the diamond tool separated from the toolholder, ending the test. Acetone used to clean the diamond may have weakened the cement holding it to the toolholder. Also, the workpiece was found to have not been surface ground, only faced, meaning the diamond tool periodically traversed the ridges left over by the turning operation. Eventually a point was reached where forces caused by the high depth of cut apparently were great enough to cause the tool to separate from the toolholder.

Figures 23 shows SEM images of the tool after approximately 6 meters of accumulated machining distance. Figure 23(a) is a medium-angle view to show the cutting region of the tool and the estimated contact area for the programmed depth of cut. No wear is evident on the rake face in this view. The rake face-clearance face edge shows no signs of damage or deformation. Figures 23(b) and 23(c) are close-up views of the estimated portion of the tool in contact with the workpiece. Even at the higher magnification, no damage is evident on the rake face, and the clearance face behind the cutting region. The rake face-clearance face edge again shows no damage or deformation. On the clearance face, immediately behind the cutting edge, striations parallel to the upfeed direction, and other superficial markings can be seen. These are outside the expected contact region for a depth of cut of 2.5–3 μm. These marks are tentatively identified as superficial features arising from cutting oil stains and/or debris particles splashed on to the tool during cutting.

Cerniway machined W2 tool steel using conventional diamond turning and EVAM [7]. This steel is both harder and higher in carbon content than the 17-4 PH stainless steel. It was noted that conventional machining (40 m distance) produced fractured, irregular, damage to the cutting edge for. In comparison, EVAM created a smooth, beveled wear land and produced good surface finish even with tool wear (20 m distance, equipment problems thereafter end the test). This wear land is not visible on the tool in Figure 23. However after only 6 meters distance, it is not possible to say whether the stainless steel wear is following the EVAM pattern.

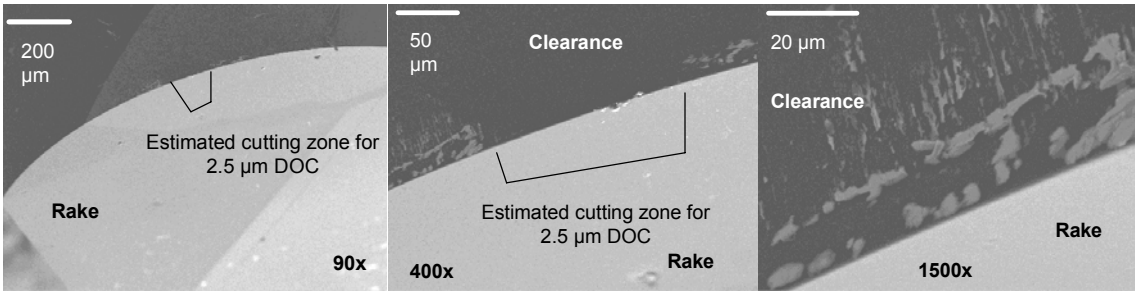

a) Orientation view (b) Close-up showing estimated cutting region (c) Detail of markings on tool

Figure 23. Detail of cutting region of diamond tool. Note lack of damage to rake face-clearance face edge. Marks and striations, just outside the nominal contact region, are believed to be superficial stains and/or debris particles adhering to the tool.

6.5 COMPLEX MICROSTRUCTURES

Figure 24(a) shows a contactor component for a micro-relay. The projecting pins visible in the SEM image are each approximately 150 µm in diameter, and are made of gold in a glass matrix. As a next project, the Ultramill will be used to machine the groove pattern shown in Figure 24(b) onto each pin. The purpose of the grooves is to provide relief space for submicron particles which might interfere with operation of the relay Each groove is 5 µm deep and 3 µm wide at the bottom, larger than a 1:1 aspect ratio. The grooves are on a side pitch of 13 µm. The sidewalls for the grooves have a sinusoidal profile. The central rib, between the two groove sets, also has a sinusoidal profile, created in the upfeed direction. All feature edges must be burr-free, to avoid interferences that might affect device operation.

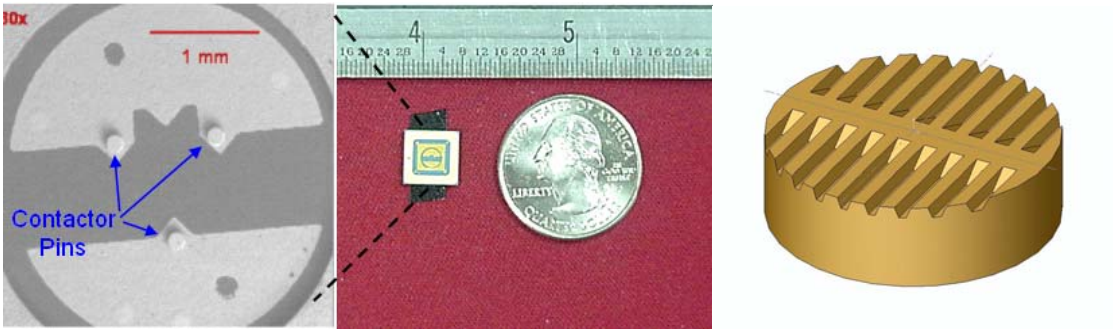

(a) Contactor element (b) Groove pattern

Figure 24. Microcontactor component with groove pattern to be machined by Ultramill onto contactor pins. Grooves are 5 µm deep and 3 µm wide at bottom. Groove sidewalls will have sinusoidal profile. Central rib will have sinusoidal profile in upfeed direction.

To machine the groove pattern onto the contactor pins using the Ultramill, two new challenges must be met:

- Tool geometry to create high-aspect ratio microstructures
- Precise XYZ location of the tool tip on the part, relative to an arbitrary feature or fiducial

6.5.1 TOOL GEOMETRY

Round-nosed tools of relatively large nose radius cannot produce closely spaced grooves and ridges. Such tools create curved sidewalls with low depth-to-width aspect ratios, intead of straight, near vertical walls.

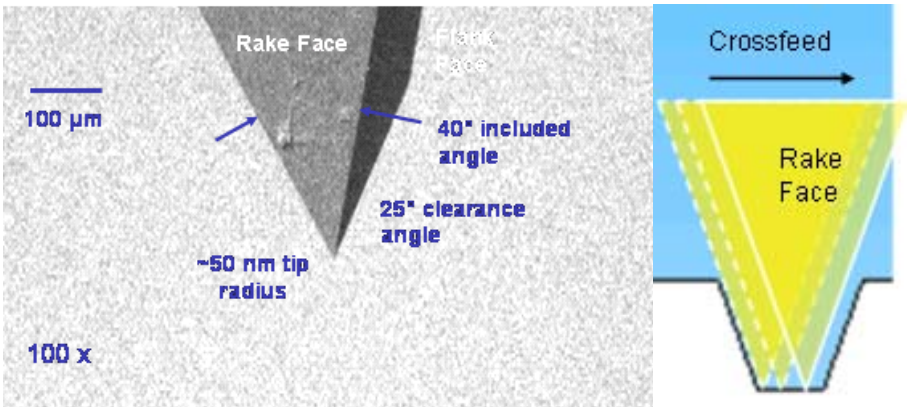

(a) Dead-sharp tool (b) Cutting high-aspect ratio groove

Figure 25. Sharp-nosed diamond tool

The “dead-sharp” diamond tool in Figure 25(a) will be used to machine the features on the micro-contactor. It has an included angle of 40 degrees, permitting straight sidewalls only 20 degrees away from vertical to be machined. This tool can be used to make deep, high-aspect ratio features, at closer side spacing than is achievable with round-nosed tools. Motion programs will need to be developed that provide Y and Z motions to produce the intended sinusoidal profile at the top portion of the sidewall.

It is anticipated that stresses in the tip of the dead-sharp tool will be greater than in a round-nose tool at equivalent machining conditions. Tool life and evenness of wear are therefore concerns. The flank edges will serve as cutting edges at an acute angle, so chip formation and extraction might differ from EVAM with round-nosed tools, with implications for surface finish. Groove cutting tests will therefore be conducted in aluminum or copper, prior to machining the contactor.

6.5.2 Precision Positioning of Tool at Part Location

For the Ultramill to be capable of machining functional features onto parts, it will need to capable of locating the tool tip at a precise location, relative to a fiducial or other part feature used as a reference.

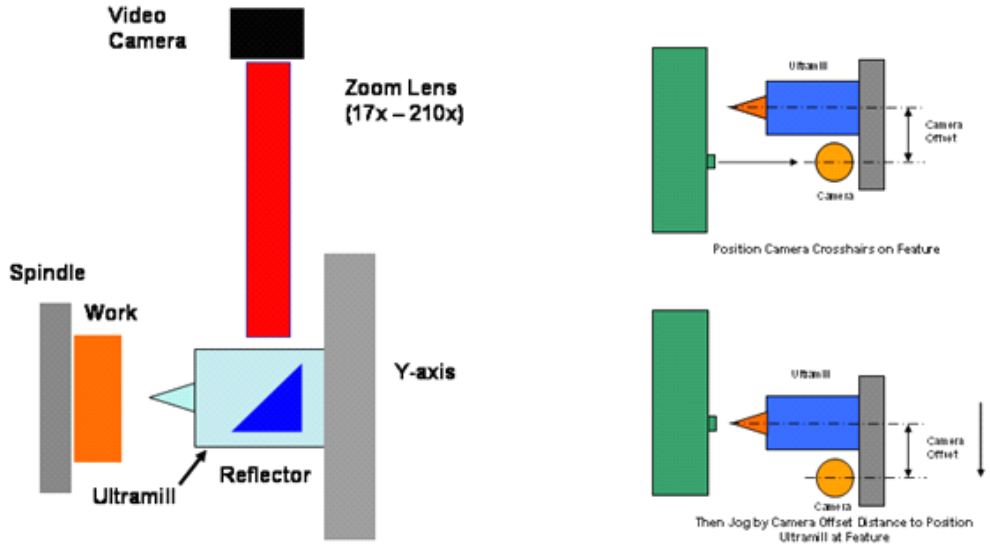

(a) Installation (b) Scheme of use

Figure 26. “Plan view” video microscope

A new “plan view” video microscope system will be installed on the Nanoform, to facilitate positioning the diamond tool at specified X and Y coordinates. Figure 26 shows the installation and scheme of use. The video microscope will be ttached to the Y-axis slide so that it moves with the Ultramill. The field of view is too small to show the tool tip at the same time as the desired feature. The working scheme will be to align the video microscope crosshairs on the location to be machined, then offset the system in X and Y coordinates to bring the diamond tool tip to the same coordinates. The offsets will be established each time the Ultramill and video microscope are set up on the Nanoform. This can be done by machining a short groove in a test piece, then bringing the crosshairs to the center of the groove and recording the displacement from the machining position.

The Z-direction coordinate origin is established by touchoff of the diamond tool to the workpiece. Touchoff is accomplished by monitoring the tool rake face with the side-view video microscope and incrementally jogging it toward the work surface. When the workpiece is prefinished to optical quality, the reflected image of the tool makes it easier to locate the tip position relative to the work surface. Touchoff is considered to occur when a chip is observed. In raster machining, at touchoff the tool is motionless in the upfeed and crossfeed directions, so the initial chip is very small-- often appearing as a rapid fleck only a few camera pixels wide.

Touching off the microcontactor pins will be more complicated than on previous Ultramill projects. The material is not reflective, so estimating the tip distance from the surface will be more difficult. More profoundly, the tip of the dead sharp tool is only about 50 nm in radius, much smaller than the video microscope resolution of ~10 μm. It may not be possible to confirm touchoff through observation of the tool tip.

An alternate approach in this situation will be to use the plan-view video microscope to look for an entry groove in the work surface. Even though the upfeed speed is zero, the tool is still moving along its elliptical path, and therefore creates a short groove whose length is related to the depth of cut by the dimensions of the toolpath ellipse. By measuring the groove length seen on the video display, it should be possible to estimate the depth of cut to an accuracy of roughly 1 μm. The estimated surface position can then be found by subtracting the estimated DOC from the Z-coordinate indicated by the Nanoform’s control system.

6.6 CONCLUSIONS

Surface Finish

- The Y-axis was upgraded from the original air-bearing unit to one with a hydrostatic oil bearing. The oil-bearing axis is stiffer in the Z-direction, resulting in an initial surface finish improvement in copper from approximately 19 nm RMS to 9 nm RMS. The best surface finish which can presently be achieved with the Ultramill is 40 to 60 nm PV.
- Single-groove cutting experiments were performed for upfeed values from 0.2 to 8 μm/cycle. The measured surface finishes are consistently greater than the theoretical prediction based on the tool and work motion. For upfeeds larger than 2 μm/cycle, peak-to-valley surface finish increases with increasing upfeed. When upfeed is below 2 μm/cycle, PV surface finish is in the range 40-60 nm.
- Depth of cut appears to have minimal impact on surface finish for ductile materials.
- When upfeed is less than 2 μm/cycle (the regime where most micro-structures will be machined) a small-amplitude vibration (10's of nanometers) appears to be the dominant cause of surface roughness.
- Tool sharpness and tool path deviation from the intended ellipse are discounted as explanations for the surface finish being consistently worse than predicted. A hypothesis based on minimum chip thickness and *spansipfel* concepts was able to provide simulated results consistent with roughness measurements. But these results require assumptions for cutting dynamics and minimum chip thicknesses that do not appear to be valid.

Materials

- Stainless steel is added to the range of materials for which the Ultramill has machined binary features. Parts have been created with an overall size of less than 1 mm, at near-optical quality finishes (15- 25 nm RMS). These parts were made with the original air-bearing Y-axis, and surface finish is expected to be improved when using the oil-bearing axis with greater Z-direction stiffness.
- The tool cutting edge showed no visible evidence of wear at 1500 x in the SEM, after 6 meters of machining stainless steel. However, the distance machined was insufficient to draw any conclusions about onset of tool wear.

High-Aspect Ratio Microstructures

- The Ultramill will next be used to machine a groove-ridge pattern with sinusoidal sidewall profiles, onto the pins of a micro-contactor.
- A dead-sharp tool with narrow included angle will be used create the grooves, which are only 3 μm wide and have an aspect ratio larger than 1:1.

- A plan-view video microscope will be added to the Nanoform, and used for accurate X-Y location of the tool on the part.
- The short groove made when the tool first contacts the workpiece will be used to confirm touchoff, and to establish the Z-coordinate origin.

6.6 ACKNOWLEDGEMENTS

This project was funded in part by the National Science Foundation under contract DMI-#042335, monitored by G. Hazelrigg.

Stainless steel machining tests, and the micro-contactor patterning project, were funded in part by Sandia National Laboratories (Albequerque, NM).

Diamond tools were provided by Chardon Tool (Chardon, OH).

REFERENCES

1. Brocato, B., "Micromachining Using Elliptical Vibration Assisted Machining", M.S. thesis, North Carolina State University, 2005

2. Negishi, N., "Elliptical Vibration Assisted Machining with Single Crystal Diamond Tools", MS Thesis, North Carolina State University, 2003

3. Garrard, K., MATLAB SLICER program, North Carolina State University, 2005

4. Arcona, C., pp. 106-117, "Tool Force, Chip Formation, and Surface Finish in Diamond Turning", PhD Dissertation, North Carolina State University, 1996

5. Shamato, E., Suzuki, N., Nakamura, A., Harada, K., Matsuo, M., Osada, M., "Ultrasonic Micromachining of Hardened Steel by Applying Ultrasonic Elliptical Vibration Cutting", IEEE International Symposium on Micromechatronics and Human Science, 2003

6. Ferguson Metals Corporation, Hamilton, OH, www.fergusonmetals.com

7. Cerniway, M., "Elliptical Diamond Milling: Kinematics, Force, and Tool Wear", MS Thesis, North Carolina State University, 2001

7 METROLOGY ARTIFACT FOR DYNAMIC PERFORMANCE EVALUATION

Karalyn Folkert
Graduate Student
Kenneth P. Garrard
Precision Engineering Center Staff
Thomas Dow
Professor
Department of Mechanical and Aerospace Engineering

Part acceptance based on dimensional inspection by comparison to tolerance specifications is influenced by the static and dynamic errors in the inspection instrumentation, typically a Coordinate Measuring Machine (CMM). Traditional calibration artifacts are used to determine static influences due to machine geometry. The goal of this project was to design and fabricate a calibration artifact that will test a CMM both statically and dynamically. The artifact developed is a diamond turned, electroless nickel plated, 17-4PH stainless steel ring gauge (6" ID, 8" OD, 1" thickness). Sinusoidal features (5µm amplitude) were machined on the inside and outside diameter (ID and OD) of the ring using a fast tool servo. The feature wavelength varies linearly along each surface between the longest wavelength (6.4 mm) and shortest wavelength (0.4 mm) without discontinuities. A reference flat was also machined on the ID and OD. The dynamics of a CMM under a specific set of measurement conditions can be found by computing a transfer function between a measurand of the ring gauge and the accepted "true" shape of the gauge. This allows an operator to devise a measurement strategy for a part that does not exceed the dynamic capabilities of the CMM and to predict the error and uncertainty in a measurement.

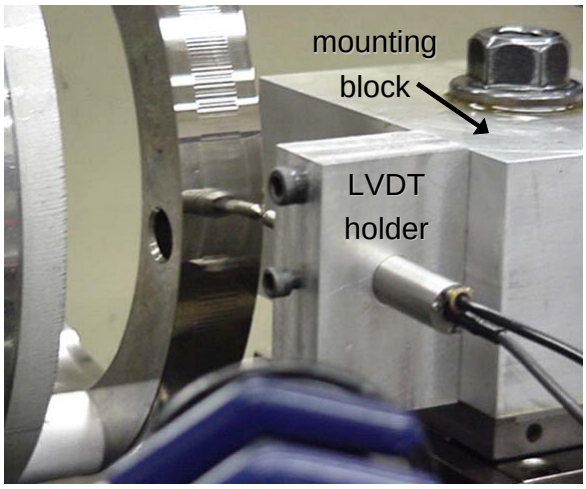

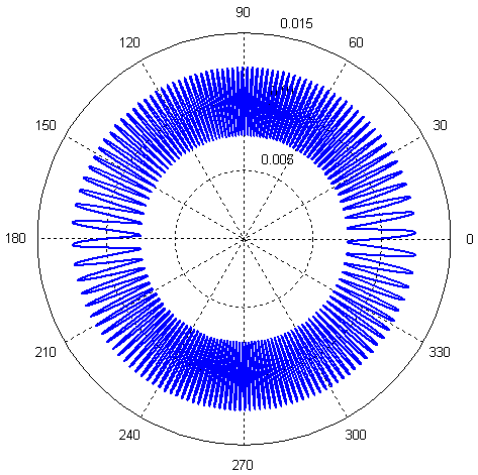

7.1 INTRODUCTION

The Y-12 National Security Complex manufactures precision workpieces for the government and private companies. Part acceptance is based on dimensional inspection by comparison to the tolerance specifications of the part drawing. In the past, Y-12 used specialized gauges such as a rotary contour gauge to measure a round part. Coordinate Measuring Machines (CMMs) are preferred because of their flexibility; yet this flexibility may make estimating uncertainty more difficult with additional input parameters defining the measurand. The goal of this project is to design and fabricate an artifact that can accurately predict the measurement uncertainty for a task, such as scanning around a workpiece, by determining a transfer function between the measurement and the artifact.

7.1.1 CALIBRATED ARTIFACTS

Since the shape of a part will influence the measurement error of that part, a standard of the same design measured prior to the part of interest will indicate where the greatest errors of the CMM measurement will occur and a correction factor may be applied. To address the measurement-specific errors, the artifact should be the approximate size and weight of a typical workpiece. Therefore, if boxes are to be measured, then a box of roughly the same size, shape and weight of the box to be measured should be calibrated. The artifact box or series of artifact boxes must exhibit the typical errors of the boxes to be measured to validate the machine capability relative to those types of errors. However, since a task-specific standard is not available for all manufactured parts, features need to be designed into an artifact to test the dynamic limits of the CMM to allow its characteristics to be defined. These features may simulate various conditions that the probe may encounter on a part. The shape of the artifact can be used to determine the static characteristics of the CMM. Some other major considerations for an artifact are ease of use, transportability, stability, time needed for calibration and ability to diagnose the error [3].

A number of artifacts have been developed to evaluate the performance of a coordinate measuring machine or to assist in its calibration [1,2]. These artifacts include gauge blocks [5], ring gauges, ball bars [6], hole bars [7], the ball and hole plate [4,8], the modular freeform gauge [10], and the multi-wave standard [11]. They may be used for a specific application or for a more generalized purpose. Artifacts may also be classified by the methods in which they are used to assess the accuracy of a CMM. These methods include the kinematic reference standard technique, parametric calibration technique, and transfer standard technique [9].

7.1.2 DESIGN OBJECTIVES

The objectives for the design of the CMM dynamic performance evaluation artifact are:

1) The artifact should be a standard shape (or several standard shapes) that can be measured on multiple machines to determine a transfer function between the artifact and the measurement.
2) Any spatial features on the artifact must permit probe radii of 0.25mm to 0.5mm to fit.
3) The artifact surface must be sufficiently robust that it is not damaged when used with various CMM probes, in either scanning or point-to-point inspection modes; probe forces may reach 2.5N.

7.2 ARTIFACT DEVELOPMENT

After considering the various artifact standards, a ring gauge was chosen for further development. The overall attributes of the ring gauge (outside diameter (OD), inside diameter (ID), and wall thickness) can be used to exercise multiple axes of a CMM. In addition, small features can be added to the ID and OD to assess the capability of the machine to deal with small temporal and spatial variations in surface features. The ring gauge can also be measured in different orientations and positions on the CMM to cover the entire working volume.

7.2.1 RING GAUGE GEOMETRY

The ring OD measures 8” (203.2mm) and the ID 6” (152.4mm) with an overall thickness of 1” (25.4mm). The dimensions are the approximate size of typical parts manufactured by the sponsor. The OD will have a groove that acts as a reference surface with the features being placed onto the ID. Figure 1 illustrates the dimensions and features of the ring.

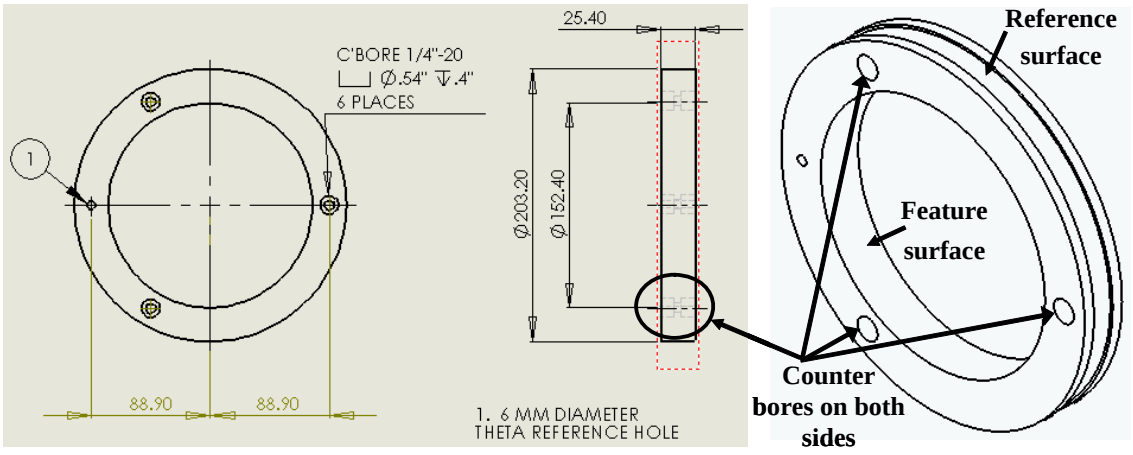

Figure 1. Ring gauge drawing and 3D image with dimensions.

Material The material chosen for the artifact was electroless nickel plated 17-4 PH stainless steel which was heat treated for maximum dimensional stability. Its coefficient of thermal

expansion is 10.8µm/m-°C or 6µin/in-°F or roughly half that of aluminum. The plating also adds to the microhardness of the stainless steel (44 Rockwell C, 430 Vickers); the actual quantity (500-700 Vickers) is dependant on the phosphorus content of the plating.

7.2.2 RING GAUGE SURFACE FEATURES

The small features on the surface should create a range of spatial frequencies for evaluation of the CMM performance in the dynamic environment. There a number of possibilities for types of features. Some of those include:

- A single frequency sine wave around the entire ring
- Addition of multiple single frequency sine waves
- Concatenation of single frequency sine waves
- A swept sine wave with varying frequencies

The analysis of such features will be discussed in the following section.

7.2.3 DYNAMIC ANALYSIS THEORY

Each of the potential features discussed above can be incorporated into the shape of a wave or combination of waves. A measurement of the feature is taken in time, or is in the time domain, which demonstrates the feature's apparent shape, but it is difficult to quantify the amount of error when compared to the true wave shape. Possible sources of error may be from a shift in the actual location of the wave with the correct magnitude or the measured magnitude may be incorrect. Either scenario will add to the overall error of the CMM, but the correction factors for each error may be different. Thus, it is important to separate the major source of error: magnitude or phase. A possible solution is to convert the time domain measurement to the frequency domain.

The desired feature is to be measured using different measurement speeds to expand the frequency range for dynamic analysis. One approach to analyzing the wave is to apply a Fast Fourier Transform (FFT) to the data set. By knowing the measurement speed, the sampling rate, and the spatial wavelength of the wave, the measurement can be placed in the frequency domain; the FFT converts the time domain measurement into the frequency domain. An FFT may be used to determine other frequencies present in a data set that would normally not be apparent in the time sampled measurement.

Single Frequency Sine Wave If a Fourier transform is performed on a 6 Hz sine wave with an amplitude of 4, the frequency spectrum will indicate the only non-zero magnitude at 6 Hz with a value of 4. Since the sine wave signal is composed of the real (cosine) component only, the phase lags by 90°; thus, the phase is equal to -90° at 6Hz. Figure 2 demonstrates these attributes.

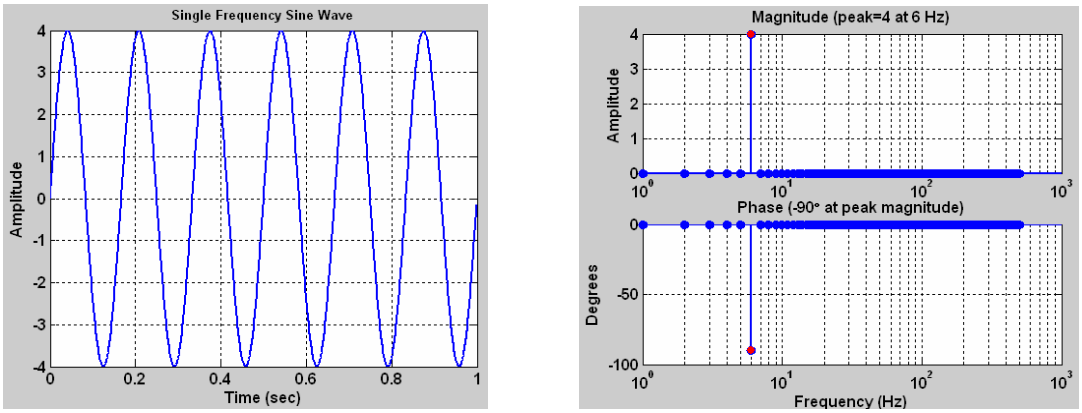

Figure 2. 6 Hz sine wave (left); FFT frequency response with peak magnitude of 4 and -90° phase at 6 Hz (right).

If any phase was added to the sine wave in Figure 2, the additional phase would be apparent on the phase plot. A phase shift of 45° to the right (delaying the sine wave in time from the reference cosine wave) increases the phase value to -135°.

A single wavelength sine wave measured with multiple speeds would create the range of frequencies necessary to determine the dynamic characteristics of the CMM. However, a considerable number of measurements would be required to produce a valid transfer function.

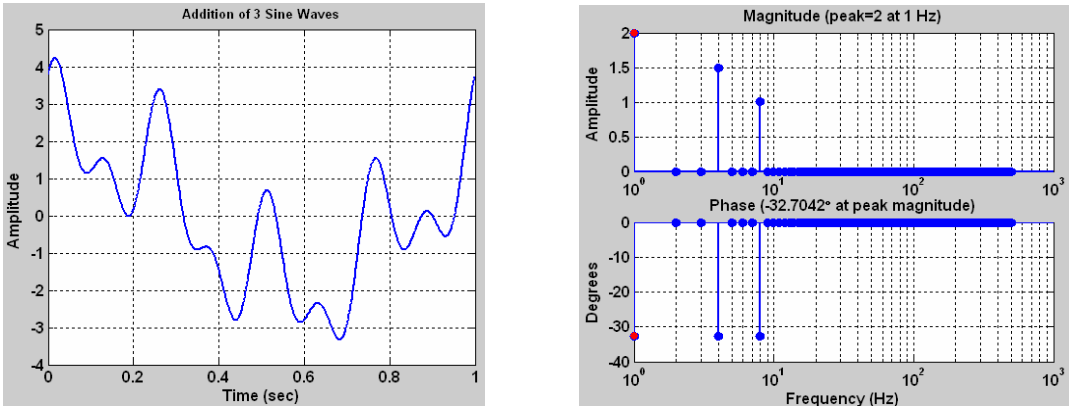

Figure 3. Addition of multiple sine waves (left); FFT frequency spectrum (right).

Multiple Single Frequency Sine Waves Consider a signal with 3 separate single frequency sine waves added together (Figure 3). The frequency spectrum indicates that the first sine wave is 1Hz with an amplitude of 2, phase shifted to the left by 57.3° to produce a value of -32.7°.

The second wave is 4 Hz, has amplitude of 1.5 and has also been shifted to the left to give a phase value of -32.7°. The final wave is 8 Hz with amplitude of 1 and -32.7° of phase.

The addition of multiple single frequency sine waves is the concept behind the multi-wave standard [11]. Multiple waves increase the number of frequencies for evaluation but it still requires an assortment of measurements to calculate a conclusive transfer function. The time domain signal is also difficult to interpret in terms of shape.

Swept Sine Wave One method to acquire a wider frequency range is to generate a swept sine wave. A swept sine wave is a sine wave with a continuously varying wavelength; each point on the swept sine wave is a different wavelength. For the ring gauge, the wave begins at a long wavelength and progresses to a short wavelength in the first 90 degrees. To produce a continuous wave, the wave is "flipped" to line up with the last wave and then the wavelength increases to the starting point as it reaches 180 degrees. From 180 to 360 degrees, the wave is a mirror image of the first 180 degrees. Four quadrants of the same wavelengths allow a smaller section to be measured. Figure 4 illustrates these features.

The allure of the swept sine wave is that it contains a wide range of wavelengths. Different measurement speeds widen the frequency range for the transfer function while the spatial wavelength remains the same. The swept sine wave creates a frequency-rich environment such that the dynamics of the CMM can be seen. The linear swept sine wave from 0-90º is given by Equation 1.

$$y = A \cdot \sin\left(\frac{2\pi t}{L}\left(\frac{d}{L}t + f\right)\right) \qquad (1)$$

where A is amplitude, t is circumferential distance, d is the modulation parameter and f is the base frequency.

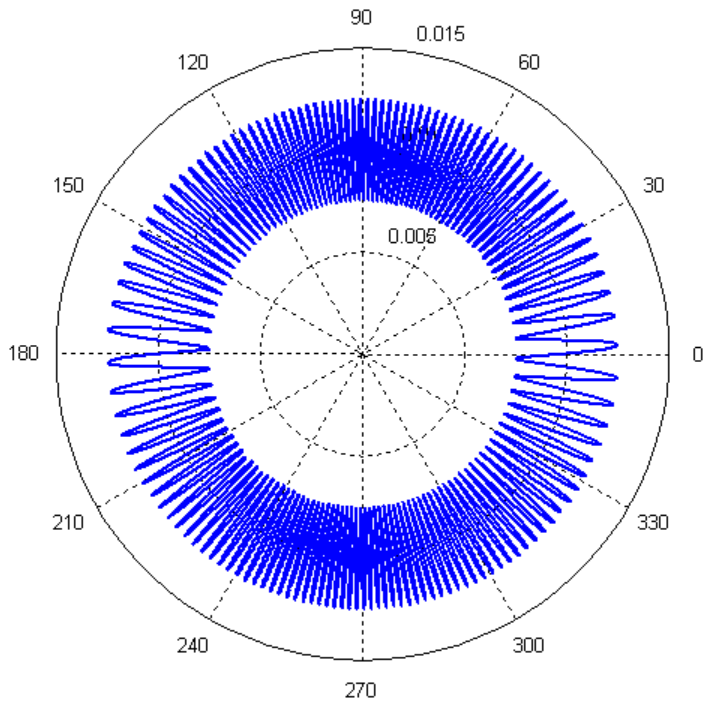

Figure 4. Swept sine wave on the OD/ID of the ring.

The swept sine wave can assess the capability of the CMM to respond to small surface anomalies and to characterize the dynamic

performance of the CMM as it traverses the varying wavelength features. Depending on the radius of the probe, measurement speed, radius of the part and size of features, the ability to detect small perturbations changes. If a small-radius probe was used to measure a part with small anomalies, the question arises of how the overall measurements would be affected. The different frequency of each wave creates a multitude of values to be evaluated which approximates different size features. The potential spatial wavelength of the entire feature may range from 1/4" (6.35mm) to 1/80" (0.317mm). (The smallest wavelength was selected to allow a 1 mm diameter probe to fit into the valley of the wave.)

Swept Sine Wave Excitation The values of the swept sine wave were produced based on a minimum and maximum spatial wavelength. Because the wavelengths can be considered as individual frequencies, an FFT can be performed on the data set. With sampled data, the units on the frequency spectrum plot are in terms of Hertz. However, with the generated spatial data, it is more useful to plot the results in terms of wave numbers[1]. The wave number is the reciprocal of the spatial wavelength. Figure 5 shows the FFT of the first quadrant of the ideal wave for the ID. The magnitude is largest near the shortest wavelength at wave number 223/λ which translates to a wavelength of 0.537µm. The phase values accumulate for half of the wavelengths and then returns to zero.

Figure 6 represents the FFT of the "perfect" swept sine wave. The swept sine wave was generated with a maximum amplitude of 5µm and 20,000 points. The plot indicates a maximum magnitude of 0.342µm and 90° phase at wave number 32.5/λ; although the magnitude looks relatively constant, every other value (or half of all values) is zero. The small magnitude is due to each wavelength occurring at exactly 4 samples and nowhere else in the continuously swept waveform. The phase is also alternating from +90° to 0° to -90° and vice versa. This is due to the repetition of the individual frequencies in each quadrant; the location of each wavelength is shifted by 90° from the previous location.

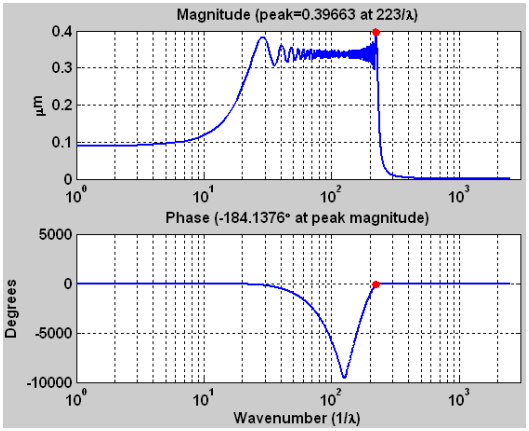

Figure 5. FFT of the first quadrant of the swept sine wave on the ID.

[1] The number of waves per unit distance (quarter of the circumference of the ring).

The FFT of the swept sine wave is difficult to interpret as compared to a single frequency sine wave due to the constantly varying nature of the wavelength. Rather than strictly interpreting the FFT and directly comparing it to an FFT of an actual measurement, the data analysis may be simplified. A CMM has dynamic characteristics that will influence the overall measurement of the artifact. Since the swept sine wave on the surface of the ring is known and the CMM measurement will generate another data set, the CMM's dynamics, or transfer function, may be found using a form of deconvolution [12]. Convolution in the time domain is the multiplication of the swept sine wave and the impulse response of the dynamic system to construct an output that shows the influence of these dynamics. Since the dynamics of the CMM are not known, the inverse of convolution, or deconvolution, is used; the CMM measurement is divided by the accepted swept sine wave. To expedite calculations, deconvolution may be executed in the frequency domain. The magnitude and phase components in the frequency domain are separated to create a Bode plot of the CMM's dynamics. Figure 7 denotes a theoretical dynamic system. Multiple measurements with different speeds will create the desired frequency range of the Bode plot to determine the natural frequency of the system.

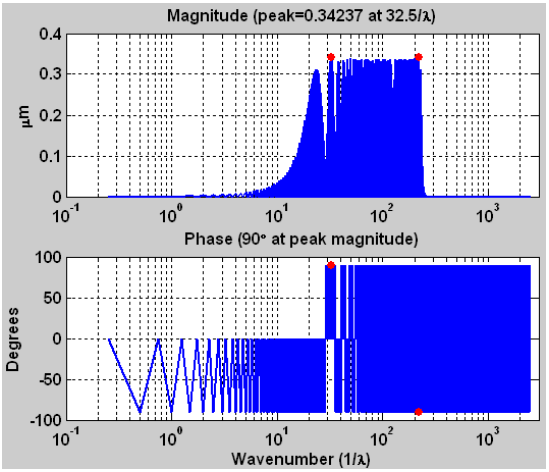

Figure 6. FFT of swept sine wave with maximum amplitude of 5μm and 20,000 points.

The transfer function of the CMM provides a significant amount of information about the machine. It specifies the natural frequency as well as the machine's performance within a frequency range. If a measurement speed is specified, the speed may be converted to frequencies present in the swept sine wave data and an appropriate CMM operating speed determined based on the transfer function and an acceptable amount of error. One measurement speed may correspond to the window illustrated in Figure 7. The actual measurement in the time domain should look similar to Figure 8. The figure shows the ideal swept sine wave with the anticipated swept sine wave measurement using the specified measurement speed on top of the ideal wave.

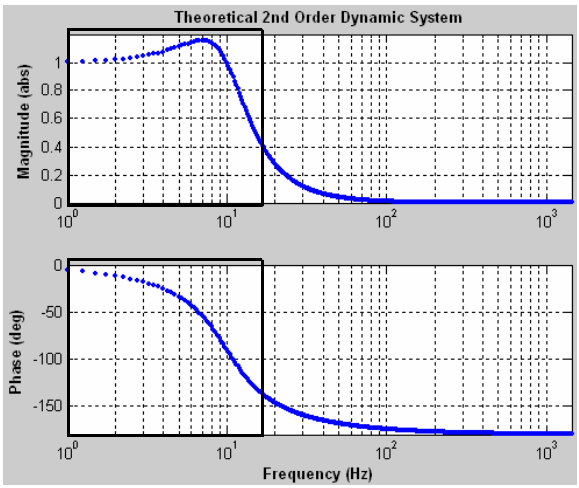

Figure 7. Theoretical second-order system.

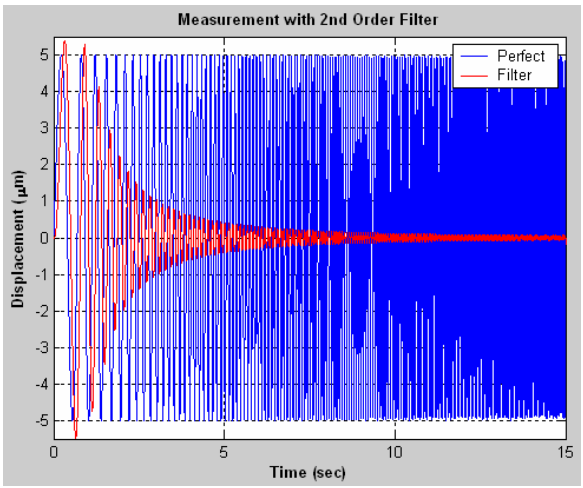

Figure 8. Simulated time response.

The Bode plot (Figure 7) suggested that the measurement would indicate an increased amplitude of the wave at the lower frequencies before it decreased when the natural frequency of the system was reached; the measurement should include some phase from the beginning. These attributes are observable in the time domain plot of Figure 8.

7.3 ARTIFACT FABRICATION

A Fast Tool Servo (FTS) was used to machine the swept sine wave on the ring. The piezoelectric stacks of the FTS are excited by the signal from a high voltage amplifier. The frequency and voltage signal affect the movement of the tool on the FTS. Any unexpected vibration of the tool would change the amplitude of the wave. Therefore, it is important to know the natural frequency of the FTS. To find the open loop characteristics, a Stanford Signal Analyzer was used to generate a sine wave that sweeps through a range of frequencies. The output from Stanford was sent to dSPACE. dSPACE is a data acquisition system that facilitates the input and output of a Simulink control model. In dSPACE, the wave was offset to make it entirely positive because the piezoelectric actuator cannot handle a negative voltage. The modified signal entered the high voltage amplifier where the signal was multiplied by 100 to drive the FTS. A capacitance gauge captured the output of the servo and that was recorded by Stanford. The swept sine wave began

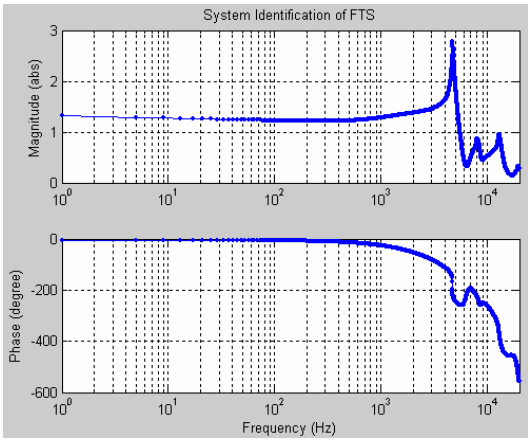

Figure 9. Open loop characteristics of the FTS.

at 1Hz and ended at 7000Hz. The amplitude magnification of the open loop system dynamics (Figure 9) begins around 600Hz and continues up to the natural frequency. The fabrication of the wave on the ID will occur below 600Hz.

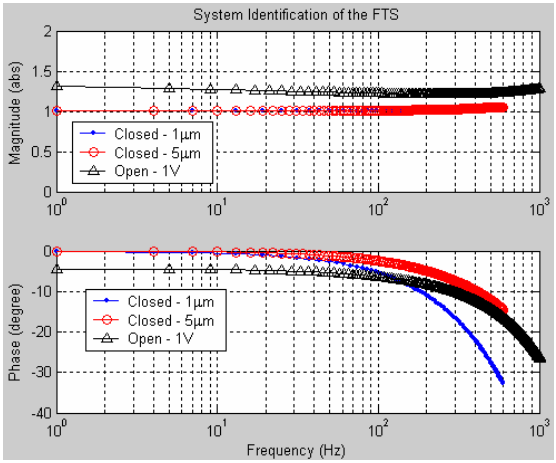

Figure 10. Comparison of closed and open loop system identifications up to 600 Hz.

7.3.1 CLOSED LOOP CONTROL

Feedback control can correct for position error at low frequency. The closed loop controller uses feedback from the capacitance gauge position sensor along with a proportional-integral (PI) control algorithm to correct position error. Gains are selected to shape the response of the system, to prevent overshoot and to correct for the following error. The final gains for the controller were chosen based on the production of the quickest response of the system without introducing instability and the realization of a constant magnitude over the operating frequency range of the FTS.

Figure 10 shows the closed loop system response with the optimized PI controller as compared to the open loop response and also demonstrates the change in the transfer function with input amplitude. The "circles" and "dots" in the figure correspond to the closed loop response using two different amplitude inputs, 5µm and 1µm respectively; the "triangles" relate to the open loop response with approximately the same input as the 1µm input of the "dots." The magnitude remains constant in the operating range of interest in all responses. For the 1µm input, there is less phase lag at low frequency but it becomes larger than the open loop value for frequencies greater than 100 Hz. For the desired amplitude of 5µm, the phase and magnitude of the closed loop system are consistently better than the open loop system.

7.3.2 DECONVOLUTION

Although the system dynamics of the FTS have improved with closed loop control, there is still significant phase error in the system at higher frequencies. Since the FTS will operate at close to 600 Hz, deconvolution is applied to the swept sine wave before it is input into the controller. Deconvolution uses the magnitude and phase characteristics of the FTS with the information of the desired wave output to adjust the amplitude, phase and shape of the command signal. Deconvolution is the complex division of the desired output over the frequency response of the system [12]. Thus, it alters the input to produce an expected output.

The deconvolution algorithm is applied in a series of steps. The first step is to determine the transfer function of the closed loop system. The transfer function was captured via LabView. A starting and ending frequency (Hz) and number of points for the sweep were specified. The voltage was sent out through LabView to the high voltage amplifier where it was input into the FTS. The closed loop system of the FTS was controlled by the dSPACE hardware. The transfer function of the closed loop system up to 800 Hz is shown in Figure 11 with a linear frequency axis. The real and imaginary components (complex values) of the system were captured and converted into magnitude and phase. After the complex values of the system transfer function are captured, they are interpolated to match the frequency step size of the FFT of the desired swept sine wave.

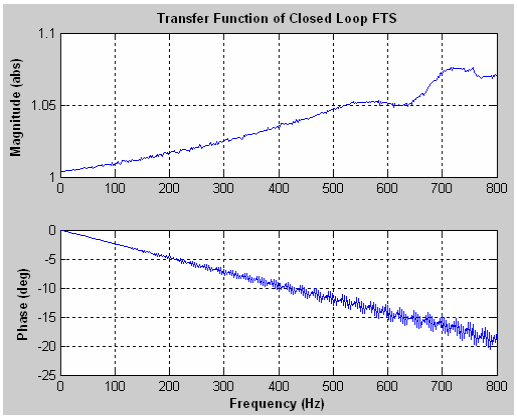

Figure 11. Closed loop FTS transfer function up to 800 Hz.

The complex values with their conjugates were interpolated again to increase the frequency range of the transfer function. Since deconvolution is implemented in the Fourier domain as element by element division of two vectors, the numerator and denominator must have the same length (number of samples) and units (frequency increment). The generated swept sine wave contains 20,000 points; so, the frequency content of the transfer function (including the complex conjugate) must contain 20,000 points as illustrated in Figure 13. When the frequency range is extended, the response inside the gap between the original response and its conjugate is unknown. The straight line links the separated responses with their last value, creating the correct frequency content. Expanding the range of the system transfer function increases the sample rate to match the sample rate of the input signal [12].

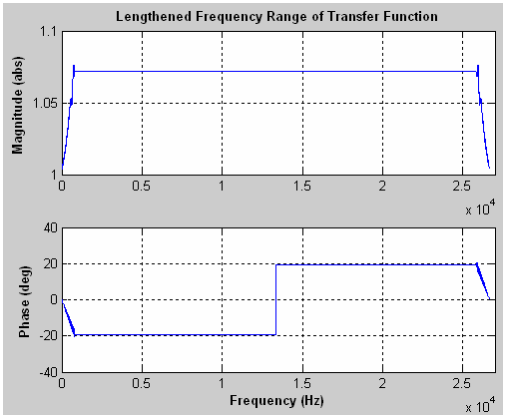

Figure 12. Frequency range of transfer function increased.

The next step in the deconvolution process is to take a Fourier transform of the desired output signal and divide by the transfer function in Figure 12. An inverse FFT is taken of this quantity to convert the signal back into the time domain. The result produces the adjusted input command for the controller. Figure 13 demonstrates the adjusted amplitude as the frequency of the wave changes. The maximum input command never reaches the full desired amplitude and is less at the highest frequencies due to the dynamics of the FTS. Figure 14

exhibits the phase lead of the input command signal to compensate for the phase lag of the system, especially at the higher frequencies. The wave with dots (adjusted) is commanded prior to the desired wave as represented by the time of each zero-crossing.

Deconvolution in combination with closed loop control greatly decreases the error in the fabrication of the swept sine wave. Much of the error in the closed loop controller alone is due to phase lag (16˚ at the highest frequency); whereas with the open loop system, the error is a combination of the phase lag and magnitude. Figure 15 demonstrates the decrease in error from open loop (left) to closed loop (middle) to closed loop with deconvolution control (right). The top subplots illustrate the system response as the bottom subplots show the difference between the desired and actual responses or the error. The error has been reduced from ±3 µm to ± 0.3 µm with deconvolution.

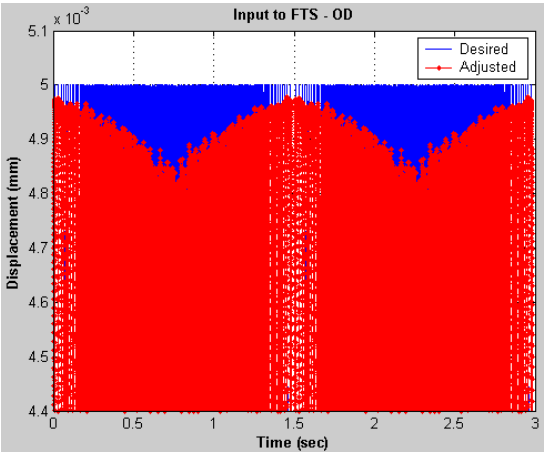

Figure 13. Expanded section of adjusted input (dots) to demonstrate altered amplitude; time relates to spindle speed.

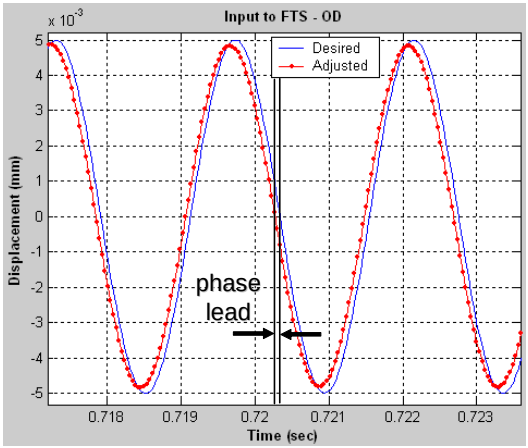

Figure 14. Expanded section of adjusted input (dots) to show phase lead and amplitude reduction of input signal.

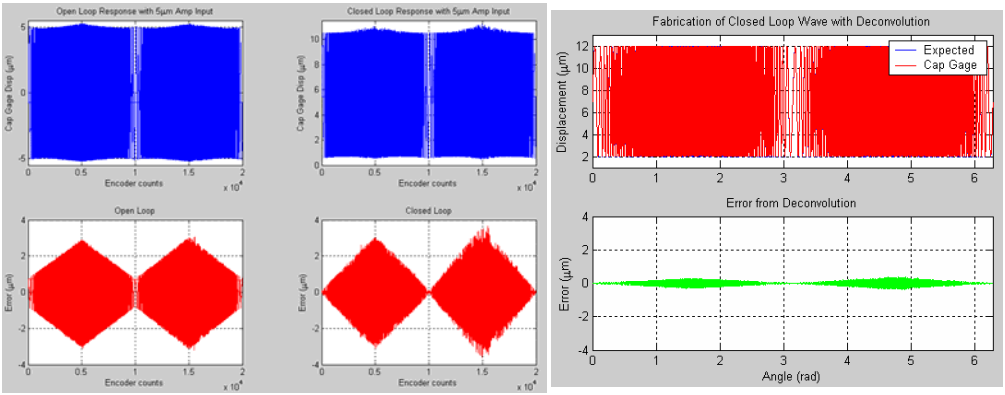

Figure 15. Reduction in following error at high frequency using deconvolution.

7.3.3 PREPARATION FOR FABRICATION

A water jet with garnet particles was used to rough machine[2] the 17-4PH rings leaving 0.100 inch excess stock on all surfaces. The rings were solution annealed[3] to relax internal stresses. The rings spent 1.5 to 2 hours residence time in an air furnace at 1900°F (1038°C) ± 25°F and then were air cooled. The annealed rings were finish machined[2]. The 45° chamfers were added to the counter bores, and the rings were machined to a 64 µin CLA surface finish and cleaned with a solvent.

The final heat treatment[3] of the rings involved aging in a vacuum furnace for 4 hours at 900 - 940°F (482 - 504°C), followed by cooling in a vacuum to below 150°F (65°C). The last step was a cycle stabilization process in a cam-controlled oven. The rings were heated up to 250°F then cooled to -50°F. The successive temperatures in the cycle were 200°F, 0°F, 100°F, and 25°F. The cycle stabilization is intended to give maximum dimensional stability to the artifact.

After the rings were heat treated, they were plated with electroless nickel[4]. Two of the existing through holes were tapped for 5/16”-24 threads for fixturing of each ring during plating. The final thickness of the electroless nickel is 0.006” or 150µm.

[2] Weststar in Holly Springs, NC

[3] East Carolina Metal Treating in Raleigh, NC

[4] Corning Net Optics in Keene, NH

7.3.4 FABRICATION

Machining the Ring Faces The disk with spacers shown in Figure 16 was mounted to the chuck on the DTM and held by 20 in Hg of vacuum. The bolts attaching the spacers to the disk were tightened before mounting. After the disk was secured on the chuck, it was centered using a lever-type electronic gauge to within 40 µm.

The next step was to machine the spacers flat. The FTS was secured on the x-axis and was aligned to be perpendicular to the surface of the spacers. A 2.4 mm radius diamond tool was used to machine the spacers. The tool traversed across the surface while the spindle was rotating 250 RPM counterclockwise. A higher spindle speed with the larger radius tool created oscillation of the tool with the interrupted cutting of the spacer lands. A total of 15 µm was removed from the surface in two machining passes. The ring was mounted to the spacers using lubricated bolts and spherical washers. The bolts were loosely tightened so that the ring could be centered on the spacers. After centering, 5in-lb of torque was applied to each bolt.

Another tool post with a smaller radius diamond tool (1 mm) was used to machine each ring face as shown in Figure 16. The tool post was attached to the x-axis and the tool was adjusted to be perpendicular to the ring surface.

The tool traversed across the surface at a feed rate of 4.47 mm/min with a spindle speed of 500RPM counterclockwise. The higher spindle speed reduced the amount of time of the interrupted cut across the counter bores and reduced tool oscillation. The first few machining passes took off an excess Ni layer (~0.001" or 25 µm), which made it level with the rest of the face. The remaining passes used a 5 µm depth of cut and took off a total of 45 µm of Ni.

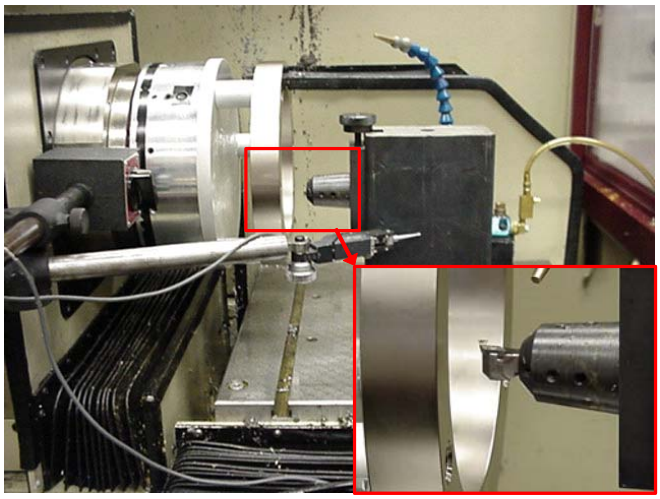

Figure 16. Setup to machine each ring face flat.

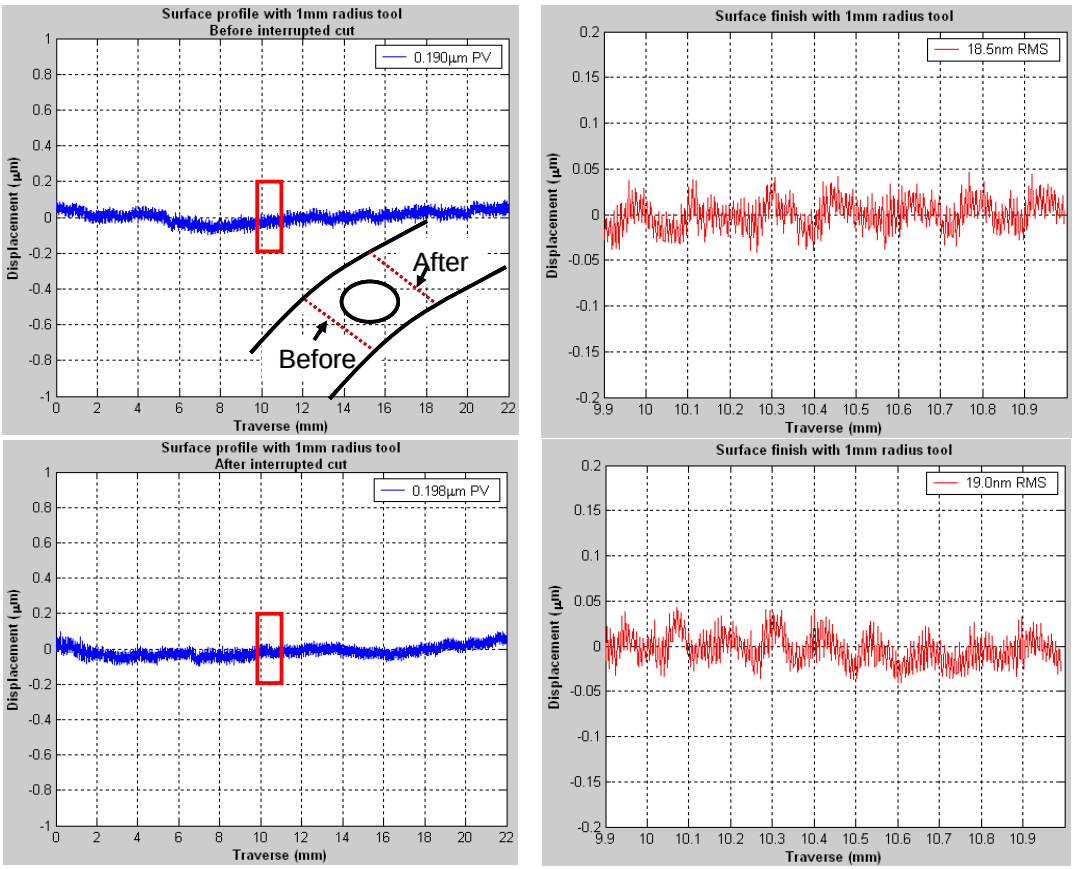

Figure 17. Surface roughness of machined face before (top) and after (bottom) interrupted cut.

After the ring face had been machined flat, it was removed from the spacers and measured with the profilometer. The probe measured 22 mm across the surface at locations before and after (see inset in Figure 19) the interrupted cut over the counter bores. The surface finish is approximately 19 nm RMS while the surface profile measures 0.194 µm PV, which will be sufficient to be used as a datum surface. Figure 17 also demonstrates the uniformity of the tool depth before and after the counter bores, indicating a lack of tool oscillation. The left image exhibits the entire surface profile while the right image displays a small (~1 mm) section of the surface which was used for the surface finish calculations.

After the profilometer measurements, the ring was flipped over and attached to the spacers. The ring was centered to within ±20 µm on the OD. 5 in-lb of torque was applied to each bolt. The spindle rotated at 500 RPM counterclockwise with the 1mm diamond tool traversing across the face at a rate of 4.40 mm/min. 33 µm of material was removed from the Ni surface. The surface of the ring face was measured using a profilometer. The surface finish averages 18.5 nm RMS while the surface profile measures 0.170 µm PV (see Figure 18).

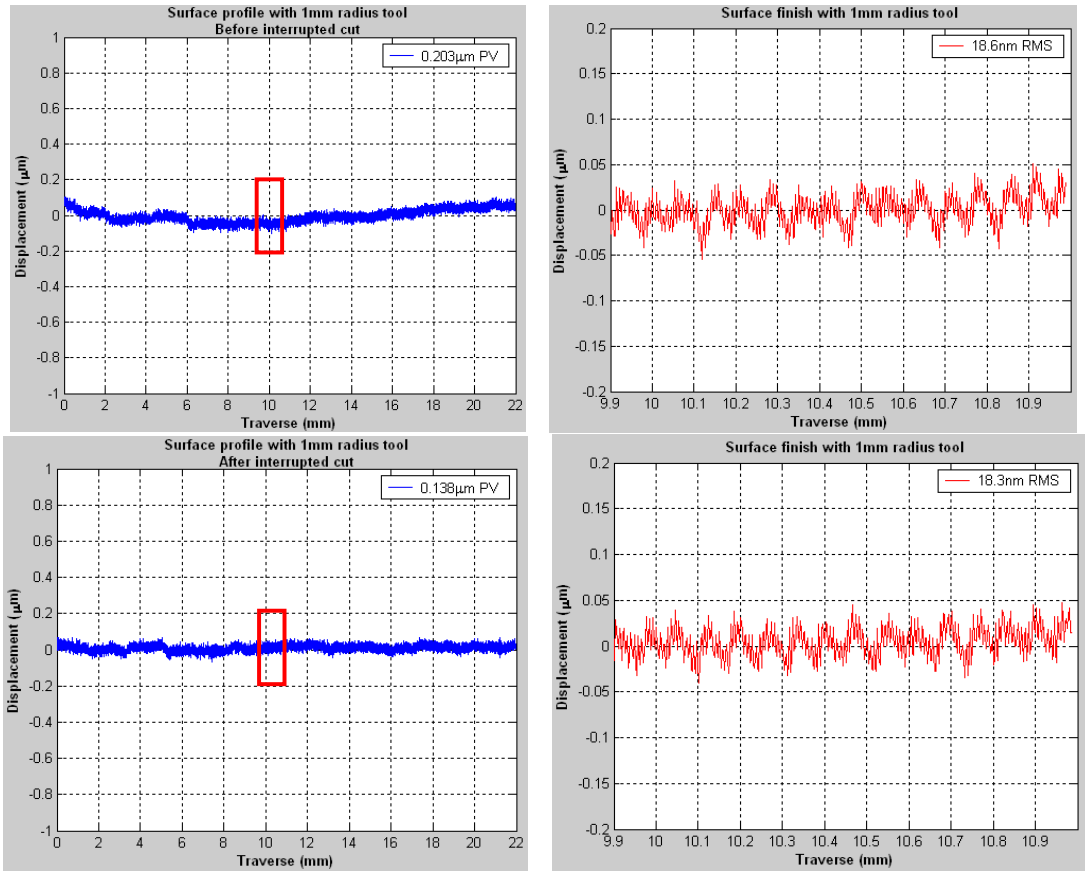

Figure 18. Profilometer measurements of second machined face of the ring before (top) and after (bottom) interrupted cut.

Machining the Ring ID The ID was to be cut before the OD as shown in Figure 19. The mounting block holding the FTS was rotated, and the x-axis was moved as needed to position the servo inside the ring. The lever-type electronic gauge head was shifted to the side of the spindle to measure the side of the mounting block. The mounting block was positioned to ensure the tool was perpendicular to the ID surface. Over a traverse of 35 mm, the gauge head displaced 1µm.

The cap gauge in the back of the FTS has a range of 20 µm. Since the swept sine wave measures 10 µm peak-to-valley, the cap gauge was positioned near the middle of its range.

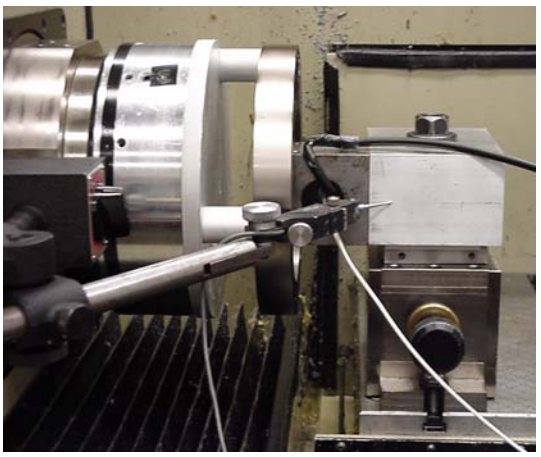

Figure 19. Measurement of the squareness of the tool to the ID.

The swept sine wave was machined onto a 10 µm raised portion on the ID and OD to allow probe access to the bottom of the sine wave. The DTM spindle was rotated 20 RPM clockwise with closed loop speed control provided by dSPACE. Two machining passes at 9 µm and 1 µm were performed. A cap gauge measurement of tool displacement of the FTS demonstrates the slight difference in the shape of the wave from one rotation to the next due to encoder interpolation. Figure 20 shows three measurements during the wave cut; only when expanding a single wave is the difference in the interpolated waves apparent.

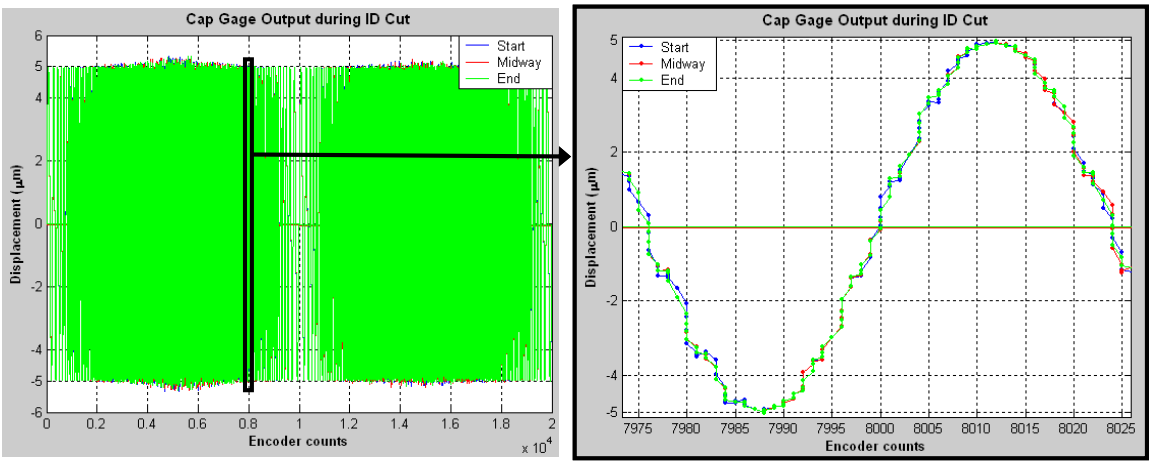

Figure 20. Cap gauge captures of the swept sine wave cut on the ID.

Machining the Ring OD After the swept sine wave was cut on the ID, the FTS was positioned for machining the ring OD. Following the surfacing of the OD with ten 5 µm deep passes, a 20 µm raised section was formed on the OD using three machining passes with depths of cut of 10 µm, 9 µm, and 1 µm.

The swept sine wave was machined onto the raised section at a controlled spindle speed of 20 RPM in two machining passes (9 µm and 1 µm). The cap gauge signal during cutting was recorded by the dSPACE. Figure 21 shows three captured data sets; the encoder interpolation effect is again noticeable when focusing on a single wave. The error in the amplitude at the highest frequencies on the OD is approximately 10% whereas it was ~5% on the ID due to the higher operational frequency of the FTS on the OD.

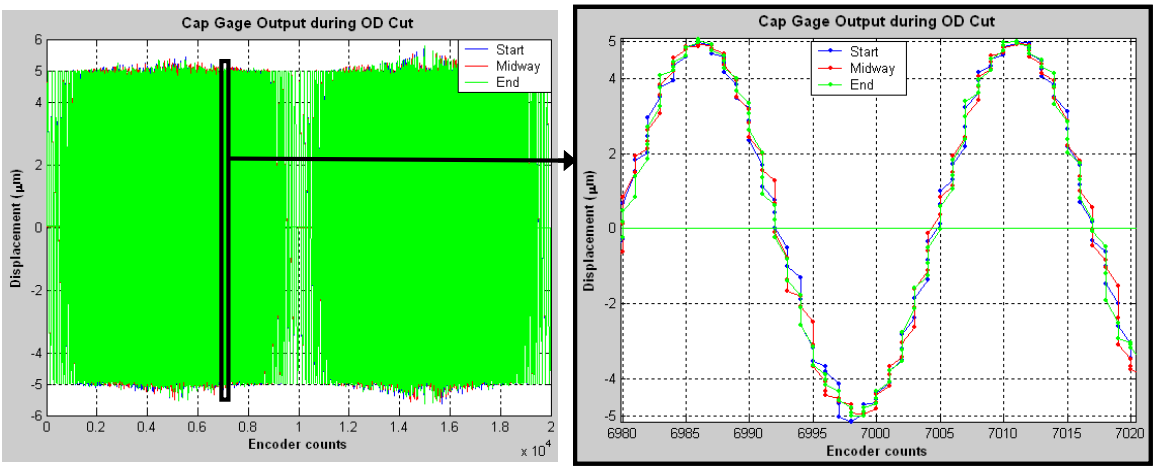

Figure 21. Cap gauge captures of the swept sine wave cut on the OD.

7.3.5 LVDT MEASUREMENT

Following the fabrication of the swept sine wave on the ID and the OD, the wave feature and the fiducial were measured with the ring mounted on the DTM. The FTS was removed from the mounting block where it was replaced with a holder for the LVDT. The LVDT slid into the hole of the holder and was held by a set screw. The building air was used as the supply for the air bearing. Figure 22 illustrates the LVDT mounting on the DTM.

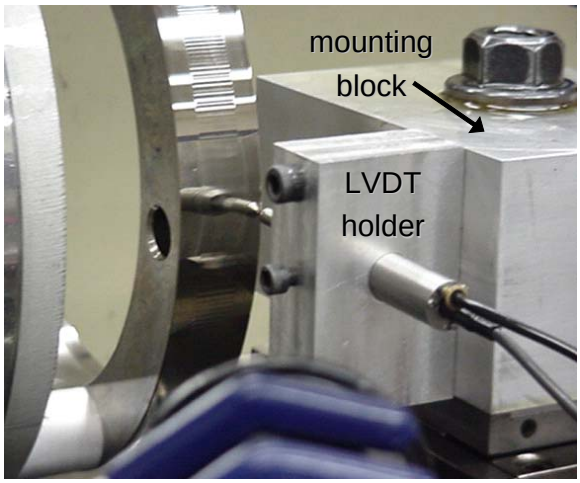

Figure 22. Set up for the LVDT measurement of the wave.

Swept Sine Wave Measurement The flat section on the OD of the ring was measured first to determine the ring's position on the spindle so that any off-center and out-of-round characteristic could be removed from the swept sine wave measurement. Thus, the probe was situated near the edge of the ridge while fully on the wave. The spindle speed was controlled using the dSPACE at 0.5 RPM counter clockwise. Approximately 2 rotations of the spindle were captured during each measurement of the wave feature. After a measurement was taken, the probe was incremented 1 mm, resulting in a total of 12 measurements taken across the OD. An additional 12 were taken across the ID along with a measurement of the its flat section.

7.3.6 COMPARISON AND VERIFICATION OF MEASUREMENTS

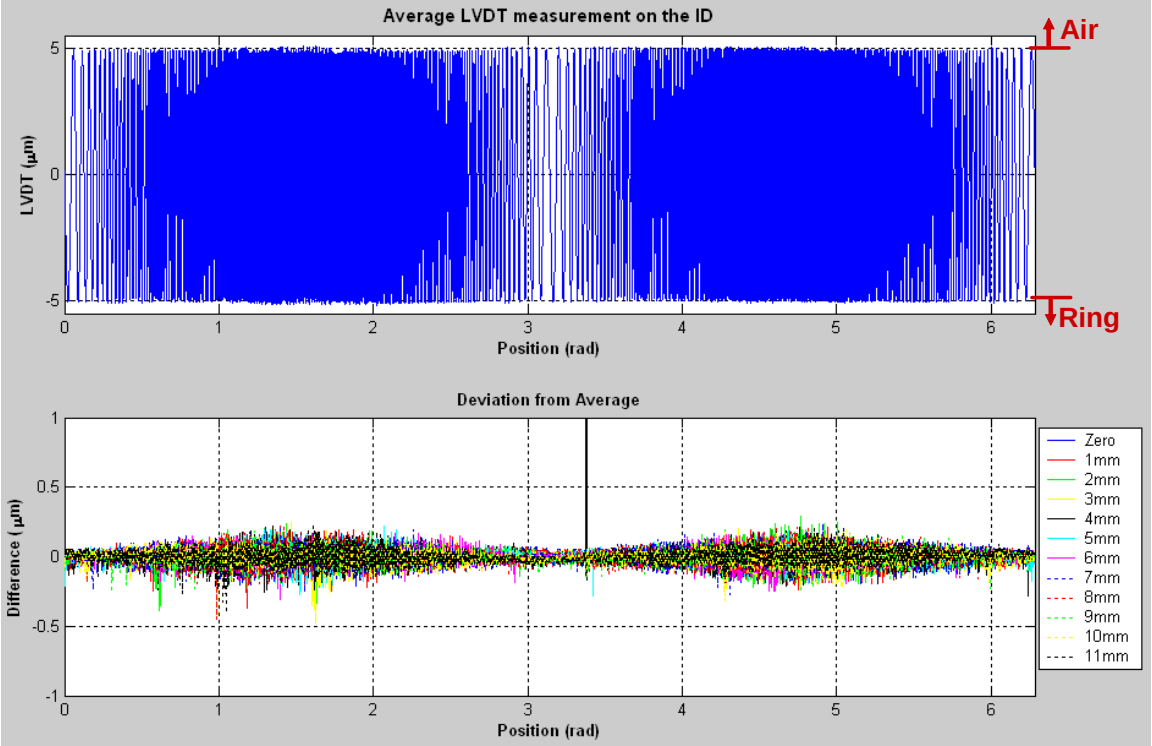

Figure 23. Average of measurements along with wave deviation on the ID.

Figure 23 shows the average of the 12 measurements taken on the ID of the ring with each measurement's difference from the average data set across the width of the wave. The mean of each data set was removed from the individual measurements and 0.2µm was added to each to center the wave about zero. Statistical analysis was performed on the measurements of the ID.

Using a coverage factor of 3 and the maximum standard deviation of 44 nm, the user can be 99% confident that the magnitude of the wave is within 0.132 µm of its true magnitude when a measurement is taken anywhere across its width.

The average wave data set was compared to the desired wave in Figure 24. For the ID, the minimum wavelength measured 0.431mm while the maximum wavelength is 6.368mm. The longest wavelength is equivalent to the desired but the measured shortest wavelength is 10% shorter than the desired wavelength of 0.479mm. A comparison with the desired wave after the probe compensation equations [13] were applied reduces the error of the shortest wavelength to

1.90%. As for the magnitude, the PV is 9.94 µm which is a difference of 0.65% from the 10 µm PV.

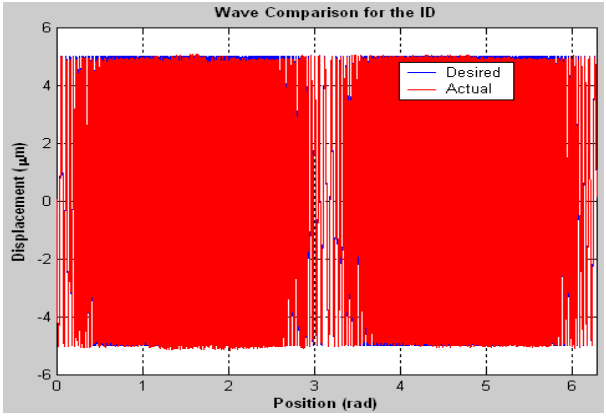

Figure 24. Comparison of the desired wave to the actual wave on the ID.

If the measured wave is subtracted from the compensated wave, the error corresponding to phase can also be determined. In Figure 25, the difference reaches ~1 µm. However, when the highest frequency region is expanded, it is still apparent that the "circles" (actual) do not match their corresponding "stars" (compensated). The distance between the waves at the shortest wavelength is 9.1 µm. The difference in the time between encoder counts due to an imperfect alignment is exemplified by the non-symmetric waves. The expanded region also illustrates the shorter than desired wavelength in the associated region.

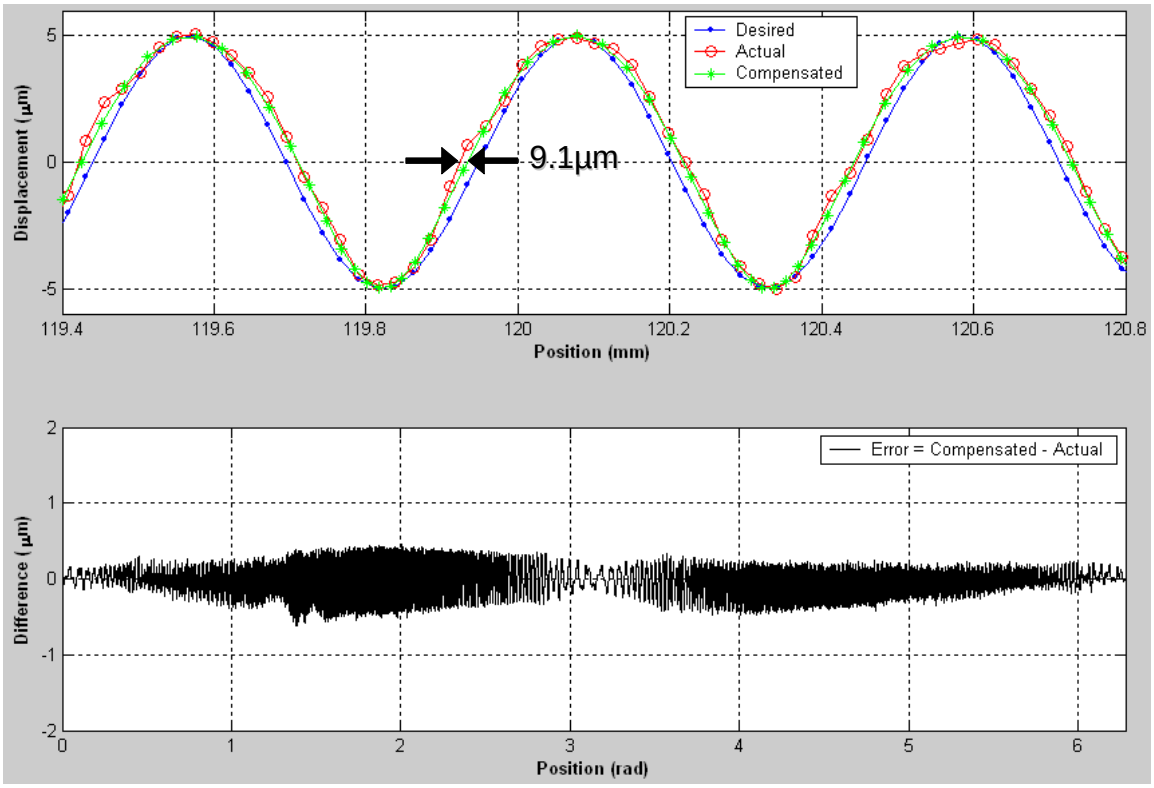

Figure 25. The measured wave subtracted from the compensated wave with an expanded view at the highest frequency on the ID.

The LVDT also measured the wave on the OD. Figure 26 shows the average of the 12 measurements taken on the OD of the ring with each measurement's difference from the average data set across the width of the wave. Lastly, the mean of each data set was removed from the individual measurements and 0.205 µm was added to each to center the wave about zero.

Statistical analysis was performed on the measurements of the OD. The median difference ranges from less than 1 nm to 3 nm among the 12 data sets. Overall, the wave feature deviates a maximum of 53 nm across its width.

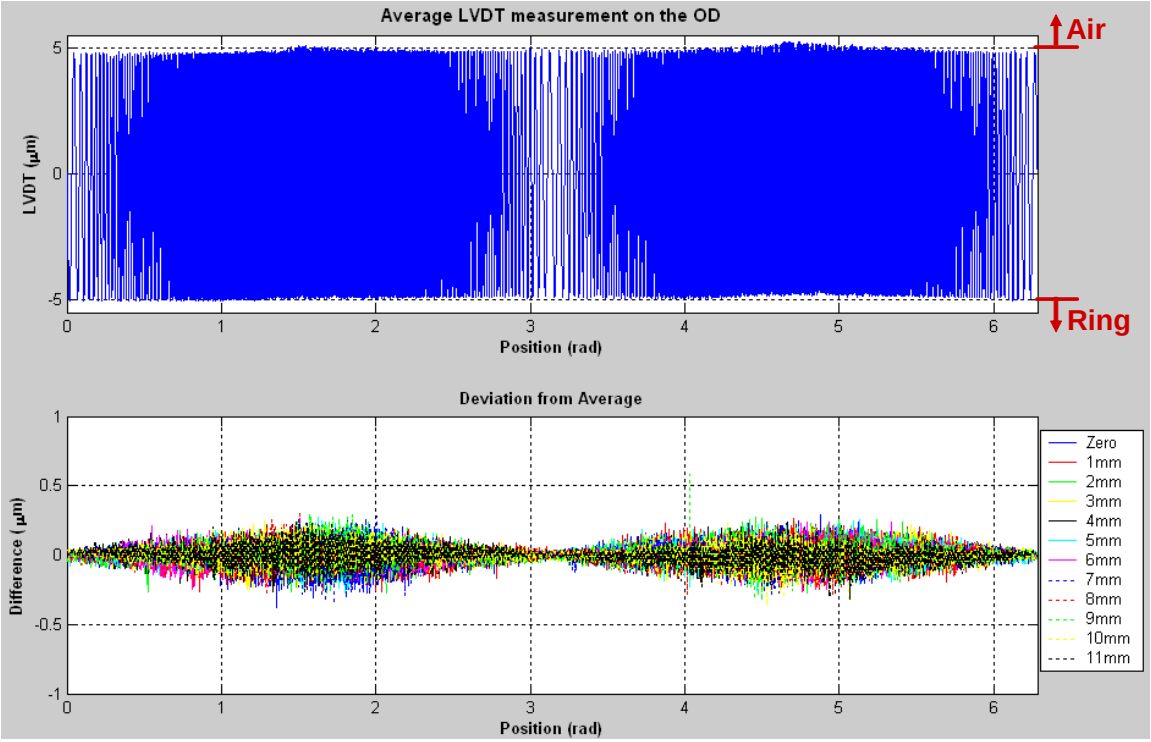

Figure 26. Average of measurements along with wave deviation on the OD.

For the OD shown in Figure 27, the minimum wavelength measured 0.383 mm while the maximum wavelength is 6.384 mm. Again, the minimum wavelength differs from the desired wavelength of 0.447 mm. The maximum wavelengths are equivalent and the measured shortest wavelength is 14% shorter than the desired. By comparing the measured wave to the probe compensated wave, the error in the shortest wavelength reduces to 1.83%. As for the magnitude, the PV is 9.75 µm which is a difference of 2.52% from the 10 µm PV.

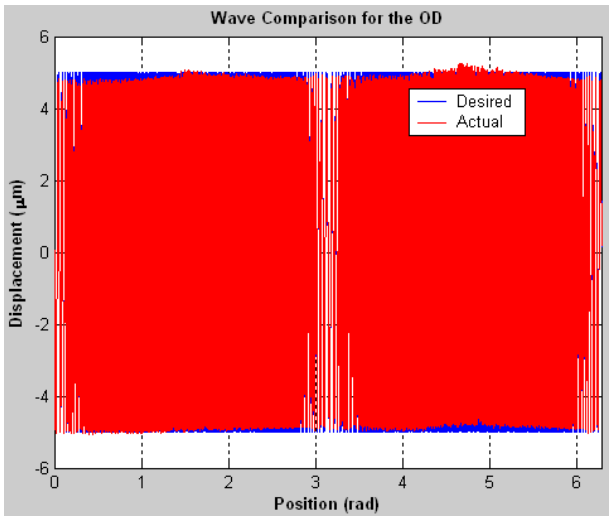

Figure 27. Comparison of the desired wave to the actual wave on the OD.

The difference in the actual wave compared to the compensated wave is approximately 1.75 µm. The error has increased from the ID to the OD due to the higher frequencies of the wave during fabrication with the FTS. Figure 28 shows an expanded view of the short wavelength section of the swept sine wave. As with the other comparable figures, the phase of the actual wave closely matches the compensated wave on the rising edge of the wave but increases at the falling edge. The maximum distance between the waves at the shortest wavelength is 8.2 µm.

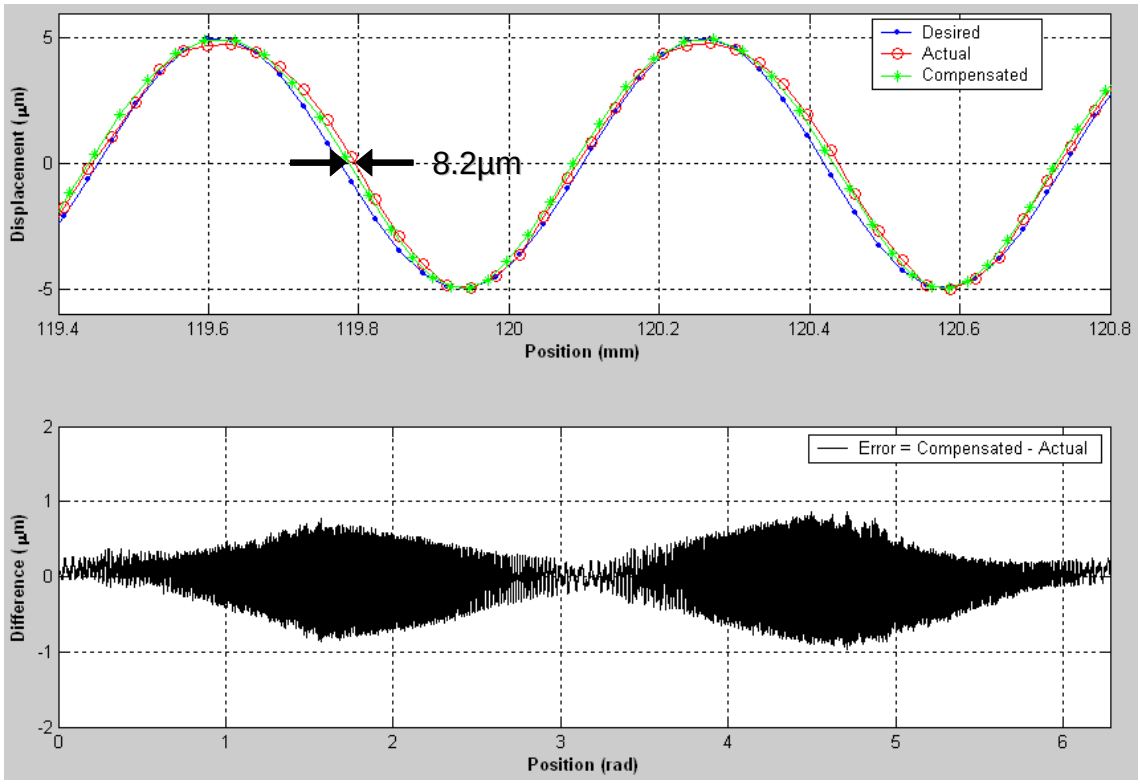

Figure 28. Expanded view of measured wave subtracted from compensated wave.

7.4 APPLICATION OF ARTIFACT TO CMM CALIBRATION

The ring gauge artifact can be used to calibrate the dynamic and static characteristics of a CMM. However, a specific procedure for implementation must be defined to facilitate interpretation of measurement results.

7.4.1 DEMONSTRATION

Measurements were taken with the air bearing LVDT on the ring gauge with the gage on the DTM spindle. The diameter of the probe tip was 1 mm. Three measurements were taken on the OD at random locations on the swept sine wave while the spindle rotated at 1RPM. The process was repeated with spindle speeds of 2 RPM and 3 RPM. The same spindle speeds were also used for the measurements on the ID. Each measurement data set contained vectors of time, encoder counts, and LVDT output in Volts. The sampling rate of each measurement was also recorded.

Following the measurements, the data was analyzed in a series of steps. The sampling rate and the multiple revolutions (at least 1 revolution per data set) of data capture created several displacement values of the wave at a single encoder count. As described in the analysis of the swept sine wave measurement (Section 7.3.6), each measurement data set was averaged to produce a total of 20,000 points on the wave and a least squares fit was applied to the data to remove the off-center and out-of-round aspects of the ring. The three measurements at one spindle speed were combined and averaged to produce one representative measurement at the specific speed. From a single measurement at the spindle speed, the true elapsed time of one revolution was determined. The time frame provided bounds for the interpolation of both the "accepted" swept sine wave data set (from Figure 23 for the ID and from Figure 26 for the OD) and the representative data set to a higher sampling rate of 20 kHz in the time domain. More points on the waves improve the determination of the transfer function of the instrument without changing the frequency content of the swept sine wave measurement.

The higher measurement speeds created a phase shift in the measurement from the "accepted" data set. Thus, the measured wave did not begin with zero displacement at the start of the wave. To facilitate the correct calculation of the transfer function, both waves were shifted to maintain the same spacing while originating the measured wave at zero. The first point of the "accepted" data set was set to equal the first point of the measurement for continuity of the FFT calculation. Also, only a quarter of the swept sine wave was necessary to determine the system dynamics; the complete wave tends to cancel values out and creates confusion in the interpretation of the transfer function. As with the first point, the last point of the quarter wave of each data set were set to be equal so that the first point begins where the last point left off due to the assumption of

infinite repetition of the signals by the FFT algorithm. After the manipulation of the data sets, the transfer function of the instrument was found.

The transfer function of the LVDT found using 1 RPM, 2 RPM and 3 RPM differ from each other slightly. The transfer functions are shown in Figure 29 using the measurements from the ID of the ring. All three figures contain the same frequency range on the horizontal axis. The magnitude plots demonstrate that the measurement of the amplitude of the wave remains constant until around 10 Hz where it begins to increase until the LVDT's natural frequency is reached where the magnitude is twice as large. The lower frequencies in the 3 RPM plot of the magnitude are not as stable due to the higher starting frequency of the wave during the measurement; however, the higher frequencies are more accurate with 3 RPM than with 1 RPM for the same reason. Also, the phase plot in each figure remains steady until 10 Hz where it gradually increases until the natural frequency is reached.

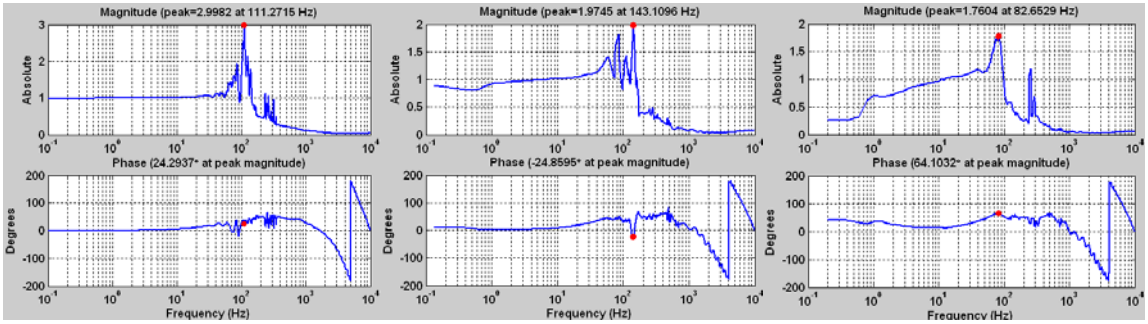

(a) (b) (c)

Figure 29. Transfer function of the LVDT on ID at (a) 1RPM, (b) 2RPM, (c) 3RPM.

For the OD of the ring in Figure 30, the transfer function of the LVDT found using 1 RPM, 2 RPM and 3 RPM also differs from each other, but is more consistent than the ID. The magnitude remains constant until 10 Hz and increases to an average of 2 near the natural frequency before decreasing to nearly zero. The characteristics of the phase plot for the OD mimics the characteristics as shown for the ID; the phase remains constant until 10 Hz where it increases before rapidly decreasing at the natural frequency.

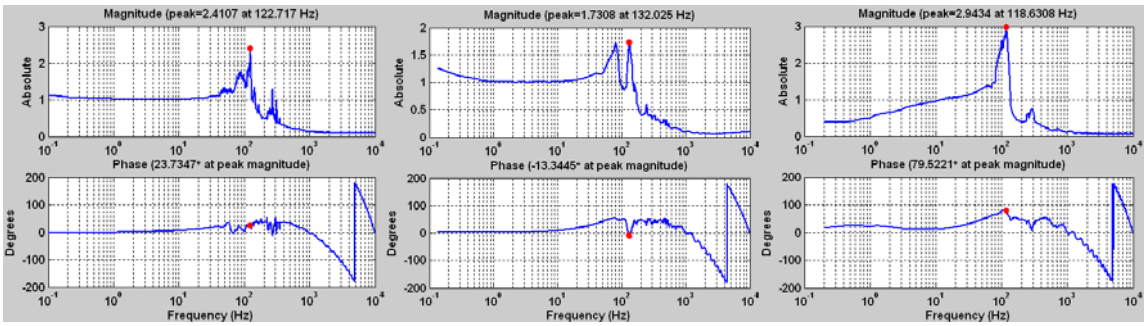

(a) (b) (c)

Figure 30. Transfer function of the LVDT on OD at (a) 1RPM, (b) 2RPM, (c) 3RPM.

The natural frequency of the LVDT appears to be between 120 and 130 Hz. The imperfect fabrication of the swept sine wave with a slightly misaligned encoder creates problems in the final application of the ring and analysis of measurement data. The values for the magnitude and phase are more accurate in the lower frequency range with the 1 RPM measurements, more accurate in the mid-frequency range with the 2 RPM measurements and more accurate in the high frequency range with the 3 RPM measurements. For this reason, the location of the natural frequency seems to be more distinct using the 2 RPM data sets.

Another potential reason for inconsistency in the transfer function plots between speeds is due to the different response of the LVDT across the sections of the swept sine wave during measurement. Figure 31 illustrates the three measurements with the "accepted" data set. The 3 RPM measurement depicts the differing responses more readily. The first quadrant of data of each measurement was used in the calculation of the transfer function. There is more discrepancy between measurements on the ID in the first quadrant than on the OD.

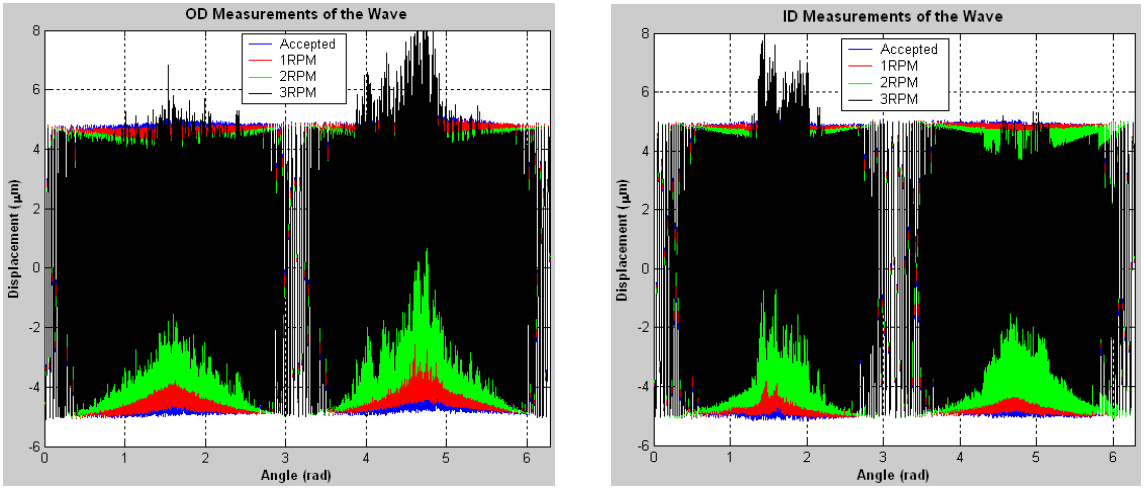

(a) (b)

Figure 31. Measurement of the swept sine wave with different speeds on the (a) OD and (b) ID.

7.4.2 VERIFICATION OF LVDT DYNAMICS

The transfer function of the LVDT was found using the FTS, a function generator and an oscilloscope. The FTS was mounted to an optical table along with the LVDT; the tip of the LVDT pressed against the FTS tool holder. Single frequency sine waves were sent to the FTS using a function generator. Figure 32 illustrates the setup to find the transfer function of the LVDT.

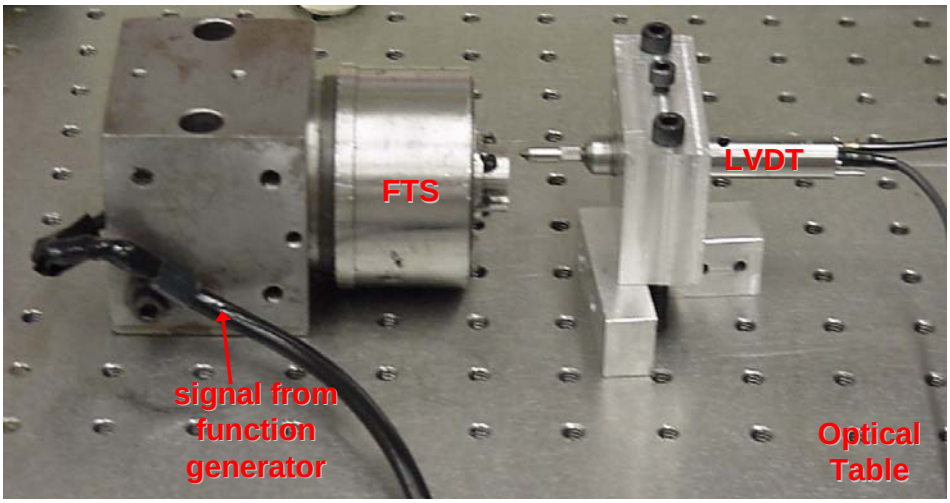

Figure 32. Setup to determine dynamics of LVDT.

The oscilloscope captured the signal from the function generator and the output of the LVDT in Volts. The oscilloscope also recorded the phase between the two signals, the amplitude of the LVDT output and the frequency of the generated sine wave. The amplitude of the LVDT output was converted to an absolute magnitude by dividing each value by the first amplitude. Figure 33 displays the results of the magnitude and phase of the LVDT. The natural frequency where the phase crosses -90° is approximately 85 Hz. The magnitude decreases to zero around 300 Hz.

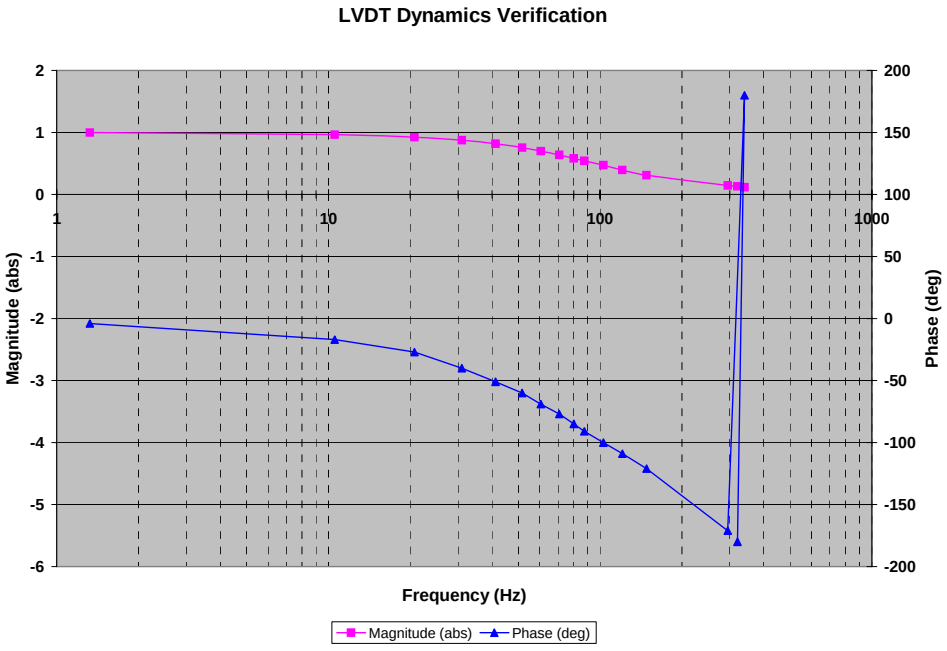

Figure 33. Transfer function of the LVDT.

The transfer functions found in Figure 29 and Figure 30 differ from the measured dynamics of the LVDT. However, if the first peak on the magnitude plot is used, the natural frequency is within the 80Hz range. The phase also approaches 90° at this frequency. Discrepancies between the transfer functions have not yet been explained.

7.5 CONCLUSIONS AND FUTURE WORK

A calibration artifact has been developed. Some of the highlights include:

- Stainless steel ring gauge with a 6" ID, 8" OD and a 1" square cross section. The shape of the ring gauge is appropriate for static measurements.
- Swept sine wave feature on the ID and the OD with an amplitude of approximately 5μm to simulate small scale features on a part.
- Variable wavelengths of the swept sine wave are for dynamic analyses.
- Used to measure the static and dynamic performance of a CMM.

The ring gauge artifact was also fabricated. The fabrication technique is as follows:

- Material: A trial artifact was made with aluminum with the final artifact fabricated out of 17-4PH stainless steel and plated with electroless nickel.
- Diamond turning: Each surface of the final ring gauge was diamond turned to produce a flat surface. A 0.5 mm radius diamond tool was used on the final artifact on the ID and the OD.
- FTS: The FTS machined the swept sine wave on the ID and OD surfaces of the ring. It was also used for the machining of the ID and the OD surfaces prior to wave fabrication.
- Deconvolution: The method of deconvolution compensated for the dynamics of the FTS prior to fabrication of the swept sine wave and decreased the total fabrication error.

Various features of the ring gauge artifact were measured. The resulting measurements were:

- Roundness: The ID of Ring 1 was 0.35 μm PV. For the OD of Ring 1, it was 0.17 μm PV. There was slight improvement with Ring 2 with roundness measured on the OD to be 0.12 μm PV and 0.32 μm PV on the ID.
- Surface Finish: The surface finish on the top and bottom surfaces of the ring were approximately 37 nm RMS which is also true for the ID and the OD. The high surface finish value from a theoretical RMS of 3 nm is attributed to machine error and tool damage.
- Wavelength: The desired wavelengths of the OD ranged from 0.447mm to 6.384 mm with the ID ranging from 0.479 mm to 6.368 mm. The actual wavelengths on Ring 1 ranged from 0.383 mm to 6.384 mm on the OD; the ID had wavelengths from 0.383 mm to 6.416 mm. For Ring 2, the OD wavelengths were 0.383 mm to 6.384 mm and the ID was 0.431 mm to 6.368 mm. The difference is due to the misalignment of the encoder.

- Amplitude: The desired amplitude of the swept sine wave was 5 µm (10 µm PV). For Ring 1, the PV is 9.63 µm (3.68% difference) on the OD and 9.80 µm (1.97% difference) on the ID. For Ring 2, the PV is 9.75 µm (2.52% difference) on the OD and 9.94 µm (0.65% difference) on the ID.

The dynamics of a CMM under a specific set of measurement conditions can be found by computing a transfer function between a measurand of the ring gauge and the accepted "true" shape of the gauge. This allows an operator to devise a measurement strategy for a part that does not exceed the dynamic capabilities of the CMM and to predict the error and uncertainty in a measurement. The ring gauge artifact was used to find the dynamics of an LVDT to demonstrate the procedure for determining the dynamics of a CMM. The natural frequency occurred ~80Hz.

REFERENCES

1. Morse, E. P., Coordinate Measuring Machines, ASPE Tutorial, Oct. 24, 2004. Orlando, FL.
2. Lim, C. K., Burdekin, M., Rapid volumetric calibration of coordinate measuring machines using a hole bar artefact. Proc. Instn Mech. Engrs, Part B, Journal of Engineering Manufacture, 2002, 216 (B8), p. 1083-93.
3. Chan, F. M. M., Davis, E. J., King, T. G., Stout, K. J., Some performance characteristics of a multi-axis touch trigger probe. Meas. Sci. Technol., 1997, 8 (8), p. 837-48.
4. Destefani, J. D., CMMs make contact. Manufacturing Engineering, 2001, 127 (3), p. 100-5.
5. Cauchick-Miguel, P. A., King, T. G., Factors which influence CMM touch trigger probe performance. Int. J. Mach. Tools Manufact., 1998, 38 (4), p. 363-74.
6. Marino, E. A., Three-Dimensional Measurement Probe. Master's Thesis, NC State University, 1999.
7. EMD Sceptre System Proportional Displacement Probe Data Sheet, http://www.emdsceptre.com/pdprobe.htm.
8. Bosch, J. A. (ed.), Coordinate Measuring Machines and Systems. New York: Marcel Dekker, Inc. 1995.
9. Wong, A., Folkert, K., and Dow, T. A., Metrology Artifact Development. Precision Engineering Center Interim Report. October 2003.
10. Weekers, W. G., Schellekens, P. H. J., Compensation for dynamic errors of coordinate measuring machines. Measurement, 1997, 20 (3), p. 197-209.
11. Bal-tec The 1216 Ball Plate Data Sheet, http://www.precisionballs.com/CMM/CMM-28.htm.
12. Cauchick-Miguel, P., King, T., Davis, J., CMM verification: a survey. Measurement, 1996, 17 (1), p. 1-16.
13. Bal-tec Adjustable Ball Bars Data Sheet, http://www.precisionballs.com/CMM/CMM-10Page1.htm.

14. Bal-tec The Geostep 3400-10 Data Sheet, http://www.precisionballs.com/CMM/CMM-26Page1.htm.
15. Lee, E. S., Burdekin, M., A hole-plate artifact design for the volumetric error calibration of CMM. Int. J. Adv. Manuf. Technol., 2001, 17 (7), p. 508-515.
16. Silva, J. B. A., Burdekin, M., A modular space frame for assessing the performance of co-ordinate measuring machines (CMMs). Precision Engineering, 2002, 26 (1), p. 37-48.
17. Savio, E., De Chiffre, L., An artefact for traceable freeform measurements on coordinate measuring machines. Precision Engineering, 2002, 26 (1), p. 58-68.
18. Jusko, O., Ludicke, F. Novel Multi-Wave Standards for the Calibration of Form Measuring Instruments.
19. Panusittikorn, W., Error Compensation using Inverse Actuator Dynamics. PhD Dissertation, NC State University, August 2004.
20. Balkey, M.M., Day, R.D., Batha, S.H., Elliot, N.E., Pierce, T., Sandoval, D.L., Garrard, K.P., and Sohn, A., Production and Metrology of Cylindrical Inertial Confinement Fusion Targets with Sinusoidal Perturbations. Fusion Science and Technology, Vol 45, No 2, p. 107-112, (2004).
21. ANSI Y14.5M – 1982, Dimensioning and Tolerancing. ASME, 1983, New York.

8 METROLOGY FOR REFLECTIVE OPTICAL SYSTEMS

Robert Woodside
Graduate Student
Dr. Thomas A. Dow
Professor
Mechanical and Aerospace Engineering

A two-mirror Richey-Chrétien telescope was designed and machined using diamond turning. To understand the limits of this fabrication process and the available machines, the shape of the mirrors and the performance of the assembled system were measured. The two mirror surfaces were hyperbolic and that complicated their measurement. Three methods were used to evaluate the machined shape; interferometry using a 150 mm Zygo GPI, a Form Talysurf with 120 mm stroke and a rotary table with contacting air-bearing capacitance gauge. These three methods combined to produce a picture of the shape of each mirror. The concave primary (150 mm OD and 27 mm thick) showed some asymmetry in the form of astigmatism and the form error was on the order of 2 µm. The convex secondary (39 mm OD and 10 mm thick) had a form error of an order of magnitude less or 200 nm. The surface finish on both mirrors were typical of 6061 aluminum with an Ra of 6 nm. The assembled system was measured in a dual pass configuration on the interferometer with a flat reference surface to return the light to the telescope. The overall wavefront error was 1.78 µm with an RMS of 0.351 µm. Other measurements presented are spot size and MTF.

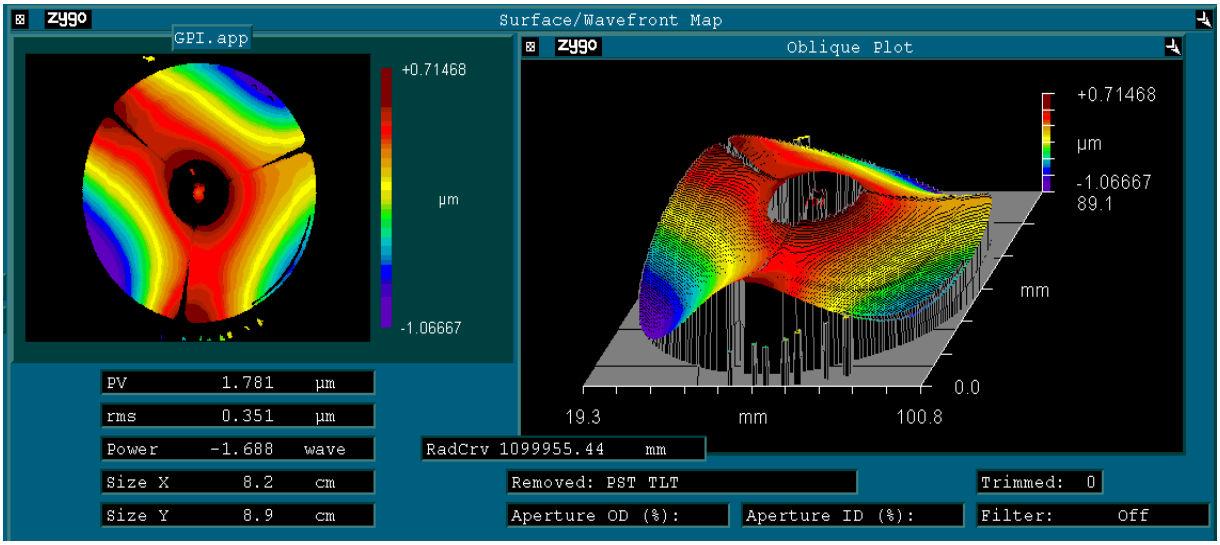

8.1 INTRODUCTION

In early 2005, a new research effort began at the PEC involving the design, fabrication and measurement of freeform optical systems. The activity was named FOCUS or the Freeform Optics Center of the US. The goal is to address the infrastructure needs raised by freeform systems and to develop new technology to address those needs. The plan was to create a series of optical systems beginning with a two-mirror on axis design, followed by an off-axis three mirror design and finally to build a freeform three mirror system. One of the glaring difficulties is the metrology of the mirror surfaces and the complete optical system. This section addresses the problems and successes related to measuring the two-mirror system components and defining the performance of the assembled system.

The optomechanical design consists of separate primary and secondary optics with a cylindrical tube connecting them. The two mirrors of the Richey-Chrétien design are hyperbolas – the primary is concave, 150 mm in diameter and has a hole in the center. The secondary is convex, 39 mm in diameter and is mounted on three radial arms from a tube that spaces and aligns the mirrors. This 135 mm long tube provides reference surfaces that locate the two optical surfaces in the axial, radial and tilt directions. The design of the system is addressed in Section 2 and the fabrication in Section 5. The theoretical wavefront error of the designed system is shown in Figure 1. This design has astigmatism that grows with the field angle as shown in Figure 1 so the performance will degrade as the field of view increases.

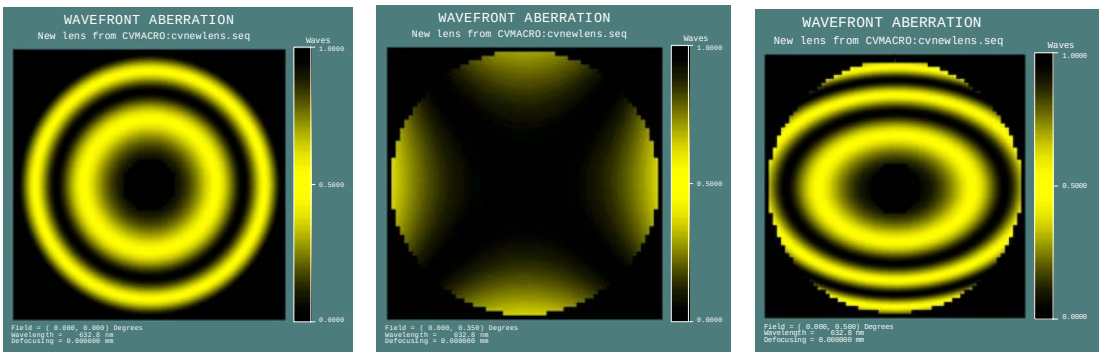

a) Error at 0º b) Error at 0.35º c) Error at 0.5º

Figure 1. Code V wavefront for two-mirror system with best focus at 0.35º

Because the mirror surfaces are aspheres rather than flats or spheres, the standard laser interferometer techniques cannot be used. Instead, more complicated methods were employed such as dual pass configurations where a second optical element is used to redirect the beam back to the interferometer. For example with a parabola, a flat mirror with a hole can be used to send the collimated beam created by a spherical wavefront reflecting from a the parabola back to the parabola and into the interferometer.

8.2 MEASUREMENT OF OPTICAL COMPONENTS

8.2.1 PRIMARY MIRROR SHAPE

The hyperbolic primary mirror was measured in a dual-pass setup on the Zygo GPI. The conic constant of the hyperbola is -1.019 (close to a parabola which has a conic constant of -1), so it could be measured as a parabolic mirror[1]. The interfermetric setup for measuring a parabolic mirror involves a spherical reference element in the GPI's aperture and a flat reference element with a hole in the middle placed between the spherical reference and the parabolic mirror.

For this measurement, an f/1.1 spherical reference element was used in the interferometer. Finding the focal point of this beam is complicated by the hole in the middle of the primary. To find the focus, the primary is shifted laterally to put the beam at the edge of the hole. Then the primary is moved away from the beam until a null fringe pattern is registered[2] in the interferometer. This is the focus point of the spherical reference. The primary mirror is again centered and moved down approximately 150 mm which is the focal length of the primary mirror. A λ/9 perforated glass reference flat was placed in a tip/tilt stage supported by 3 posts about 150 mm above the primary mirror as shown in Figure 2. This places the center of the mirror at the focal point of primary mirror and allows all of the light to pass through the hole. At this point, the focal point of the primary mirror and the focal point of the reference sphere are close to being coincident. Small adjustments are made until fringes again appear. At this point, the spherical wavefront is transformed to nearly collimated light by the hyperbolic mirror (a parabola would make collimated beam) which bounces off the reference flat, returns to the mirror to become a spherical wavefront returned to the interferometer. Because the primary is not a parabola, corrections for this measurement geometry were made as discussed next.

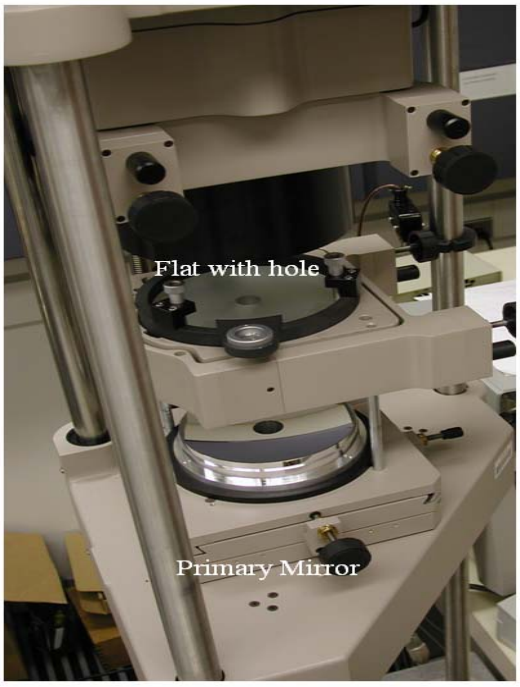

Figure 2. Primary Mirror Interferometry Setup

[1] The result will be the actual shape compared to the best fit parabola and not the shape compared to the desired hyperbolic surface.

[2] A illustration of the location of the cat's eye is found at <http://www.phase-shift.com/products/interferometer-sphericity.shtml>

Code V Model

Because the desired hyperbolic surface is close to a parabola and a perforated flat was available on loan, this dual-pass configuration was used for the measurements. However, the perfect hyperbola will not give a null measurement in this configuration because of it hyperbolic shape. The expected wavefront for the desired hyperbolic mirror in this configuration is shown in Figure 3 and shows a positive wavefront error of about 5 waves over most of the field of view. To compare the actual surface to the desired hyperbola, the measured wavefront from the Zygo interferometer was modified with the result of Figure 5. This was done by adding the Zernike terms from the model below to the measured optical surface.

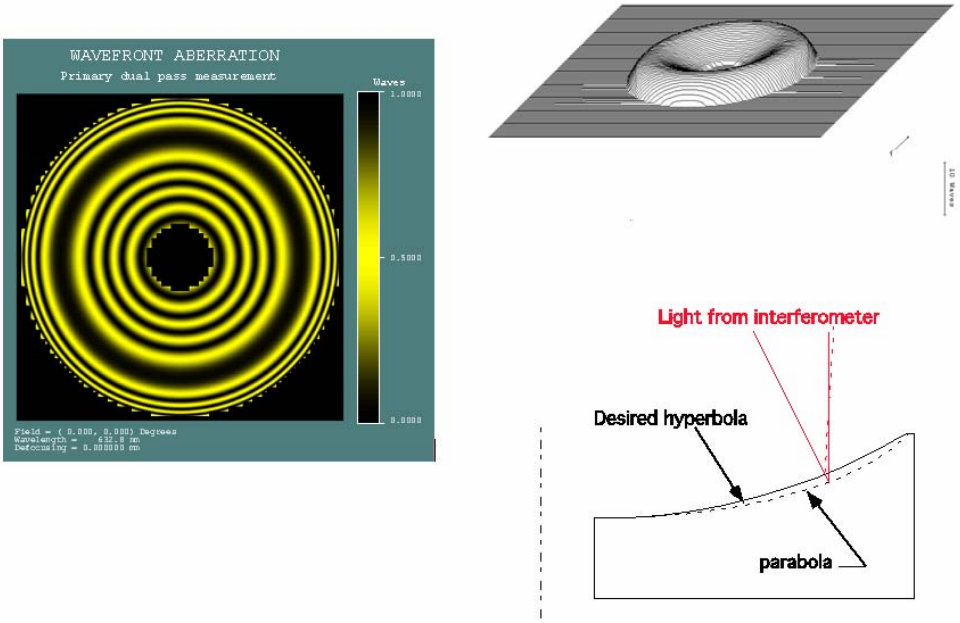

Figure 3. Wavefront error from Code V model for desired Hyperbolic Mirror measured with a flat reference, top down view at left, isometric view at upper right and surface shape comparison at bottom right

Primary Surface Waveform Error The wavefront measurements in Figure 4 were made using the setup shown in Figure 2. Figure 4 (a) is the baseline measurement without correction for the hyperbolic primary shape. The first 16 Zernike coefficients are shown on this image; the largest values are #1 (tilt about the x axis), #2 (tilt about y axis), #5 (astigmatism ±45º) and #6 (x coma and tilt). Figure 4 (b) is the wavefront error in the primary when corrected for the dual-pass geometry using the Zernike coefficients from the Code V model. The Zernike coefficients were #8 (spherical and focus). and #15 (5^{th} order focus) and each was divided by two (because of the dual-pass model) and subtracted from the coefficients of the measurements.

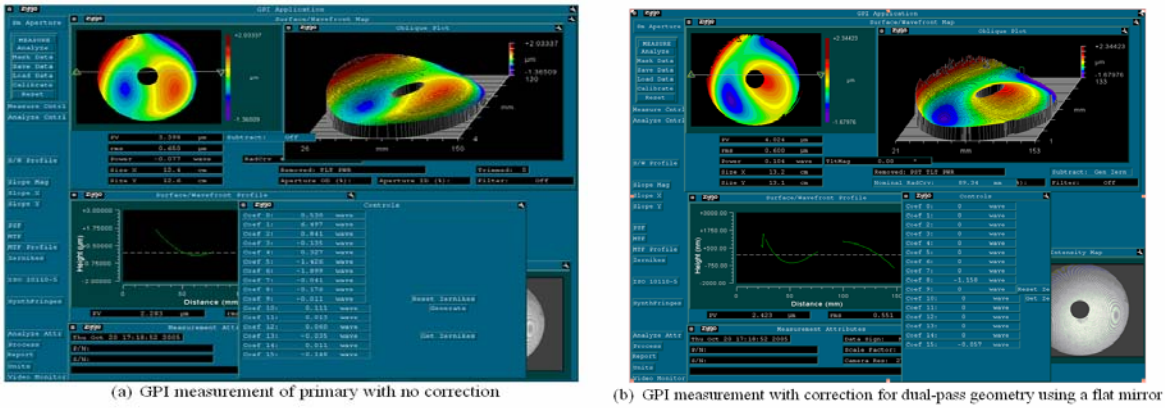

(a) GPI measurement of primary with no correction

(b) GPI measurement with correction for dual-pass geometry using a flat mirror

Figure 4. Primary Mirror Interferogram from Dual-Pass Measurement of Figure 2

The primary surface shown in Figure 4 (b) has a significant Non-Rotationally Symmetric (NRS) component that is on the order of 4 μm. This value is much higher than the λ/4 (~ 160 nm) form error anticipated from past fabrication efforts. Careful evaluation of the components in the measured shape (astigmatism, coma and tilt) pointed to the possibility that Figure 4 was not a measure of the mirror shape but rather the result of an alignment error in the dual-pass setup. The astigmatism and coma could result from an angular misalignment of the flat mirror with respect to the optical axis of the primary and a decenter of the primary mirror in the interferometer.

The model of the measurement developed in Code V was used to evaluate this hypothesis. It showed that if the mirror was tilted 0.025º and the primary was decentered 2.75 mm the wavefront map shown in Figure 5 would result. The Zernike coefficients for this model are close to those of the Zygo measurements in Figure 4.

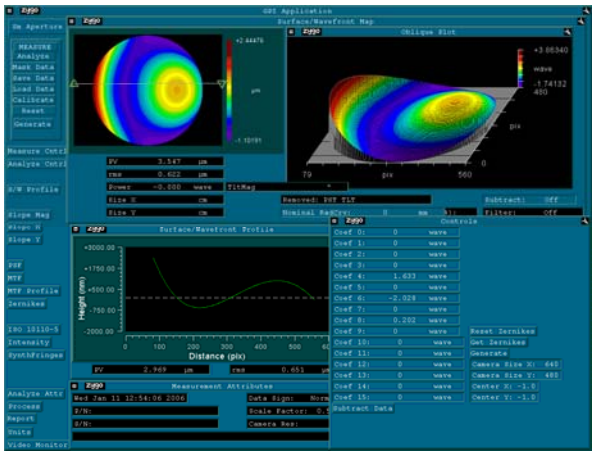

Figure 5. Model of the Primary Measurement from Code V with 0.025º Tilt of the Flat Mirror and 2.75 mm Decenter of the Primary

So the measurement problem turned out to be a lack of experience with dual-pass measurements by the PEC and an appreciation for the extra care required to align the elements to produce a correct surface profile measurement. Because the perforated flat mirror which was on loan from Ruda Associates was no longer available, other techniques were utilized to assess the shape of the primary.

Talysurf Measurements

To provide an alternative measure of the shape of the mirror, the Form Talysurf was used. This linear motion, contacting instrument was used to measure a series of seven radial scans from the edge of the hole to the OD of the mirror. The seven scans were made at 60° angular increments with the 7^{th} being a duplicate measurement at the zero degree orientation. The sag of the mirror (9 mm) is larger than the range of the Talysurf stylus (6 mm) so the mirror had to be tilted to measure each segment. Positioning the mirror for each trace required lifting the mirror, rotating it and replacing it on the three balls in three of the the six holes in the back of the mirror. The ball/holes keep the orientation close to the 60º increments desired. However, because the mirror was moved, the seven scans do not have a common reference point.

The desired hyperbolic shape (R = 300, K = -1.0195) was fit to each trace by the "large-scale trust-region reflective Newton method" of nonlinear least squares using the Matlab optimization toolbox. The parameters of variation for the least squares minimization was the center location in x and z of the desired hyperbola in Cartesian coordinates. The measurement data was rotated (i.e., tilted in the XZ plane) and the fit repeated until a minimum residual RMS value was obtained for each trace.

All of residual data is shown in Figure 6. The bold lines are the result of smoothing the residual data with a linear least squares robust polynomial algorithm using a 1 mm spatial scale centered at each successive data point. As shown in Figure 6, the scans are essentially the same, supporting a hypothesis that the unassembled primary mirror is rotationally symmetric and the interferometer measurements were due to misalignment. Also note that the positive error at the ends and negative error in the middle of the plot indicates that the concave mirror surface is "low" in the center and at the outer edge with respect to the desired hyperbola. For the combined residual primary mirror data with the smoothing filter applied the peak-to-valley is 289 nm ($\lambda/2.5$) and the RMS form deviation is 54 nm.

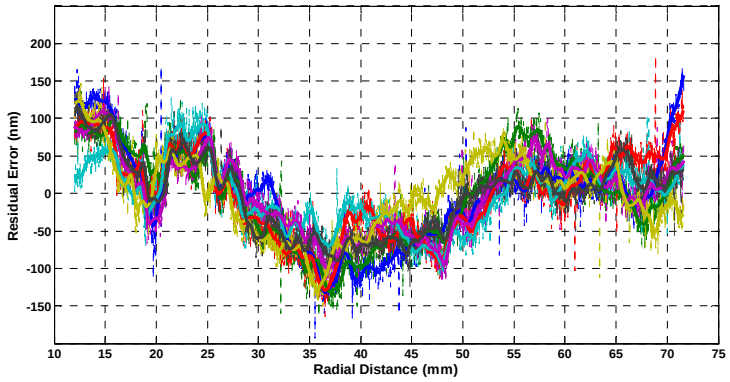

Figure 6. Primary Mirror Form Error - Talysurf Profilometer. Error is with Respect to Hyperbola with R = 300 mm and k=-1.01948378

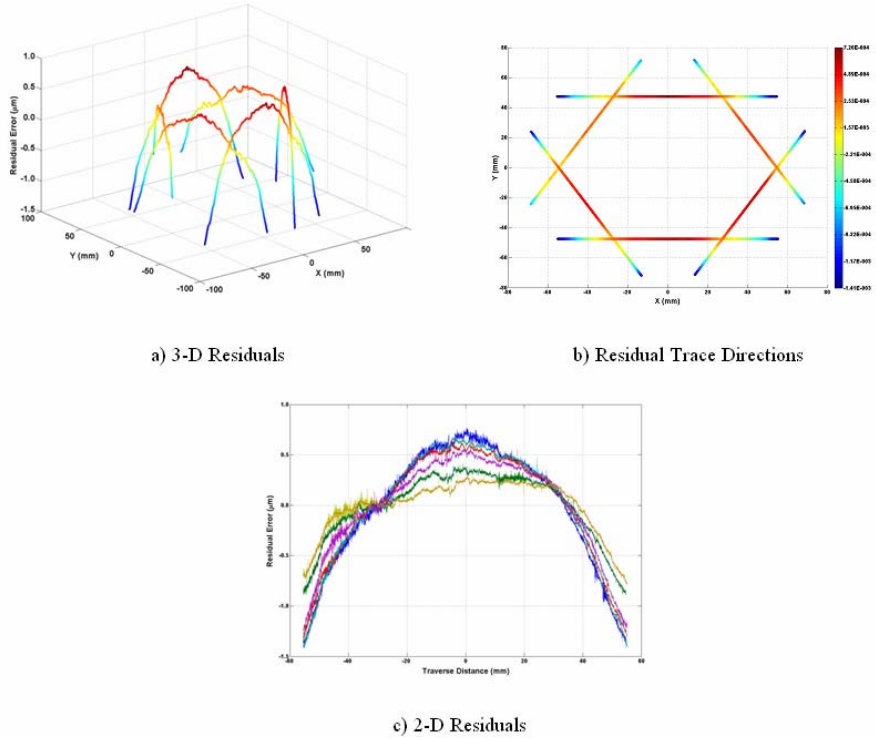

Figure 7. Hexagonal Primary Mirror Talysurf Traces fit to the Expected Hyperbola

To further address the astigmatism in the primary, traces were also made with the Talysurf in a hexagonal shape around the outside of the optical surface as shown in Figure 7(b). These traces were then fit to the expected hyperbola. The residuals of the fits, shown in Figure 7(a) and Figure 7(c), showed that the traces did not fit the expected hyperbola and showed errors of over 2 μm in some cases. Figure 7(a) also shows that the traces have clear NRS components as the peaks of some traces are higher than others.

Rotary Measurements

Figure 8. Rotary measurement apparatus

To provide additional data on the shape of the primary, the surface was measured on a rotary measuring machine. The mirror was rotated on a vertical axis air bearing spindle and a low-contact force air-bearing capacitance gage measured the shape of the primary in annular rings. A photograph of the measurement setup is shown in Figure 8. Before the mirror was placed on the spindle, the stage was leveled to a P-V value of 400 nm by adjusting tip-tilt screws in the stage. A federal gage was used along the outside edge of the mirror to center the part to within 2 μm. The contacting probe of the capacitance gage was placed on the optical surface approximately 25 mm from the outer edge. The rotary spindle was set in motion and data from the capacitance gage was captured by a connected oscilloscope.

The rotary spindle rotates at slightly less than 2 rpm with a rotation period of 32 sec. Using the oscilloscope, 100 seconds of capacitance gage data were collected comprising slightly more than 3 full rotations of the spindle. A small mark was made with a ink marker on the optical surface for use as a fiducial to orient the data. The marks make a slight perturbation of the contacting probe that can be resolved during post processing of the data. Figure 9 shows a full 100 seconds of data from a measurement of the primary optical surface with fiducial mark locations circled. Each mark lasted approximately 0.1 sec on the time scale which amounts to 0.003 of a rotation or about 1º. Using this mark, the data can be split into 3 individual rotations and concatenated to obtain repeatability information.

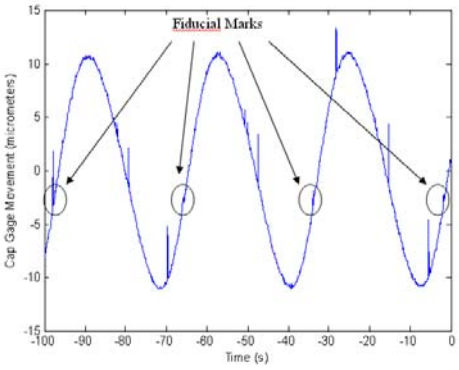

Figure 9. Primary Optical Surface Rotary Measurement with Fiducial Markings

Once the data has been sufficiently manipulated, MATLAB's curve fitting tool is used to remove any tilt or any other once per rotation error. Once this is removed, only the non-rotationally symmetric error should remain. This is done by fitting a sine wave with a 32 second period to the data and viewing the residuals as shown in Figure 10. This shows a trace of the primary optical surface along with the residuals from the sine wave curve fit. The residuals show 2 μm of

non-rotationally symmetric error with a twice per revolution cycle.

Discussion – Primary mirror shape

Three different techniques were used to assess the shape of the primary mirror. Because it is a hyperbola, dual pass measurements must be made when using an interferometer. These measurements require the alignment of several optical elements in translation and rotation. As a result alignment errors can make the measured shape better or worse than the actual shape. The Zygo measurements of the primary (corrected for the flat mirror configuration) clearly shows non-rotationally symmetric, saddle-shaped errors. However, it was shown that this error could be a result of misalignment between the primary and the reference surfaces. The Talysurf radial traces appear to show a very small form error, on the order of 300 nm. However, the Talysurf traces taken perpendicular to the radial direction show deviation from the expected hyperbola by 1.8 µm. The rotary measurements confirm this conclusion and show NRS features with a similar magnitude of 2 µm. Also, the primary back surface and fiducial surface each have some clear NRS components as shown in Sections 8.2.2 and 8.2.5. The conclusion is that there is NRS error in the primary but the radial shape of the mirror is within 300 nm of the desired shape. The most likely culprit for this error is the low aspect ratio of the mirror (diameter/thickness = 5.5) coupled with a lack of flatness of the vacuum chuck during machining (see Section 5). Future mirror blanks will have an aspect ratio closer to 4 as did the secondary in this telescope.

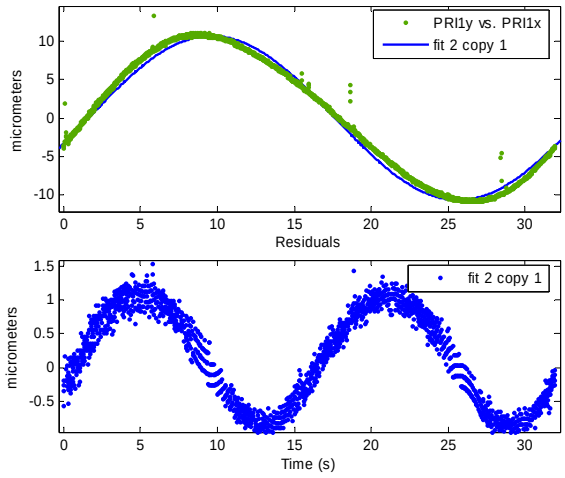

Figure 10. Primary Mirror Rotary Data and Curve Fit (top) and Curve Fit Residuals (bottom)

8.2.2 Primary Back Surface

The Zygo GPI was used to measure the flatness of the back of the primary. For this measurement, a flat reference element is used and Figure 11 illustrates the result. The surface has a saddle shape similar to the optical surface but the PV error is only about 20% of the mirror surface at 0.66 µm. One reason for this difference may be the way that the front and back were supported during machining. When the mirror surface was machined, the back contacted the vacuum chuck from the hole to the OD; but when the back was machined, only the periphery of the mirror touched the vacuum chuck. As a result, any lack of flatness on the chuck would have

more impact on the shape of the mirror surface than the back. This points to the need for a stiffer mirror blank.

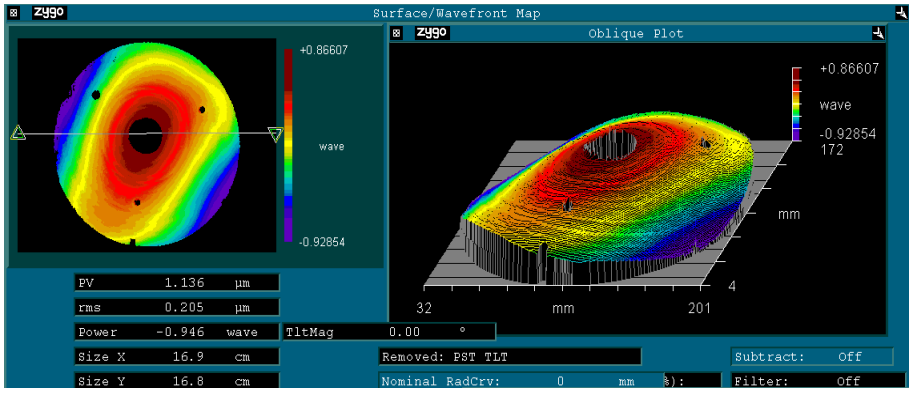

Figure 11. Flatness of the Back of the Primary Mirror

8.2.3 SECONDARY MIRROR SHAPE

The secondary mirror has is a convex hyperbolic shape with a larger conic constant (k=-2.166) than the primary (k=-1.0048). As a result, it cannot be measured using the flat mirror as discussed in Section 8.2.1. Because the shape is close to a sphere, an attempt was made to measure the surface as a sphere but there were too many fringes for the MetroPro to digest. The proper way to measure this mirror is to use a spherical reference mirror, as shown in Figure 12. This was deemed too difficult and expensive so more direct methods were used.

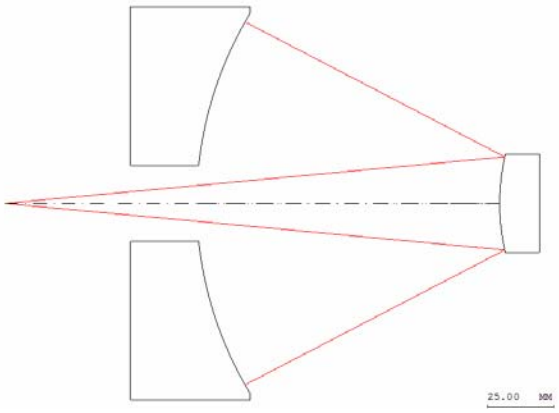

Figure 12. Hindle test for hyperbolic mirror

Talysurf Measurements

The Talysurf profilometer has enough range and resolution to measure the entire width of the mirror. However, because this instrument produces a linear scan, a series of scans must be pieced together to provide a view of the entire surface. The six holes in the secondary mount were used to index the mirror in 30º increments and 12 measurements were made across the width of the mirror. The second 6 measurements cover the same region of the mirror but are taken in the opposite direction as the first 6 to address the repeatability of the measurements.

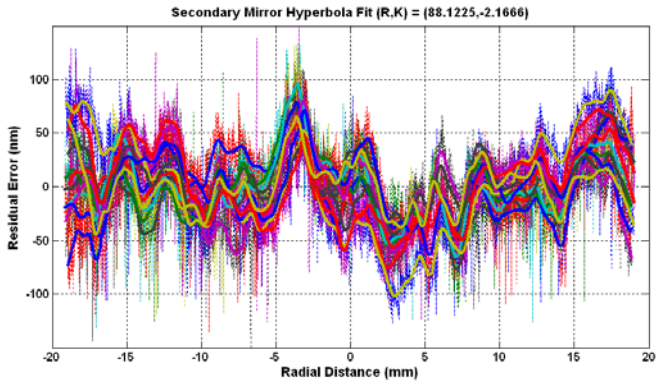

Figure 13: Secondary mirror form error – Talysurf profilometer. Error is with respect to desired hyperbola R = 88.1225 mm and k=-2.1666

For each scan, a crowning procedure was used to ensure that the scans crossed the apex of the mirror. The same fitting and smoothing procedure was followed for the twelve scans as that described for the primary mirror in Section 8.2.1 and only the center location and in-plane tilt were varied. The residual errors from the least squares fit to the desired secondary hyperbola (R = 88.1225, K = -2.1666) are shown in Figure 13. With the exception of one scan, the measurements are very similar and the unassembled secondary mirror appears to be rotationally symmetric. The positive error at the edges and negative error in the middle indicate that the convex mirror is "high" in the middle with respect to the reference hyperbola or has a larger radius of curvature than desired. The form error is the desired hyperbola minus the measured sag at each radial location. For the combined residual secondary mirror data with the smoothing filter applied the peak-to-valley is 198 nm and the RMS form deviation is 31 nm.

Rotary Measurements

The surfaces were also measured using the rotary table and the air-bearing capacitance gage. The cap gage was set at different radii and circular traces were made of the surface of the mirror. These traces were put together to provide a similar but different representation of the mirror compared to the Talysurf measurement discussed above. The data was analyzed using the same fiducial and data analysis method discussed in Section 8.2.1. The secondary mirror trace and best fit residuals are shown in Figure 14. This data confirms the Talysurf measurements' assertion that the part is rotationally symmetric. There are no low frequency errors in the measurement such as those in the primary measurement. The 1 μm P-V of the residual data comes from a combination

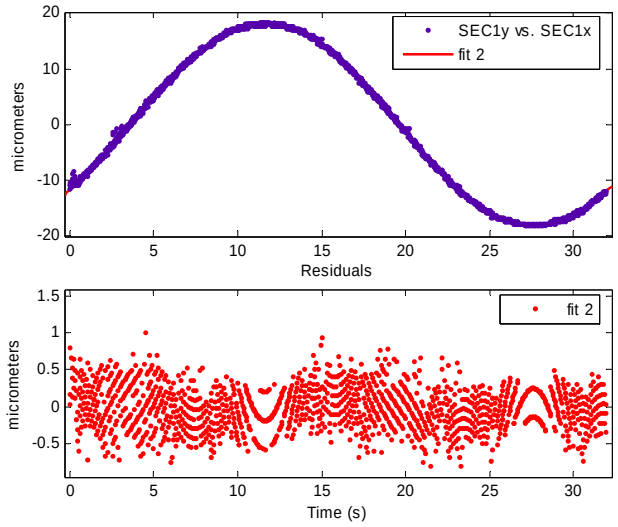

Figure 14. Secondary Mirror Rotary Measurement Data and Best Fit Line (top) and Best Fit Line Residuals (bottom)

of the capacitance gage sensitivity and the measurement repeatability but all errors are at a high frequency compared to a revolution of the surface.

8.2.4 TUBE SHAPE

The tube shape was measured using the same technique as the secondary mirror. When fit to a once per revolution sine wave, the data shows a twice per revolution error on the order of 5 μm, as shown in Figure 15.

.

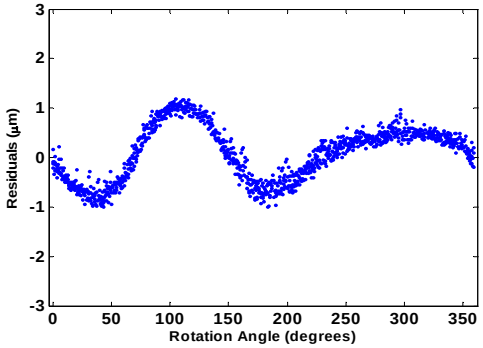

Figure 15. Tube primary end fiducial surface rotary measurement data

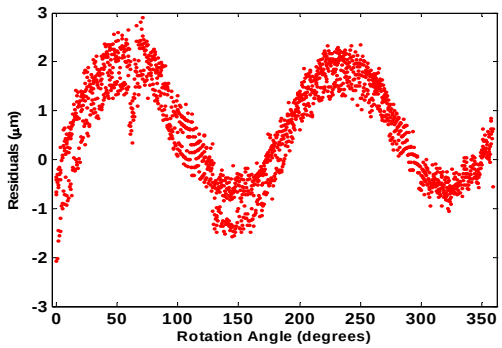

Figure 16. Primary mirror fiducial surface rotary measurement data

8.2.5 PRIMARY FIDUCIAL SURFACE

The fiducial machined on the face of the primary was measured using rotary table. When the best fit once per revolution sine wave is subtracted (tilt or the part), the data shows a twice per revolution error on the order of 5 μm, as shown in Figure 16. This shape of this data is similar to the primary surface but the magnitude is larger as may be expected since it is farther from the center. The data in Figures 15 and 16 indicate that the primary must deflect when pulled down on the tube with the mounting screws. However, because the fiducial surface is thin (7.5 mm) compared to the primary thickness at the edge (32 mm), the deflection of the primary will be less than indicated by the NRS error.

8.2.6 PRIMARY ASSEMBLED TO TUBE

The concept for the mirror fabrication for the RC telescope was to machine the fiducial surface at the same time as the optical surface. This was possible because the fiducial is on the same side as the mirror. As a result, if there is distortion of the mirror blank; it will be present on both the optical surface and the fiducial surface. In many snap-together designs, the back surface is used as the reference surface for assembly and therefore it cannot be created at the same time as the optical surface.

When the primary is assembled to the tube, the shape of the system will be a function of the shape and stiffness of the mating components. The tube has an large aspect ratio (length to diameter) and is much stiffer than either the primary or secondary mirror blanks; therefore, the tube shape will determine the shape of the assembly. To test this hypothesis, the primary mirror was measured both assembled to the tube (with and without screws) and alone. The shape of the primary is improved by attaching it to the tube. The mirror alone (3.6 μm) has over twice the error of the screwed together assembly (1.4 μm) and removing the screws (2.0 μm) increases the error. Each of these measurements is shown in Figure 17.

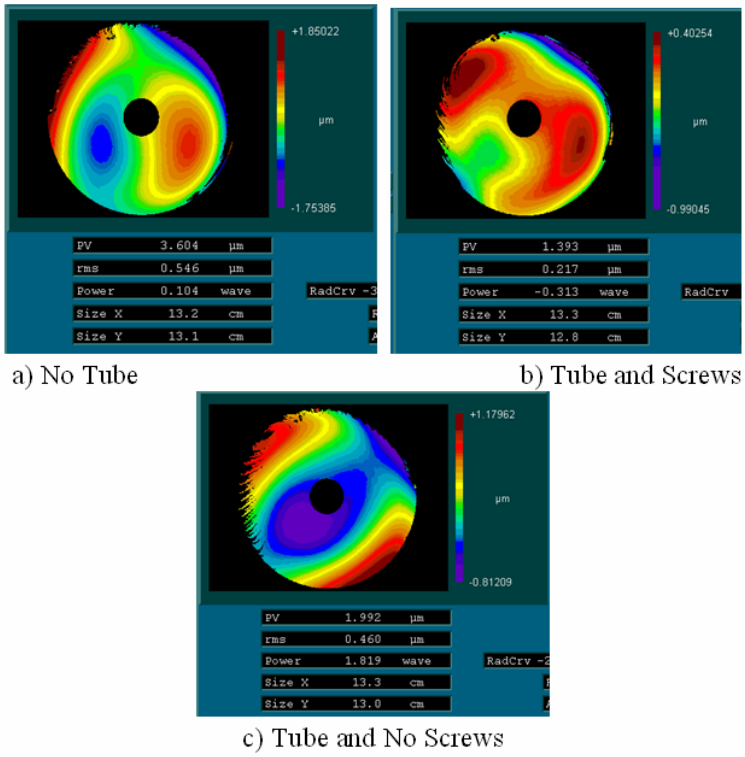

a) No Tube b) Tube and Screws

c) Tube and No Screws

Figure 17. Measurement of the primary mirror

The back of the primary mirror was also measured when assembled to the tube to see how it changed as a result of assembly. The fiducial surface with the mounting screws is larger than the area that can be measured with the 150 mm flat reference surface so only the thick mirror blank is visible. Because the fiducial ring is thin, it could exhibit more distortion. The measurements also indicate that assembling the mirror to the tube has an effect on the astigmatic error. The back surface of the mirror clearly deforms upon assembly as the error in Figure 18 indicates. This error (3.3 μm) is three times that of the unassembled surface (1.1 μm) shown in Figure 11.

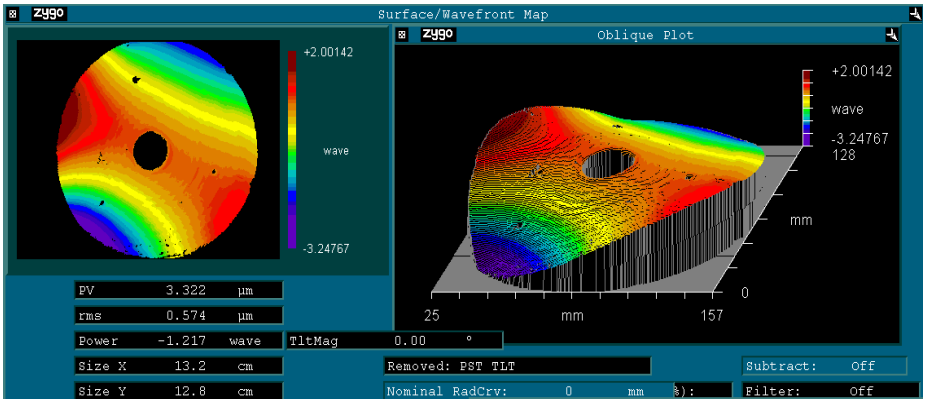

Figure 18. Measurement of the primary back surface when assembled to the tube

The change in shape of the back of the primary is another indication of the flexibility of the mirror blank. A lower aspect ratio – larger mirror thickness – is needed to keep the distortion from influencing the shape of the optical surface during fabrication and assembly.

8.2.7 Optical Surface Finish

Primary

The surface finish of the optical surfaces was measured with the Zygo New View white light interferometer. The primary mirror was machined at 530 rpm with a feed rate of 2 mm/min and a 3.135 mm tool nose radius. This will produce a feed of 3.77 µm/rev and a theoretical PV of 0.57 nm and an RMS of 0.19 nm. At this feed rate, one pass of the primary would take 77 minutes indicating the need for excellent temperature control.

Figure 19 shows the surface finish of the primary measured over an area of 50x70 µm. The actual PV and RMS (23 nm and 5 nm respectively) are much higher than the theoretical values by about 40x. The profile plot in the lower left of Figure 19 shows a trace perpendicular to the feed direction covering 17 µm over which 4+ tool passes should be visible. While not obvious to the naked eye, the autocovariance function in the lower right shows a peak near 3.7 µm indicating a repetitive feature at that spacing. Unfortunately, other features such as the second phase particles in the 6061 structure and scratches from chip management failures disguise the feed rate and increase the surface finish.

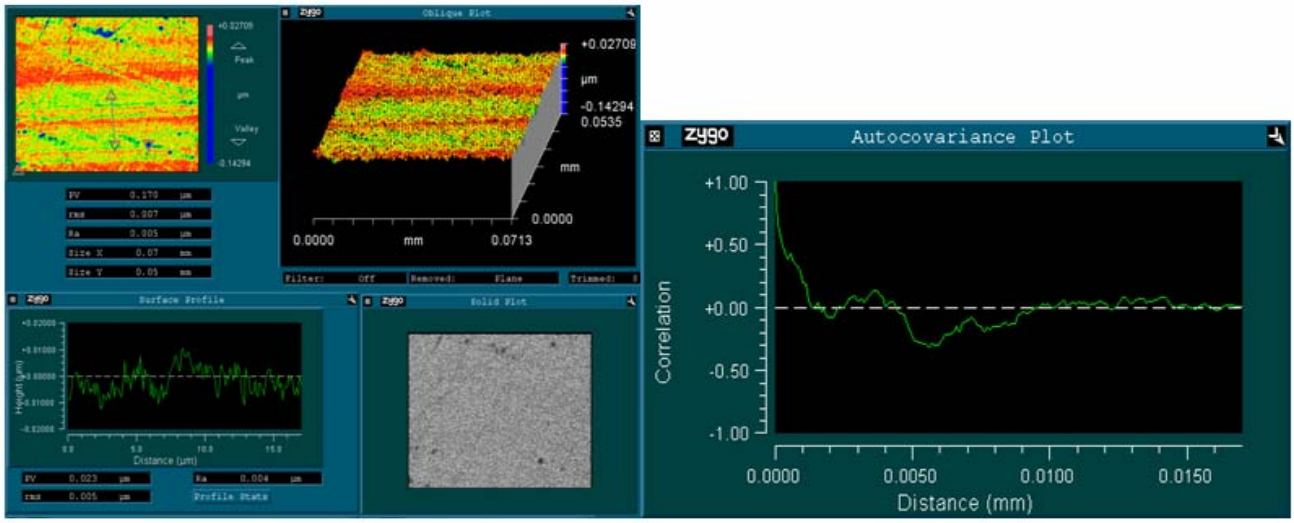

Figure 19. Surface finish of the primary mirror optical surface using Zygo NewView

Secondary

The secondary mirror optical surface was machined at a lower feed rate because it is smaller. The feed rate was 1 mm/min which will produce a feed/rev of 1.89 μm and an expected PV of 0.14 nm and an RMS of .05 nm. Figure 20 shows the measured surface finish over the same field of view as Figure 19. The profile plot in the lower left shows a trace perpendicular to the feed covering a width of 10 μm or about 5 tool passes. The surface has a PV of 18 nm and an RMS of 4 nm, which are two orders of magnitude greater than the theoretical value. Again, the material properties, spindle dynamics and chip management limit the actual surface finish possible. The vertical lines on the profile plot represent the theoretical wavelength and the arc represents on the nose radius of the tool. The autocovariance function in the lower right shows a slight peak at 2 μm which is the feed rate. As with the primary, the particles and contamination in the 6061 limits the surface finish possible to about 20 nm. The smaller feed rate does improve the surface finish (18 nm vs. 23 nm), but the effect is small.

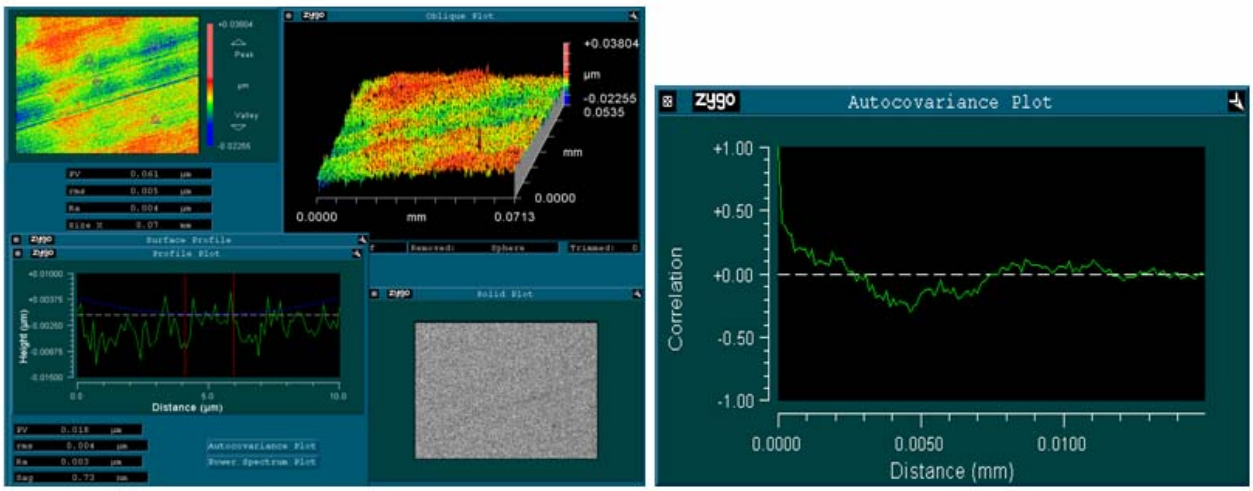

Figure 20. Secondary mirror surface finish and tool profile using Zygo NewView

8.3 SYSTEM PERFORMANCE

The previous measurements describe the shape and spacing of the individual mirrors that make up the telescope. These dimensions were related to the desired profiles to address errors in the manufacturing process earlier in this section. When the components are assembled into a system, the performance was related to that predicted by the Code V model. Several techniques were used for this comparison including dual-pass interferometry, modulation transfer function, spot diagrams and photographs made with the telescope.

8.3.1 CODE V DUAL-PASS MODEL

The dual pass measurement was setup in Code V to visualize the wavefront error plots generated in the experiments. The wavefront error for this measurement should be twice that of the RC telescope because the wavefront passes through the telescope twice. A schematic of the system is shown in Figure 21. The two telescopes are on top of each other but the optical path in Code V goes from left to right and returns from right to left. A spherical wavefront is generated from the focus point at the left, passes through the telescope and creates collimated light that impinges onto the flat mirror. The light is collimated because the system was designed for infinite conjugates. Light from the mirror is reflected back through an identical telescope and focused onto the original point. To test the system for the 0.35º and 0.5º fields, the telescope is translated from the nominal optical axis until the off-axis focus coincides with the nominal optical axis. Then, the flat mirror is tilted respectively to reflect the collimated light back through the telescope. The theoretical wavefront error for the different fields is shown in Figure 22.

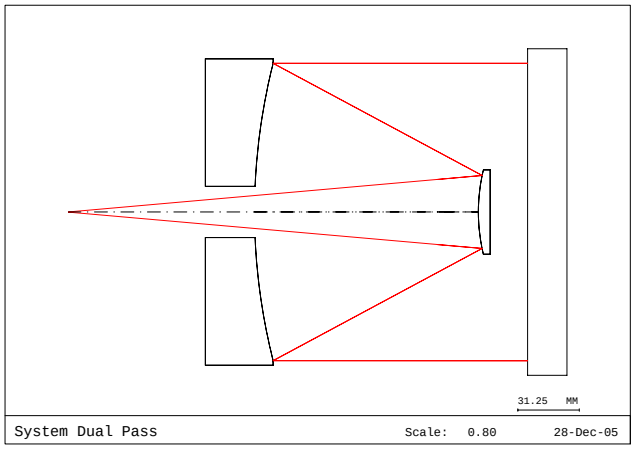

Figure 21. Dual Pass setup for telescope testing showing on axis rays

The results agree with the assumption that the wavefront error is double the error generated by the single pass. The wavefront error for the 0˚ field shows circular interference fringes which indicate that the system is out of focus. Aberrations are at a minimum at the 0.35˚ field angle where astigmatism dominates the wavefront. The wavefront error for the 0.5˚ field shows both focus and astigmatic error based on the oval interference fringes. This figure shows wavefront errors that are double those of the telescope model in Figure 1 because of the dual pass.

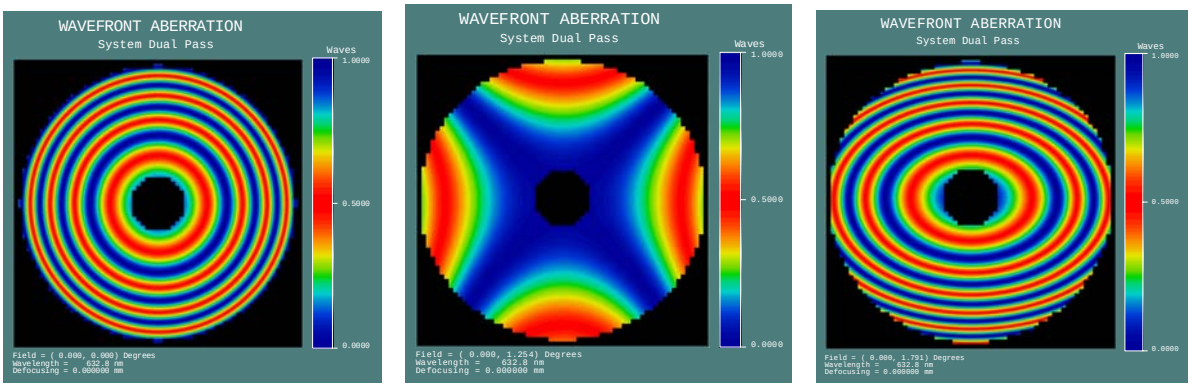

a) Error at 0º b) Error at 0.35º c) Error at 0.5º

Figure 22. Wavefront error for the dual pass model in code v with best focus at 0.35º

8.3.2 DUAL-PASS OPTICAL SETUP

Figure 23. Dual pass measurement setup

To setup the system measurement, a tip/tilt stage is placed on the bottom of the GPI and tip/tilt and x-y translation stages with six inch holes are placed on the moving z-stage. A 6-inch reference flat is placed on the bottom tip/tilt stage and a 4 inch reference flat is placed in the aperture of the GPI. The 6-inch flat is tilted until it gives a null fringe pattern compared to the 4-inch flat. This ensures that the flat is parallel to the interferometer to begin the measurement. Next, the telescope is placed on the tip/tilt stage on the z-stage and is rotated to make the back surface parallel to the interferometer. This levels the telescope system. The f/3.3 reference element then replaces the 4-inch flat; this setup is shown in Figure 23. To find the focus point of the spherical reference element, an optical flat with known thickness is placed on the primary back surface. When the focus of the reference sphere is on the surface of this optical flat, the beam is reflected back to the interferometer and fringes are observed. This is the so-called "cat's eye" point of the system which gives the location of the f/3.3's focal point. The HP interferometer readout is zeroed at this point. The system is then translated down until a fiducial sphere machined on the back of the primary around the center hole produces fringe patterns. The system is then translated on the x-y translation stage until the fringes have their max spacing. At this point, the system is centered.

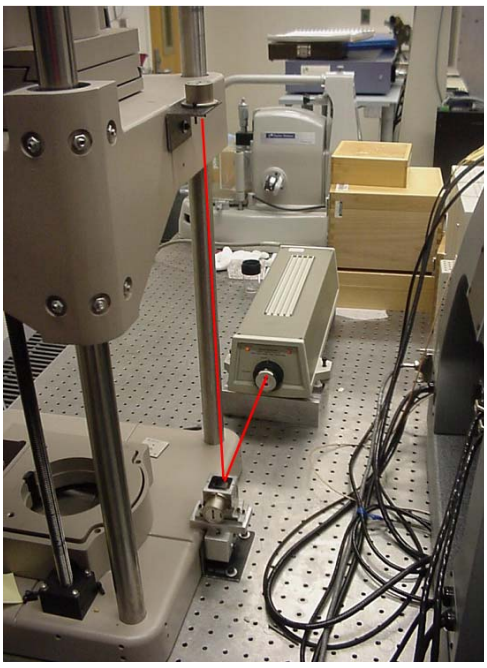

Figure 24. Interferometer setup for telescope position measurement

One of the first steps in the system setup is to find the location of the focal point of the telescope. To determine this location, the motion of the z-stage of the Zygo GPI must be accurately monitored. The lead screw that moves this stage is driven by a motor with an integral encoder. Due to the weight of the moving stage, there is considerable torque on the motor and the coupling between the motor and screw sometimes slips and creates error in the z-stage position and uncertainty in its location. To provide an independent measurement of the z-stage position, HP

interferometer was setup to measure the z-stage travel. A retroreflector is attached to this stage near the center of the axis of measurement. The laser head is mounted to the table and the interferometer is mounted to the GPI base. This setup is shown in Figure 24. This allows for an accurate and repeatable measurement of the telescope position.

8.3.3 Dual Pass System Measurement

Focal Point Error

Once the system has been leveled and centered, it is translated in Z to its theoretical focal point, 72.4mm behind the back primary surface. At this point, fringes should be visible and power should be minimized. The power was not minimized at this location so the system was translated until the power in the system was close to zero, as shown in Figure 25. This was called the system's focal point and the Z location was recorded from the HP interferometer. Then, the known thickness of the optical flat used for the cat's eye was added back into the Z location. This gave the location of the system's on-axis best focus point based on the back surface of the primary mirror. This process was repeated multiple times with an average result of 72.4395 mm with a larger number being farther from the back surface of the primary. The theoretical focal point is 72.394 mm behind the back surface of the primary and which indicates the actual system focal point is 45.5 µm too long.

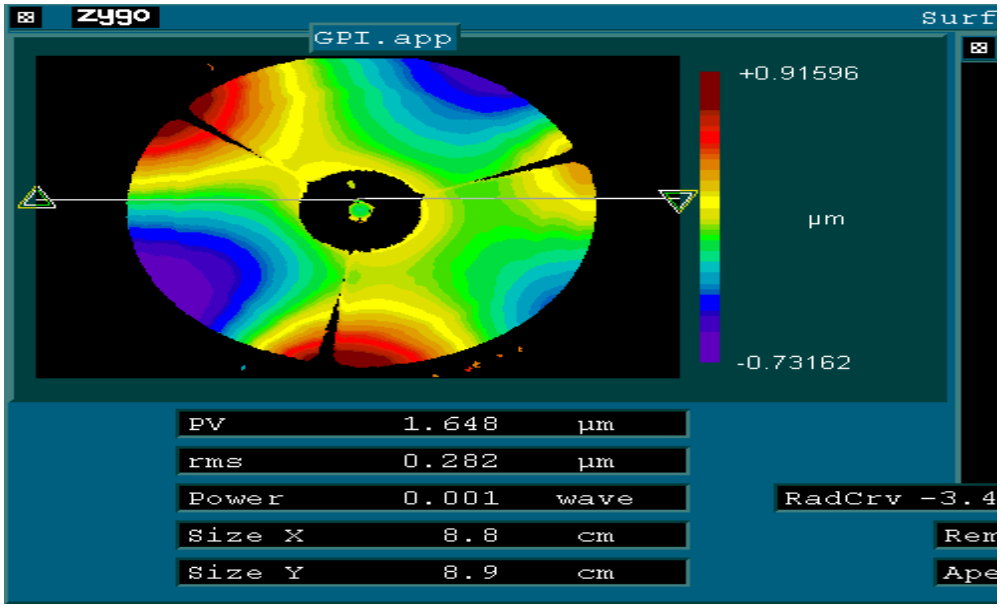

Figure 23. System "minimized" wavefront error to indicate system location for focal point measurement.

This point is the best focus point on-axis, however the theoretical overall best system focus is located 343 µm closer to the primary than the on-axis best focus. At this point, the 0.35º field should have no power because the system was optimized for 0.35º.

Therefore, to determine the location of the actual system best focus point, the telescope was setup for 0.35º and translated up until power is removed. This is the measured focal point of the system at 0.35. This process is done multiple times and the actual system focal point is located 400 µm closer to the primary.

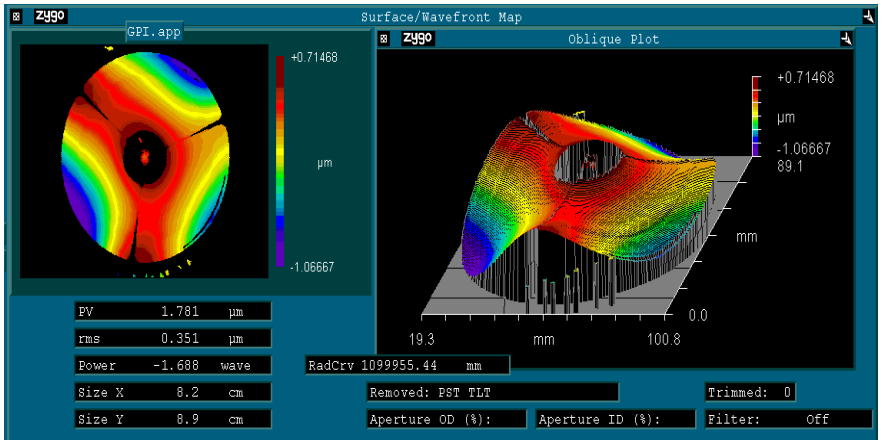

Figure 24. On-Axis System at System Best Focus

Wavefront Error

At the system's focal point, the interferograms can be compared to those produced in Code V. Code V produces a wavefront error plot at the best focus location with the system on-axis and off-axis by 0.35 and 0.5 degrees as shown in Figure 22. Therefore, the system must be measured at each of these field locations and at the measured best system focus. The on-axis component of these measurements and the resulting interference plot, shown in Figure 26, is comparable to Figure 22(a). The real interference shows a small upside down bowl shape, as expected, however the plot is dominated by other errors similar to those in Figure 25. The interferogram shows a distinctive trefoil shape.

To measure the off-axis components, the reference flat must be tilted by, first, 0.35 degrees and then 0.5 degrees. Once the flat mirror is tilted, the system must be translated using the x-y stage to find the new focal point of the system. The 0.35 and 0.5 degree off-axis measurements are shown in Figure 28 and Figure 27, respectively. The four lobed shape expected at 0.35 degrees (Figure 22-b) is not perceptible because the system is again dominated by trefoil errors. However, the 0.35 degree field should be at its best focus and, therefore, have minimum power

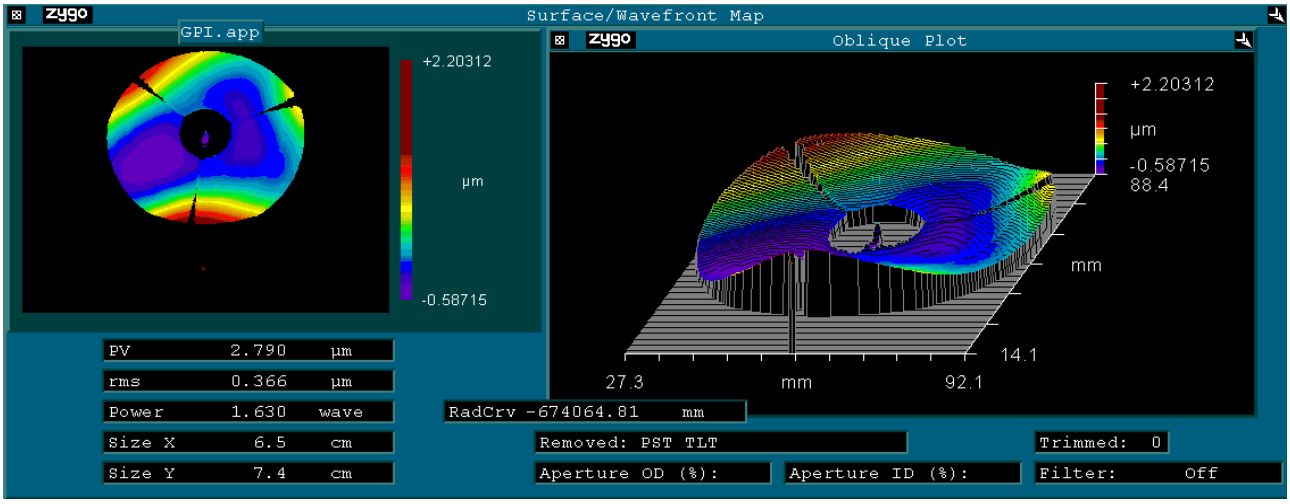

Figure 25. Off-Axis Interference Plots for 0.5

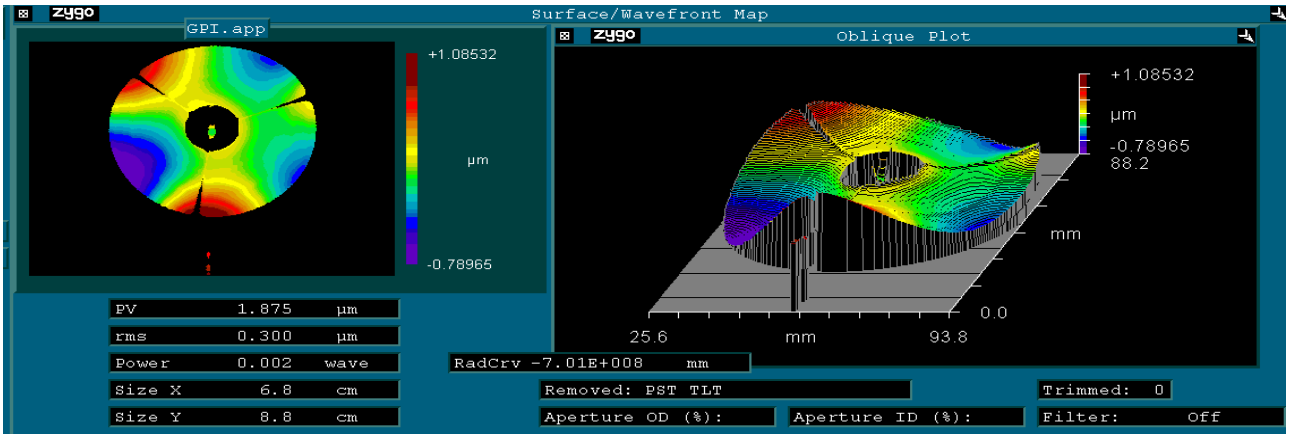

Figure 26. Off-Axis Interference Plots for 0.35 Degrees

as shown in Figure 28. Also, the 0.35 degree field should have a reduced error compared to the on-axis at this focus location but the P-V errors are almost identical. However, it is clear that if the trefoil is removed from each measurement the wavefront error at 0.35 degrees would be minimized while significant power based wavefront error would remain in the on-axis measurement. The 0.5 degree field does have the slight oval shape as expected from Figure 22(c) but is still dominated by trefoil errors.

8.3.4 MODULATION TRANSFER FUNCTION

The Modulation Transfer Function (MTF) is a measure of the ability of an optical system to transmit contrast from an object to an image plane. MTF testing is frequently done by viewing an optical target, such as that in Figure 27, and analyzing the quality of contrast transferred to the image. The MTF target uses square and sin wave patterns of black and white with a progressively higher frequency. MTF is measured by determining the maximum wave frequency at which the individual lines are still visible and have not become a uniform gray. This frequency is returned as cycles/mm. A common watermark for MTF measurements is the frequency at which 50% of the original contrast remains, known as the MTF50 point. An MTF value of 1 indicates full resolution whereas a 0 indicated no resolution. MTF 0.1 is generally regarded as the frequency below which resolution is unknown and is called the cutoff frequency. Code V gives expected MTF plots for an optical system, as shown in Figure 29. These plots can be compared to those produced by the GPI, shown in Figure 28.

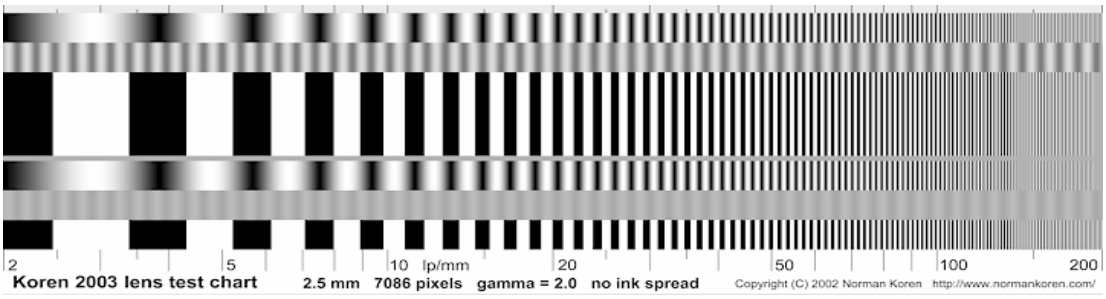

Figure 27. MTF target with varying lines per mm

The GPI produces a three dimensional MTF plot that analyzes the system MTF in all directions of the aperture. Figure 28 is a plot of four slices from this plot taken from the center to the outside edge. The GPI produced MTF plot is normalized by dividing the X-scale by a normalization factor. This normalization factor is based on the *f/#* of the element and the wavelength of light. The normalization factor, Norm, is calculated by Equation 1 where the X-scale is divided by *Norm*.

$$NA = \frac{1}{2*(f/\#)} = \frac{1}{2*3.3} = 0.1515$$
$$\text{Norm} = \frac{2\text{NA}}{0.6328\,\mu\text{m}} = 0.479\,cycles/\mu m = 479\,cycles/mm \quad (1)$$

Based on this calculation, the maximum x-value in Figure 28 is 479 cycles/mm. The expected MTF 0.5 value from Figure 29 is approximately 60 cycles/mm whereas the actual value is approximately 40 cycles/mm. This shows that the theoretical system is able to clearly resolve finer features than the actual. Also, the expected MTF levels off at higher frequencies whereas the actual MTF quickly drops below 0.1. This shows that the theoretical system can make out features of a size that the actual system would not be able to differentiate from the features

surroundings. The surface roughness of the optical surfaces contributes to this by scattering light which reduces the sharpness of the image. Also, focus error would blur the features and reduce the MTF in the actual system. Each of these errors is present in this system and combine to cause the lower MTF values.

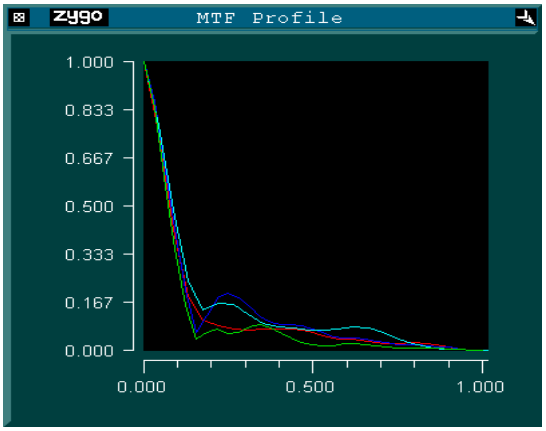

Figure 28. Actual 0.35 deg off-axis MTF plot at best focus

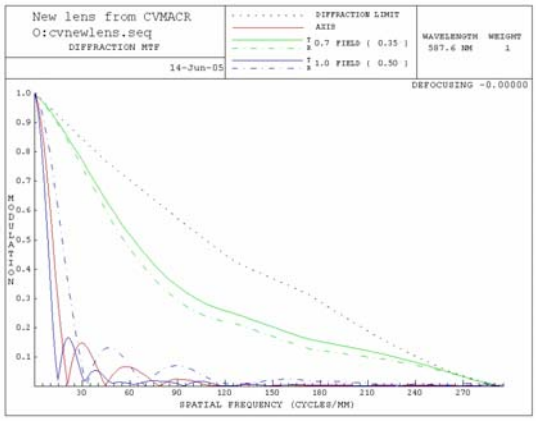

Figure 29. MTF for optimized 2-mirror system presented on-axis and at two locations off-axis (0.35º and 0.5º).

8.3.5 System Functional Test

These tests were made with the camera back in place on the telescope and the focus was adjusted by shims between the primary mirror and the spacer plate. The unavailability of shims in very small increments made this process difficult. Micrometer errors in focus location result in very visible errors in the ability of the system to focus on a target.

Moon Photograph

Leaving the system assembled and the camera attached, the mount was added and the entire system was placed on a tripod. The moon was photographed to gain a human perspective on the performance of the system. The image of the moon, Figure 30, was taken on ASA 50 color slide film and digitized with a Nikon CoolScan V scanner at a resolution of 6.3 µm. The moon takes up about 0.5 degrees of the image and it was cropped fill the frame. The image appears blurry and seems to be out of focus. There are two possible sources of focus error for this photograph. Once the distance from the best focus was found in the interferometer, the distance to the back of the primary was determined. The spacer plate and shims were used to put the camera film plane at the telescope focus. Unfortunately the smallest shims available were 25 µm and such steps will not be sufficient to successfully focus the system on the image plane. The second problem was the change in temperature between the focus adjustment in the lab and the moon picture made at night over a lake at 4 ºC. The temperature should not be a major problem because the camera and telescope are aluminum and should stay in focus for the small temperature difference

of -16 ºC. The atmospheric effects from water vapor off the lake may have an effect, but this should also be small. The focus was the main reason for the lack of image sharpness.

Figure 30: Telescope Photograph of the Moon

Spot Size Pictures

Another method for testing the system is spot size measurements. To measure the spot size, the telescope with camera was placed under the interferometer and lit with collimated light from the HeNe laser. With collimated light coming in, the telescope should output a spot onto the image plane. Multiple photographs using 200 ASA slide film were taken over a range of exposure times for on-axis, 0.35 degrees off-axis, and 0.5 degrees off-axis setups. The resultant spots showed a lot of light scatter around the most intense actual spot area, as shown in Figure 33. These photographs were digitized in a Nikon Cool Scan V scanner and the intensity is compared to the model in the following figures.

The spots in the photographs were compared to Code V expected spot sizes. To compare real versus expected, the width of the spot at half the maximum intensity was used. The real spot plots have an x-unit of pixels. The photographs were taken with 35x25 mm film and the scanned picture size is 5782x3946 pixels which gives a pixel size of 6.3 μm/pixel. For the on-axis element, Figure 32 shows that the expected spot size is approximately 10 μm and symmetric whereas the actual spot sizes, also in Figure 32, are 133 and 82 μm respectively. The expected

0.35 degrees off-axis element, shown in Figure 33, has a spot size of 35 µm radially and 50 µm tangentially and the actual spot sizes, also shown in Figure 33, are 158 and 82 µm. Finally, Figure 34 shows the expected 0.5 degrees off-axis spot size as 80 µm radially and 110 µm tangentially compared with the actual spot sizes of 209 and 133 µm.

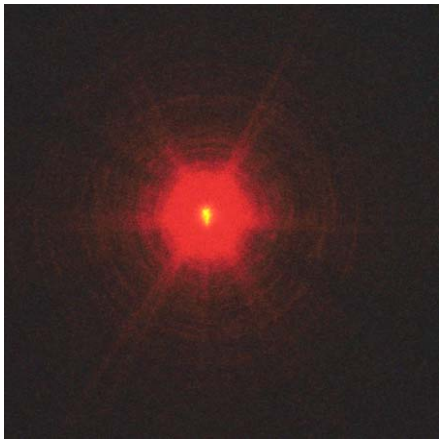

Figure 31. Spot size photograph made with the telescope mounted in the interferometer with camera attached.

The actual spot sizes are larger than expected from Code V. This indicates errors in the system. Spot size error indicates a focusing error as well as form errors. If the spot appears larger than expected but has the same shape, the system may be out of focus [2]. If the spot is a different shape than expected, there may be form error that gives the actual spot its distinctive shape. In this case, the spots are both larger than expected and of a different shape. The expected spots are symmetric on-axis and 0.35º off axis, as shown in Figure 32 and Figure 33, whereas the actual spots have a triangular shape that is slightly upside-down and isosceles. The triangular shape shortens and fattens from on-axis to 0.35º off-axis, shown in Figure 33, and even more so to the 0.5º off-axis spot in which the triangle appears equilateral as shown in Figure 34. The non circular shape of the spots shows that the system has form errors that cause the light to spread in a non-uniform manner. The increase in size of the spots shows some focusing error causing the spot to lose its sharpness.

A perfect system would produce a lone spot high in intensity such as the bright spot in the center of the photograph of this system. However, the spot for this system is accompanied by a large halo of lower intensity light. This shows light scatter present in the system. This light scatter seen in the actual spot diagrams is associated with the surface finish of the optical surfaces. Because the actual surface finish is high compared to the expected, the light will be scattered and will form a large halo around the central spot. Code V is only designed to deal with perfect optical surfaces and as such shows none of the low intensity light seen in the spots produced by this system. As discussed in Section 8.2.6, the surface finish is a good as could be expected for the fabrication process. Therefore, the light scatter present in these spot pictures may be unavoidable in a system that has been diamond turned.

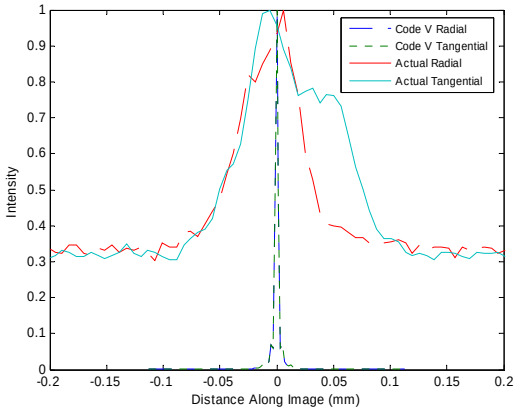

Figure 32. On-axis spot sizes from experiment and model

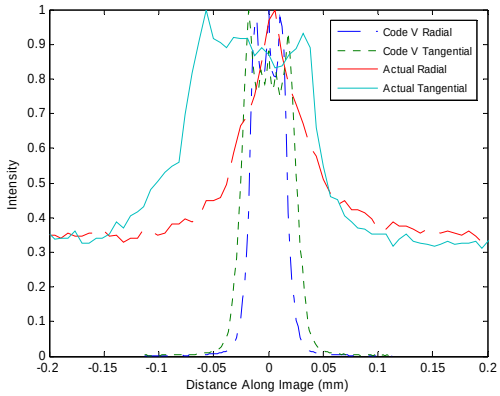

Figure 33. 0.35º Off-axis spot sizes from experiment and model

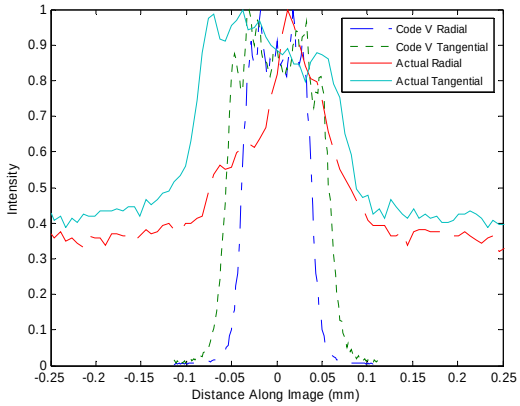

Figure 34. 0.5º Off-axis spot sizes from experiment and model

8.4 ASSEMBLY ISSUES

8.4.1 ASSEMBLED PRIMARY SHAPE

The bolts used on the primary mirror lead to the trefoil shape observed in the system measurement. The primary shape is dominated by astigmatism when assembled. However, with the astigmatism removed a trefoil shape is evident as shown in Figure 36. This shape is not present when the primary is simply held by the tube or unassembled as shown in Figure 35. Also, when the bolts do not have full torque applied, the trefoil shape disappears from the system.

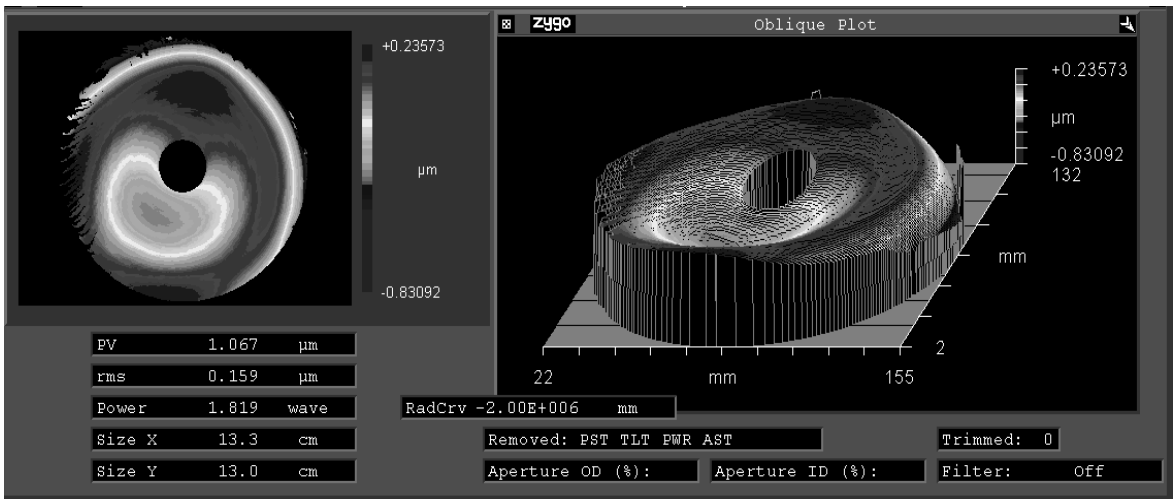

Figure 35. Primary with No Screws and Astigmatism Removed

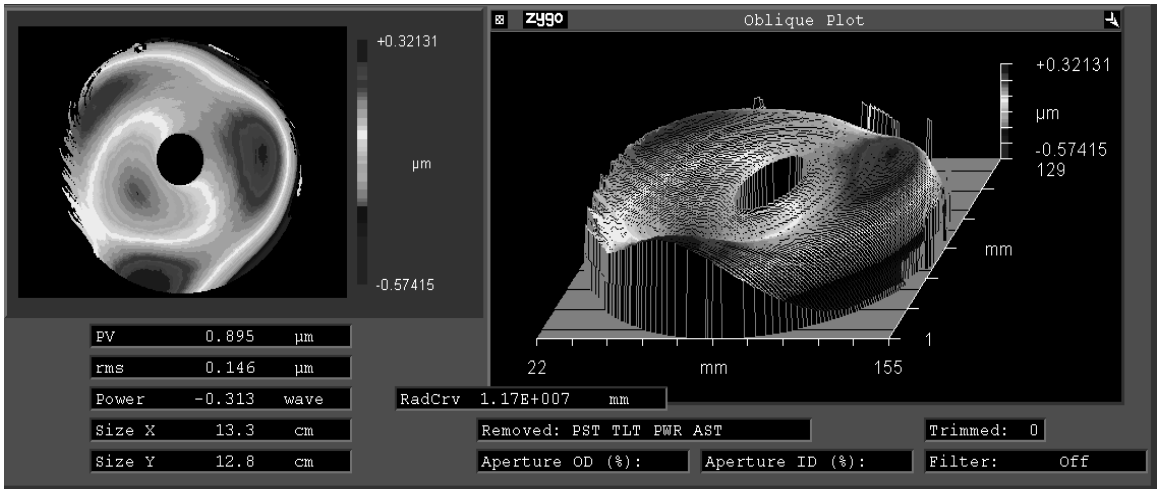

Figure 36. Primary Assembled with Astigmatism Removed

Multiple assembly processes and lack of consistent assembly procedure can add error as well. Upon disassembly, burrs were visible on the edges of the bolt holes at the fiducial surfaces. These burrs were cleaned by scraping the edges of the holes with a deburring tool. However, some burring could remain after this process. This could add error as the burrs could stop the mirrors from fully seating. The resolution on the torque wrench is about 0.25 in lbs, so the application of 1 in-lb could lead to ± 25% variation in torque.

8.5 CONCLUSIONS

The individual optical components and entire telescope system have been analyzed. The component measurements showed surface finishes on the order of 5 nm RMS for both the secondary and primary mirrors. This is greater than the theoretical P-V and RMS values but there are no clear tool marks visible in the measurement which leads to the assertion that the surface finish is as good as can be expected for diamond turned aluminum 6061 with the ASG 2500.

The form error of the secondary is λ/3 which is close to the expected form error of λ/4. The primary mirror shows an asymmetric and astigmatic form error of 2 μm. This indicates that the low aspect ratio of the primary allowed for more deviation than in the secondary. When the primary is pulled down to the chuck, the low aspect ratio causes the mirror to bend to the shape of the chuck. The thin fiducial surfaces are especially liable to bending forces on the vacuum chuck and when bolted to the tube. This explains the 4 μm error seen on the fiducial surfaces as well as why the optical surface does not change by 4 μm when the fiducial surface is pulled flat to the tube's fiducial surface.

The system showed focus and assembly errors. One source of focus error in the system were the interference fits that placed too much pressure on components. The interference fits put pressure on the secondary mirror causing it to deflect. They also prevented the primary mirror from seating on the tube's fiducial surfaces in a repeatable manner. This caused ambiguity as to the location of the primary mirror in the system. This resulted in the system's actual best focus location being 45 μm away from the expected best focus location. In future designs, interference fits should be avoided as an alignment tool.

The inability to accurately place a film plane at the system's best focus location also resulted in focus errors in some of the measurements. The spot size errors that range from 50 μm to 120 μm were affected by the inaccuracy of the film plane location when taking the spot photographs. The photograph of the moon also has focus errors because of the inaccuracy of the film placement.

The system also showed errors resulting from the assembly process. The bolting forces caused a trefoil shape in the system wavefront measurement with a magnitude of 1.5 μm. This wavefront error also affected the spot size by causing asymmetric shapes and was a factor in reducing the

magnitude of the system's MTF. In future designs, flexures should be used to uncouple the bolting forces from the optical surfaces. Also, threaded bolt holes should be countersunk below the surface as burring of the holes caused seating ambiguity in this system. The assembly process for this design did not contain proper steps to ensure repeatability. Future designs will include a step-by-step assembly process with labels on each surface to maintain proper orientation. The surface finish of the mirrors' optical surfaces could not be simulated in Code V. As a result, the light defraction from the surfaces adds a halo effect to the spot photograph that cannot be repeated in Code V. This reduces the actual MTF value of the system.

This system was designed to gain an understanding of optical metrology to prepare for the measurement of more complicated systems. Many problems were faced during the measurements, however, for off-axis conic systems, many of the metrology techniques outlined in this report could be used with slight modifications. The dual-pass primary measurements discussed in 8.2.1 could be modified to measure off-axis components by moving the intermediary reference element off-axis. Also, the fiducial surfaces on the tube and the primary mirror were too large to be measured on the Zygo GPI. This is easily solved by slightly reducing the diameter of designed mirrors so that the fiducials can be measured in the 150 mm diameter aperture of the GPI. An HP linear interferometer was added to the Zygo GPI to obtain accurate vertical location for the optical stage. The Talysurf measurements can be repeated for off-axis components. Adding a rotary index to rotate the mirror would increase the repeatability of the measurements and allow for more specific location knowledge. The hole in the primary mirror made taking full hemispherical measurements with the Talysurf impossible. Removal of holes from the optical surface in future designs will solve this problem.

The next stage of this project will involve measuring the optical components and optical system of a three mirror anistigmat made with off-axis conics. This will allow for the modification and improvement of these measurement techniques. The goal will be to supplement the techniques outlined in this report so that they may be used to accurately measure any optical surface or system.

REFERENCES

1. Lamonds, L., Wanna, N., Woodside, R., Dow, T.A., Garrard, K., Sohn, A., "Design and Fabrication of a Two-Mirror Diamond Turned Telescope", Progress Report #1, Navy Electro-Optics Center, August, 2005.

2. Horne, D.F., "Optical Production Technology," Adam Hilger, 2nd Edition, Bristol UK, 408-410, 1972.

3. ZYGO's Guide to Typical Interferometer Setups

4. Malacara, Daniel, "Optical Shop Testing", John Wiley & Sons, 2nd Edition, New York, 1992.

9 TEM AND RAMAN SPECTROSCOPIC ANALYSIS OF HIGH PRESSURE PHASE TRANSFORMATIONS IN DIAMOND TURNED SINGLE CRYSTAL SILICON

Timothy Kennedy
Graduate Student
Ronald Scattergood
Professor
Department of Materials Science and Engineering

Diamond turning and parallel flycuts were performed on (100) Si along the <011> direction using both -30° and -45° diamond tools with feedrates falling with in a 1 to 15 µm/rev range. All samples were analyzed with both micro and macro Raman, polarized Raman, and preliminary cross sectional TEM has been completed on the 1 and 5 µm/rev samples. A correlation between the Raman spectra and cross sectional TEM images of the diamond turned silicon will be attempted. Dislocation loops and slip planes were found at depths up to 250 nm below the surface of both feedrates; along with a previously unseen structure below the amorphous layer. Flycut samples were machined with two separate set of tools, and it was found that depending on tool edge design an amorphous layer was not always created. TEM analysis is still needed to analyze subsurface damage, and to determine the deformation mode (i.e. high pressure phase transformation (HPPT) or dislocation movement). Recent results have provided more insight into the lack of dependence between feed rate and the depth of the amorphous layer.

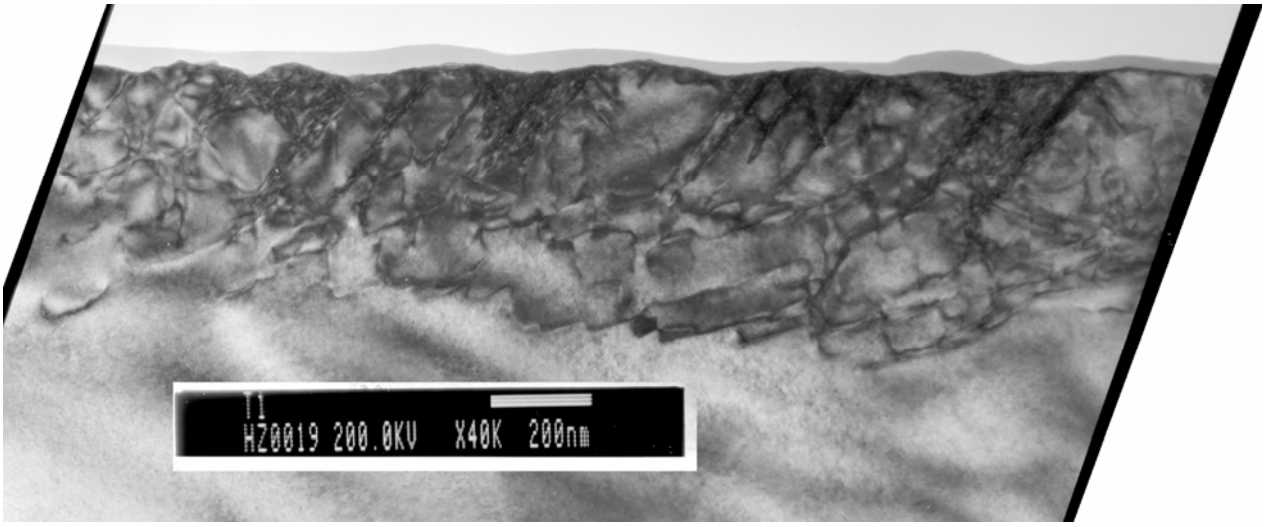

9.1 INTRODUCTION

Diamond cubic silicon (Si-I) is a brittle material under standard temperature and pressure, but when exposed to a high pressure environment the crystal structure transforms into a ductile β-tin metallic phase (Si-II). Once the Si-II is unconstrained it back transforms into multiple forms of Si, mainly amorphous Si (a-Si) and Si-I. The total transformation of silicon depends on loading, unloading, and temperature is shown in the transformation schedule in Figure 1. This transformation allows silicon to be machined without brittle fracture occurring, but the back transformation alters the subsurface (~500 nm in depth). This alteration can be divided into two layers: an amorphous layer and a damage layer. The amorphous layer extends from the surface down as far as 200 nm; this is the byproduct of the back transformation process which creates amorphous silicon (a-Si). Below the amorphous layer a damage layer extends another 300 nm; this layer is comprised of dislocation structures. In situ analysis of this transformation during the manufacturing process is impractical. Using transmission electron microscopy (TEM) and Raman spectroscopy a portrait can be formed of the deformation mechanism in diamond turned silicon.

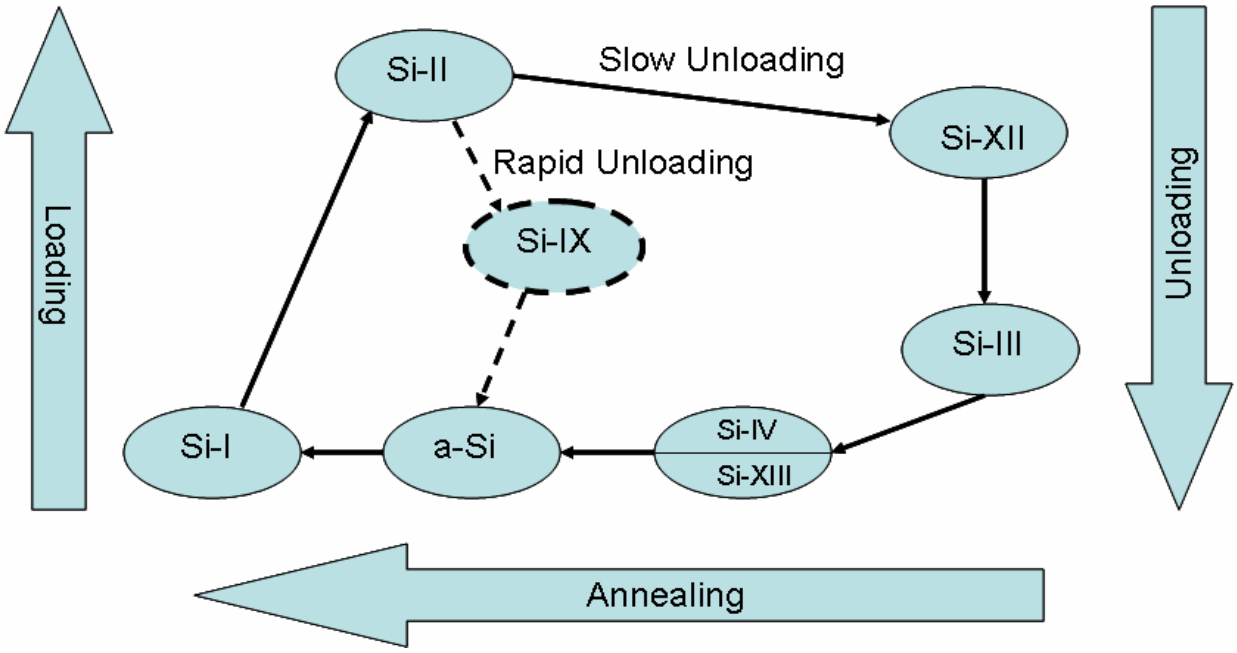

Figure 1. Silicon transformation schedule. [1]

9.2 PROJECT DETAILS

TEM and Raman data was collected from (100) oriented silicon that was diamond point turned along the <110> type direction. Different crystal orientations are available but it has been shown

[2] that (100) oriented silicon provides the best ductility. Samples were machined using a traditional diamond turning setup and a parallel fly cutting technique the latter using two sets of tools consisting of a -30° and -45° rake angle round nose diamond tool.

9.2.1 EXPERIMENTAL SETUP

A Rank Pneumo ASG 2500 Diamond Turning Machine was used to create the samples for this study. Two diamond turning setups were used; the first a traditional T-lathe setup and the next a parallel fly cutting setup. The fly cutting samples were 10 mm wide by 20 mm long, and are oriented so that the cutting direction follows the <110> type direction across the 10 mm width; as compared to an entire wafer for the lathe operation. Two sets of tools were used; one set sharpened by IMT and the other manufactured by Edge Technologies. The tools used were 3 mm radius round nosed diamond with rake angles of -30° and -45°. Unlike the traditional T-lathe setup where the tool is on the x-axis and the sample in on the spindle; parallel fly cutting has the tool on the spindle while the sample is on the x axis parallel to the tool so that a flat cut can be produced. Since carbon reacts with silicon, the latter technique reduces the diamond tool wear since the diamond is not always in contact with the silicon. Spindle speed and feed rate need to be optimized so that the layered structure can be controlled through machining, instead of other processes such as thermal annealing. Samples have been prepared with feed rates between 1 and 15 μm/rev for the lathe operation, while only 1 μm/rev and 5 μm/rev was used for the fly cutting.

9.2.2 MATERIAL CHARACTERIZATION

To characterize the machined silicon two techniques will be used; Raman spectroscopy and transmission electron microscopy (TEM). Raman spectroscopy measures the intensity and wavelength of inelastically scattered light from molecules. The scattered light is shifted by the molecular vibrational energy, which is directly controlled by the interatomic bond length of the atoms in the sample.5 In the case of silicon each crystalline phase has its own interatomic bond length, thus each phase would have a unique and sharp Raman spectrum. In the case of a-Si, the interatomic bond lengths vary so the Raman spectrum from a-Si is broadened. For this study it is important to know crystalline silicon (Si-I) has a peak at around 520 cm^{-1} while amorphous silicon (a-Si) centers around 470 cm^{-1}.

A different Raman technique known as polarized Raman (non-polarized Raman was described previously) was also used to analyze the machined silicon. In polarized Raman different structures have different Raman active modes, which will scatter photons with energy (cm^{-1}) different from the incident wave. The scattering intensity *I* is given by

$$I = C\sum_j \left| e_i \cdot R_j \cdot e_s \right|^2$$

Where C is a constant, e_i and e_s are the incident and scattered polarization vectors, respectively, and R_j is the Raman tensor, determined from group theory for the different crystal structures. Linear polarizers were used to fix the directions of e_i and e_s, and the Si wafer was on a rotating sample stage. Rotating the stage by an angle θ changes R_j such that

$$I \propto \sin^2 2\theta$$

for single crystal Si cut along the (100) plane. Amorphous Si has no directional dependence, so the intensity for its peak should remain constant as θ varies. Scans were done on wafers machined at different rates and with different tool tip rake angles. The incident polarization was set vertical, and the scattered was set horizontal. The [110] direction of the sample initially pointed vertically. The angle θ with the vertical was increased in increments of 10° for each scan. Data was taken for the first quadrant, and the values of the others were extrapolated by symmetry. Intensities of the peaks at 470 cm^{-1} (a-Si) and 520 cm^{-1} (Si-I) were plotted on polar graphs as a function of θ[1]. Even though Raman spectroscopy is a useful tool for its qualitative information it does not provide quantitative data like TEM.

TEM can provide high resolution micrographs through the use of a high energy electron beam (200 kV) that is transmitted and diffracted through the electron transparent sample. Cross-sectional TEM (XTEM), selected area diffraction (SAD), and bright field-dark field (BFDF) imaging were utilized for this study. XTEM provides the proper view of the subsurface layers compared to the more traditional planar view. To corroborate the Raman spectroscopic data SAD was used to determine the phases present in the subsurface. SAD involves the use of an aperture to reduce the intensity and the area of the incoming beam, and then viewing the diffraction pattern. A diffuse halo pattern would indicate amorphous material, while evenly spaced spots would indicate a crystalline phase. In TEM images can be created from both transmitted and diffracted beams by the use of apertures. Bright field images result from the from the selection of the transmitted spot, while dark field images are created by selecting the diffracted spot that appears to the left of right of the transmitted spot. BFDF can show differences in the phases in the sample, the presence of dislocations, and strain fields.

[1] All Raman spectroscopy data and information provided by Benjamin Gilbert, Masters Student, Department of Physics, NCSU

9.3 RESULTS

9.3.1 LATHE MACHINING RAMAN RESULTS

Samples were lathe machined using the IMT tools with -30° and -45° rake angle tools at feed rates of 15, 7, 3, 2, and 1 μm/rev, and then analyzed through non-polarized Raman spectroscopy. A possible dependence between feed rate and the thickness of the a-Si layer can be seen in Figure 2 when machinied with a -30° rake angle tool. This dependence is based on the decreasing Si-I peak at 520 cm^{-1} as feed rate lowers until it is consumed by the shoulder of the a-Si peak at 1 μm/rev.

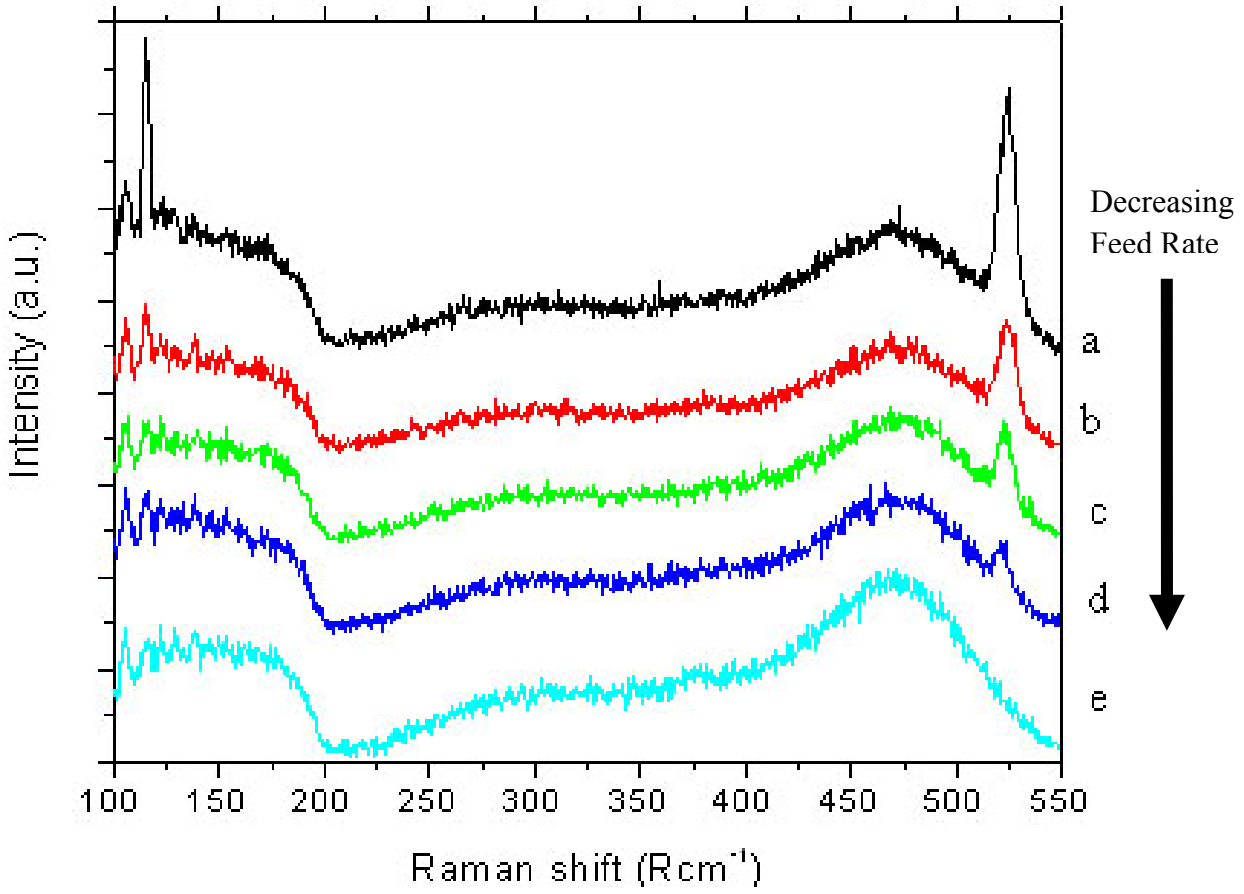

Figure 2. Raman spectra at feed rates a) 15, b) 7, c) 3, d) 2, and e) 1 μm/rev IMT -30° tool, showing a possible dependence on feed rate and a-Si thickness. [2]

When samples that were machined with the -45° rake angle tool the same possible dependence was not evident as seen in the Figure 3. The Si-I peak does not disappear into the a-Si shoulder as in Figure 2. A comparison between the results of the two tools is impractical due to the various factors. Tool forces, tool wear, stress states at the tip all depend on the rake angle, and

the condition of the tool. Little is known about the tip condition at the time of machining the measured areas. Silicon wears the tip aggressively thus making it difficult to know the sharpness of the tool, or whether damage was incurred. Because the machining forces are highly dependent on the condition of the tip, the stress states imposed on the materials will differ largely. This may result in different material accommodation mechanisms, specifically the size of the transformation zone, making comparison between machining runs difficult. [2]

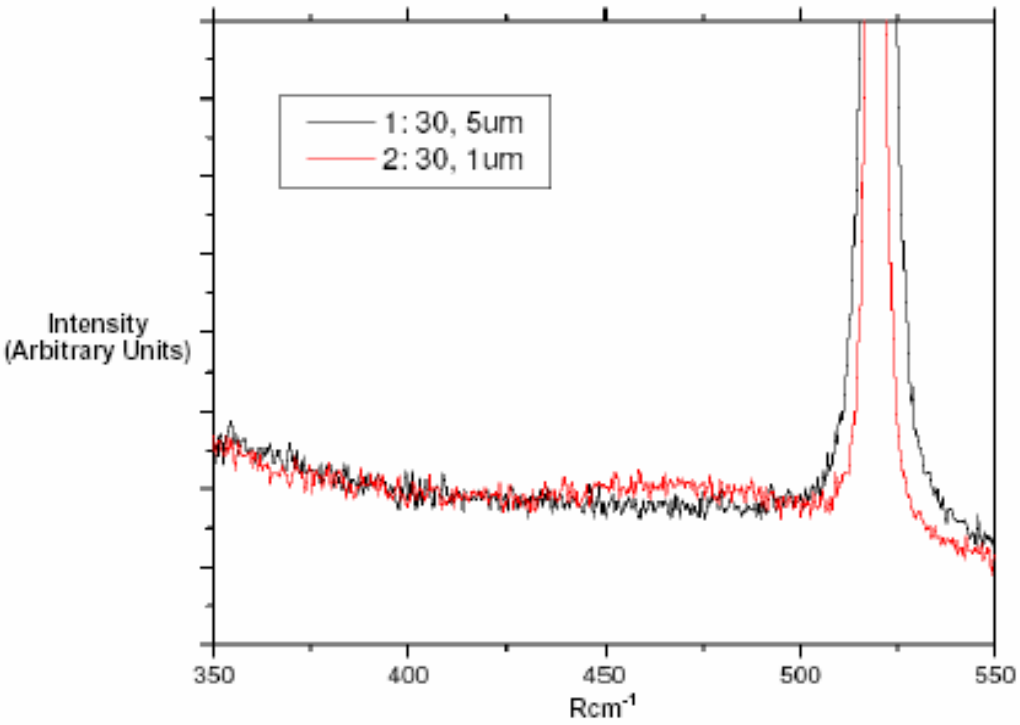

Figure 3. Raman spectra showing no dependence between feed rate and a-Si layer thickness with a -45° rake angle tool. [2]

9.3.2 LATHE MACHINING TEM RESULTS

Once the Raman spectra were recorded the silicon samples were made into TEM samples. It was determined that only the samples machined with the -30° IMT tool at 5 and 1 µm/rev would be viewed since the Raman spectra showed that these parameters would provide the best view of the differing thickness of the a-Si layer. The micrograph in Figure 4 provides the best view of the subsurface layers for silicon machined at 5 µm/rev. Starting from the bottom up the following layers are present; undisturbed silicon, then a layer of dislocations 400 nm thick, above the dislocations is the a-Si layer which is on average 44 nm thick. Inside the dislocation layer slip planes and dislocation loops exist. The slip planes lie at a 54° from the (100) surface, signifying a (111) slip system. The (111) slip system is the most common in plastic deformation in diamond cubic materials. Figure 5 shows that the a-Si and the beginning of the dislocation layer

do not have the same topography which is somewhat unexpected. SAD indicated a diffuse halo, showing that he top layer was indeed amorphous silicon.

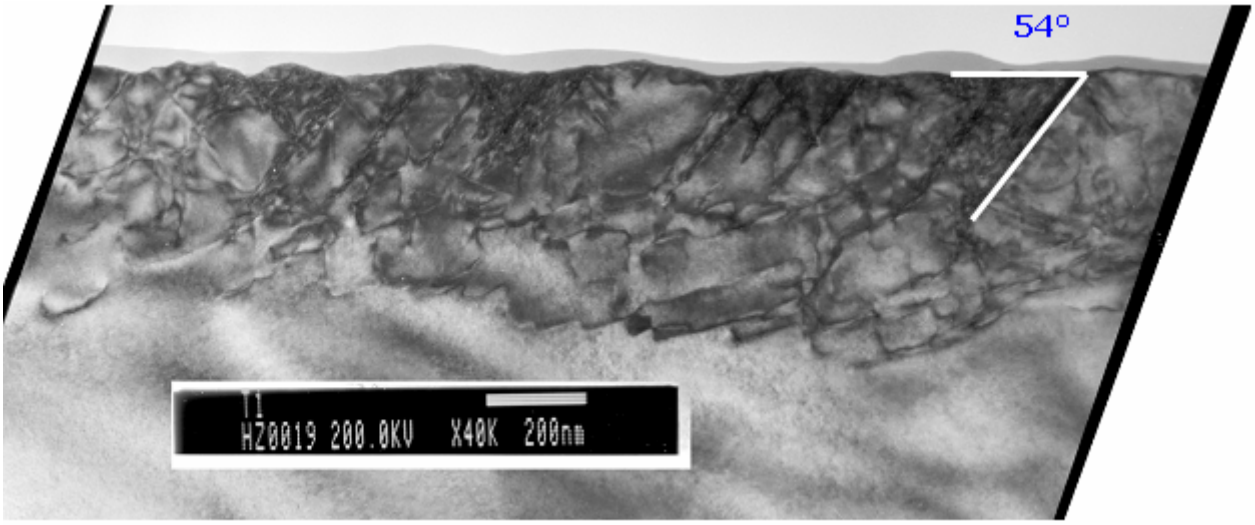

Figure 4. TEM micrograph machined 5 µm/rev with a IMT -30° tool at 40,000x. The (111) slip system angle is shown along with the a-Si layer and the dislocation microstructure.

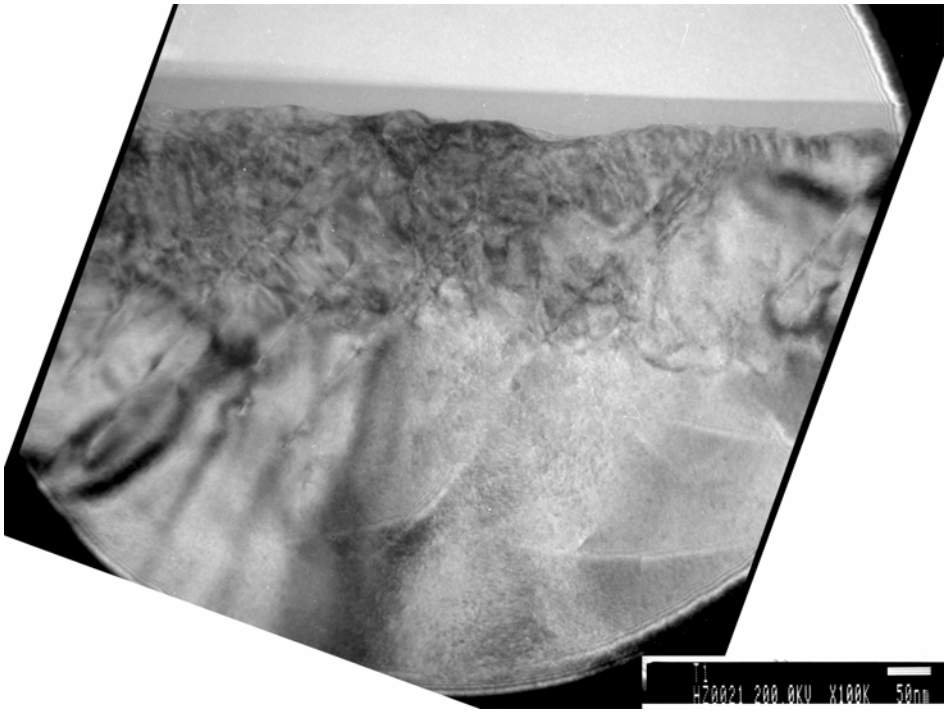

Figure 5. TEM micrograph machined 5 µm/rev with a IMT -30° tool at 100,000x. Showing detail view of the a-Si layer.

The use of bright field/dark field (BFDF) pairs helps to view the dislocation structures, any phase contrast, and the strain filed that are present in the silicon. Strain fields and dislocation loops are present in the BFDF pair in Figure 6. When the lattice of a crystalline material is strain, it changes the way electrons are transmitted through the structure. This change is usually seen by contrast change. It is another way to help indicated a strained lattice, view dislocations, and view alloying elements or precipitates.

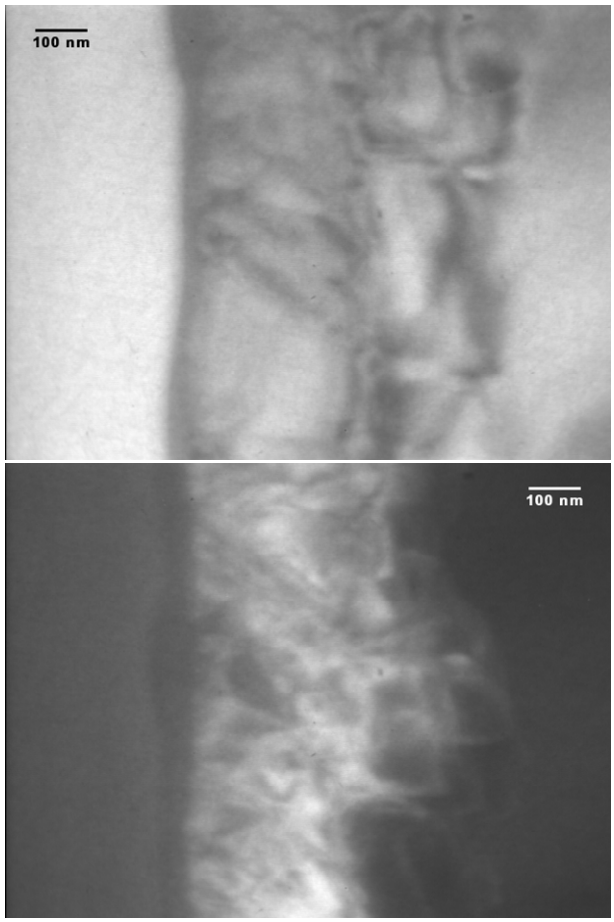

Figure 6. BFDF pair, machined at 5 μm/rev with a IMT -30° tool, 196,764x. Notice the strain induced contrast change in the dislocation layer.

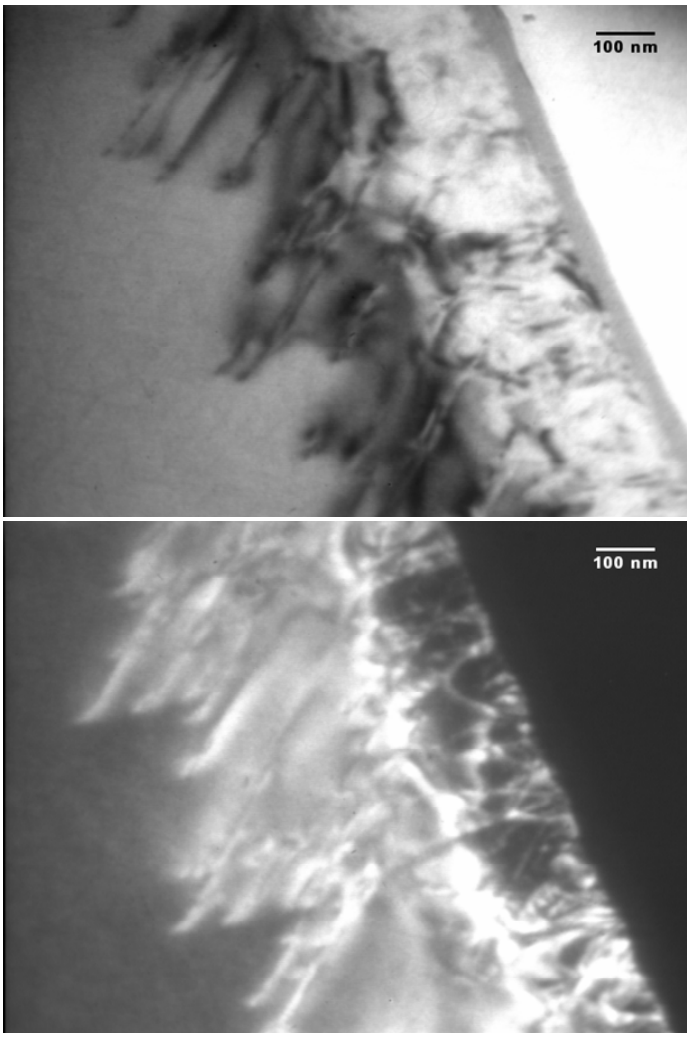

Figure 7. BFDF pair, machined at 1 μm/rev with a IMT -30° tool, 196,764x. Notice the slip planes going deep into the undisturbed silicon.

The machining parameters in Figure 7 and 8 are the same, 1 μm/rev with a IMT -30° tool. Even though one does not see the same structure in the subsurface, it all depends on the angle of the sample and the angle of the diffracted electron beam. So in Figure 7 slip planes penetrate deeply (400nm) into the undisturbed silicon. While Figure 8 shows dislocation loops and a highly strain dislocation layer.

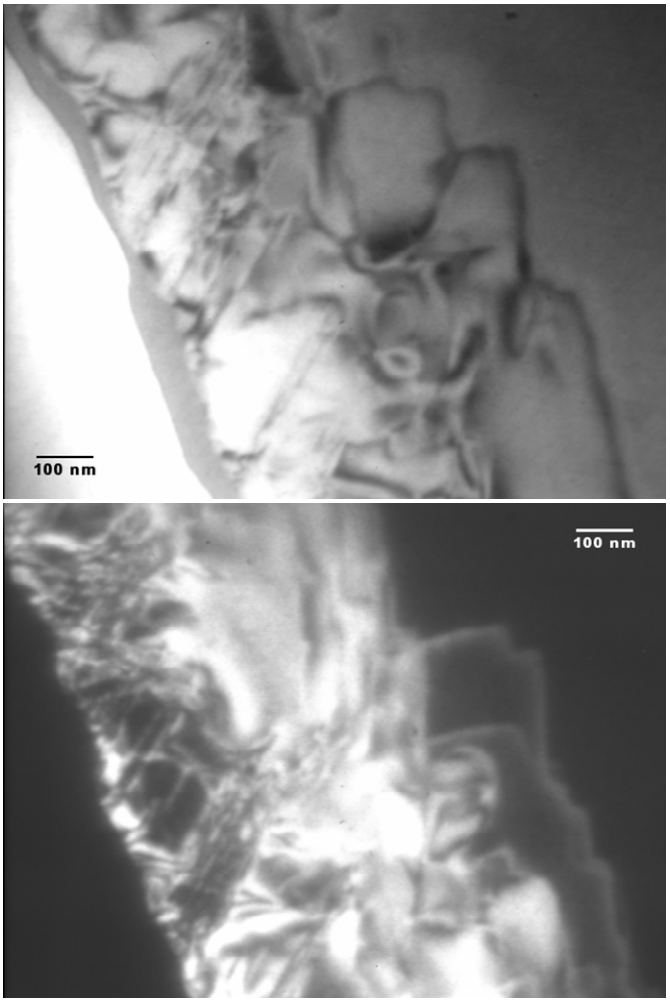

Figure 8. BFDF pair, machined at 1 μm/rev with a IMT -30° tool, 196,764x. Notice the dislocation loops going in and out of the undisturbed silicon.

It is important to try to compare the TEM and Raman spectroscopy results. The Raman results indicate that the a-Si layer at a feed rate of 1 μm/rev should be thicker than the a-Si at a feed rate of 5 μm/rev. To compare the TEM results, the a-Si layer is measured and then plotted versus feed rate, Figure 9. The result form this comparison is surprising. There is no statistical difference between the thickness of the a-Si layer at the two feed rates. Only 4 nm separate the layers, and this is contradictory to the Raman spectroscopy results. Due to time constraints no fly cutting samples were imaged in the TEM.

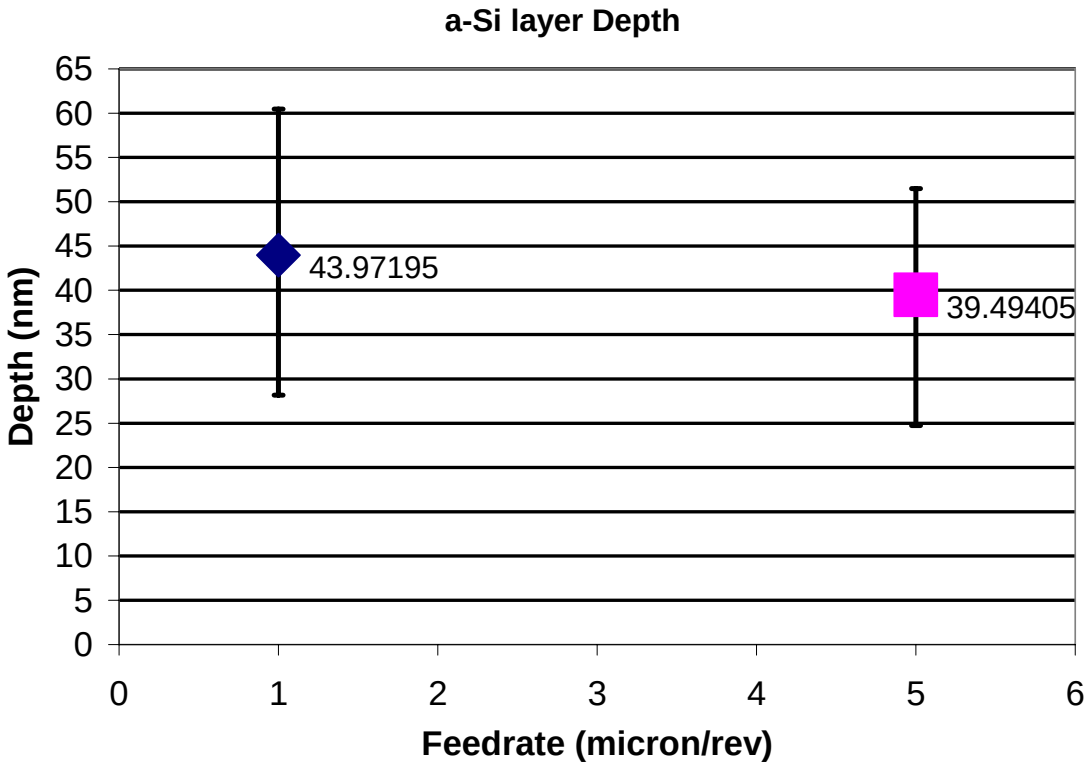

Figure 9. Depth of the a-Si layer versus feed rate. There is no statistical difference between the to feedrates, which counters the Raman spectra for those feed rates.

9.3.3 FLY CUTTING RAMAN RESULTS

An important step was to make sure that the lathe machining and fly cutting created the same Raman spectra. None of the fly cutting Raman spectra matched the lathe machining spectra; Figure 10 compare to Figure 2, and Figure 11 compared to Figure 3. The spectra did not have the same relative ratio between a-Si and Si-I. It was determined that the spectra were near enough to each other as to not machine all the sample using lathe machining.

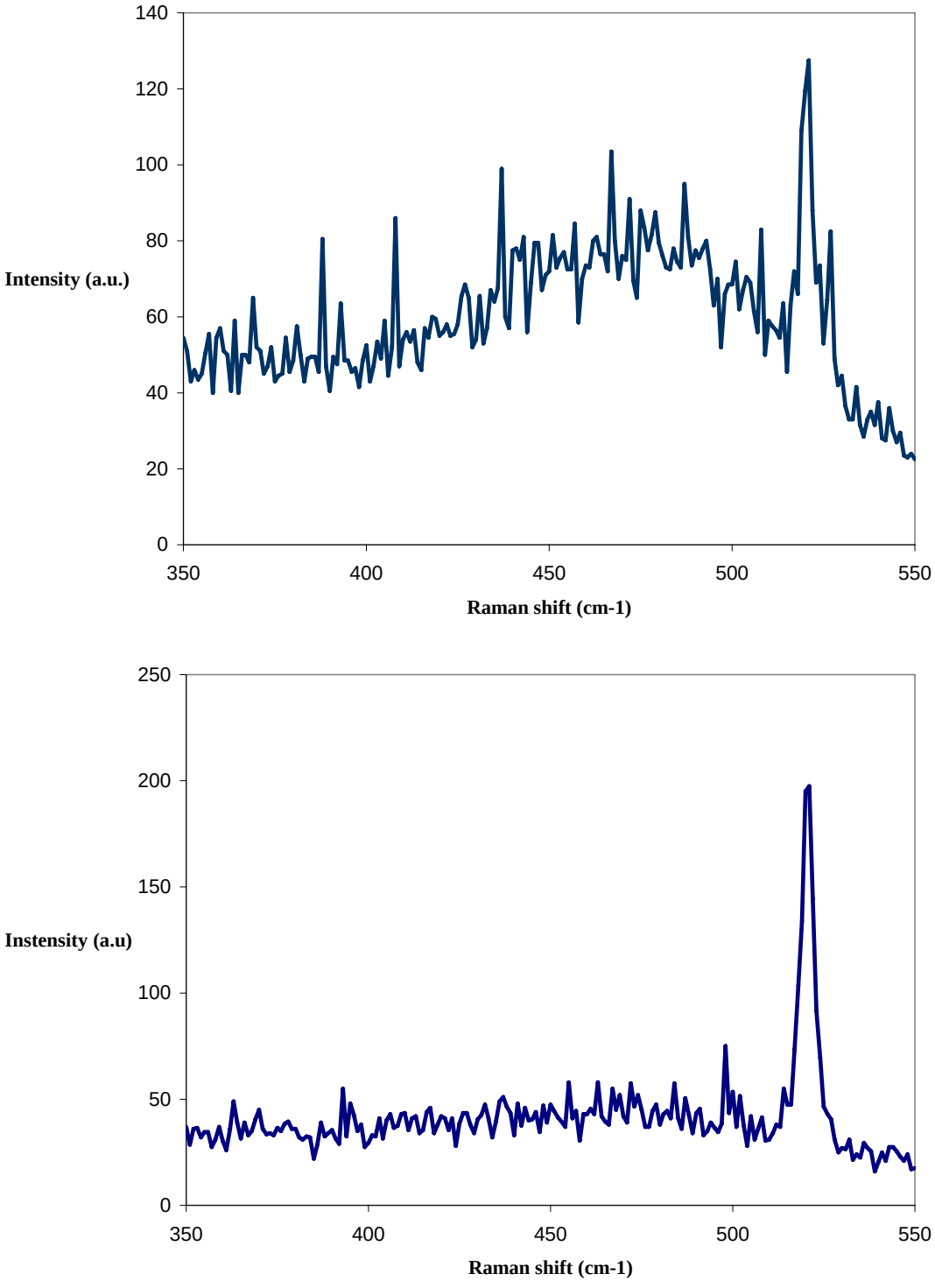

Figure 10. Top: Raman spectrum, silicon machined at 1 μm/rev with a IMT -30° tool
Bottom: Raman spectrum, silicon machined at 5 μm/rev with a IMT -30° tool

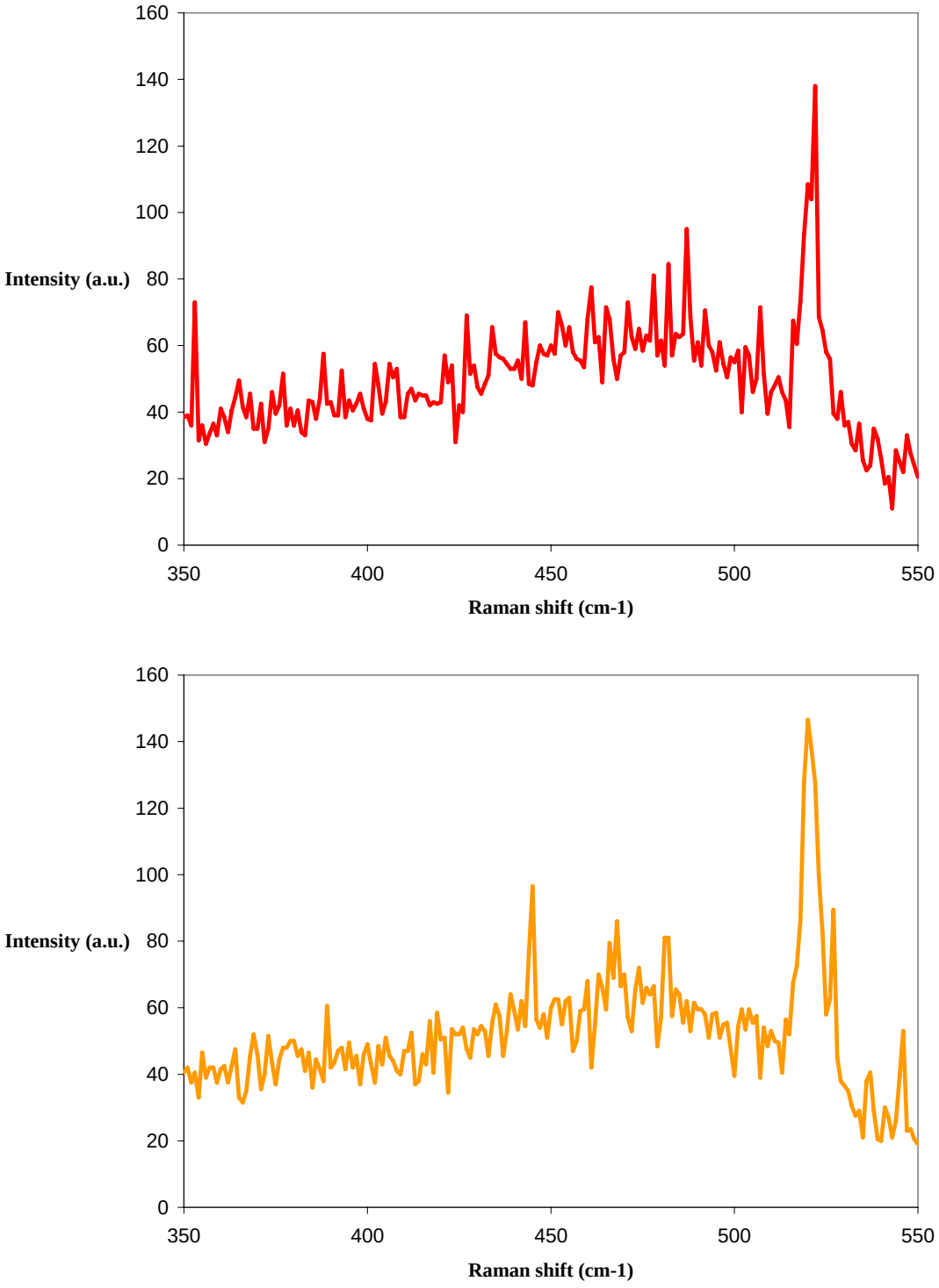

Figure 11. Top: Raman spectrum, silicon machined at 1 µm/rev with a IMT -45° tool
Bottom: Raman spectrum, silicon machined at 5 µm/rev with a IMT -45° tool

When samples were machined by the Edge tools with both -30° and -45° rake angle tools at 5 and 1 μm/rev there was no sign of any amorphous material, only a sharp Si-I peak at 520 cm^{-1}. This is troublesome since the surface showed no signs of brittle fracture. When machining silicon it is usually assumed that when brittle fracture occurs on the surface that no amorphous material is created. One of the ideas behind ductile machining of brittle materials is that a second phase is formed through a high pressure phase transformation to facilitate the plastic deformation of the machining process. The Raman spectra of both the -30° and -45° Edge tools, regardless of feed rate, showed the same lack of an a-Si peak at 470 cm^{-1} so only the -30° Edge tool at 1 μm/rev is shown in Figure 12. All of the tool parameters are the same between the IMT and Edge tools, so it is unclear to why there should be a difference between the two sets of Raman spectra. So to ensure that the Raman spectra were accurate from both tool sets, polarized Raman was utilized. The results that come from the polarized Raman help to clear the picture of the characterization of the subsurface.

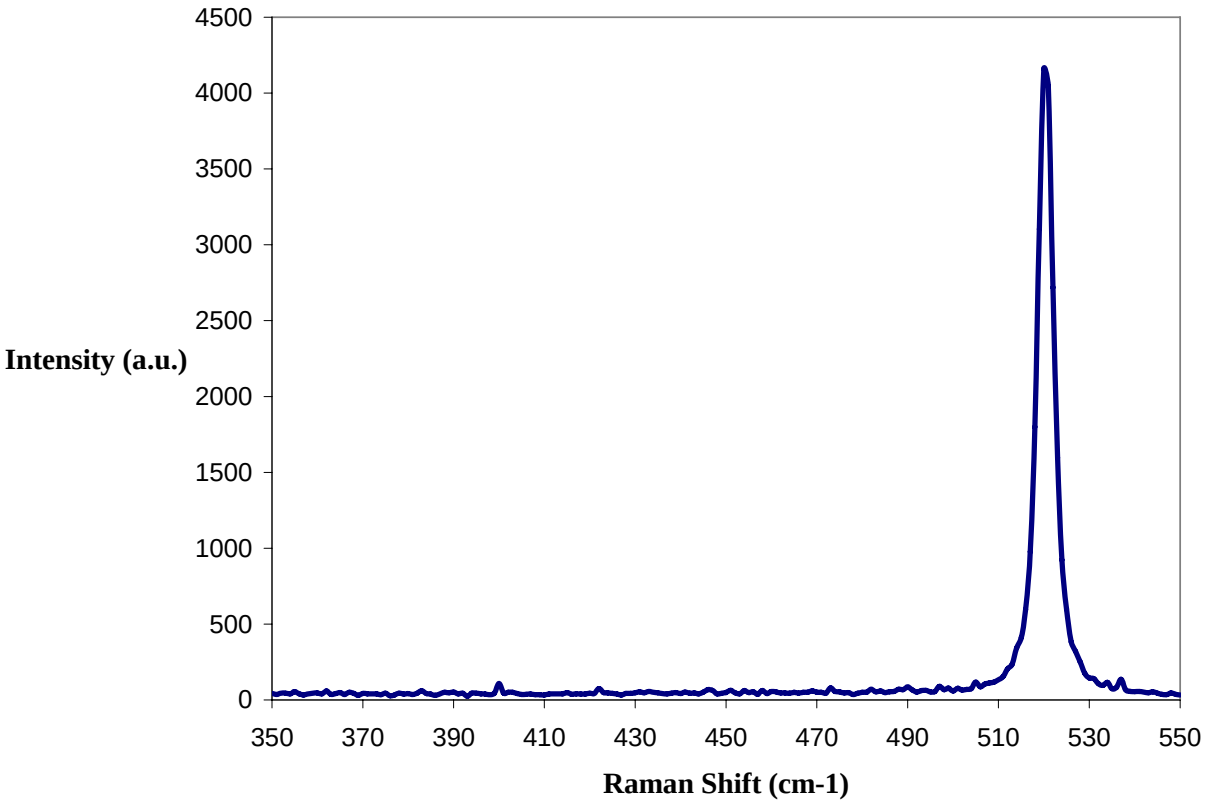

Figure 12. Raman spectrum of silicon machined at 1 μm/rev using a -30° Edge tool showing lack of a-Si at 470 cm^{-1}

As mentioned previously the intensities of the a-Si and Si-I were plotted as a function of polarization angle. The a-Si peak has no dependence on angle since it has no crystal structure. Si-I follows a clover leaf pattern that is expected from the physics of Raman and the direction <110> as can be seen in Figure 13 and 14.

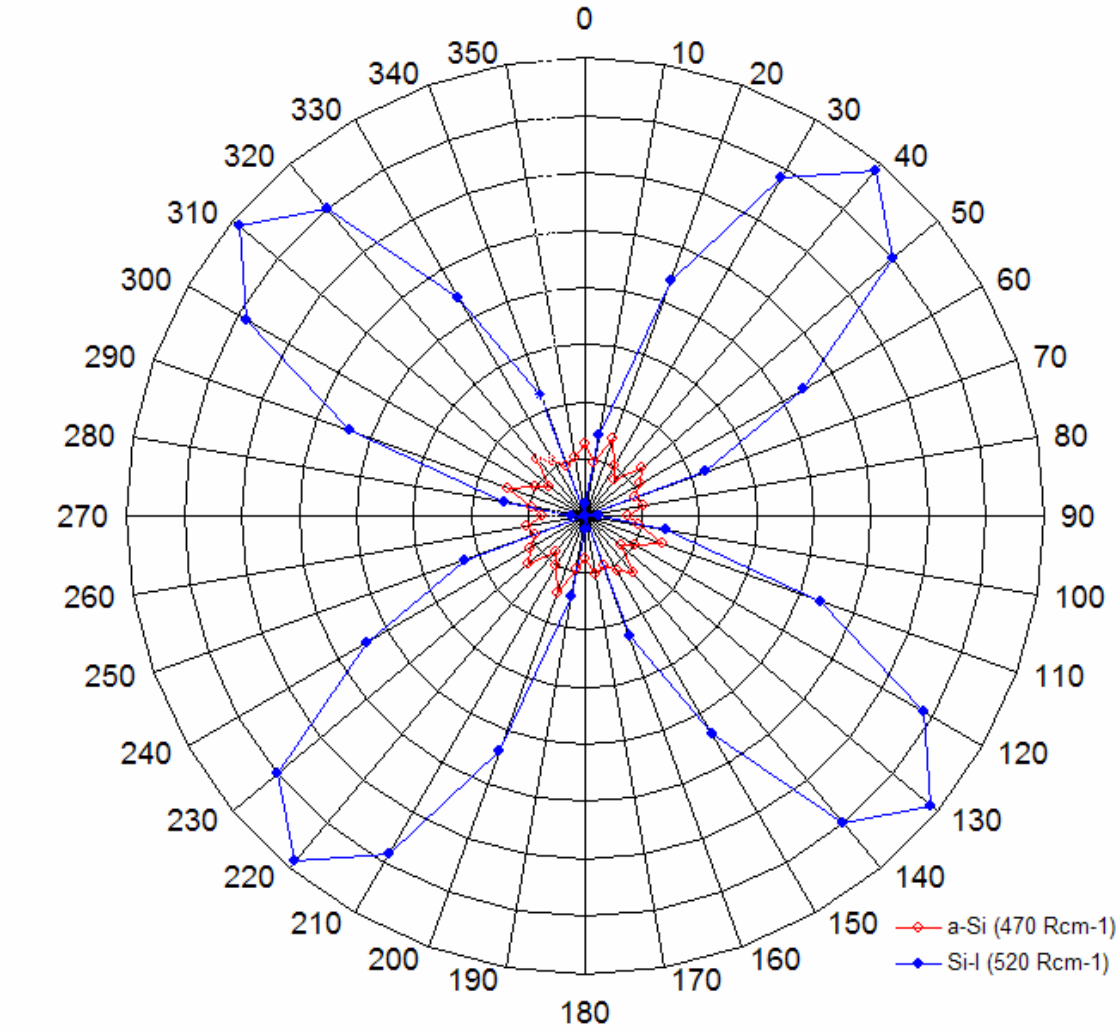

Figure 13. Polar Raman plot of silicon machined at 1 µm/rev with a IMT -30° tool.

The question that arises from the new polarized Raman and the Raman spectra previously recorded is that the previous spectra were recorded without regard to polarization orientation. For example, the previous Raman shows complete amorphization at 1 µm/rev, but as the polar plot shows in Figure 13 the measurement could have been taken at an angle of 0°. This can explain the fact that preliminary Raman results had been contradictory to the previous results. The new polar plots also show that there might not be a dependence between feed rate and amorphous layer thickness as previously theorized. The layer thicknesses shown in Figure 9 can now be considered valid knowing that there could be no dependence.

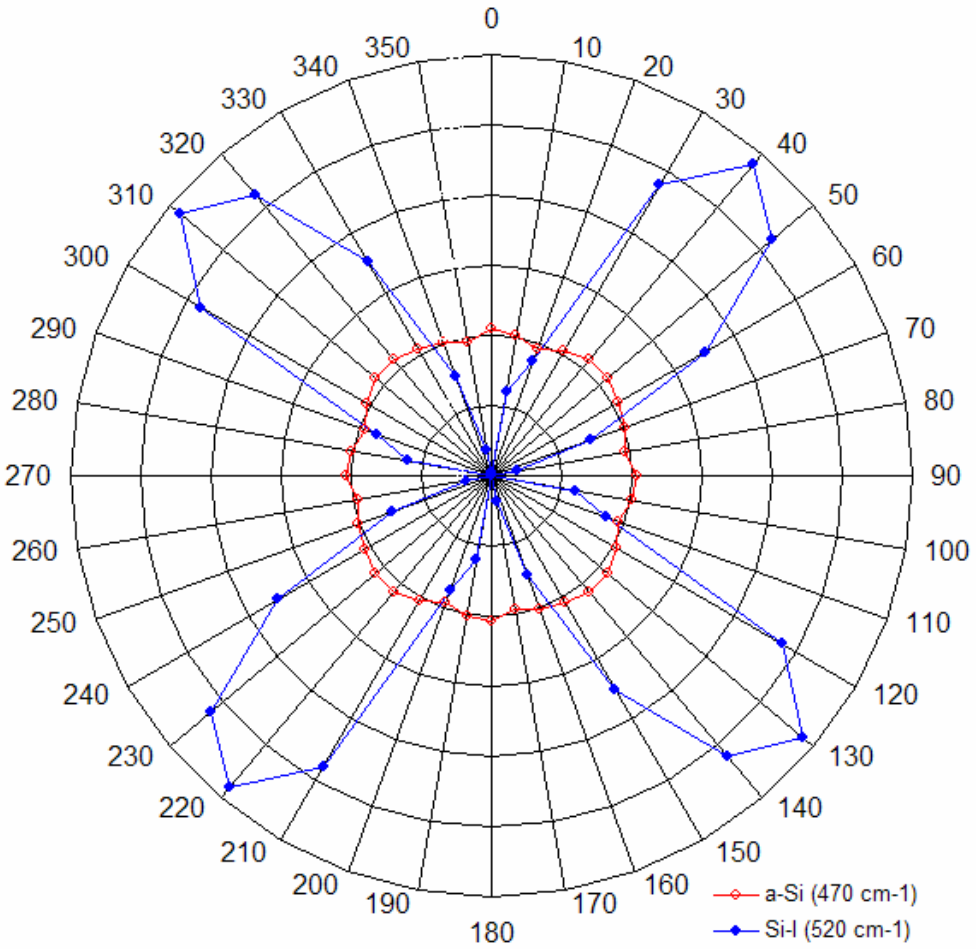

Figure 14. Polar Raman plot of silicon machined at 1 μm/rev with a IMT -45° tool.

9.4 COMPARISONS AND CONCLUSIONS

To make sure that the TEM results are on par with what other research groups have seen a comparison is need. Other groups [3, 4] have reported dislocations, dislocation loops, and slip planes. If an HPPT is occurring then the loops and slips planes indicate a normal metallic deformation mode when the silicon transforms into ductile Si-II. Another point is the existence of the amorphous layer. Once again there is evidence for either an HPPT or other deformation mode. The theory in silicon HPPT is that upon unloading the Si-II will back transform through various phases until it reaches the amorphous stage, at which time it does not have enough energy to recrystallize into Si-I leaving a metastable a-Si, as illustrated in Figure 2. If viewed through a traditional deformation mode, the amorphous layer exists due solely to the extreme high pressure at the surface under the diamond tool, and the dislocations underneath follow

traditional silicon slip mechanisms. More in depth studies will need to be performed to pin point the true deformation mechanism.

From the TEM and Raman data it is clear that the back transformed material contains an amorphous layer and a deeper damage layer. Multiple research groups have also seen this structure, but it is important to note that there has been no in depth evaluation of the damage layer before. Before the polar plots were recorded the Raman spectra and TEM images were contradictory to each other, due to the lack of a statistical difference in a-Si layer thicknesses. Now taking into account the polar plots the TEM data and Raman data can now be seen in good comparison to each other. At this point, the existence of an HPPT in silicon during diamond turning is still questionable, and any mode or mechanisms set forth are only theoretical. To determine whether or not silicon undergoes an HPPT, more samples at various feedrates need to be created and analyzed though both TEM and Raman spectroscopy both in cross section and plan view.

9.5 FUTURE WORK

A complete study of surface roughness will be conducted using optical profilometery, after which any remaining Raman data will be collected. Once the non-destructive analysis is complete, TEM samples will be created. If the TEM data is inconclusive to the difference between tools, tool edge measurements will be made to determine the difference in tool geometry.

REFERENCES

1. Domnich, V. and Y. Gogotsi. “Phase Transformations in Silicon Under Contact Loading”, Rev. Adv. Mater. Sci. 3(2002) 1-36

2. Randall, T., M.S. Thesis, *Characterizing the Ductile Response of Brittle Semiconductors to Dynamic Contact Processes*, North Carolina State University, 2004. http://www.lib.ncsu.edu/theses/available/etd-06182004-104005/

3. Shibata, T. “Cross-section transmission electron microscope observations of diamond-turned single-crystal Si surfaces”. Appl. Phys. Lett. 65 (20), 14 November 1994. 2553

4. Kunz, R. “High Resolution studies of crystalline damage induced by lapping and single-point diamond machining of Si(100)”. J. Mater. Res., Vol. 11, No. 5, May 1996. 1228

10 NON-CONTACT TRANSPORTATION SYSTEM USING ULTRASONIC FLEXURAL WAVES

Yanbo Yin
Graduate Student
Paul I. Ro
Professor, Mechanical & Aerospace Engineering, Department of,

A non-contact transportation system using traveling waves generated by two-mode excitation is presented. The system consists of two actuators powered by amplifiers whose phase angle difference can be adjusted. To investigate the object motion performance, the steady-state speed changes with the mass of the objects on the beam, input power, and phase difference and excitation frequency are investigated. With the input voltage of ±300V, the steady-state speed reaches 17cm/s. The motion direction reverses when the phase angle difference changes from 90 to 270 degrees. The transportation mechanism is derived using sliding film and Finite Element Method (FEM). The FEM results show that the air streaming flow moves along the traveling wave propagation direction. The the object motion is simulated with Matlab. The results agree well with the experimental results.

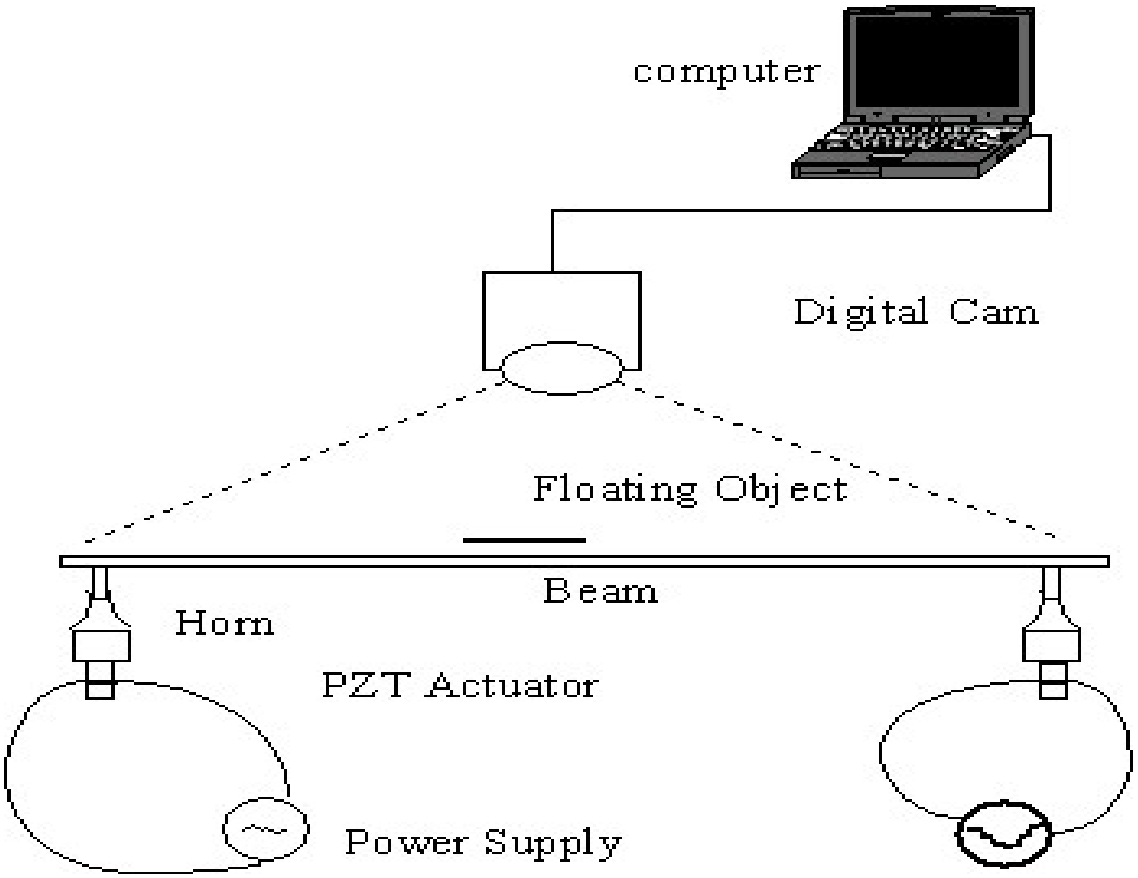

10.1 INTRODUCTION

Handling and processing precision products, such as Compact Disc, LCD, LSI and silicon wafers require strict conditions to keep the products from acquiring tiny defects, scratches and stains. A non-contact method of transferring these products will satisfy these conditions. There are several techniques proposed for such transportation, for example, gas bearing and transportation with an electromagnetic or static electric force. However, several problems in these systems have to be overcome. In the electric or electromagnetic systems, the levitated objects are constrained to electrically conductive materials. In the gas bearing systems, not only the volume of gas needed but the levitation and transportation mechanism is too complicated and expensive to be conducted. Acoustic levitation can be employed in non-contact transportation systems because of the following advantages: (1) the materials type is no limited for the levitated object, (2) compact size, (3) free of noise and (4) no demand for a large amount of clean gas.

The Near Field Acoustic Levitation (NFAL) mechanism is evaluated by Hashimoto [2] and Adi Minikes[3],respectively. The levitation experiment is conducted based on the theoretical results [12]. A non-contact transportation system is designed to transport planar light object [2] [8]. The non-contact transportation of large sized planar object system is investigated by Takafumi[9]. The serial and parallel connections of the transportation systems are also investigated by Hashimoto [10]. A non-contact linear air bearing based on NFAL is designed [11]. The transportation system designed by Hashimoto uses an actuator at one end of the beam and absorber with resister and conductance at the other end. This design, however, constrains the ability to change motion direction during the transportation. The mechanism of the transportation is not derived out yet.

This paper discusses a transportation system using two actuators powered by amplifiers. The system has the ability to change the motion direction by adjusting the phase angle difference between the two amplifiers. Based on this, the stop-and-go close-loop control can be realized. The transportation mechanism is derived using sliding film and Finite Element Method.

10.2 NON-CONTACT TRANSPORTATION SYSTEM

10.2.1 EXPERIMENTAL SET-UP

The schematic of the transportation system is shown in Figure 1, and Figure 2 shows the experimental setup. The system consists of one Aluminum beam, two Langevin type Transducers (BLT) and two mechanical horns. The vibration displacement of the transducers is amplified by the mechanical horns. The position to attach the horn to the beam is defined at a length of $\lambda/4$ from the end. The parameters of the system are given in Table 1.

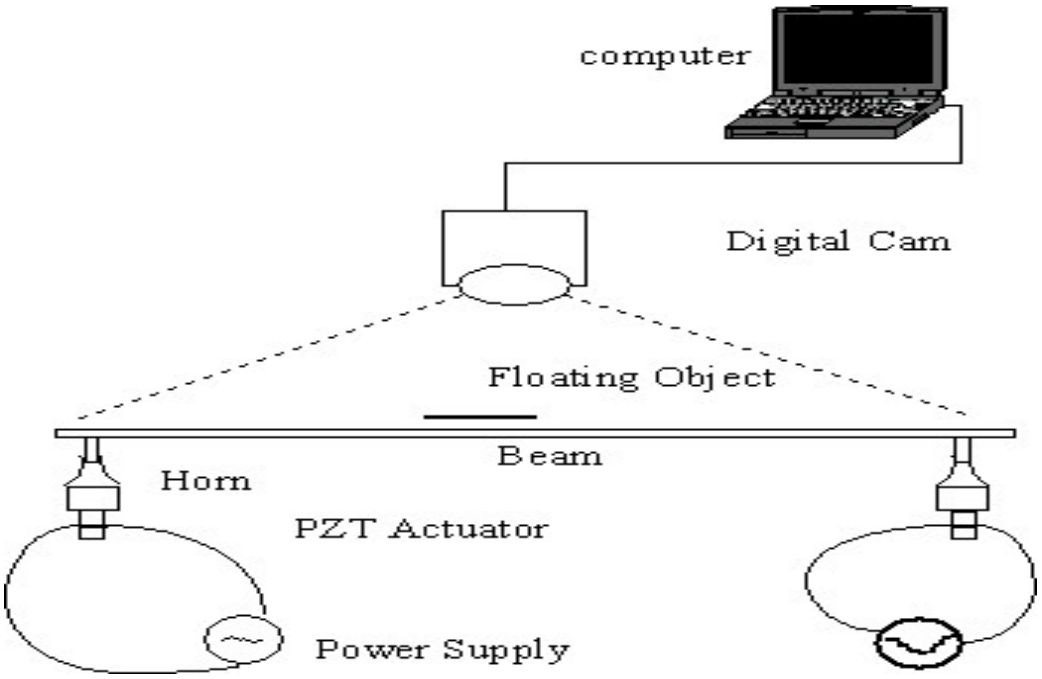

Figure 1. The transportation system schematic

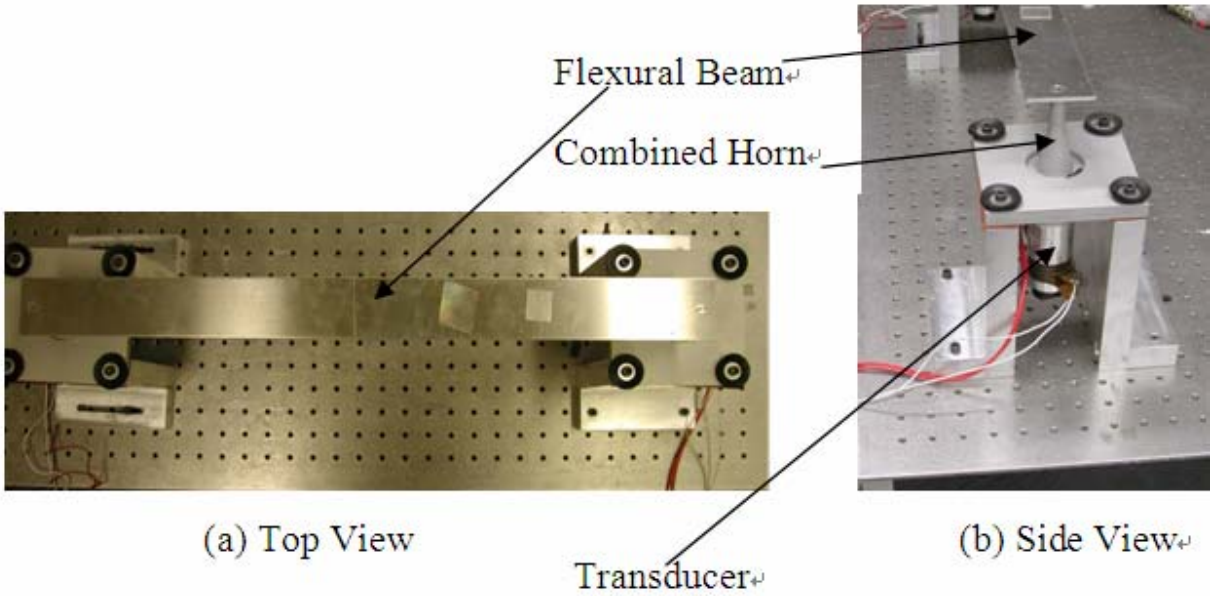

Figure 2. Experimental setup

Table 1 Parameters of the Experiment

Beam	Dimensions	400 X 50.8X 3 mm
	Material	Aluminum
	Density	2700 Kg/m3
	Young's Modulus	7e10 Pa
	Poission's Ratio	0.33
Horn	Type	Step and exponential combine
	Length	113.642 mm
	Top /Bottom Diameter	12/48 mm
	Magnification factor	4
	Node Position	41.951 mm
Levitated Object	Dimension	R=36.1 mm
	Mass	4e-3 Kg
	Material	Silicon
PZT Transducers	Type	Langevin
	Manufacturer	NTK
	Model Number	DA4427
Webcam	Type	Logitech QuickCam

A shallow T-section of the beam is fabricated to keep the moving object from falling off. A frequency of 25.6 KHz is utilized to produce the most desirable traveling wave on the beam. When a flat plate is put on the vibrating beam, it levitates and then gradually accelerates to a constant speed due to the near boundary streaming induced by the traveling wave.

Web Cam is used to capture the motion, and the video is then analyzed using Matlab to derive the position with respect of time. To facilitate use of the technique, the plate is marked with a dark dot at the center. A video camera is used to capture frames which are then imported into Matlab workspace. The video file is divided into frames. From the frames, the position can be obtained by deriving the position of the dark dot where it has the minimum intensity. The speed can then be obtained by differentiating the derived displacement with respect to time. Figure 3 shows the frames derived from the video, where the marked dots can be seen at the center of the plate.

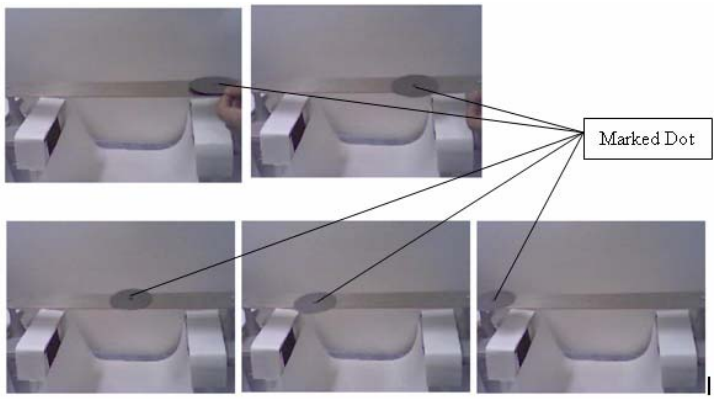

Figure 3 The floating Plate with marked dot

10.2.2 EXPERIMENTAL RESULTS

Figure 4 shows the derived position data. The velocity first gradually increases and then comes to a final steady-state speed of 0.17 m/s. The graph shows six trials of motion. The first three show the same motion from left to right of the vibrating beam, and the other three represent motion from right to left.

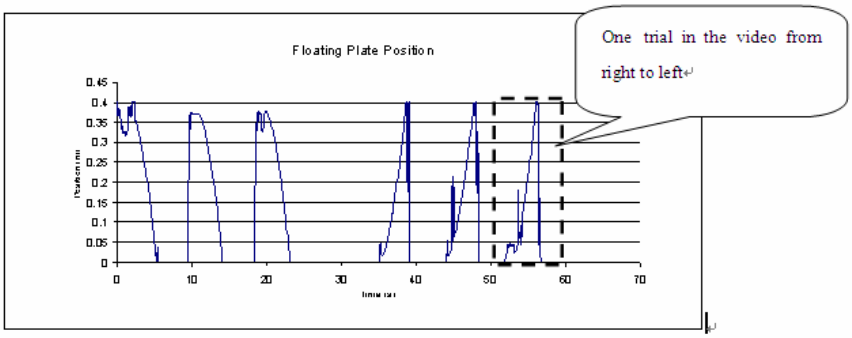

Figure 4 The derived Position vs. Time

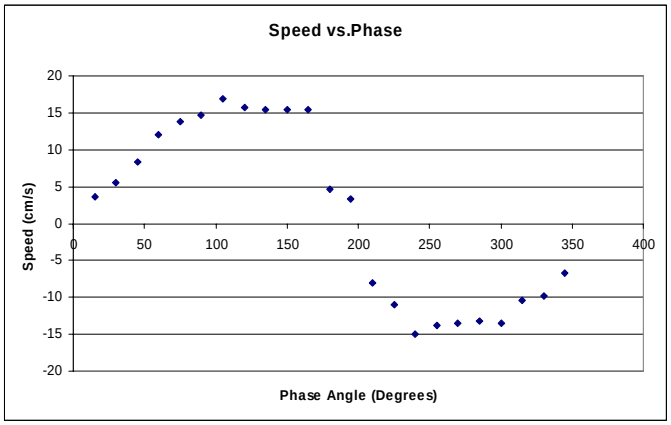

Figure 5 Steady-state velocity vs. Phase angle

The steady-state transportation velocity as a function of phase angle difference is shown in Figure 5. When the phase angle between the two transducers reaches 90 degrees, the maximum steady speed of 0.17 m/s is achieved. When the phase angle changes to 270 degrees, the transportation direction will reverse and reach a maximum speed of -0.15m/s.

The relationships between steady-state speed, input voltage and Mass Area ratio are shown in Figure 6 through Figure 8. Notice that in Figure 6 the steady-state speed is linear to the input voltage. The speed ranges from 12cm/s to 20 cm/s when the input voltage increases from 100v to 300v. In Figure 7 the steady-state speed decreases when the mass increases but the area of plate remains the same. Figure 8 is the steady-state velocity with respect of input voltage and mass area ratio. When the mass area ratio remains the same, the steady-state

speed of the plate will increase as the input voltage rise up. At the same input voltage, the steady-state speed is inversely proportional to the mass area ratio.

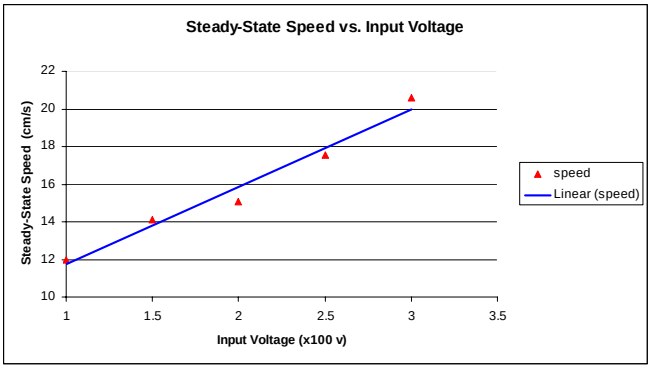

Figure 6 Steady-state velocity vs. Input voltage

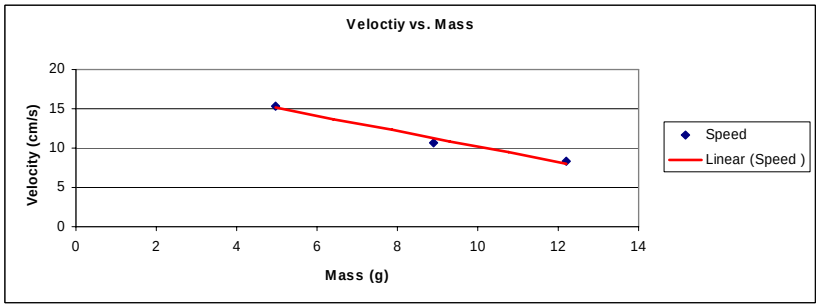

Figure 7 Steady-state velocity vs. Mass with the same area

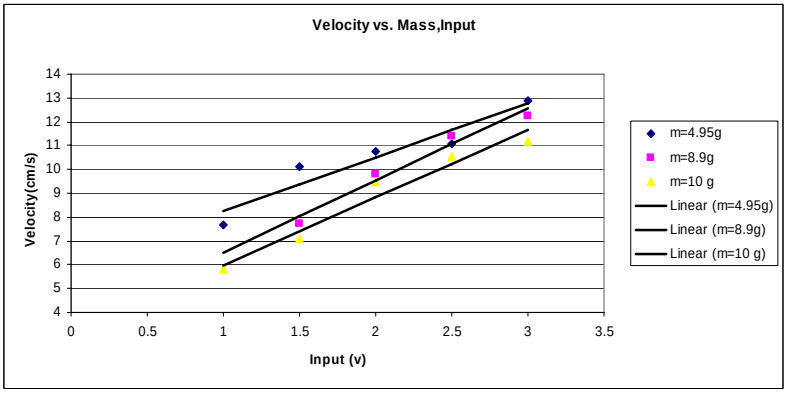

Figure 8 Steady-state velocity vs. Input voltage

10.3 THE TRANSPORTATION MECHANISM

10.3.1 THE VIBRATION EQUATION OF A FLEXURAL BEAM

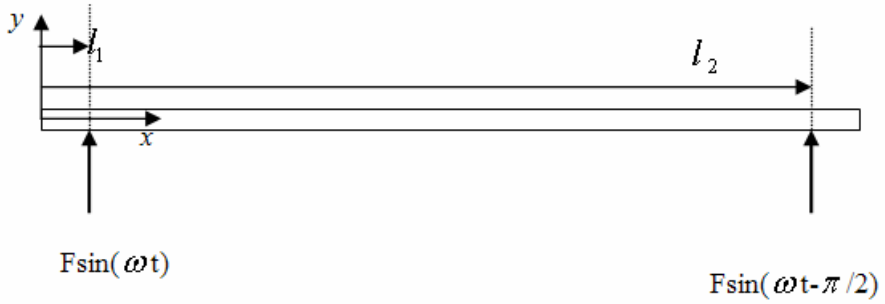

Figure 9 the forced vibration of flexural beam

$$\frac{\partial^4 w}{\partial x^4} + \frac{\rho A}{EI}\frac{\partial^2 w}{\partial t^2} = 0 \qquad (1)$$

According to the traditional beam theory, the governing equation of a vibrating beam is : where the ρ is the mass density of the beam, A is cross section area, E is Young's Modulus, and I is the moment of inertia.
The solution to Equation (1) is:

$$w(x,t) = C\sin(\omega t - kx) \qquad (2)$$

where C is the vibration amplitude, ω is Periodic frequency of the flexural waves and k is the wave number defined as $k = 2\pi/\lambda = (\omega^2 \rho A/EI)^{1/4}$.
In the steady state forced flexural vibration of the beam, the vibration can be expressed using normal mode as the following:

$$w(x,t) = F\sin(\omega t)\sum_{n=1}^{\infty}\frac{\Phi_n(x)\Phi_n(l_1)}{\omega_n^2 - \omega^2} + F\sin(\omega t - \pi/2)\sum_{n=1}^{\infty}\frac{\Phi_n(x)\Phi_n(l_2)}{\omega_n^2 - \omega^2} \qquad (3)$$

And the longitudinal vibration of the beam is derived as:

$$u(x,y,t) = -z\frac{\partial w}{\partial x} = ayk\cos(\omega t - kx) \qquad (4)$$

10.3.2 THE ANALYSIS ON TRANSPORTATION MECHANISM

Sliding Film Theory

The traveling wave on the flexural beam can be assessed as lateral motion of the beam as shown in Figure10.

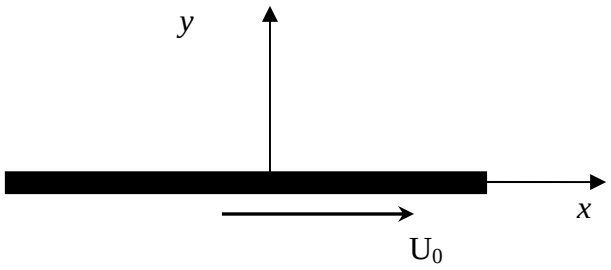

Figure 10 Stroke streaming on the lateral motion

It is assumed that the sliding film near the surface of the beam is isothermal and the pressure is constant during the movement of the beam. The basic governing equation and initial boundary conditions are [5]:

$$\begin{aligned} &\frac{\partial u}{\partial t} = \nu \frac{\partial^2 u}{\partial y^2} \\ &t \le 0, y \ge 0 : u = 0 \\ &t > 0, y = 0 : u = U_0 \\ &t > 0, y \to \infty : u = 0 \end{aligned} \qquad (5)$$

u is the fluid velocity, ν is the Kinematic viscosity and U_0 is the traveling wave speed of the beam.

To solve this equation, two variables are introduced:

$$\eta = \frac{y}{2\sqrt{\nu t}} \qquad (6)$$

$$\frac{u}{U_0} = f(\eta) \qquad (7)$$

Using the variables, the Equation (7) becomes function of η:

$$\begin{aligned} &f'' + 2\eta f' = 0 \\ &f(0) = 1, f(\infty) = 0 \end{aligned} \qquad (8)$$

Solving the equation, it is obtained:

$$\frac{u}{U_0} = f(\eta) = 1 - erf\left(\frac{y}{2\sqrt{\nu t}}\right) \qquad (9)$$

where $erf(\frac{y}{2\sqrt{\nu t}}) = \frac{2}{\sqrt{\pi}}\int_0^{\eta}\exp(-\eta^2)d\eta$ is an error function.

The velocity distribution is shown in Figure 11.

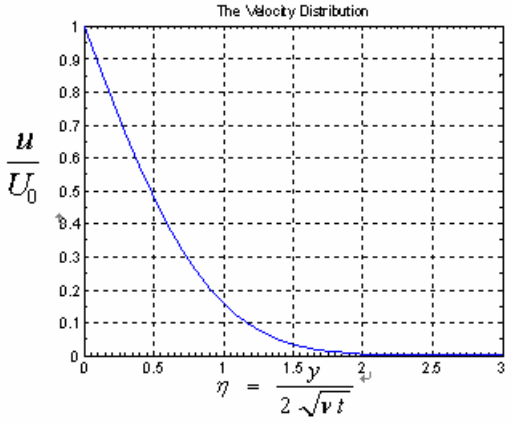

Figure 11 Velocity distribution

At a certain location of the fluid field, the velocity increases with time, only when time reaches infinity does the velocity reach to U0. At the same time, the velocity will decrease in terms of $\exp(-y^2)$ as the distance y increases. The moment of the fluid mainly concentrates near the surface of the beam.

The shear force of the fluid is expressed as:

$$\tau_w = \mu(\frac{\partial u}{\partial y}) = -0.5642\mu U_0 \frac{1}{\sqrt{\nu t}}\exp(-\frac{y^2}{4\nu t}) \qquad (10)$$

Where μ is the dynamic viscosity.

At the surface of the beam the shear force would be:

$$\tau_w = \mu(\frac{\partial u}{\partial y})_{y=0} = -0.5642\mu U_0 \frac{1}{\sqrt{\nu t}} \qquad (11)$$

The FEM on the Near Boundary Air Streaming

The fluid streaming is modeled as a rectangle with dimension 0.4x0.001m2. The boundary condition on the bottom line is set as the vibration of the beam. Due to the low density of air, the fluid pressure applied to the beam can be neglected. The time response of the beam is not affected by the fluid pressure. The progressive wave condition applied to the bottom of the fluid can be derived as:

$$x-velocity=3e\text{-}6\times\omega\times mfd\times 0.003\times k(\cos(\omega t)\cos(kx)+\cos(\omega t-\phi)\sin(kx)) \qquad (12)$$

$$y\text{-}velocity = 3e\text{-}6\times\omega\times mfd\times(\sin(\omega t)\cos(kx)+\sin(\omega t-\phi)\sin(kx)) \qquad (13)$$

where ω is the period frequency, *mfd* is the mode participation factor, and ϕ is the phase angle difference. The phase angle difference is set to be 90 degrees, the vibration frequency is 25.6KHz, and the amplitude is set as 3 micrometers. The velocity of the air streaming is derived by FEMLAB and the streamline plot of velocity distribution at time =2.2e-5 second is shown Figure 12. In the continuous time step, the animation of the velocity moves along the traveling wave direction.

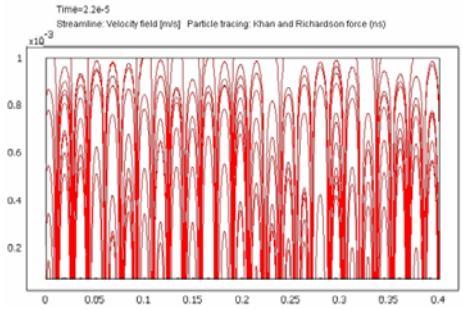

Figure 12 the streamline plot of the air streaming

Figure 13 shows the beam response at different time steps, where the air velocity can be clearly seen moving from left to right.

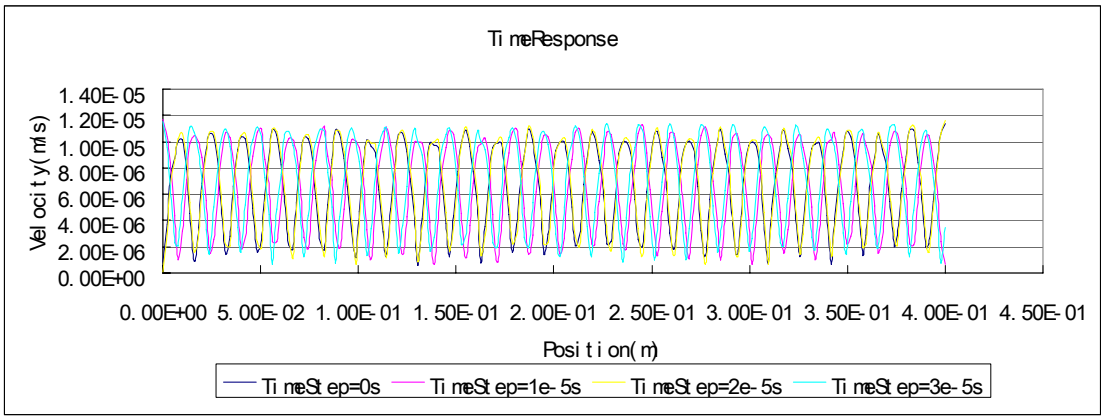

Figure 13 The fluid velocity at different time step

Figure 14 shows the maximum velocity with respect of amplitude from which it can be seen that the fluid velocity is linear to the vibration amplitude, which corresponds well to the experimental results.

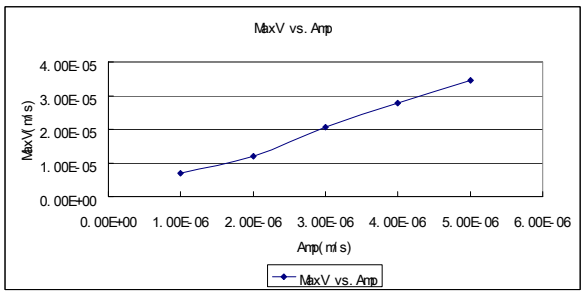

Figure 14 MaxV vs. Amplitude

Figure 15 shows the relationship between maximum velocity and frequency. When the beam vibrates at the mode frequency the fluid will have the largest vibration amplitude, therefore it has the largest MaxV.

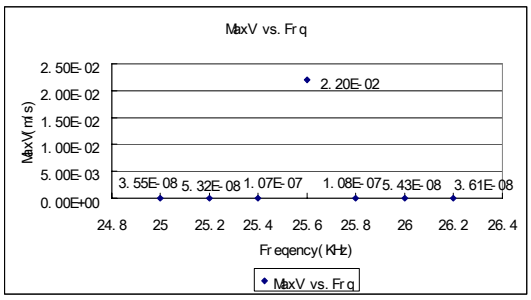

Figure 15 Maximum velocities vs. applied frequency

Figure 16 shows plot of maximum velocity versus air gap. The velocity decreases rapidly as the gap increases. This corresponds to the sliding film theory shown Figure 11.

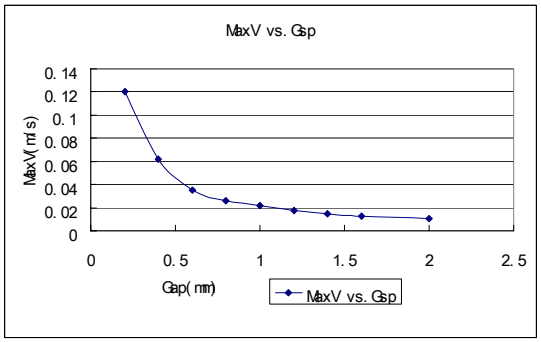

Figure 16 MaxV vs. Gap

Figure 17 shows the x-velocity distribution along the longitudinal direction of the beam when the vibration phase is 0. There is no phase angle difference in the fluid response at different time steps, which means there is no progressive wave produced. Only standing waves are produce in the beam.

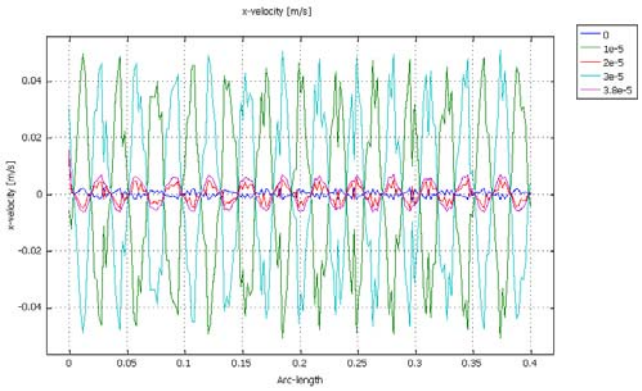

Figure 17 the x-velocity distribution along the length of the beam with Phase=0

Figure 18 (a) shows the x-velocity distribution along y direction at different time step. The x-velocity vibrates at different amplitudes along y direction. (b) shows the x-velocity time response at different x location. There is no phase angle difference. The x-velocity at different x position vibrates synchronously. Finally (c) is the time response at different y location, there is no phase angle difference. All the results above mean that in the fluid domain there is only standing wave motion when the phase angle is set zero.

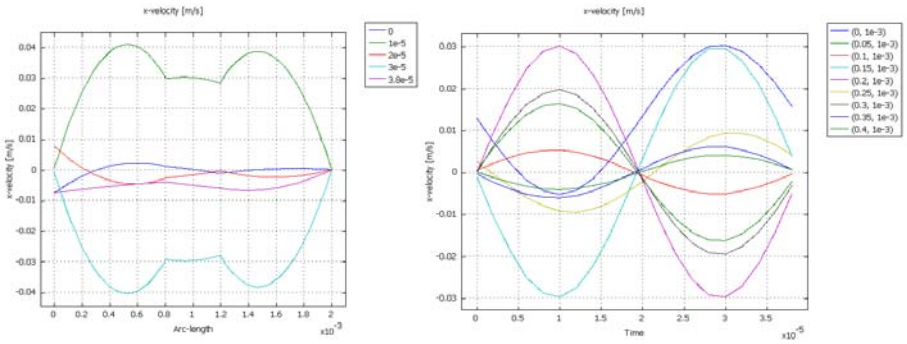

(a) x-velocity distribution along y direction (b) Time response

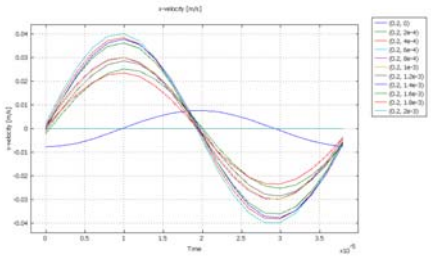

(c) the x-velocity time response

Figure 18 the x-velocity characteristics at phase =0

Figure 19 (a) and (b) shows the x-velocity time response along x-direction with phase angle 90 and 270, respectively. The phase angle difference can be clearly seen in the figures. The amplitude crest moves along traveling wave direction. The wave crest motion direction reverses when the phase angle difference changes to 270.

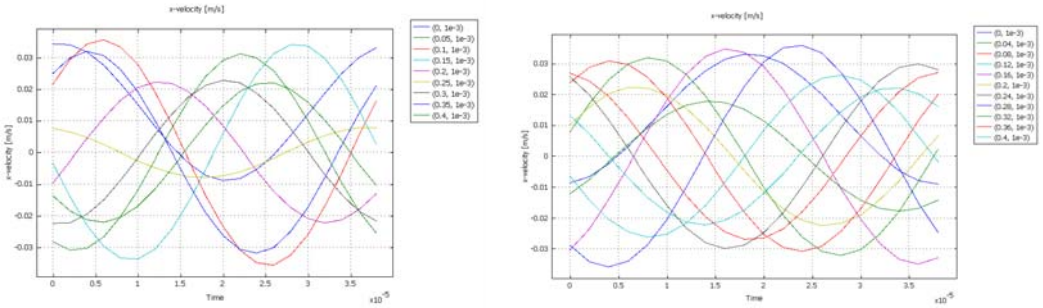

(a) Phase 90 (b) Phase 270

Figure 19 the x-velocity time response along x-direction

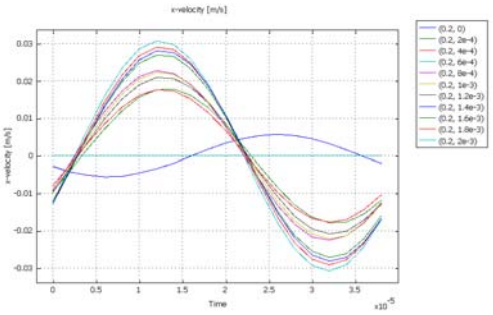

(a) Phase 90

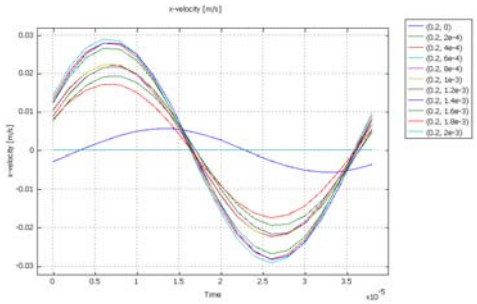

(b) phase 270

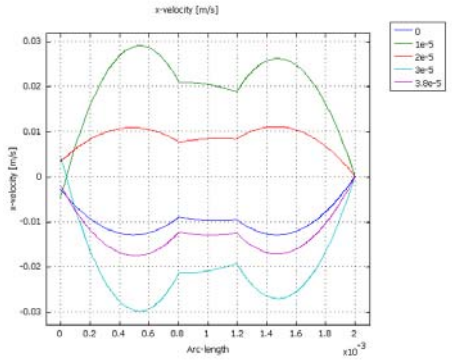

(c) phase 90

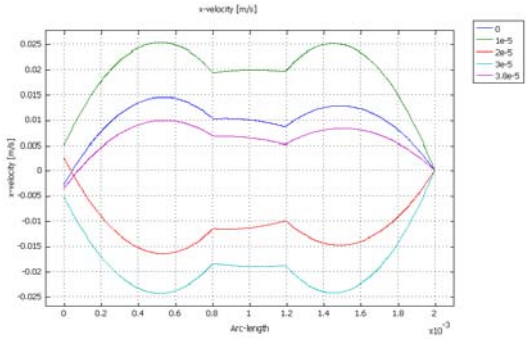

(d)phase 270

Figure 20 x-velocity distributions in time and y-direction domain

Figure 20 (a) and (b) show the x velocity time response along y direction with phase angle difference of 90 and 270, respectively. There is no phase angle difference in any location, which means there are no progressive waves along y direction. Figure (c) and (d) are the x-velocity distribution at different time step. The wave crest varies at it own position and does not move along y direction.

When there is phase angle difference between the two applied forces, the x-velocity time response along the beam direction will have a phase angle difference correspondingly. The maximum x-velocity inside the fluid will move along the traveling wave direction. That forms a sliding film between the beam and the levitated object.

Figure 21 shows the relationship between maximum x-velocity and phase angle. When the phase angle difference reaches 90 degrees, the maximum x-velocity occurs. And x-velocity motion reverses at 270 degrees. This agrees with the experimental results in the non-contact transportation.

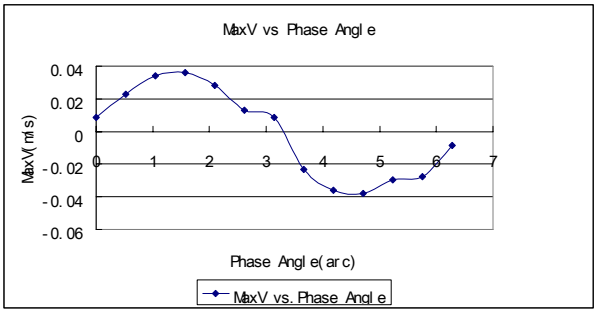

Figure 21 MaxV vs. Phase Angle

10.3.3 THE MOTION OF THE FLOATING PLATE

There are two forces acting on the beam shown in Figure 22. One is the shear force from the vibration of the beam:

$$F_b = \tau_{wb} A = -0.5642 \mu A U_0 \frac{1}{\sqrt{\nu t}} \exp(-\frac{y_0^{\ 2}}{4\nu t}) \qquad (14)$$

The other is shear force due to the motion of the floating plate but has a reverse direction on the plate:

$$F_p = \tau_{wp} A = -0.5642 \mu \dot{x} \frac{1}{\sqrt{\nu t}} \qquad (15)$$

The governing equation of motion of the plate is expressed as:

$$F_b - F_p = m\ddot{x} \qquad (16)$$

Where m is the mass of the transported object.

Figure 23 shows the simulated results using Simulink in Matlab. The plate gradually increases due to the shear forces acting on the object. The object finally reaches a stable velocity. Figure 24 shows a good agreement between the experimental displacement of the plate and the simulated result.

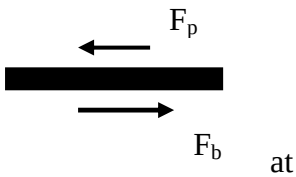

at

Figure 22 the forces acting on the plate at the longitudinal direction.

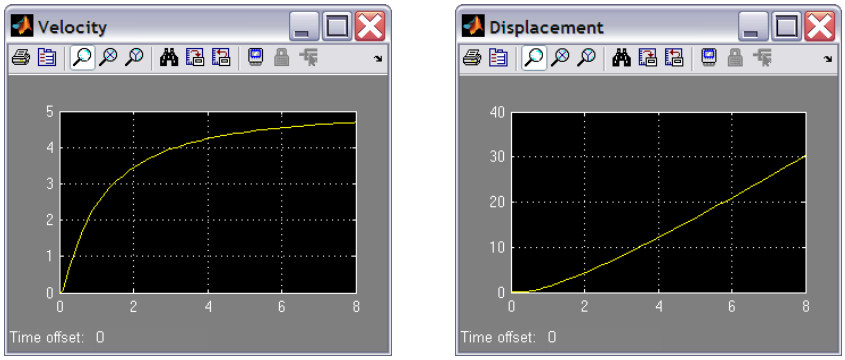

(a) Velocity vs. Time (b) Displacement vs. Time

Figure 23 the Analytical results

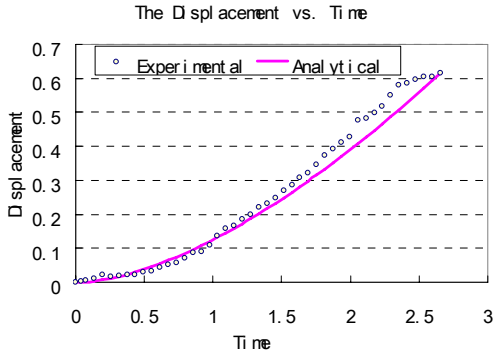

Figure 24 the comparison between analytical and experimental

10.4 CONCLUSION

For the purpose of reducing damage during handling precision products, one non-contact transportation system using two-mode excitations is developed. The transportation of the object is successful. The motion direction can be changed by adjusting the phase angle difference. The transportation mechanism derivation is conducted using sliding film theory and Finite Element Method, respectively. The theoretical results agree with experimental results.

10.5 REFERENCE

1. Yoshikau Koike,Sadayuki Ueha,Atsushi Okonogi, Takafumi Amano and Kentaro Nakamura,"Suspension Mechanism in Near field acoustic levitation phenomenon," IEEE ULTRASONICS SYMPOSIUM,671-674,(2000)
2. Yoshiki Hashimoto, Yoshikazu Koike and Sadayuki Ueha, "Near-field acoustic levitation of planar specimens using flexural vibration," J.Acoust.Soc.Am.100 (4), 2057-2061, (1996).
3. Adi Minikes , Izhak Bucher and Shimon Haber "Levitation force induced by pressure radiation in gas squeeze films," J.Acoust.Soc.Am. 116(1), July 2004

4. Ansys Inc., Release 9.0 Documentation for Ansys , 2004
5. V.N.Constantinescu, Laminar Viscous Flow, Springer, 1995
6. Comsol Multiphysics™ Inc., Comsol Documentation, 2005
7. Byong Loh, Paul Ro "An Object Transporation System Using Flexural Ultrasonic Progressive Waves Generated by Two-Mode Excitation", IEEE Transaction on Ultrasonic,Ferroelectrics, and Frequency Control, Vol. 47. No. 4. July,2000
8. Yoshiki Hashimoto , Yoshikazu Koike and Sadayuki Ueha,"Transporting objects without contact using flexural traveling waves," J.Acoust.Soc.Am.103(6),3230-3233,(1998).
9. Takafumi Amano, Yoshikazu Koike, Kentaro Nakamura, Sadayuki Ueha and Yoshiki Hashimoto,"A multi-tranducer near field acoustic levitation system for noncontact transportation of large-sized planar objects," Jpn.J.Apple.Phys., vol 39, 2982-2985,2000.
10. Y. Hashimoto, Y. Koike, and S. Ueha, "Magnification of transport range using noncontact acoustic levitation by connecting vibrating plates," Jpn. J. Appl. Phys. 1, Reg. Rap. Short Notes, vol. 36, no. 5B, pp. 3140–3145, May 1997.
11. T.Ide,J.Friend,K.Nakamura and S.Ueha,"a Non-contact linear bearing by ultrasonic levitation," WCU 2003,Paris.2003.
12. Yoshikau Koike,Sadayuki Ueha,Atsushi Okonogi, Takafumi Amano and Kentaro Nakamura,"Suspension Mechanism in Near field acoustic levitation phenomenon," IEEE ULTRASONICS SYMPOSIUM,671-674,(2000)

FACULTY, STAFF, AND STUDENTS OF THE PRECISION ENGINEERING CENTER
Standing (L to R): N. Wanna, L. Lamonds, R. Woodside, N. Buescher, R. Scattergood, T. Dow and K. Garrard
Sitting: (L to R): D. Brehl, K. Folkert, A. Sohn, B. Brocato, T. Kennedy and L. Masters
Students Not Pictured: Y. Yin
Faculty Not Pictured: G. Buckner, J. Eischen, P. Ro, and D. Youden
Staff Not Pictured: R. Gold

FACULTY

THOMAS A. DOW

Director, Precision Engineering Center
Professor, Department of Mechanical and Aerospace Engineering

BS, Mechanical Engineering, Virginia Polytechnical Institute, 1966
MS, Engineering Design, Case Institute of Technology, 1968
PhD, Mechanical Engineering, Northwestern University, 1972

After receiving his PhD degree from Northwestern University in 1972, Dr. Dow joined the Tribology Section of Battelle Columbus Laboratories and worked there for ten years. His research interests were in the areas of friction and wear and included studies on a wide variety of topics from lubrication of cold-rolling mills using oil-in-water emulsions to wet braking effectiveness of bicycle brakes to elastohydrodynamic lubricant film generation in ball and roller bearings. He developed experimental apparatuses, established analytical models, and corroborated those analyses with experimental measurements. Dr. Dow joined the faculty at North Carolina State University in 1982 and was instrumental in developing the academic and research program in precision engineering. His current research interests include the design of precision machining systems, real-time control, and metrology. He was one of the founders of the American Society for Precision Engineering and currently acts as the Executive Director.

GREGORY D. BUCKNER

Associate Professor, Department of Mechanical and Aerospace Engineering

BS, Mechanical Engineering, Louisiana State University, 1986
MS, Mechanical Engineering, Virginia Polytechnic Institute, 1987
PhD, Mechanical Engineering, University of Texas at Austin, 1996

Dr. Buckner is an Associate Professor of Mechanical and Aerospace Engineering at North Carolina State University (NCSU) in Raleigh, NC. His research interests include electromechanical systems, intelligent system identification and control, and precision engineering. Dr. Buckner has researched active and semi-active vehicle suspension systems since 1997, and has demonstrated innovative and effective control strategies for implementations on military HMMWV's and other off-road vehicles. His additional research projects include the development of intelligent control algorithms for active magnetic bearings, medical instruments for robotic surgery, and electromechanical actuators for manufacturing processes. Dr. Buckner is a recipient of the Faculty Early Career Development (CAREER) Award from the National Science Foundation, the New Faculty Research Award from the American Society for Engineering Education, and the Outstanding Teacher Award from NCSU. Prior to his appointment at NCSU, Dr. Buckner was a research engineer at the University of Texas Center for Electromechanics in Austin, TX. He received a Ph.D. in mechanical engineering from the University of Texas at Austin in 1996.

JEFFREY W. EISCHEN

Associate Professor
Department of Mechanical and Aerospace Engineering

BS, Mechanical Engineering, UCLA, 1978
MS, Mechanical Engineering, Stanford University, 1981
PhD, Mechanical Engineering, Stanford University, 1986

Dr. Eischen has been with N.C. State since 1986 and his research areas of interest include: linear and nonlinear finite element analysis, multi-body kinematics/dynamics/control, fabric mechanics, and stress analysis in microelectronic devices. He teaches undergraduate courses in strength of mechanical components and mechanical design. His graduate courses include fracture mechanics and advanced machine design. He has collaborated with colleagues in the Precision Engineering Center for several years on computer simulation related projects dealing with precision shape control of disk drive read/write heads, stress and deformation analysis of high energy physics equipment, and contact lens mechanics.

PAUL I. RO

Professor
Mechanical and Aerospace Engineering Department

BS, Mechanical Engineering, University of Minnesota, 1982
MS, Mechanical Engineering, Massachusetts Institute of Technology, 1985
PhD, Mechanical Engineering, Massachusetts Institute of Technology, 1989

Dr. Ro joined the faculty of North Carolina State University in January 1989, as an Assistant Professor in the Mechanical & Aerospace Engineering Department. He became a Professor in July 2001. Dr. Ro has developed two graduate courses in the department (multivariable Control and Robotics) and has taught undergraduate Automatic Control and Dynamics courses. His research covers a wide range of controls and various applications of control theories in precision engineering, robotics, vehicle dynamics and control, and mechatronics.

RONALD O. SCATTERGOOD

Professor
Materials Science and Engineering Department

BS, Metallurgical Engineering, Lehigh University, 1961
MS, Metallurgy, Massachusetts Institute of Technology, 1963
PhD, Metallurgy, Massachusetts Institute of Technology, 1968

R.O. Scattergood is a Professor in the Department of Materials Science and Engineering. He received BS degrees in Mining Engineering and Metallurgical Engineering from Lehigh University. His MS and PhD degrees were obtained in Metallurgy from M.I.T. In 1968 he became a member of the basic research staff in the Materials Science Division at the Argonne National Laboratory. In 1981, he joined the faculty as a Professor of Materials Engineering at North Carolina State University.

Professor Scattergood's major research interests have been focused on the mechanical behavior of solids. He has worked in the areas of strengthening mechanisms in solids, mechanical testing, fracture, tribology, nanocrystaline materials and precision machining processes. He has expertise in He has published over 200 technical papers, books and reports.

DAVID YOUDEN

Technical Associate, Eastman Kodak Company
Adjunct Lecturer, Department of Mechanical and Aerospace Engineering

ASME, Central New England College, Worcester, MA, 1965

Prior to joining Eastman Kodak's Manufacturing Systems Technology Division in 1997, Mr. Youden was Research and Development Manager at Rank Pneumo, a division of Rank Taylor Hobson Inc. for ten years. Before that, he was Director of Engineering at the Cone Blanchard Machine Company. He has also worked at Ocean Systems, Inc. of Reston, Virginia and the Heald Machine Company, a division of Cincinnati Milacron. During his professional career, Mr. Youden has been granted numerous patents in the field of machine tools, and he has published and presented technical papers on the design and testing of ultra-precision machine tools in the US, Japan, and Germany.

Mr. Youden graduated from Central New England College and attended Worcester Polytechnic Institute and Clark University. He is a charter member of the American Society for Precision Engineering.

STAFF

KENNETH P. GARRARD

Research Assistant
Precision Engineering Center

BS, Computer Science, North Carolina State University, 1979
MS, Computer Studies, North Carolina State University, 1983

As a full-time research assistant, Mr. Garrard is studying the design of systems software that supports the development of high-speed real-time applications for special purpose multiprocessor computer systems. He has several years experience in academia and industry designing and implementing real-time systems. As a Precision Engineering Center staff member, Mr. Garrard's current activities include the design and implementation of software for Diamond Turning Machine and Fast Tool Servo controller projects.

ALEXANDER SOHN

Research Assistant/Lecturer
Precision Engineering Center

B.S., Physics, University of Texas at Arlington, 1992
M.S., Physics, University of Texas at Arlington, 1994

Mr. Sohn joined the Precision Engineering Center in August, 1997 as a member of the technical staff. His current research interests range from machine design and metrology to the design and fabrication of nonimaging optics. Mr. Sohn's varied research activities began in microwave optics and atomic physics as a student at the University of Texas at Arlington and later progressed to precision machine design, design and fabrication of plastic optics as well as automation and machine vision at Fresnel Technologies, Inc. in Fort Worth, Texas.

ROXIE B. GOLD

Administrative Assistant
Precision Engineering Center

BA, Accounting, North Carolina State University 1983

Ms. Gold became a member of the PEC Staff in September 2005. Her previous jobs include product manager for Wireless Technologies at Progress Energy and Project Manager for Online Banking Mergers and Acquisitions projects at BB&T. Ms. Gold provides the overall administrative support for the Center.

GRADUATE STUDENTS DURING 2005

DAVID BREHL's extensive industrial career includes a range of design, development, and project engineering roles with AERCO International, BOC Gases, and Babcock & Wilcox. A deepening interest in design of integrated electromechanical systems, along with a desire to focus his career on technology development, led him to pursue a PhD in Mechanical Engineering at NC State; this follows a recent Master's in ME program at Stevens Institute of Technology (Hoboken, NJ). He joined the PEC in August 2004.

BRETT BROCATO interned at Fort James Paper and TRW Vehicle Safety Systems prior to graduating from the University of Alabam in 1999 with his bachelor's degree in Mechanical Engineering with a minor in the Computer Based Honors Program. Before enrolling in the NC State master's program, he worked for Bell Helicopter and Corning Optical Fiber. Brett completed is degree in spring 2005 and is working for General Atomics in San Diego, CA.

NATHAN BUESCHER was born and raised in Raleigh, NC. He received his BS in Mechanical Engineering as well as a Minor in Mathematics from NC State University in May 2003. He began work with the PEC in August 2003. Some of his prior work experience includes Stantec Consulting, Inc. and Joel Wittkamp Design. Nathan completed his degree in fall 2005 and is working for Consolidated Diesel in Rocky Mount, NC.

KARALYN FOLKERT is originally from Zeeland, MI. She received her BS in Mechanical Engineering from Western Michigan University. While completing her undergraduate workk, she participated in Tribology research and was published. Her senior design project involved the design of a range interlock system for a heavy-duty, 10-speed transmission. She began her work at the PEC in the fall of 2003. Kara completed her degree in summer 2005 and is working for Consolidated Diesel in Rocky Mount, NC

TIM KENNEDY was born and raised in Chapel Hill, NC. Tim received his BS from NCSU in May 2004. Before working at the PEC, he work at the Analytical Instrumentation Facility for two years as an undergraduate research assistant. He started working with the PEC August 2004.

LUCAS LAMONDS interned for RJ Reynolds, AMP and Getrag Gears. He began work at Getrag Gears in July 2002 and held the positions of Qualty Engineer, Six Sigma Black Belt, and India-Joint Venture Project Engineer. Most recently, he managed the company's production yeilds, quality levels, and product launches for India.

NADIM WANNA was born and raised in Beirut, Lebanon. Nadim received a BS in Mechanical Engineering from North Carolina State University in December 2004. He participated in a research project on object transportation using ultrasonic wave propagation and his prior work experiences include Lebanon Chemical CO.

ROB WOODSIDE was born and raised in Greenville, NC. He started at UNC-Asheville in 1999 and transferred to NCSU in 2001, where he received his BS in Mechanical Engineering in December 2004. He began work with the PEC in January 2005. Some of his prior work experience includes MACTEC/PES consulting.

YANBO YIN received his BS and ME in Precision Instrument and Mechanology from Tsinghua University Beijing in 2000 and 2003 respectively. For his undergraduate thesis, he joined the micro-mechanical lab with experimental research on Micro-jet. For his master's degree,Yin developed a computer aided system on wireless communication on base station distribution. Currently, he is pursing his Ph.D. degree in Mechanical Engineering under guidance of Dr.Ro. His research involves Non-contact object transportation using ultrasonic.

UNDERGRADUATE STUDENTS DURING 2005

ROBERT POWELL

GRADUATES OF THE PRECISION ENGINEERING CENTER

Student	Degree	Date	Company/Location
Jeffrey Abler	PhD	December 1994	ETEC Systems, Inc. Tucson, AZ
William Allen	PhD	December 1994	North Carolina State Univ. Raleigh, NC
Kelly Allred	MS	June 1988	
Christopher Arcona	PhD	May 1993	Norton Worcester, MA
Bradford Austin	MS	June 2000	IBM Corporation Fishkill, NY
Markus Bauer	PhD	December 2001	SCYNEXIS Chemistry & Automation, Inc. Research Triangle Park, NC
Tom Bifano	PhD	June 1988	Phillips Automation Pittsburgh, PA
Scott Blackley	MS	May 1990	Motorola Austin, TX
Peter Blake	PhD	December 1988	NASA Goddard Greenbelt, MD
Brett Brocato	MS	June 2005	General Atomics San Diego, CA
Nathan Buescher	MS	May 2005	Consolidated Diesel Rocky Mount, NC
Mark Cagle	MS	June 1986	NASA-Langley Norfolk, VA
John Carroll	PhD	January 1986	Cummins Engine Co. Columbus, IN
Matthew Cerniway	MS	October 2001	Naval Surface Warfare Ctr West Bethesda, MD

Damon Christenbury	MS	June 1985	Michelin Tire Co. Spartanburg, SC
Stuart Clayton	MS	May 2003	Naval Depot Cherry Point
James Cuttino	PhD	December 1994	UNC – Charlotte Charlotte, NC
Bob Day	PhD	July 1998	Los Alamos National Lab Los Alamos, NM
Joseph Drescher	PhD	May 1992	Pratt & Whitney East Hartford, CT
William Enloe	MS	December 1988	ITT Roanoke, VA
Karl Falter	MS	December 1989	Eastman Kodak Company Raleigh, NC
Peter Falter	PhD	May 1990	Lockheed-Martin Orlando, Florida
John Fasick	MS	May 1998	Kodak Rochester, NY
Steven Fawcett	PhD	June 1991	MicroE Natick, MA
Karalyn Folkert	MS	May 2005	Consolidated Diesel Rocky Mount, NC
Andre Fredette	PhD	May 1993	IBM Research Triangle Park, NC
Karl Freitag	MS	August 2004	Northrop Grumman Baltimore, MD
David Gill	PhD	August 2002	Sandia National Laboratories Albuquerque, NM
Jim Gleeson	MS	June 1986	Battelle Columbus Labs Columbus, OH

Mary Smith Golding	MS	May 1990	Harris Corporation Melbourne, FL
David Grigg	PhD	August 1992	Zygo Corporation Middlefield, CT
Hector Gutierrez	PhD	October 1997	Florida Inst. Of Tech. Melbourne, FL.
Christian Haeuber	MS	December 1996	Harris Corporation Melbourne, FL
Simon Halbur	MS	December 2004	
Matias Heinrich	MS	July 2001	Vistakon Jacksonville, FL
Gary Hiatt	PhD	May 1992	Caterpiller Zebulon, NC
David Hood	MS	May 2003	
Peter Hubbel	MS	December 1991	Delco Electronics Kokomo, IN
Konrad Jarausch	PhD	December 1999	Intel Corporation San Jose, CA
Bradley Jared	PhD	December 1999	3M Cincinnati, OH
David Kametz	MS	August 2002	Naval Air Warfare Center Aircraft Division Patuxent River, MD
Jerry Kannel	PhD	June 1986	Battelle Columbus Labs Columbus, OH
Byron Knight	MS	May 1990	US Air Force Washington, DC
Mark Landy	MS	June 1986	Battelle Columbus Labs Columbus, OH
Mike Loewenthal	MS	December 1988	SVG Norwalk, CT

Michael Long	PhD	June 2000	Eastman Kodak Rochester, NY
Bryan Love	MS	May 2001	Virginia Tech
Michael Hung-Tai Luh	MS	June 1989	Proctor and Gamble Cincinnati, OH
Dan Luttrell	MS	1987	Luttrell, Inc. New Boston, NH
Edward Marino	MS	September 1999	Pratt Whitney Hartford, CT
Edward Miller	MS	December 2000	General Electric Greenville, SC
Michele Miller	PhD	December 1994	Michigan Tech. University Houghton, MI
Paul Minor	MS	September 1998	Hartford, CT
Gary Mitchum	MS	June 1987	Harris Corporation Melbourne, FL
Charles Mooney	MS	December 1994	AIF – NC State University Raleigh, NC
Patrick Morrissey	MS	May 2003	
Larry Mosley	PhD	June 1987	Intel Corporation Chandler, AZ
Patrick Moyer	PhD	May 1993	UNC-Charlotte Charlotte, NC
Nobuhiko Negishi	MS	August 2003	
Ayodele Oyewole	MS	October 1997	Barnes Aircraft East Hartford, CT
Hakan Ozisik	PhD	December 1989	
Witoon Panusittikorn	PhD	December 2004	Thailand

John Pellerin	MS	May 1990	Sematech Austin, TX
Travis Randall	MS	August 2004	MBA student NCSU
Ganesh Rao	MS	December 1994	Oak Ridge National Lab Oak Ridge, TN
John Richards	MS	September 1997	Intel Corporation San Jose, CA
Walter Rosenberger	MS	May 1993	The East Group Kinston, NC
Alex Ruxton	MS	December 1996	Pratt &Whitney Palm Beach, Florida
Anthony Santavy	MS	August 1996	Ford Dearborn, MI
Keith Sharp	PhD	May 1998	Morgan Crucible Dunn, NC
Gordon Shedd	PhD	March 1991	
Wonbo Shim	PhD	May 2000	Seagate Inc. Oklahoma City, OK
Robert Skolnick	MS	September 1997	San Diego, CA
Denise Skroch	MS	May 1989	IBM Corporation Raleigh, NC
Elizabeth Smith	MS	April 1989	
Stanley Smith	PhD	May 1993	
Ronald Sparks	PhD	May 1991	Alcoa Corporation Pittsburg, PA
Brent Stancil	MS	December 1996	Harris Corporation Melbourne, FL
Gene Storz	MS	May 1994	

Anand Tanikella	PhD	August 1996	Norton Industrial Ceramics Northboro, MA
Donna Thaus	MS	May 1996	Northern Telecom Research Triangle Park, NC
John Thornton	MS	December 1993	Digital Instruments Santa Barbara, CA
Michael Tidwell	MS	December 1991	
John Tyner	MS	June 1995	Naval Depot Cherry Point
Tao Wu	PhD	December 2003	

ACADEMIC PROGRAM

Problems and limitations associated with precision manufacturing can originate in the machine, the process, or the material. In fact, most problems will probably be caused by a combination of these factors. Therefore, improvement of current processes and development of new manufacturing methods will require knowledge of a multi-disciplinary array of subjects. The educational goal of the Precision Engineering Center is to develop an academic program which will educate scientists and engineers in metrology, control, materials, and the manufacturing methods of precision engineering.

The graduate students involved in the Precision Engineering Center have an annual stipend as research assistants. They can take up to 3 classes each semester while spending about 20 hours per week on their research projects. These students also work in the Center full-time during the summer months.

The Precision Engineering Center began in 1982 with an emphasis on the mechanical engineering problems associated with precision engineering. As a result, the original academic program proposed was biased toward courses related to mechanical design and analysis. However, as the research program has developed, the need for complementary research in sensors, materials, and computers has become obvious. A graduate student capable of making valuable contributions in the computer area, for example, will require a significantly different academic program than in mechanical engineering. For this reason, the Center faculty has set a core curriculum and each student in the program is required to take at least 3 of these core courses. The remainder of the courses for the MS or the PhD degree are determined by the university or department requirements and the faculty committee of the student.

The required courses are:

- MAE 545 Metrology in Precision Manufacturing
- PY 516 Physical Optics
- MAT 700 Modern Concepts in Materials Science
- CSC (ECE) 714 Real Time Computer Systems

PhD DEGREE PROGRAM

The PhD program in Precision Engineering has been set up as a multi-disciplinary program, drawing upon courses throughout the University to provide background and expertise for the students. It should contain required courses to insure solid grounding in the fundamentals plus electives to prepare the student in his area of specialization. Because Precision Engineering is concerned with an integrated manufacturing process, students interested in computer control, materials, machine structure, and measurement and actuation systems are involved in the program. Student research projects include the wide variety of topics addressed in this report. Each student's thesis should have an experimental component because Precision Engineering is basically a hands-on technology.

MS DEGREE PROGRAM

The Master of Science degree will have a higher percentage of application courses than the PhD degree. The emphasis will be to develop the foundation for involvement in precision engineering research and development. A total of 30 credits including 6 credits for the MS thesis is required. The thesis, while less comprehensive than the PhD dissertation, will be directed at important problems in Precision Engineering. Typically the MS program will take four semesters plus one summer.

UNDERGRADUATE PROGRAM

The undergraduate degree broadly prepares an engineering student for industrial activities ranging from product design and engineering sales to production implementation. Because a large share of engineers only have the BS degree, these will be the people who must implement the new technology developed in research programs like the Precision Engineering Center. Therefore, a way must be found to acquaint engineers at the BS level with the techniques, problems, and potential of precision manufacturing.

In most undergraduate degree programs only limited time is available for technical electives. However, these electives offer the student the opportunity to expand his knowledge in many different directions. Beginning graduate courses (such as metrology) can be used as undergraduate electives.

Undergraduate projects and summer employment have also been utilized to include undergraduate students into the research program of the Center. During the 1998-1999 academic year, four undergraduate students in Mechanical Engineering were involved various projects at the PEC.

STUDY PLANS

Study plans for several example students are given below both for the MS and the PhD degree. Because of the breadth of the field and the wide range of thesis topics, few if any study plans will be exactly the same. The plan will depend upon the student's background, his interests, his thesis topic, the department, and the chairman and members of his committee.

PhD PROGRAM IN MECHANICAL ENGINEERING

Major Courses:

- MAE 740 Advanced Machine Design I
- MAE 741 Advanced Machine Design II
- MAE 706 Heat Transfer Theory & Applications
- MAE 713 Principles of Structural Vibration
- MAE 760 Computational Fluid Mechanics and Heat Transfer
- MAE 545 Metrology in Precision Manufacturing
- MAE 715 Nonlinear Vibrations
- MAE 716 Random Vibration
- MAE 714 Analytical Methods in Structural Vibration
- MAE 742 Mechanical Design for Automated Assembly
- MAE 895 Doctoral Dissertation Research

Minor Courses:

- MA 511 Advanced Calculus I
- MA 775 Mathematical Methods in the Physical Sciences I
- CSC 780 Numerical Analysis II
- PY 516 Physical Optics
- ECE 716 System Control Engineering
- MAT 700 Modern Concepts in Materials Science
- ECE 726 Advanced Feedback Control
- ECE 764 Digital Image Processing

PhD PROGRAM IN MATERIALS ENGINEERING

Major Courses:

- MAT 710 Elements of Crystallography and Diffraction
- MAT 700 Modern Concepts in Materials Science
- MAT 556 Composite Materials
- MAT 715 Transmission Electron Microscopy
- MAT 795 Defect Analysis/Advanced Materials Experiments
- MAT 753 Advanced Mechanical Properties of Materials
- MAT 712 Scanning Electron Microscopy
- MAT 895 Doctoral Dissertation Research

Minor Courses:

- PY 414 Electromagnetism I
- ST 502 Experimental Statistics for Engineers I
- MAE 740 Advanced Machine Design I
- MAE 741 Advanced Machine Design II
- MAE 545 Metrology in Precision Manufacturing
- PY 516 Physical Optics
- MA 401 Applied Differential Equations II

PhD PROGRAM IN ME (FOR STUDENT WITH MS DEGREE)

- ECE 716 System Control Engineering
- ECE 791 Gate Array Design
- MAT 700 Modern Concepts in Materials Science
- PY 516 Physical Optics
- MA 502 Advanced Mathematics for Engineers and Scientists II
- MA 775 Mathematical Methods in the Physical Sciences I
- MA 780 Numerical Analysis II
- MAE 732 Fundamentals of Metal Machining Theory
- MAE 740 Advanced Machine Design I
- MAE 741 Advanced Machine Design II
- MAE 545 Metrology in Precision Manufacturing
- MAE 716 Random Vibration

MS PROGRAM FOR ME STUDENT

- MAE 713 Principles of Structural Vibration
- MAE 740 Advanced Machine Design I
- MAE 545 Metrology in Precision Manufacturing
- MAT 700 Modern Concepts in Materials Science
- PY 516 Physical Optics
- MA 501 Advanced Math for Engineers and Scientists I
- MA 502 Advanced Math for Engineers and Scientists II
- MAE 695 Master's Thesis Research

MS PROGRAM FOR COMPUTER SCIENCE STUDENT

- CSC 501 Operating Systems Principles
- CSC 506 Architecture of Parallel Computers
- CSC 512 Compiler Construction
- ECE 521 Computer Design and Technology
- CSC 715 Concurrent Software Systems
- MAE 545 Metrology for Precision Manufacturing
- MAE 789 Digital Control Systems
- ECE 764 Digital Image Processing

MS PROGRAM FOR MATERIALS SCIENCE STUDENT

- MAT 700 Modern Concepts in Material Science
- MAT 710 Elements of Crystallography and Diffraction
- MAT 715 Transmission Electron Microscopy
- MAT 712 Scanning Electron Microscopy
- MAT 722 Advanced Scanning Electron Microscopy and Surface Analysis
- MAE 545 Metrology for Precision Manufacturing
- PY 516 Physical Optics
- ECE 738 IC Technology and Fabrication
- MAT 695 Master's Thesis Research

MS PROGRAM FOR PHYSICS STUDENT

- PY 516 Physical Optics
- PY 552 Introduction to Structure of Solids I
- PY 753 Introduction to Structure of Solids II
- PY 781 Quantum Mechanics I
- PY 782 Quantum Mechanics II
- PY 783 Advanced Classical Mechanics
- PY 785 Advanced Electricity and Magnetism I
- PY 786 Advanced Electricity and Magnetism II
- MAT 700 Modern Concepts in Material Science
- MAE 545 Metrology for Precision Manufacturing
- PY 695 Master's Thesis Research

SHORT COURSES AND TV COURSES

Six graduate level courses: Scanning Electron Microscopy (MAT 712), Advanced SEM Surface Analysis (MAT 722), Modern Concepts in Material Science (MAT 700), Mechanical Properties of Materials (MAT 705), and Metrology (MAE 545) have been offered as video courses nationwide via National Technological University. In a typical year, approximately 120 students from industry and national laboratories participate in these courses. Future plans call for a MS program in Precision Engineering to be offered via the television network.

TECHNICAL REPORTS

Volume 1 - 1983	December 1983	136 pages
Volume 2 - 1984	January 1985	168 pages
Volume 3 - 1985	January 1986	294 pages
Volume 4 - 1986	January 1987	255 pages
Volume 5 - 1987	December 1987	336 pages
Volume 6 - 1988	December 1988	362 pages
Volume 7 - 1989	March 1990	357 pages
Volume 8 - 1990	March 1991	385 pages
Volume 9 - 1991	March 1992	382 pages
Volume 10 - 1992	March 1993	289 pages
Volume 11 - 1993	March 1994	316 pages
Volume 12 - 1994	March 1995	268 pages
Volume 13 - 1995	January 1996	251 pages

Volume 14 - 1996	January 1997	232 pages
Volume 15 - 1997	January 1998	298 pages
Volume 16 – 1998	January 1999	258 pages
Volume 17 – 1999	January 2000	232 pages
Volume 18 – 2000	January 2001	274 pages
Volume 19 – 2001	January 2002	201 pages
Volume 20 – 2002	January 2003	328 pages
Volume 21 - 2003	January 2004	208 pages
Volume 22 – 2004	February 2005	207 pages
Volume 23 – 2005	February 2006	255 pages

PUBLICATIONS

PAPERS PUBLISHED

1. Bolotin, G., G. Buckner, N. Jardine, A. Kiefer, J. Raman, V. Jeevanandam, "A Novel Instrumented Retractor to Monitor Tissue Disruptive Forces during Lateral Thoracotomy", *41st Annual Meeting of The Society of Thoracic Surgeons*, Tampa FL, (2005).

2. Brehl, D., Sohn, A. and T.A. Dow, "Micro-Maching Using EVAM", *Proceedings of the Twentieth Annual Meeting of the ASPE,* 37, 407-410, (2005).

3. Buescher, N., T.A. Dow, A. Sohn, J. Roblee, B. Norland, "Live-Axis Turning", *Proceedings of the Twentieth Annual Meeting of the ASPE,* 37, 25-28, (2005).

4. Dixit, R.K. and G.D. Buckner, " Sliding Mode Control and Observation for Semiactive Vehicle Suspensions", *Vehicle System Dynamics,* 43, (2), (2005).

5. Garrard, K. P., T. Bruegge, J. Hoffman, T. Dow and A. Sohn, "Design Tools for Freeform Optics," *Proceedings of the SPIE*, 5874, (2005).

6. Gibson, N.S., Buckner, G.D., Choi, H. and F. Wu, "Confidence Interval Networks for Bounding Model Uncertainty: Experimental Evaluations on an Active Magnetic Bearing System", *Proceedings of the 2005 IEEE Mid-Summer Workshop on Soft Computing in Industrial Applications, Helsinki Finland,* June (2005)

7. Kuniholm, J., Buckner, G.D., Nifong, W. and M. Orrico, "Automated Knot Tying for Fixation in Minimally Invasive, Robot Assisted Cardiac Surgery," *ASME Journal of Biomechanical Engineering,* 127, (6) 1001-1008, (2005).

8. Lamonds, L., N. Wanna, R. Woodside, T.A. Dow, K.P. Garrard and A. Sohn, "Design and Fabrication of Optical Systems," *Proceedings of the Twentieth Annual Meeting of the ASPE,* 37, 41-44, (2005).

9. Lamonds, L, Wanna, N., Woodside, R, Dow, T., Garrard, K., Sohn, A., "Design and Fabrication of a Two-Mirror Diamond Turned Telescope", *Progress Report #1, Navy Electro-Optics Center*, August, 2005.

10. Lawrence, B., Mirka, G. and G.D. Buckner, "Adaptive System Identification Applied to the Biomechanical Response of the Human Trunk during Sudden Loading", *Journal of Biomechanics,* 38, (12), 2472-2479, (2005).

11. Palmer, J., B. Dessent, J.F. Mulling, T. Usher, E. Grant, J. W. Eischen, A. Kingon and P. Franzon, "The design and Characterization of a Novel Piezoelectric Transducer-Based Linear Motor," IEEE/ASME Transactions on Mechatronics, June (2004).

12. Panusittikorn, W., M.C. Lee, P.I. Ro, "Modeling and Sliding Mode Control of Friction-based Object Transport using Two-mode Ultrasonic Excitation," *IEEE Trans. on Industrial Electronics*, 51 (4), 917-926, (2004).

13. Ro, P.I. and Y. Yin, "Intelligent Industrial Transport System using Ultrasonic Flexural Vibration," *Proceedings of the National Science Foundation DMII Grantees' Meeting*, Scottsdale, AZ, (2005).

14. Sohn, A., K.P. Garrard, T. Dow and T. Bruegge, "Simulation of Manufacturing Errors for Freeform Optics," *Proceedings of the Twentieth Annual Meeting of the ASPE*, 37, 45-47, (2005).

15. Stevens, J.M. and G.D. Buckner, "Actuation and Control Strategies for Miniature Robotic Surgical Systems", *ASME Journal of Dynamic Systems, Measurement and Control*, 127 (4) 537-549, (2005).

16. Wan Q et al, P.I. Ro, "Forced Convective Cooling via Acoustic Streaming in a Narrow Channel Established by Vibrating Piezoelectric Bimorph," *Flow, Turbulence, and Combustion*, (2005).

17. Wu, T. and Ro, P.I., "Heat Transfer Performance of a Cooling System Using Vibrating Piezoelectric Beams," *Journal of Micromechanics and Microengineering, 15,* 213-220 (2005).

16. Zohni, O., Buckner, G.D., Kim, T., Kingon, A., Maranchi, J. and R. Siergeiej, "Adhesion Layer Effects on the Fabrication of MEMS-based PZT Devices Deposited on Silicon Nitride Coated Substrates", *Proceedings of the Second International Symposium on Adhesion Aspects of Thin Films,* Savannah, GA, November (2005)

REPORTS PUBLISHED

1. Bruegge, T., Hoffman, J., Dow, T.A., Garrard, K.P. and A. Sohn. "Advanced Design Tools for Freeform Optics", *US Army Space and Missile Defense Command Scientific and Technical Report W9113M-04-P-0149,* March 2005."

2. Dow, T.A., K.P. Garrard, K. Folkert, "Metrology Artifact Design", *2005 Precision Engineering Center Interim Report,* pp. 9–14, September 2005

3. Dow, T.A., N. Wanna, "Design of Reflective Optical Systems", *2005 Precision Engineering Center Interim Report,* pp. 1-8, September 2005

4. Dow, T.A., A. Sohn and N. Buescher, "Live Axis Turning", *2005 Precision Engineering Center Interim Report,* pp. 15-22, September 2005

5. Dow, T.A., T. Bruegge, A. Sohn and K.P. Garrard, "Simulation of Manufacturing Errors for Freeform Optics", *2005 Precision Engineering Center Interim Report,* pp. 23-28, September 2005

6. Dow, T.A. and L. Lamonds, "Fabrication of Optical Systems", *2005 Precision Engineering Center Interim Report,* pp. 29-34, September 2005

7. Dow, T.A., A. Sohn and D. Brehl, "Micro-Machining Using Elliptical Vibration Assisted Machining", *2005 Precision Engineering Center Interim Report,* pp. 35-40, September 2005

8. Dow, T.A. and R. Woodside, "Metrology of Reflective Optical Systems", *2005 Precision Engineering Center Interim Report,* pp. 49-54, September 2005

9. Dow, T.A. and K.P. Garrard, "Design Tools for Freeform Optics", *2005 Precision Engineering Center Interim Report,* pp. 63-71, September 2005

10. Ro, P.I. and Y. Yin, "Non-Contact Transportation Using Flexural Ultrasonic Wave", *2005 Precision Engineering Center Interim Report*, pp. 55-62, September 2005

11. Scattergood, R. and T. Kennedy, "TEM and Raman Spectroscopic Analysis of Single Point Diamond Turned Silicon", *2005 Precision Engineering Center Interim Report,* pp. 41-48, September 2005

PAPERS SUBMITTED OR ACCEPTED FOR PUBLICATION AND PRESENTATIONS

1. Eischen, J. W., "A Study of the Relationship Between Buckling and Wrinkling of Membranes," Proceedings of the Ninth Pan American Congress of Applied Mechanics, Merida, Mexico, January (2006).

2. Jernigan, S., G. Buckner and J. W. Eischen, "Finite Element Modeling of the Left Atrium to Facilitate the Design of an Endoscopic Atrial Retractor," Proceedings of BIO2006 2006 Summer Bioengineering Conference, Amelia Island Plantation, Ameilia Island, FL, June 21-25 (2006).

PATENTS GRANTED

1. United States Patent No. 6,895,682
   A. Sohn, K. Garrard, T. Dow, Polar Coordinate-based profilometer and methods, May 24, 2005

THESES AND DISSERTATIONS

1. Brocato, Brett, *Micro-Machining Using Elliptical Vibrtation Assisted Machining (EVAM),* MS Thesis, North Carolina State University, May 2005

2. Buescher, Nathan, *Live-Axis Turning,* MS Thesis, North Carolina State University, October 2005

3. Folkert, Karalyn, *Metrology Artifact Design,* MS Thesis, North Carolina State University, August 2005